Bridging scales in the Arbsucular Mycorhizal Symbiosis

Corentin Bisot

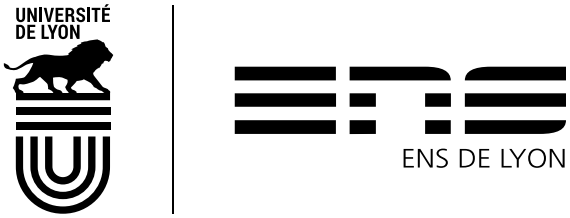

THÈSE
en vue de l'obtention du grade de Docteur, délivré par
l'ÉCOLE NORMALE SUPERIEURE DE LYON

École Doctorale N° 512
École Doctorale en Informatique et Mathématiques de Lyon

Discipline : Informatique

Soutenue publiquement le 10/10/2024, par :

Corentin Bisot

Bridging scales in the Arbuscular Mycorhizhal Symbiosis

Relier les échelles dans la symbiose mycorhizienne à arbuscules

---

Devant le jury composé de :

Schnepf, Andrea	Prof. Forschungszentrum Jülich	Rapporteure
Fricker, Mark	Prof. University of Oxford	Rapporteur
Herbert, Eric	Dr. MCF Université Paris Cité	Examinateur
Latapy, Matthieu	Prof. Sorbonne Université	Examinateur
Kiers, Toby	Prof. Vrije Universiteit Amsterdam	Examinateur
Shimizu, Tom	Prof. AMOLF	Co-directeur de Thèse
Godin, Christophe	Prof. ENS Lyon	Directeur de Thèse

À Pierre, Ségolène et celles et ceux avant eux, les docteurs
À Grand-Marthon et Bonne-Maman

Contents

Chapter 1

Introduction

1.1 Acknowledgement

PhD students, like plants and fungi, do not just grow out of thin air. In French, "thinking hard" can be translated to "phosphorer" which would literally translate to something like "phosphorate". In order to "phosphorate", one needs to be brought phosphorous. While I had my own roots, the environment around me allowed my own "phosphoring" to happen.

Data was the bread and butter of my work, and there would simply have been none of it without Loreto Oyarte Galvez. I grew on a fertile ground that she cultivated with hard work. She was herself helped by AMOLF software, electrical and mechanical engineers Marko Kamp, Marco Seynen, Bas Steenbeek and Jan Zomerdijk.

At the root of everything, there would also have been no data if there had not been fungi growing, and I was very lucky to never worry about this thanks to Marije Van Son and Bianca Turcu. There would also have been no phosphorus data without the help and patience of Rob Broekman.

I guess I should also thank *Rhizophagus irregularis* and *Daucus carota*, especially the ones from plate 94_20201123, for their cooperativity both together and with me.

Finding the rich patches of ideas in a wide open research space requires scouts. Felix Kahane, Kai-Kai Lin, Simon van Staadlduine, Thomas Clerc, Daan Te Rietmole, Antoine Babu and Amin Hamzaoui have all contributed over their internship with me to the final work presented here.

Working close to my roots, rhizospheric fauna, feeding me through their own "phosphoration", all the PhD students and colleagues from France and Netherland. Philippe Bourrianne, Justin Stewart, Victoria Terry, Rachael Cargill, Julien Derr, Olivier Ali, Annamaria Kiss, Romain Azais, Malin Klein, Ibrahim Cheddadi, Jeanne Abitbol-Spangaro, Jonathan Legrand, Antoine Chevallier, Landry Duguet, Elsa Gascon, Lucie Poupardin, Max Kerr Winter, Isaty Melogno, Marianne Lang, Isaac Williams, Guillaume Cerutti, Guillaume Mestdagh, Manuel Petit, Karamoko Samassa and others...

Vasilis Kokorris, more than just a root name, AMF wizard, and rising star to whom I wish future

nuclear fusion. Merlin Sheldrake whose book I still haven't finished because I lost myself in the bibliography. Stuart West for the rigorous writing advises. Howard Stone for his insights into the world of low-Reynold number fluid dynamics.

All the support staff (administrative, hygiene, cooking...) from all institutions in France and the Netherland for their patience, care and smiles.

Theodora Jacobs for the illustrations in 1.3 and also to the whole team of the Living Soils Workshop. Telling a scientific story to a multidisciplinary audience I learned as much preparing talks than facilitating "L'Atelier des Sols Vivants".

Christophe Godin, multifaceted soil particle, reflecting simultaneously on plant meristem, general relativity maths and fungal flows, multiplied in an almost supernatural way to ground and structure a whole lab and my own work. Storms can easily blow away plants that are not lucky to have solid soil to root themselves.

Tom Shimizu, limpid water, migrating across rainy countries, infiltrating every interstice of detail to clear out the dust and slowly seeping to the essential. Vast ocean of knowledge, crossed by waves, leaving space to grow and explore.

And of course Toby Kiers, the warm sun on top of all this, worldwide superstar, energy source of everything, leading the way from east to west.

And all the peripheral life above and below ground: housemates, family, friends.

1.2 Navigating this document

1.2.1 Thesis summary

The microscopic life of soils is responsible for large macroscopic flows of matter at a planetary scale. However, the complexity of ecosystems and the organisms that comprise them makes it difficult to scale from one level to another. The thesis titled "Linking Scales in Arbuscular Mycorrhizal Symbiosis" establishes connections between objects ranging from the size of a lipid droplet ($\sim$ 500nm) to the total length of fungal hyphae at a planetary scale ($\sim 10^{20}$ m).

The first chapter (2) introduces a framework for analyzing fungal colonies through 'travelling waves', connecting the microscopic scale of individual hyphal behavior to macroscopic variables such as density and propagation speed. These results constitute the first analysis of experimental data with high degree of spatiotemporal resolution of a branching organism's morphogenesis dynamics.

The second (3) details the ecological consequences of this macroscopic propagation by quantifying the resource exchange it entails. This result sheds new light on mycorrhizal science by linking phenotypic traits of fungal colonies to their impact on trade with plants in different environments.

The third chapter (4) focuses on the microscopic underpinning of bidirectional resource trade within the Arbuscular Mycorhizhal (AM) fungal colonies. It aims at characterizing the robust physical mechanisms that allow the directed transport of carbon and phosphorous over the centimeter wide colony.

In an annex chapter (5), the results are projected at the scale of ecosystems. The work on the radius of the hyphae particularly helps to reduce the calculation uncertainty on the total biomass

of mycorrhizal fungi in an ecosystem and at a planetary scale.

I thought it would be an interesting exercise to see how this PhD would sound if it was being told to my niece. The result can be found in an Introduction "hors des sentiers battus" 1.3. It is in French since she does not speak English yet. As the title states, I went a bit off-road, both from this initial project and from classical ways of telling science. The result is probably not fully understandable by my niece. But I personally enjoyed finding other words to tell a story where my own three years journey entangles itself with the 400 million year one of my object of study.

A more classical introduction can be found in 1.4. It introduces what the system is and builds from the literature what the main questions were before the start of this PhD.

In the conclusion (6), we summarize what answers to these questions were found and what kind of new questions and line of research they open up. We also give a brief note about potential applications of the present work.

1.2.2 Chapter context

- Chapter 2 has been submitted to the journal Nature in an almost identical form a first time in August 2023 and a second time in May 2024.
- Chapter 3 has been widely reviewed within the team and is close to submission.
- Chapter 4 is a first draft of a paper. Further work is needed but it lays down important elements for understanding flow in the AM fungal colony.
- Chapter 5 has been widely reviewed within the team and is close to submission. The work presented there has mostly been performed by another PhD student but I decided to include it within this manuscript as it provides interesting outlook on the potential applications and it bridges yet another scale.

Exact personal and external contributions are detailed at the beginning of each chapter.

1.3 Introduction "hors des sentiers battus"

La parole nous introduit dans le temps. Elle nous fait vivre sans fin dans le malentendu, les interprétations, les harmoniques. [...] Il y a deux ordres de connaissance, deux sortes de références pour l'homme. Celles qui se rapportent à cette réalité concrète expérimentale qui l'entoure, et celles qui proviennent de cet univers parlé qu'il invente, qu'il institue, qu'il "origine" par la parole, et où il puise sens et compréhension, où il dépasse cette condition réelle de sa vie pour entrer dans un autre univers, qu'on l'appelle fantasmatique, schizophrène, imaginaire, tout ce que l'on veut, peu m'importe : je constate que depuis que l'homme est homme il a éprouvé la nécessité impérieuse de se constituer un autre univers que le constatable et qu'il l'a constitué par la parole, et que cela, il l'a dénommé vérité. [...] Le discours est toujours discret, même quand il se veut démonstratif. Il contient cet arrière-plan d'inconnu qui le rend secret et révélé. Il est discret parce qu'en lui-même il ne s'impose jamais. Lorsqu'il utilise le haut-parleur, lorsqu'il écrase les autres par la puissance des appareils, lorsque la TV parle, il n'y a plus de parole, parce qu'il n'y a aucun dialogue possible.
Jacques Ellul

Brin d'herbe dans le vent

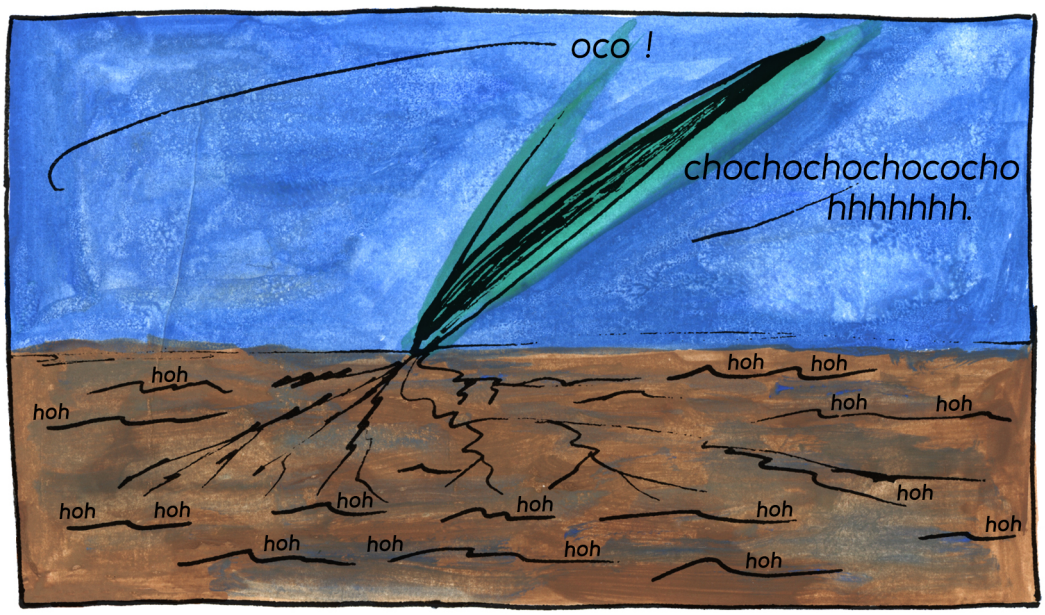

Regarde ce brin d'herbe dans le jardin, que fait-il ? Regarde bien plus près, plus longtemps. Souviens-toi, il y a un mois quand le printemps évaporait peu à peu la rigueur de l'hiver. Ce même brin d'herbe n'était alors qu'une petite pointe verte sur le sol brun et humide. Maintenant c'est un fier ruban déroulé vers le soleil. Il a grandi. La matière alentour s'est réunie pour devenir brin d'herbe. Par quelle magie ?

Le temps passe et autour d'un être le monde flue et reflue laissant parfois une trace. C'est la vie, cette capacité à écrire son histoire. Mais pour écrire, il faut des lettres. Beaucoup de lettres...

Imagine s'il fallait décrire ce brin d'herbe dans tous ses détails. Comment il s'agite quand une brise du sud légèrement turbulente s'écoule le long du pli de sa tige. Comment la goutte de rosée au petit matin s'accroche à sa pointe. Comment son vert rougeoie sous le soleil de midi. Il faudrait des pages et des pages, des millions ou même des milliards de lettres. Pour se simplifier la vie le brin d'herbe n'utilise principalement que cinq lettres. Ces cinq lettres qui permettent d'écrire tous les sortilèges dont le vivant se sert pour faire face au monde sont C H O N P. Mais où trouve-t-il toutes ces lettres ?

Dans le monde... L'air est un désert plein d'indicible. Comme si une malédiction ancienne l'avait bâillonné et qu'il tentait en vain de former des mots. "nn !!!" "nn !!!" "nn !!!" "nn !!!" Et parfois "oo!!" Et seulement rarement un son presque articulé "oco !!!!".

L'eau est un murmure régulier et constant. Elle se coule partout en répétant "hoh hoh hoh hoh hoh..." comme la suggestion joyeuse d'une vie plus simple. Et il y a le sol, mystérieux et secret, qui s'exprime par énigme. Au détour d'un recoin terreux, on trouve parfois des inscriptions étranges "oopoo ?" ou encore "onoo ?"

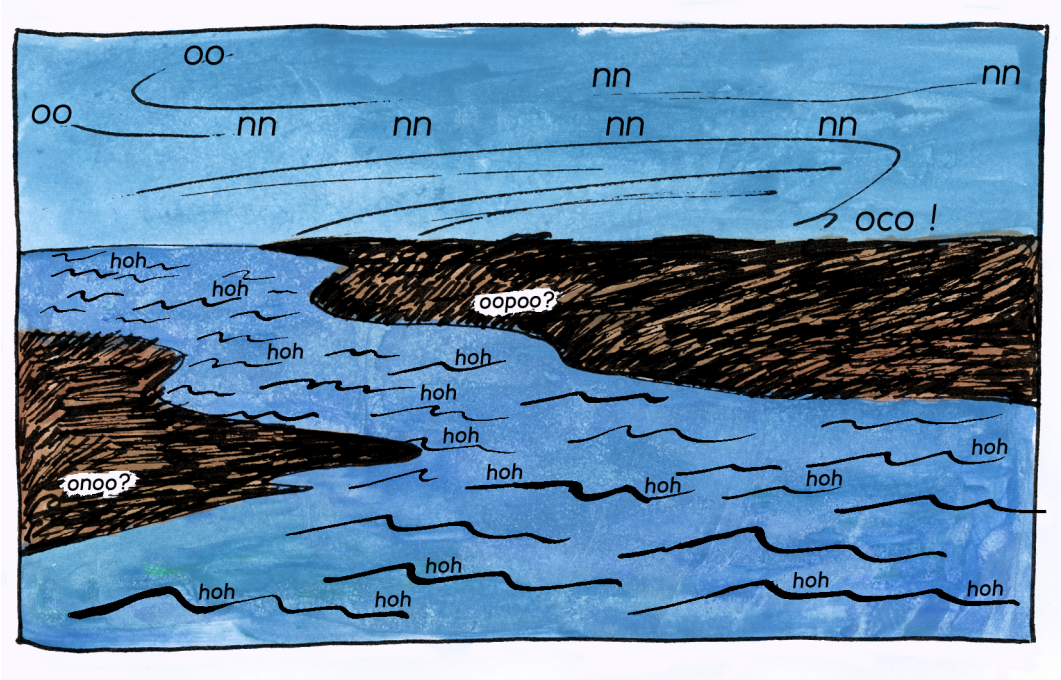

La magie du brin d'herbe est faite d'air, d'eau et de feu. Alors que ses racines trempent dans le " hoh hoh hoh... " régulier de l'eau, que sa feuille accumule le soleil, il attend que l'air se fende d'un de ses rares " oco !!!! ", il le saisit au vol et, riche de toutes ces lettres, écrit joyeusement en cercle un premier mot : "chochochochocochohhhhhhh."

C'est un mot plein d'énergie, quand on le casse il explose dans une ribambelle joyeuse de " oco !!!! ", libérant le feu que lui avait prêté le soleil. Cela est bien amusant. Mais plutôt qu'un feu d'artifice, c'est une machine bien huilée que notre brin d'herbe veut faire tourner. Une bien étrange machine qui permet de sentir, d'absorber, de bouger, mais surtout d'écrire. D'écrire des mots complexes qu'il faudrait une page entière de grimoire pour épeler entièrement. Des mots aux pouvoirs puissants capables de canaliser l'eau, de dompter le feu, de solidifier l'air, de trouver son chemin dans le sol. Non seulement la machine sait écrire ces mots, mais elle en est faite. Ce qui fait sa puissance c'est qu'elle sait s'écrire elle-même. Regarde le jardin, il n'y a pas qu'un seul brin d'herbe mais des milliers. La vie se répand en s'écrivant.

Et les sortilèges supérieurs, ceux qui s'écrivent eux-mêmes ont besoin de plus d'articulation que ce que permettent seulement des C, des H et des O comme on en trouve dans ce mot "chochocho-chocochohhhhhhh." Il faut des N qui, comme un engrenage, enroulent les lettres. Et il faut des P dont le rythme percutant sonne la cadence de la phrase. Où les trouver ? Ces lettres sont enfouies sous terre, et c'est dans ce théâtre que se déploie notre histoire.

Brin d'algue au gré de l'eau

Elle commence il y a bien longtemps. Un lointain ancêtre de notre brin d'herbe – appelons-le brin d'algue - flotte sur l'océan. Le soleil et l'eau lui suffisent presque. De temps en temps il pêche un N ou un P qui dérive au gré des vagues.

Mais un jour, parce que les nuages n'étaient pas au bon endroit, le feu du soleil s'accumule à un des bords de l'océan. C'est comme une démangeaison, l'océan doit se rééquilibrer, résoudre cette tension. Il tente de se circuler, se heurte contre lui-même, et soudain éclate en tempête. Alors que le feu des éclairs se déchaîne, air, eau et terre se mélangent. Tout est sens dessus dessous. Et quand tout se calme, que chacun retourne à sa place, l'algue est surprise de se retrouver loin de l'océan, sur une motte de terre qui lui paraît bien aride.

Le soleil brille aussi bien ici que sur les eaux. Mais il lui manque des lettres pour continuer à écrire son histoire. Elles sont là, tout proche, l'algue peut presque les sentir. Mais elle ne connaît pas les tours et détours, les tunnels secrets, les caves mystérieuses du sol qui reposent sous elle.

Vient alors un intrigant personnage. Il est difficile à décrire ; appelons-le Myco. Il a survécu ici en se nourrissant des débris de mots apportés par les tempêtes. Un peu mercenaire, un peu roublard, partout et nulle part à la fois, il est en même temps la tête et le bras armé d'un vaste réseau de contrebande. Souterrain et secret, c'est le cœur de son existence de connaître les coins et recoins de la motte de terre, d'y trouver des lettres, pour sa propre consommation ou à échanger à prix d'or là où elles manquent le plus.

Le brin d'algue s'attend à être digéré. Il est plein de ces C arrachés à l'air sous la lumière du soleil et qui manquent cruellement dans les souterrains sombres. Mais une idée lui vient et il s'exprime à peu près en ces termes.

" Oh Myco, maître de la terre et de l'eau. J'entends d'ici un bruissement de " hoh hoh hoh... " le long de tes membres. Érudit des royaumes souterrains, tu sais en déchiffrer les " oopoo ? " et les " onoo ? " griffonnés sur les murs. Moi je suis un maître du feu et de l'air, je sais entendre les rares " oco !!!! " dans le vent autrement désert. Je sais accueillir le feu du soleil sans me brûler. Je sais formuler patiemment le mot d'artifice " chochochochocochohhhhhhh.". Unissons nos forces pour

naviguer les quatre éléments, collectionner rapidement les lettres, s'écrire se réécrire. Couvrons de vert le dessus de cette motte de terre et de blanc son dessous. "

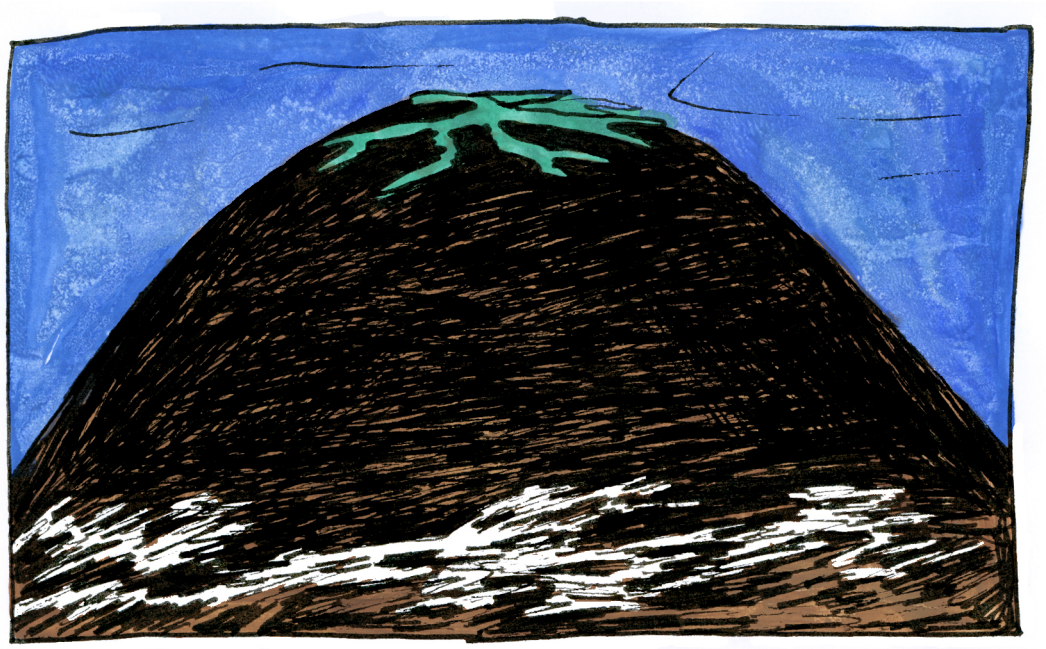

Brin d'herbe partout

Quand notre histoire reprend, les terres arides ont été remplacées par une matrice humide brune tachetée de noir, couverte d'une dense chevelure verte. La magie symbiotique de Myco et du brin d'algue a enchanté le monde. Parfois un insecte vrombissant mâchonnant un bout de feuille dorée se fait saisir par un oiseau vorace. Parfois Myco, maintenant gavé de C, attire la convoitise d'un ver qui passait par là. Myco y perd un ou deux membres de son organisation. Mais sa hiérarchie est suffisamment souple pour que cet incident ne l'ébranle pas. Et Myco sait aussi nourrir ses alliés, ils s'occuperont bien assez vite de ce ver dérangeant.

De plus grandes menaces pèsent sur lui. En effet, longtemps la séparation des pouvoirs est restée équilibrée. L'air et le feu pour l'algue, l'eau et la terre pour lui. Mais une méfiance s'est peu à peu installée. Un jour Myco s'est plaint de ne plus trouver ni N ni P. Il a affirmé qu'il lui faudrait plus de C pour grandir et chercher plus loin. L'algue les lui a cédés en toute confiance. Mais la situation s'est prolongée. L'algue se privant de presque tous ses C.

Elle décida d'aller voir elle-même pour en avoir le cœur net. Plutôt que de pousser vers le soleil elle mit toute sa ressource à tendre vers les profondeurs. Elle remarqua vite que Myco lui avait menti. Les " oopoo ? " et les " onoo ? " étaient partout, comme les hiéroglyphes au cœur d'un tombeau égyptien. L'algue laissa là sa racine, périscope vers les mondes souterrains lui permettant de s'assurer de la bonne foi de Myco. C'est ainsi qu'elle devint brin d'herbe. Mais le brin d'herbe

s'aperçut vite que sa racine pouvait être plus qu'un outil de surveillance. Cette nouvelle interface avec les profondeurs invitait à développer la magie de l'eau et celle de la terre.

Peu à peu les " hoh hoh hoh hoh... " du murmure de l'eau commencent à couler le long de sa tige avant de s'ennuager vers le soleil. Et la racine bifurque, se branche, s'affine, explore les interstices. Le sol et ses textes cryptiques deviennent son terrain de jeu.

Mais Myco conserve un avantage. La magie du brin d'herbe reste un art des espaces aériens. Les racines sont grosses, pataudes, fixes, l'eau s'y écoule au goutte à goutte. Seul Myco sait être partout et nulle part à la fois. L'espace et le temps s'indifèrent dans son déploiement. L'eau est sa circulation, son sang. Le brin d'herbe ne peut s'en passer, surtout qu'un nouvel arrivant l'inquiète.

Brin d'herbe en rangs serrés

La quadruple magie opérée par le brin d'herbe avec la participation active de Myco attire en effet les convoitises. Il y a bien eu par le passé les insectes. Certaines années ils ont bien semblé prendre le dessus. Arrivés soudain en nuées, ils avaient rasé de larges étendues de vert. Mais ils avaient de ce fait directement signé leur propre fin. Privés de lettres pour continuer leur multiplication, ils étaient tombés comme des mouches sur le sol. Et les lettres qu'ils avaient volées au brin d'herbe avaient vite été remises à la disposition des graines qui avaient joyeusement germé peu après.

Et puis il y avait eu les animaux en tout genre qui broutaient mollement. Mais eux aussi avaient leurs prédateurs. Et le brin d'herbe s'était rendu difficilement digeste. Si bien que la plus grande partie des phrases avalées d'un trou ressortait aussitôt d'un autre, découpées en petits mots.

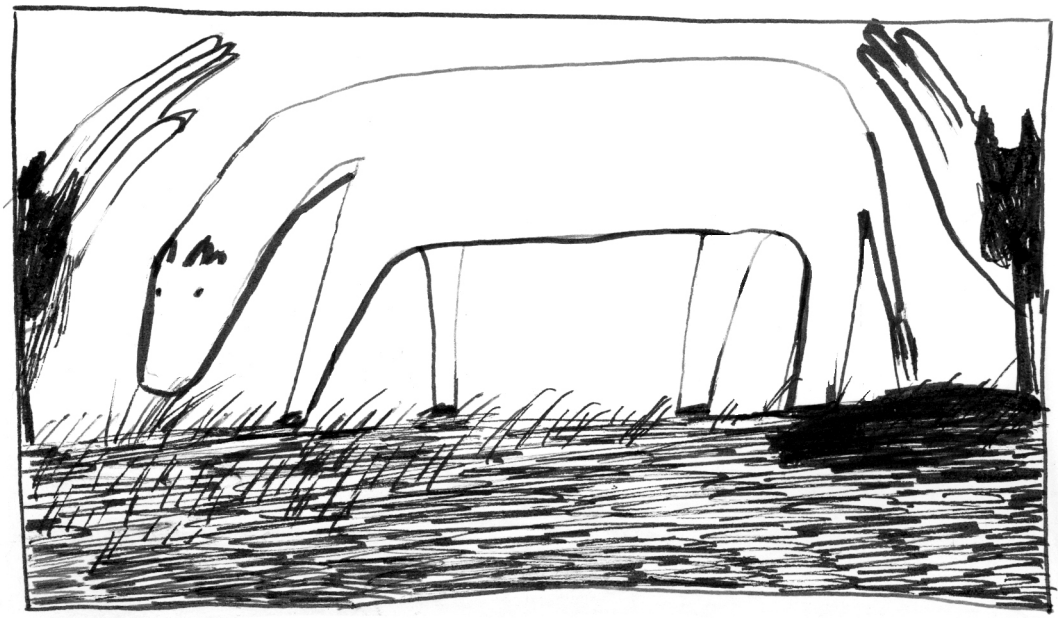

Un jour vinrent des sorciers d'un autre genre. Quoiqu'eux aussi faits de lettres et de mots, leurs langages et leur logique étaient incompréhensibles pour le brin d'herbe, l'insecte, l'herbivore et Myco. Alors que la quête des lettres était le lot commun des mortels, ils croyaient fermement que leur histoire était faite d'autres signes. Elle s'écrivait dans un monde hors de l'air, de l'eau, du feu et de la terre, un monde qui n'existait qu'à leurs yeux, un monde d'idées.

Quoique ces sorciers aient semblé mépriser la brutale immanence de l'alphabet à cinq lettres CHONP, ils savaient pourtant qu'ils en dépendaient. Ils commencèrent donc par conclure un accord avec les herbivores. En échange d'une protection contre leurs prédateurs, il leur serait permis une ponction régulière de leurs troupeaux. Puis, soit parce que les brins d'herbe qui nourrissaient les herbivores vinrent à manquer, soit parce qu'ils pensèrent soudain qu'ils pourraient eux-mêmes manger le brin d'herbe si seulement il se laissait digérer, ils conclurent un marché avec ce dernier. Pour lui ils exhumeraient les secrets souterrains au grand jour, iraient quérir là où nécessaire les N et les P qui lui manqueraient, apporteraient le "hoh hoh hoh..." de l'eau, éloigneraient les insectes et toute chose qui lui ferait ombre. En échange le brin d'herbe dorerait en épis devenant brin de blé.

Spectre des brins

Plus tard, les sorciers entamèrent une puissante nécromancie. Des tréfonds de la terre et de l'océan ils firent revenir à la vie les spectres anciens d'algues et d'herbes pour un ultime feu d'artifice.

Loin sous la terre, ils avaient aussi trouvé des pierres brillantes aux pouvoirs étranges. Leurs effets visibles les avaient fascinés.

Leur corps savait écrire avec les cinq lettres C, H, O, N et P. Mais leur tête ne savait pas, et ce manque de contrôle les troublait. Ils voulaient des machines dont ils seraient maîtres et créateurs, qui feraient exactement ce qui était attendu d'elles. Des pierres brillantes du sous-sol ils développèrent une magie créatrice. Ils s'en servirent pour encapsuler les esprits anciens et capturer l'énergie de leur dernier souffle, animant de nouveaux êtres aux reflets métalliques. Paradoxalement, ils projetèrent que ce plan leur permettrait de s'extraire de la dure matérialité du monde et qu'ils pourraient ainsi se fondre dans le monde des idées si cher à leurs yeux.

Il leur fallait donc montrer qu'ils ne dépendaient plus de personne pour trouver les lettres nécessaires à leur survie. Ils développèrent un sort capable d'arracher des N aux sons étouffés du vent. De ses "nn!!!" étouffés, à force d'explosion et d'énergie, ils arrachèrent des "nhhhh." Presque vivants. Il leur fallait de même un moyen pour obtenir des P. Plutôt que de chercher patiemment dans le sol, ils se mirent alors à broyer les montagnes avec des mâchoires de métal et à isoler les P de la poussière obtenue.

C'était un nouveau coup porté aux affaires de Myco. Le brin de blé avait renouvelé son pacte avec les sorciers, signant sa complète soumission. Les sorciers assureraient l'ensemble de la vie du

brin de blé. Il serait planté au soleil avec pour seule mission de répéter "Chochochochohcocho." le plus vite possible, tandis qu'on s'assurerait entièrement du reste de sa subsistance à partir des nouvelles sources "infinies" développées par les sorciers. La concurrence pour Myco était trop difficile et il dut se retirer. Mais une rébellion montait chez les sorciers. Certains disaient que la puissance récemment acquise n'avait été que le remplacement d'une matérialité par une autre. Que même si certains clamaient qu'ils s'étaient libérés de la quête des lettres, c'était pour s'enchaîner avec des maillons de fer à une poursuite dont nul ne maîtrisait plus la finalité. Il y avait eu une trahison interne au groupe des sorciers. Non satisfaits de soumettre le brin de blé et l'herbivore, un sous-groupe plus malin, plus brutal, ou simplement plus peureux avait entrepris de subjuguer les autres. Ils avaient inventé de toute pièce ce récit d'émancipation : que le métal et la nécromancie permettraient de s'extraire du monde physique pour vivre pleinement d'idées.

C'était l'équilibre des forces fondamentales qui était en jeu. L'abondance soudaine de lettres arrachées au vent, à la montagne et aux morts devenait paradoxalement un danger pour la vie. Les histoires s'écrivaient à toute vitesse, concaténation de mots plus que vraies phrases, voire graffitis inintelligibles. L'air se mettait à dire "non!!!!" de temps en temps et "oco!!!" plus fréquemment. Le feu du soleil, effrayé par ces cris, tentait de rester près du sol. Ce faisant il évaporait l'eau de la terre ou surchauffait tellement que des pluies torrentielles tentaient de venir éteindre l'incendie. Pressé lui aussi, le "hoh hoh hoh..." de l'eau, d'un doux murmure était devenu un halètement et, impatient, se hâtait vers l'océan. Il n'avait pas le temps d'un détour dans les creux de la terre. Plus inquiétant encore, des êtres marins et lacustres, autrefois inoffensifs mais qui florissaient aux temps d'abondance, profitaient de l'omniprésence des lettres pour se multiplier, étouffant poissons, crevettes et coquillages.

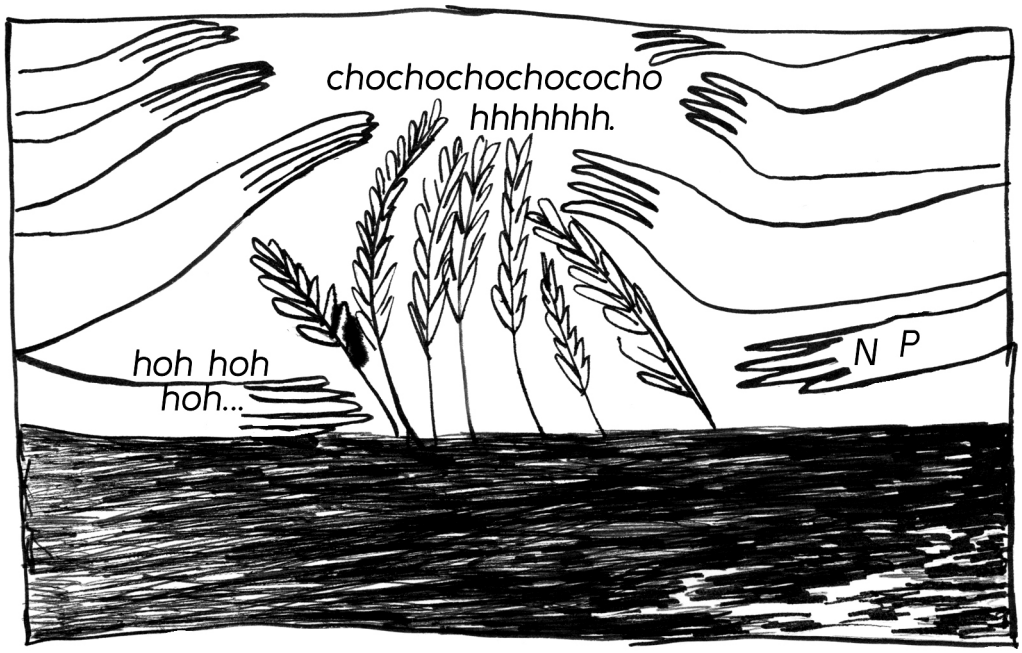

Quoique ce constat soit effrayant, c'était mal comprendre les sorciers que de croire qu'il suffirait à faire prendre un tournant à l'histoire qu'ils voulaient écrire. D'autant qu'alors que toute la vie partageait les mêmes lettres pour s'écrire, aucun sorcier n'était sûr qu'un autre sorcier partageait son monde d'idées. Ainsi tandis que certains voulaient que le futur raconte de confortables coussins, d'autres rêvaient des étoiles. D'autres aussi voulaient passer la nécromancie à son dernier stade et subsister au-delà de l'espace et du temps. Cette cacophonie de désirs n'avait en commun que la peur terrible qu'ils ne soient pas accomplis.

Bien pâle, en comparaison, semblait l'idée, portée par quelques rebelles, que l'histoire se dirait mieux si elle était rythmée par la mesure. Ce serait une mélodie au thème répété mais que de légères variations feraient lentement changer. On pouvait rêver d'étoiles ou de coussins profonds, mais des centaines de générations étaient nées et disparues sans coussins profonds ni balade dans les étoiles. Celle-là pouvait bien aussi passer son tour, tant qu'elle pouvait se donner l'illusion qu'elle aurait écrit quelques phrases qui y mèneraient. On ne se débarrasserait pas de la souffrance, mais on pouvait au moins se libérer de l'angoisse étouffante de ne pas atteindre son but. Ce dernier était de toute façon si mal défini et si mouvant qu'on était à peu près sûr de ne jamais y arriver.

Il fallait écrire cette musique. Mais elle ne devait pas être simplement tissée d'idées vaporeuses. Elle devait s'ancrer dans le réel, s'écrire avec les mêmes lettres qu'utilisent le brin d'herbe, l'herbivore, l'oiseau et Myco.

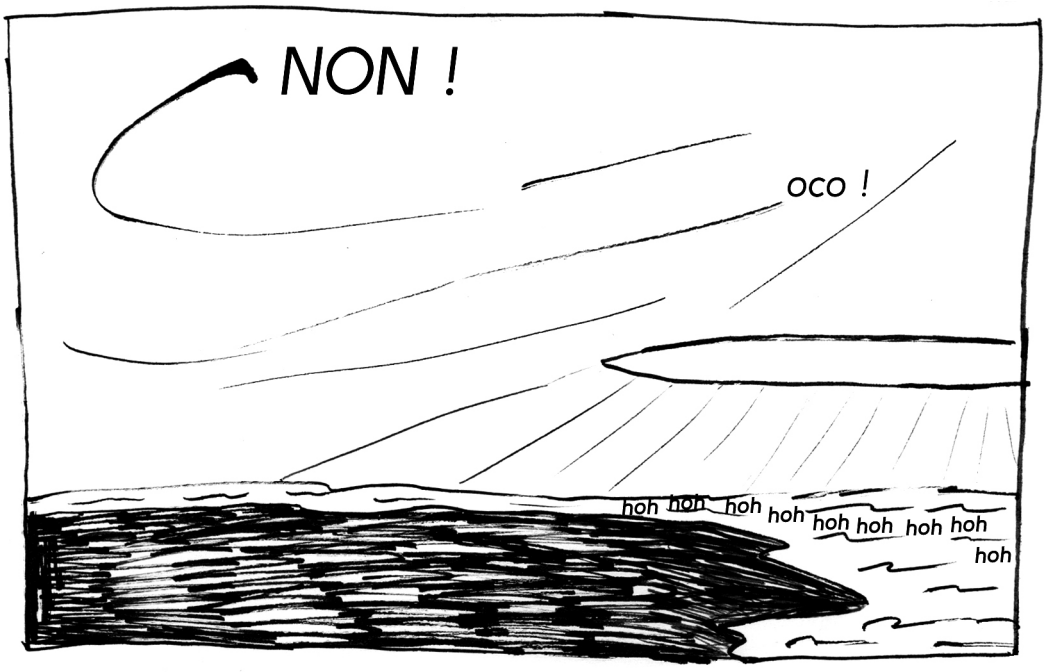

Brins de fils

C'est là que commence mon histoire. Je suis un de ces sorciers. Quoique le monde des idées, avec ses sommets blancs et éthérés, m'attire, j'ai voulu plonger ma tête dans les boues brunes du monde pour tenter d'y dérouler un fil. En tirant sur ce fil, j'espère démêler l'enchevêtrement complexe des récits que le vivant tente d'écrire. Ce fil on l'appelle hyphe et c'est un des membres du gang de Myco. Il est dix à cent fois plus fin qu'un cheveu, et, entièrement déroulé, on pourrait l'étendre sur un dixième de la voie lactée. Mais Myco ne rêve pas d'étoiles, et l'hyphe s'immisce dans les interstices de presque toutes les terres émergées. Peut-être qu'en suivant ce fil blanc dans ses tours et détours, une histoire s'écrit. Une de celles gorgées de terre qui nous enracinerait. Ou plutôt, car ce dernier mot a des résonances douteuses, "qui nous emmycerait".

D'autres sorciers sont plus terre à terre. Ils voient dans mon travail l'espoir qu'on pourrait, en apprenant à le connaître, dompter Myco; jusqu'à pouvoir le semer par grandes poignées avec le blé. Ou ils pensent que par sa magie de la terre, les trop fréquents "oco!!!! " de l'air pourraient être enfouis dans des recoins profonds, où leurs sons étouffés n'effraieraient plus le feu du soleil.

Je les laisserai écrire ces histoires si elles tiennent debout. Pour ma part je crois que c'est l'intrigante beauté de ces fils blancs que j'aimerais raconter avec des C, des H, des O, des N et des P. Une beauté qui tire son éclat du fait qu'elle a été dégrossie et affinée du roc de l'expérience par une méthode scientifique.

Il est facile d'inventer des contes qui flottent librement dans le monde des idées. Il est plus laborieux de tisser patiemment un aller-retour de cordes entre les mondes, que d'autres pourront dans le futur parcourir avec confiance. Peut-être que certaines cordes céderont sous le poids de leurs

investigations, peut-être que la toile entière lâchera si on trouve que les pitons où on l'avait ancrée étaient faits de roches friables. Mais peut-être qu'il restera un fin fil à parcourir.

Du fil au filet

J'ai dit que j'avais plongé la tête dans la terre. C'est un léger mensonge. Les cordes que l'on tend entre le réel et les idées sont soumises à des examens rigoureux. Pour qu'elles résistent, j'ai cédé au fait de les tisser de fil de fer. C'est bien à force de métal et de feu fossile que nous avons sorti Myco de terre et réussi à l'observer là, suspendu entre deux mondes. Pas tout à fait là où il pourrait déployer toute sa magie de la terre, mais bien vivant quand même.

C'est un tour classique dont on connaît les limites, mais qui nous permet de dévoiler les ficelles de l'organisation de Myco sans les casser. Ainsi nous avons pu l'observer suffisamment longtemps pour voir ses hyphes se déployer. Comme notre mémoire imparfaite ne suffisait pas à retenir tout ce que nous voyions, et que la multitude des fils qui s'étendaient dépassait notre entendement, nous avons délégué à des machines de métal de se souvenir de ce qui se passait et d'en extraire les traits les plus saillants.

Dans le bruit de l'expérience un motif se détachait. Alors que les hyphes se divisaient régulièrement en deux, et que nous pensions qu'ils se multiplieraient ainsi jusqu'à couvrir l'espace d'un dense tapis blanc, c'est un filet aux larges mailles qui se déposait lentement. Nous nous sommes posé la question : comment des centaines d'hyphes, chacune traçant son destin, s'entendaient-elles pour maintenir cet ordre ?

Parcourant les cordes de connaissances tendues par d'autres, je me suis rendu compte qu'un tel motif pouvait émerger à partir de deux règles simples. Non seulement les hyphes devaient se diviser, mais elles devaient aussi pouvoir se réunir, et l'une d'elles arrêter sa pousse dès que les mailles du filet devenaient trop fines.

En rejouant les images pour retracer l'histoire de chaque hyphe je me suis aperçu que de telles règles étaient effectivement en place. Un premier pont semblait se dessiner entre l'expérience et les idées. Il reliait Myco à d'autres formes de vie qui se déploient dans l'espace selon des principes similaires.

Ce mouvement collectif fait de fusion pourrait-il inspirer une réflexion sur l'identité ? En moi cohabitent d'innombrables fantômes aux contours flous. Parfois quand un visage doit se présenter au comptoir, l'un d'entre eux se contraint dans une forme. Mais ce n'est qu'un être de chiffon qui s'évapore aussitôt que les regards disparaissent. "Je" n'est pas "un" à l'intérieur. Mais il ne l'est pas non plus à l'extérieur. Cette masse informe et chaotique des moi semble contenue sous la coquille de ma peau, mais elle déborde par tous les pores. Si je suis avec un groupe d'amis, elle commence à s'hybrider et laisser lentement gonfler la vague d'un être en commun.

Il n'y a que maille qui m'aille

Mais j'ai à nouveau légèrement menti en décrivant Myco comme un être unique. Quoique ses frontières soient floues et en constante redéfinition, il en existe bien plusieurs types ou variétés qui ne s'hybrident pas. La taille de la maille semble varier selon la variété choisie. Les types à mailles plus grosses se propagent plus vite plus loin, tandis que ceux à mailles fines colonisent plus lentement l'espace.

Cela nous a donné l'idée que peut-être quelque chose contraint Myco à faire un choix entre densifier sa maille ou la projeter plus loin.

Il faut du fil pour un filet. Et chaque bout de fil s'écrit avec des C. Et chaque C à la disposition d'un Myco vient de la plante, et, par un contrat vieux de plusieurs centaines de millions d'années, il ne s'obtient que contre des P. Mais il faut un filet pour attraper les P comme des poissons, et du fil pour ce filet... Nous voulions résoudre ces dépendances circulaires en mesurant ce qu'il se passait.

Nous étions en mesure de dire combien de C étaient utilisés par Myco pour grandir à chaque instant. Cela dépendait fortement de la taille des mailles : plus elles étaient fines, plus il fallait de fil pour les tisser. Mais il fallait aussi prendre en compte l'épaisseur des fils eux-mêmes. Plus ces derniers étaient épais, plus ils étaient coûteux à construire. Tout cela nous pouvions l'observer sur les images successives que nous prenions de Myco.

Cependant y capturer la capture de nos poissons de phosphore était difficile. Il aurait fallu les prendre sur le fait, regarder en continu. Ce sont en plus de tout petits poissons.

Nous avons donc retourné le problème : plutôt que de regarder combien de poissons étaient pris, nous avons mesuré combien de poissons restaient après un certain temps du déploiement de Myco.

Ce que nous avons remarqué, c'est que plus longtemps le filet est posé, plus il est grand et plus ses mailles sont fines, moins il reste de P, c'est-à-dire plus le nombre de P capturés par Myco est grand. Cette observation n'est pas très étonnante. Mais notre décompte a mis des chiffres précis sur ce phénomène. Nous avions ainsi une nouvelle corde à notre arc. Nous pouvions observer Myco grandir et savoir directement la quantité de P qu'il était en train d'absorber.

Il était temps de raccorder les fils pour voir si le problème s'éclairait. Des images nous pouvions savoir à tout moment combien de P étaient capturés et combien de C étaient dépensés. Ce que nous avons vu, c'est que quelle que soit la variété de Myco, rapide à mailles larges ou lente à mailles fines, pour chaque P capturé il utilisait environ trois C de la plante. De là à dire qu'un prix de trois lettre C par lettre P était fixé par la plante il n'y avait qu'un pas dont d'autres expériences nous ont convaincu.

Tête aqueux

Une question nous obsédait depuis le début de notre travail. Les hyphes ne sont pas simplement des fils inertes, ce sont des tuyaux vivants dans lesquels la matière flue et reflue. Ces tubes sont transparents, et des yeux de métal et de verre peuvent donc en les grossissant regarder à l'intérieur. Se dévoile alors à nous toute la logistique interne de l'organisation de Myco.

C'est un monde avec des lois que nos yeux acclimatés au doux écoulement des fleuves ont du mal à saisir. Nous avons souvent tenté de remonter à la source du courant, espérant trouver ce qui le produisait, suivant à chaque nœud de la maille la direction qui nous semblait la plus prometteuse. Mais quand nous pensions approcher du but, le flot s'arrêtait soudain. La matière que nous voyions bouger, sorte de mayonnaise magmatique, ne semblait pas se couler comme de l'eau. Il y avait ce phénomène étrange par-dessus tout qui ne facilitait pas notre quête : où que nous regardions, l'intérieur de l'hyphe s'écoulait dans les deux sens. Se plonger à l'intérieur des hyphes avait un effet hypnotisant, on y perdait facilement le fil de sa recherche, découvrant à chaque pérégrination un nouveau phénomène qui nous fascinait.

Il fallait pourtant mettre de l'ordre. Tenter de démêler ce qui pouvait unir toutes ces observations. Tout ne coulait pas de source mais il devait bien y avoir une sorte d'organisation que nous ne comprenions simplement pas. Myco s'y retrouvait dans ce chaos après tout, puisque c'était celui-là même qui lui permettait de vivre. Mais le réseau était si complexe qu'il semblait bien difficile de savoir où tirer pour commencer à dérouler un semblant de compréhension. Par un réflexe de réductionnisme qui pourrait paraître presque stupide au vu de l'apparente unité de toute l'organisation de Myco, nous avons décidé de séparer ses membres pour y voir plus clair.

Muni d'une aiguille à coudre nous avons donc coupé les fins liens qui les unissait pour tenter d'en observer une partie plus simple. D'une maille entremêlée, nous avons réussi à obtenir un fil isolé mais encore bien vivant. Ainsi les sources des courants contraires ne pourraient plus nous échapper, il suffirait de suivre cet unique fil d'un bout à l'autre. Étrangement, même isolés du reste, les flux continuent à exister dans deux sens. Cela suggérait qu'il n'y avait pas de source, ou plutôt qu'elle était partout. Puisque notre dissection radicale n'avait même pas stoppé un des deux courants et que nous n'observions presque jamais l'un sans l'autre, il semblait que les deux étaient liés.

En parallèle nous avions commencé une inspection plus détaillée du mouvement à l'intérieur des hyphes. Alors que nous regardions auparavant tout bouger de manière indifférenciée, nous avons réussi à introduire des mouchards au sein de l'organisation de Myco. Ce ne fut pas très difficile de lui faire avaler la pilule. Dépendant pour sa surviede l'absorption continue de son environnement, ce dernier ne pouvait pas se permettre de fermer hermétiquement les frontières de son organisme. Nos mouchards avaient pour rôle de suivre à la trace les gouttes de C dans le corps de Myco. A chaque fois que nous leur envoyions un signal bleu, ils nous répondaient par un signal rouge ou jaune. Par ce jeu de lumière nous pouvions voir les C bouger dans le corps même de Myco. Ils semblaient se suivre parfois à la queue leu leu tous dans la même direction. Nous ne pouvions pas remonter à leur source mais nous savions de toute façon que ce ne pouvait être que la plante. En revanche nous pouvions suivre là où ils allaient, et cela nous menait invariablement à une des têtes de l'organisation. Ce n'était d'ailleurs pas étonnant que le réseau travaille à fournir le haut de sa hiérarchie en C. Ce sont bien ces têtes qui travaillaient activement au recrutement de nouveaux membres, et ils devaient bien nourrir leur intégration.

Toutes les gouttes de C se mouvaient à une vitesse fixe, attirées par leur but. Nous savions aussi que toutes les cellules vivantes sont parcourues de sorte de rails sur lesquels pèlerinent d'étranges marcheurs. Comme des zombies, ils marchent à un rythme régulier en suivant le rail tous dans la même direction. Il nous semblait donc que nous commencions à comprendre un des deux sens du courant. Les gouttes de C étaient transportées par des marcheurs et entraînaient avec elles un peu d'eau comme des pagaies.

La suite est intuitive pour qui a déjà ramé dans un bain. En ramant des deux côtés on produit invariablement un flux contraire au centre. C'est donc le mouvement des gouttes de C, portées chacune par leur minuscule Sisyphe, qui produisait à lui seul les deux directions du courant. Cette explication avait l'avantage de donner un enracinement physique à la réciprocité des échanges. Il suffisait que le P se dissolve dans le contre-courant pour que le simple mouvement des C dans l'autre direction l'amène jusqu'à la plante.

à suivre...

1.4 Scientific introduction

Abbreviations

AMF: Arbuscular Mycorrhizal Fungi

ERM: Extra Radical Mycellium

C: Carbon

P: Phosphorus

MGR: Mycorrhizal Growth Response

Life in the soil

I give here a general introduction to the Plant–Arbuscular Mycorrhizal Fungal symbiosis. Additional introductory elements are also given in the introduction of each chapter. I here limit myself to introducing the elements of the system that are critical to understand the main questions asked in this work.

Soil is a particularly challenging environment to navigate (Fig. 1.1a). To do so, one needs to alternate between air gaps, mineral particles surface, bulk water and occasional organic matter patches. Soil life needs to obtain essential elements for growth and survival (C,N,P,H,O). These can be found in the dead organic matter, dissolved in water, in the air or in other living organisms. Getting those elements from the air will usually require "fixing" them (plant photosynthesis for C, bacterial nitrogen fixing for N) and therefore requires specific biological machinery. Most living organisms therefore rely on the dead organic matter which only need to be decomposed with enzymes to release the essential elements it contains. Some also invest in predation/parasitism/pathogeny i.e. find ways to attack cells from living organisms and extract the ressources from them. Finally, some living organisms that have an assymetry in the nature of their most limiting nutrients can form mutualistic relationships where each partner is being supplied the missing element. The Plant–Arbuscular Mycorrhizal Fungal symbiosis is an example of such mutualistic interaction.

Its intimate nature, with fungal arbuscule cells forming inside the root cortex in close contact with plant cells (Fig. 1.1), qualifies it as an example of "endosymbiosis". One of its uniqueness is in the fact that, despite this intimacy, one fungal colony can be trading resources with multiple plant hosts and reciprocally, a plant host can be interacting with multiple fungal partners.

I first discuss in 1.4.1 the different costs and benefits of the symbiosis. Then in 1.4.2, I introduce what the outcome of such exchange of resources can be. Finally, in 1.4.3, I present what mechanisms may be in place in order to maintain beneficial outcomes for both partners.

1.4.1 Cost and benefits of the symbiosis

Benefits to the plant

Phosphorus (P) : The most well-established benefit of the symbiosis for plant is P nutrition. Plants can receive more than 90% of their P from AM fungi[2]. P is notoriously difficult to capture in soils because of its low mobility. In its anionic form, it tends to bind to Calcium, Aluminium, Iron and Manganese cations in a pH dependent manner[3]. The kinetics of the chelation reaction are

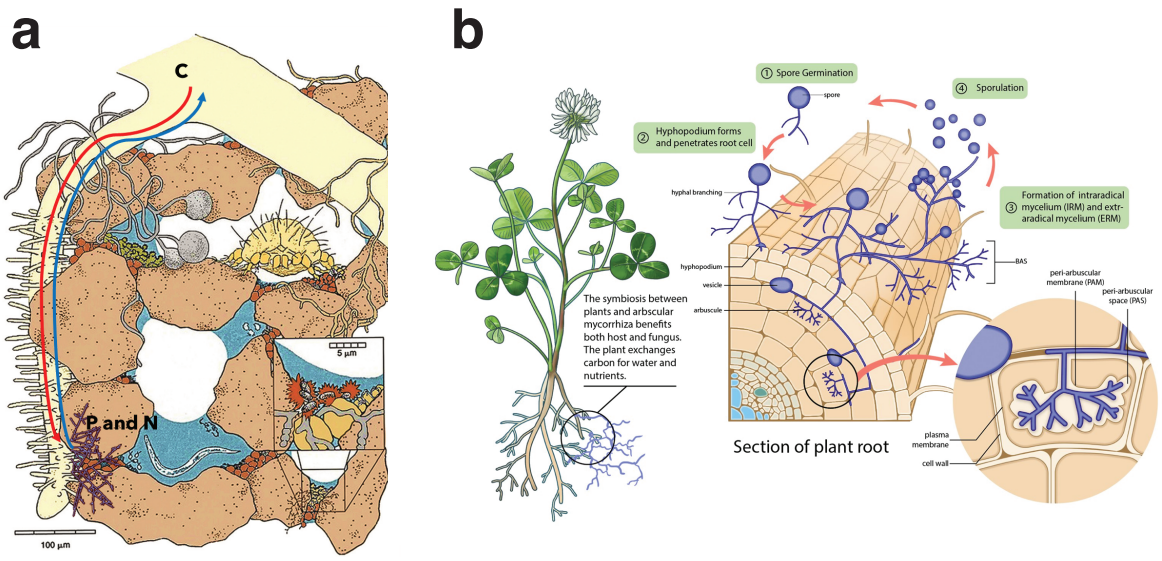

Figure 1.1: **The Plant–Arbuscular Mycorrhizal (AM) Fungal symbiosis (a)** Adapted from [1]. The soil is mostly made of four phases. Mineral grains (brown) of micrometer (clay) to millimeter (sand) size form the framework of the soil. The empty space between those particles can be filled with water (blue) or air (white). Different living organisms, of sizes ranging from micrometer (bacteria, fungi, archaea etc...) to millimeter (plant roots, worms, insects etc...), navigate between these phases in order to find essential resources for survival. Their living or dead matter forms a fourth phase. Fuelled by plant carbon (C, red arrow), AM fungal colony extend their fungal hyphae (purple) in the soil. This allows them to find nutrients like Phosphorous and Nitrogen (P and N) as well as water which is transported back to the plant and can fuel plant growth (blue arrow). **(b)** AMF lifecycle is generally thought to be starting with spore germination. Fungal hyphae emerging from a spore can then grow inside the plant root forming an Intra-Radical Mycellium (IRM). It develops tree like structures inside plant cells that are called "arbuscules". Bidirectional ressource exchange is generally thought to happen at the arbuscule-plant cell interface. It allows the fungal colony to grow its Extra-Radical Mycellium (ERM). ERM can then directly colonize new roots from the same or another plant individual or produce new spores. Credits to Madelyn Neufeld for the illustration.

slow. Efficient acquisition of P is therefore efficiently done by a fast-advancing front of absorbing surface area mowing the not-yet P-depleted or already-P-replenished soil. As I will discuss in Chaper 2, this is exactly what an AMF colony can do: expand in space a "just dense enough" colony of absorbing hyphae. The absorbed phosphorous then needs to be transferred where it's needed. There is some evidence that this is actively mediated and done intracytoplasmically[4].

The specific transport abilities of AMF will be discussed in further details in Chapter 4.

Nitrogen (N) : The role of AMF in plant N nutrition is still controversial to date. N is more mobile than P in soil and a significant amount of plant N nutrition happens through the water uptake pathway. AMF genome displays many different N transporter genes[5] enabling uptake from the soil to the fungal hyphae and transfer with the plant at the intraradical level. Nutrient labelling experiments also have given evidence of N transfer from AMF to plants[6]. There is however to date no direct evidence of active nitrogen transport within AMF hyphae. Depending on the soil nutrient status, it has been hypothesized that AMF could also compete with plants for soil N[7]. In that sense, the growth of the AMF mycelium could also represent a N cost from the plant point of view.

Water : It has been widely acknowledged that AMF can change plant-water relation though many indirect mechanisms[8]. Among these, the extra radical mycelium (ERM) is generally thought to play a role in soil aggregation properties. This is the so called "sticky-string bag" function[9]. This in turn can affect the hydraulic properties of the soil pore space and consequently plant access to water. There is a possibility that AMF ERM hyphae could limit embolism or passively increase hydraulic conductivity of soil pores by bridging air gaps. It has however not been explored in these terms in the literature. Recently however, attention has been drawn to the possibility that a significant amount of water could be transported toward plants extracytoplasmically on hyphae across air gaps[10]. It is however unclear to what extent this transport could be passively mediated by the simple presence of hyphae bridging air gaps (in which case the net transport of water will go whatever way the largest water sink is) or actively driven by fungal "pumps". It is worth pointing out that the study discussed above is reasonably recent and goes against previously hold assumptions on the insignificant role that AMF could directly play in water transport to the plant[11].

Micronutrients and potassium : AMF have also been shown to increase plant uptake of micronutrients like Cu, Zn, Mn and Fe[12]. Radiotracer studies tend to prove that these increased plant uptake, in the case of Zn at least, is due to ERM hyphae mediated transport[13, 14]. It is however to this date unclear if there exists specific transfer pathway for each of these micronutrients at the arbuscule interface. Specific transport mechanisms for these micronutrients within the fungal hyphae have not been described. It is however possible that they could be transported dissolved in water within the cell wall matrix without specific uptake by the fungus. The contribution of AMF to plant potassium (K) nutrition is very little studied and similar unanswered questions remain on the ability of fungal hyphae to transport K actively and on the possibility that this could be traded for at the arbuscule level[15].

Protection against pathogens AM have been reported to promote plant tolerance to arthropod herbivores and pathogens[16]. This happens indirectly through priming of plant defences by AMF[17] or more directly through the competition with fungal pathogens for root space[18]. This effects are still controversial with some considering them inconsistent and small[16] while others identified it as one of the main driver of the benefit conferred by AM inoculation[18].

Benefits for the fungus

Carbon (C) : This is the most obvious nutritional benefit that the fungus is getting from the plant. All the carbon used by the fungus to grow comes from the plant. In that sense, AM fungi are generally considered "obligate symbiont" which means they can't survive in normal conditions without a plant host.

Protection dispersal Although the matter is not often in the literature, it is worth highlighting that spores are not the only AMF propagules. AMF indeed produce vesicles inbetween the plant cells. These thick walled structures contain numerous nuclei and resemble spores in many ways[19]. Dead root fragment can themselves be AMF propagules which means root colonization also plays a role in AMF dispersal. The formation of fungal structures inside the plant roots also provides some level of protection from the soil environment.

The cost of the symbiosis

Direct cost of the symbiosis For both plant and fungus, whatever resource is provided to the partner represents a cost. The magnitude of these costs and their relevance are discussed in 1.4.2.

Indirect competition for nutrients By providing carbon to their AM partner, plants are allowing them to expand in the soil and acquire nutrients. Some of them are traded with the plant (see benefits). But some might either be hoarded by the fungus or simply used for its own growth making them unavailable to the plant. It's been especially argued in the past, that AMF may compete with plant for soil N in low N conditions[20, 21].

Migration of pathogens? Although the matter is not really discussed in the literature it is possible that AMF hyphae could constitute a path for pathogens. If these are simply able to follow hyphae in the right direction, they have direct information about where to find plant root and an ideal "highway" to reach it[22].

1.4.2 Outcome of the symbiosis

What is the outcome of the symbiosis when integrating those costs and benefits? The expectation from a mutualistic interaction is that the net outcome is beneficial for both partners. The usual way of measuring the outcome of the symbiosis is by comparing the growth of the partners together and separately. In the case of the mycorrhizal symbiosis, the fungus is an obligate symbiont. This means it is not able to grow without a host plant. For this reason, the outcome of the symbiosis is generally considered always positive for the fungus although some rare example of myco-heterotrophic plants using AMF for carbon nutrition have been observed[26]. The latter might suggest that for AMF to initiate the symbiosis with some plants might eventually lead to a negative outcome. The obligate symbiont status of the fungus also entails that it is not possible to compare the growth of the fungus to a control experiment with no plant. It is however possible to compare the growth response of the fungus in different plant host and soil abiotic conditions. Plants can however be grown without their fungal partner. To do so, the soil is usually sterilized, and a control plant is grown in this sterilized soil. Other plants are grown in a sterilized soil where AMF fungal inoculum has been added. One can then observe how a given quantity Q relative to plant growth or reproductive success varies between treatments (see Fig. 1.2a). The variation relative to control is called the "Mycorrhizal

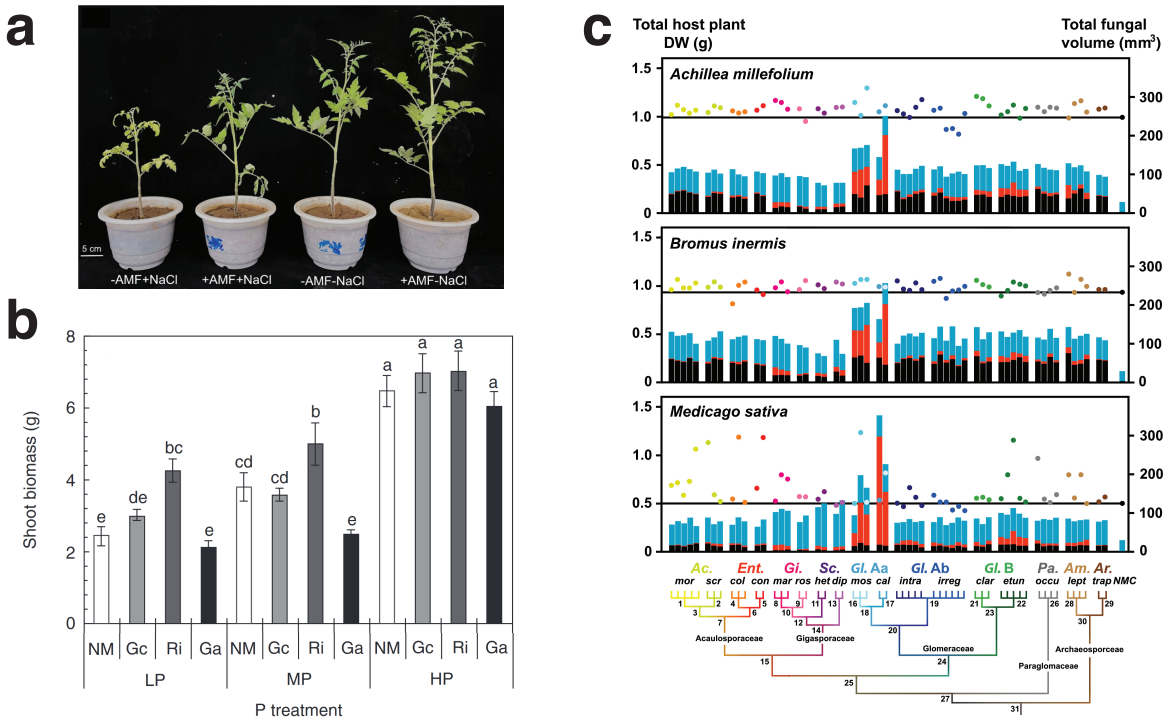

Figure 1.2: **Outcome of the symbiosis can vary depending on plant×fungus×enviroment** **(a)** Taken from [23] to illustrate the fact that AM inoculation can have visible effects on plant growth. In this case a tomato plant was grown with (+AMF) our without (-AMF) an AM fungal partner. The osmolarity of the soil was varied which has the effect of changing the access of the plant to water and therefore to nutrients. **(b)** Taken from [24], Shoot biomass of soybean genotype HN112 after inoculation with three different AM fungal species. The plants were grown for 7 weeks under low (LP), medium (MP) or high (HP) P supply conditions. Shown in the figure are the means of five biological replicates ± s.e.m.; NM, non-mycorrhizal controls; Gc, Ri and Ga, plants colonized with Glomus custos, Rhizophagus irregularis or Glomus aggregatum, respectively. Different letters on the bars indicate significant differences among treatments of one soybean genotype according to Duncan's multiple comparison test ($P \leq 0.05$). **(c)** Taken from [25]. Functional variability across Glomeromycota taxa at final harvest. Average total plant DW (colored dots) and total fungal volumes (bars). The phylogenetic tree at the bottom of the figure depicts the phylogenetic relationship among arbuscular mycorrhizal (AM) fungi. The shaded portions of the estimated fungal volumes represent the estimated volumes of total intraradical fungal volume (black), spore volume (red) and extraradical hyphal volume (blue). The total DW of nonmycorrhizal controls (NMCs) is displayed as the black horizontal line.

response" (MR). One can then write $MR(Q) = \frac{Q(M)-Q(NM)}{Q(NM)}$ where Q(M) is the average value of

the quantity when the plant is grown together with a given group of AMF genotypes and Q(NM) the average value of that quantity in the non-mycorrhizal control treatment. Most studies choose plant dry weight (m_{DW}) as the quantity Q to compare between treatments. The "Mycorrhizal response" is then called "Mycorrhizal growth response" (MGR) and can be computed as follows: $MGR = \frac{m_{DW}(M) - m_{DW}(NM)}{m_{DW}(NM)}$ Other quantities like the N or P uptake mycorrhizal response can also be considered.

Soil x Plant x fungal host matters

Soil and plant nutrient status A consistent pattern across studies is the fact that MGR tends to decrease with the concentration of P in the soil[24, 27, 28] (see Fig. 1.2b also). This doesn't necessarily mean that AMF become less collaborative in high P availability conditions or transfer less P. Indeed, even in high P conditions, a significant part of plant P nutrition can happen through the AM pathway[27] which means plants still rely heavily on the AMF partner for P nutrition. In high P conditions plants without AMF can however also acquire P through their roots directly which explains why the MGR is smaller. A simple paradigm to understand the outcome of the symbiosis from the soil nutrient status is the law of the minimum[28, 29]. It states that the growth rate of an organism will be given by the rate of acquisition of the most limiting resource (water, energy, P, N, Fe...). The highest MGR will therefore only arise in the case where one of the limiting resources can be acquired through the AM pathway. The applicability of this law of the minimum has been explored in the context of the AM symbiosis[28]. It was specifically hypothesized that high MGR are most likely in P-limited systems while low or negative MGR are expected in N-limited systems. The latter is based on the hypothesis that in low N conditions, instead of contributing to N nutrition, AMF would compete for soil Nitrogen. Even though the total biomass of AMF is lower than the plant (see 1.4.2), their higher C:N stoichiometry (4 to 10 times higher than the plant's) would lead them to immobilize significant amount of nitrogen from the soil. The general reasoning is that while more extraradical hyphae usually leads to better P acquisition by the colony it also immobilizes more N. Instead of being positively correlated, P and N provision benefit by the AM colony become anticorrelated. More recently, a wide study in agricultural soil found that the concentration of P in the soil was however a poor predictor of MGR. Instead, the presence of pathogenic fungi was a large driver of the variance in MGR for maize across 54 fields[18].

Plant genotype The specific identity of the plant partner can significantly impact MGR[27]. Variability in responses is observed even within a single species, such as maize, where different lines exhibit distinct reactions. These variations are believed to stem from differential levels of ERM abundance for each strain. Interestingly, the ERM abundance appears to be linked with certain plant genes active at the periarbuscular interface, which are associated with phosphorus (P) transport. However, these genes are not directly involved in P uptake; rather, they seem to play a critical role in adjusting the symbiosis's cost-benefit balance. In essence, plants with different genotypes might regulate P exchange in varied ways. This differential regulation of P trade could then account for the observed differences in MGR through the influence it has on the development of the ERM colony. Another hypothesis is that the regulation of N:P stoichiometry may drive phenotypic outcome of the symbiosis[30].

Fungal identity Symbiont identity also plays a role in the outcome of the symbiosis. The difference may happen at all level of the phylogeny from species/family [25, 31, 32] to within species[25,

32, 33] (see Fig. 1.2c). There is however no consensus in the literature on the fungal traits that explain these differences. Some studies argue that the key parameter explaining the difference is the maximal distance from roots reached by the fungal colony more than the total biomass of mycelium[32, 34]. Some other concluded that "host performance cannot be predicted from AM fungal morphology and growth traits"[25]. The divergent conclusions can be explained by the differences in experimental design. Due to the tedious nature of the measurement, only one study to this day reported explicit spatio-temporal dynamic of AM fungal hyphae in soil[34]. Most studies however rely on single spatiotemporal points to draw their conclusion[25]. Interestingly the studies concluding that AMF growth trait impact the outcome of the symbiosis tend to acquire spatially explicit data[32, 34]. There seem to be a point of convergence on the fact that total fungal biomass is a poor predictor of plant performance. This immediately raises the questions of whether the extra radical mycelium represents a significant carbon cost from the plant point of view.

Does extra radical mycelium matter?

While this question sounds like a rhetoric one, the last paragraph highlights the existing controversy on this topic in the literature. I here bring up two important considerations to the discussion. The first one is a back of the envelope calculation to compare the size of the two partners in typical conditions. This allows to discuss how the carbon cost of the fungus compares to the total dry mass of the plant and whether significant amount of P and N can be hoarded. The second important consideration is one of dynamics. I show that the dynamics of P in a soil are complex and explain why the amount of extra radical mycelium may not matter as much as its spatiotemporal dynamics.

Size matters: how big are carbon and nitrogen cost for the plant?

What's the plant/AMF mass ratio? This is a difficult estimation to do. Very few studies report all the components of AM biomass, and none can report it without large error prone extrapolations. When sampling is done without spatial considerations, the hyphal length density needs to be extrapolated to the whole pot. To convert spore or hyphal counting into volumes, one must use average estimates of hyphal and spore radius. Uncertainty on the value of these parameters can have quadratic or even cubic (in the case of spores) consequences on the final estimate. I will report the result found in three pot studies as well as the results from our own experiment with root organ culture. Highlighting in each case the methodological flaws leading to uncertainties (Table 1.1).

It is important to note that the shown value are averages. In the Thonar et al. study, dry weight ratio as high as 7% are reported and the Koch et al. study occasionally reports extremely high value of spore volume leading to 2 or 3 times higher ratios. The variability of the observed ratios can be the consequence of the diversity of experimental conditions. They however give orders of magnitudes to provide a thoughtful discussion.

Can AMF cost significant amount of C? The estimates of biomass that precede must also be put in perspective with previous estimates of carbon allocation by plant to their fungal partner. In a recent meta-analysis, it was reported that AM plants would allocate on average about 6% of their annually photosynthetically fixed carbon to their fungal partner[35]. This slightly higher ratio compared to the biomass ratio suggests that AMF biomass turnover may be faster than the plant one. In all cases the evaluated ratio, both in terms of rate (share of net primary productivity) and

Table 1.1: Plant-fungal biomass ratio in the AM symbiosis

Study	Explicit spatial sampling	reported intra radical biomass	reported spore number/volume	Used average value for conversion to biomass	pot volume (L)	mean computed total fungal dry mass (g)	mean total plant dry weight (g)	mean plant dw/fungal dw	remarks
Thonar et al. [32]	Yes	No	Yes	Yes	/	0.21	5.3	4%	
Sawers et al. [27]	No	No	No	Yes	1	0.15	17.5	0.90%	Largely overestimated hyphal radius
Koch et al. [25]	No	Yes	Yes	Yes	0.2	0.075	0.8	4%	
PRINCE	Yes	No	Yes	No	/	1E-04	0.1	0.14%	Missing all root side and under cellophane biomass

Table 1.2: Summary of studies

stocks (share of dry biomass) suggest that the plant incur significant C cost when investing in their AM partner. It is therefore likely that limiting this cost and increasing the return on investment (how much P it brings back and how well it matches the demand for P) is under high selection pressure.

Can AMF hord P and N ressources? Large share of plant P nutrition can happen through the AM pathway[36]. Typical C:P ratio for plants are between 0.1 and 1%. Given the results shown above, it is fair to assume a 1% AM/plant dry weight ratio. For the AM partner to hoard an amount of P equivalent to 0.1% of the plant P would mean that the fungus would have an additional 10% of its dry weight in the form of phosphorous. While this is not entirely unlikely, this means some fungal structure should have extremely high C:P ratios. In some case where the AM/plant dry weight ratio is higher, the scenario is however not entirely implausible. The core argument is the following: given the size difference, any significant resource manipulation from the plant point of view by the AM partner is challenging. It requires large storage capabilities in proportion with the size of the organism. This storage capabilities can be achieved by adapting the stoichiometric ratios in fungal hyphae or by developing specific structures. Spores and intraradical vesicles may be playing a role in this resource management strategies. The same kind of reasoning goes for N resources. It has been reported that concentration of N in the external hyphae of AMF could be 4 to 10 times bigger than typical plant stoichiometric ratios. This ratio difference may compensate the size difference and explain low to negative MGR in N limited systems[28].

Why dynamics matter? Phosphorous dynamics in soils are complex and are characterized by two well separated timescales. Due to chemical equilibrium, a fraction of phosphorous is readily available in ionic form in solution. The rest is bound to other ions and solubilizes with slow kinetics (up to days) when the equilibrium is shifted. It has been acknowledged that catalysing this slow kinetics can be key to making P available at a sufficient rate. Bacteria present in the AM hyphosphere can perform such catalysation[3]. Effective diffusion of P in soils is also much slower than other ions , in part due to the same chemical affinities of P ions. The slow diffusion of P and its slow solubilization hints at the fact that the spatiotemporal dynamics of the AM colony

in the soil could be key to determining its ability to absorb P. The growing colony must escape a self-generated P depletion zone. How fast and far the colony spreads will also ultimately impact the possible benefits it provides in terms of N, water or micronutrient.

But a fast and far spreading AM partner can also be costly from the plant point of view. It is possible that fast growing hyphae incur a lower carbon use efficiency. Transport cost (both construction and operating) within the fungal network may grow with the size of the colony making fast partners more expensive in terms of carbon investment.

The volume over which root pathogens could potentially find fungal hyphae would also be increased by a more spread-out colony. These pathogens could then find direct paths to the root more easily. Finally, a widely spreading colony will be interacting with more other plants. The latter could allow the AM partner to leverage competition between more partners and increase C costs.

MGR is the integrated result of the plant resource access rate over all its growth. Rates matter more than final balances when it comes to resource exchange. Growth of an organism inherently has an exponential component to it since its size determines its ability to access resources. An amount of C cost that might appear significant at a certain plant growth stage may be insignificant when it reaches a larger size. This is another reason to look at instantaneous resource exchange rate rather than their integrated results.

All the above highlight the fact that the plant best interest is to interact with a fungal partner which spatiotemporal dynamics matches its evolving demand for resources. It directly calls for a better understanding of the dynamics of spatial propagation of fungal colonies. Such propagation is however tightly constrained by the availability of carbon and therefore to trade with the plant host. I highlight in the following what is known about plant control of its supply of carbon to the fungal colony.

1.4.3 Tit for Tat, what do we know about control of the symbiosis?

How to keep a symbiosis stable?

We've highlighted above (1.4.1) that providing nutrients represented a cost for both partners. The evolutionary expectation would be that, to avoid that cost, partners may defect from mutualistic duties. One way in which the symbiosis can be kept stable is if the host plant and fungal symbiont interests are aligned. Then by helping the plant grow, the fungal symbiont will increase its own fitness and the other way around. This is true to some extent. If the AM partner relaxes some of the nutritional limitations of the plant, its ability to capture carbon through photosynthesis will grow, eventually benefiting the potential for carbon investment in the symbiosis. By providing carbon to its AM partner, the plant allows the fungus to extend its ERM in the soil which in turns allow the capture of nutrients that will eventually be transferred to the host. This stabilizing elements of interests alignment is however counterbalanced by the fact that plants are typically colonized by multiple fungal species and strains and fungal "individuals" can interact simultaneously with multiple plant individuals. This in theory, can lead to the selection of "cheaters" phenotypes that would exploit the benefits of the symbiosis without incuring the costs. This suggests that both partners could have evolved mechanisms that actively enforce cooperation.

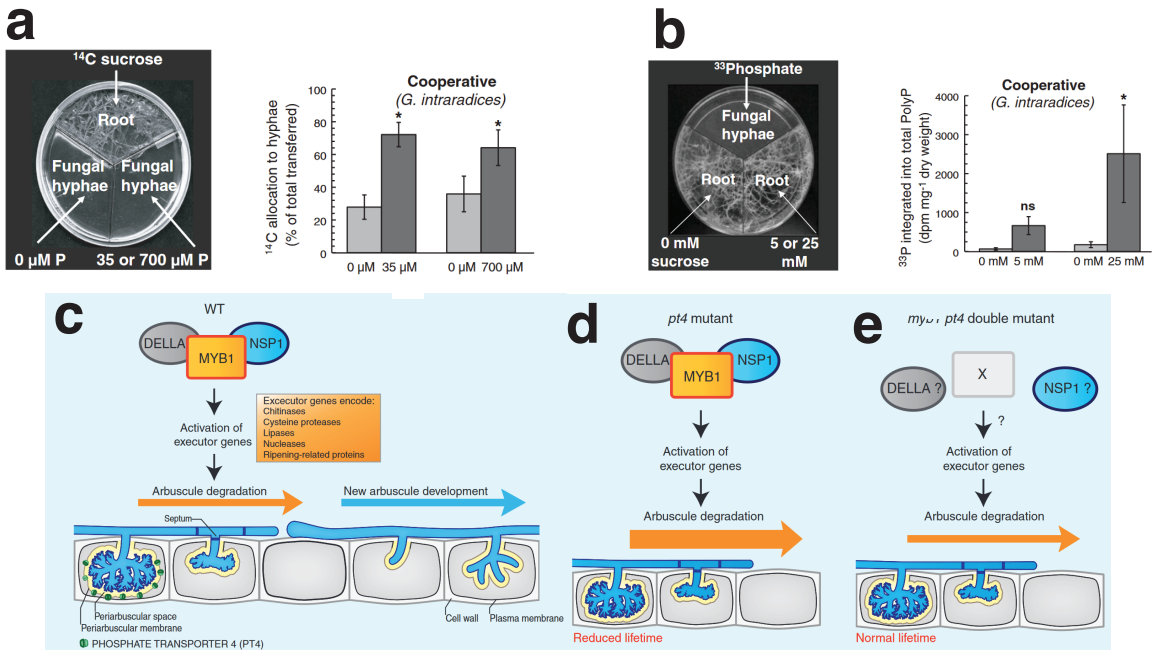

Figure 1.3: **Control of ressource exchange in the AM symbiosis (a)** From [37]. Triple-compartment experiments where a root host was confronted to fungal colonies growing in compartment with different availabilities of P. A significant effect of P availability on C allocation patterns was found, with preferential allocation of C to the fungal compartments with access to more P in *G. intraradices*.**(b)** In the reciprocal experiment (also from [37]), a growing fungal colony was confronted to two root hosts with varying C availability. A significant effect of the C availability on P allocation patterns was found, with a higher allocation of fungal P to root compartments with higher C in both *G. intraradices*. **(c)** In normal conditions, Arbuscocytes (arbuscule-containing cells) undergo an arbuscule turnover process that involves the maturation, degradation and re-initiation of an arbuscule. It was shown by [38] that this process is controlled by multiple plant genes (DELLA, MYB1, NSP1). After an arbuscule has been degraded, the same cell can support the development of a new arbuscule. **(d)** The timing of arbuscule degradation is controlled by the nutrient status of the plant and supply via the arbuscule. The pt4 mutant suffers from accelerated degradation of arbuscules, presumably triggered by the lack of phosphate delivered by the arbuscule. This scenario calls for a surveillance system for the symbiotic performance of the fungus. **(e)** In the myb1 pt4 double mutant, this accelerated arbuscule degradation is suppressed, demonstrating the central role of MYB1 in premature arbuscule degradation an the possibility that arbuscule degradation is under plant control. **(c)**,**(d)** and **(e)** are taken from [39]

Macroscopic trade patterns

The existence of such mechanisms was tested in an experiment where plants were grown with competing fungal partners that differed in their cooperative behaviour measured as their P supply

to the plant. The rate of carbon allocation was found to be higher for the most cooperative partners. In a follow up experiment, where a single plant was grown with a single fungal partner, it was shown that more carbon would be allocated to fungal hyphae growing in a compartment enriched in P than to a compartment with lower P concentration. Symmetrically, when fungal hyphae could deliver P to two different hosts that had variable access to carbon, they would be able to deliver P preferentially to the host that had most access to carbon([37], Fig. 1.3a,b).

These experiments suggest a tight control of the symbiosis by both partners. It is however important to state that alternative microscopic interpretations can also be given to this macroscopic observation. AM fungal hyphae are able to anastomose and form a single network. When a fungal colony has access to two compartments that vary in their P availability, it is unclear whether the hyphae growing on the two sides can really be discriminated by the plant. An alternative explanation is that the AM colony allocates carbon given by the plant preferentially to the compartment with higher P availability. In the case of two root compartments that vary in their C availability connected to a single hyphal compartment with available P, it is unclear if the fungal colony that grew in the P compartment did really bridge the two root compartments. The timing of this bridging also matters. If the colony primarily crossed from the root compartment with high C supply, the higher P supply to that compartment can simply be explained by the physical disconnection from the other compartment.

The study was carefully designed to observe immediate trade patterns raising the question of the timescale of the control of plant-fungal exchange during the symbiosis. It suggests that the rate of carbon transfer by the plant to a partner could be instantaneously proportional to the rate of P transfer by that partner.

The microscopic determinants of trade at the arbuscule level/root level

Whatever macroscopic effects of the control of the symbiosis are observed they emerge from microscopic components. Arbuscules are the microscopic interface where it is generally thought that resources are being exchanged, their dynamic is worth scrutinizing in more details.

Control of arbuscule lifetime It has been widely reported that arbuscules have a limited lifetime of 1-3 days at maturity ([38–42], Fig. 1.3c). This lifetime appears to be critical for the control of the symbiosis. I discuss in Chapter 2 that the existence of a finite lifetime coupled with the impossibility of recolonization of the same root region inherently leads to an alignment of interest between the two partners by enforcing AM spatial exploration. There is also the possibility that beyond this 'passive' control, the 'length of the lifetime' itself is under plant control and directly related to AM mediated P nutrition. Evidence for this more 'active' control emerges from mutant studies where inhibition of P transporters specific to the AM symbiosis would lead to reduced arbuscule lifetime([43],Fig. 1.3d). Further studies showed that accelerated arbuscule degradation was under the control of another plant gene further highlighting the possibility of arbuscule degradation as a surveillance system of the symbiotic performance of the fungus ([39],Fig. 1.3e). Indeed, under the simple hypothesis that any existing arbuscule transfers carbon at a fixed rate to the fungal partner, then reducing the lifetime in a proportional way to the P transfer could create a dependence between AM P provision and C transfer to the fungus. It would also have the advantage of requiring no specific recognition of partner's identity since only the information about the rate of P transfer would be used by the plant to reward partners proportionally. It can also

be highlighted that integrating the result of all arbuscule lifetime over a whole root segment can lead to an apparent direct reciprocal reward at the organism level. Indeed, desynchronized timing of arbuscule development and degradation, when integrated spatially, could effectively lead to a proportional rate of bidirectional resource exchange.

Control of colonization Upstream of the regulation of arbuscule lifetime, plants are also able to regulate the initiation of arbuscule development as a function of their nutrient status[44]. This however does not per se allows to reward specific partner for their P provision. It however may play a role on the competitions between different fungal strains on the same root system. Fast colonizing strains could quickly lift the P limitations of the plant hindering further colonization by slower strains.

Transporter network thermodynamical reciprocal exchange It is also possible that resource exchange rate through the periarbuscular space is inherently dependent of the difference in nutrient concentration on both side due to charge exchanges and the nature of P and N network of transporters[45]. Such models can indeed predict the reciprocal exchange of resources. They however seem to rely on the hypothesis that the main form in which carbon is being traded is sugar which is inconsistent with other reports of lipids being a significant share of the carbon transferred during symbiosis[46].

Gene network involved in regulation of the symbiosis While this direct thermodynamic reciprocal exchange is a tempting explanation. The necessity for control of lipid biosynthesis and export to the AM partner may require longer range feedback loop involving complex regulation of gene networks. Such gene networks are beginning to be unravelled[42] but it is yet unclear whether it leads to control by influencing exchange rate during arbuscule existence or by acting directly at the level of arbuscule lifetime.

Betting on future benefits? How to reward non-specific benefits, the information bottleneck

A problem of these microscopic reciprocal exchange models at the arbuscule level is that they tend to exclude benefits of the AM symbiosis that cannot be specifically measured at the individual arbuscule level. For example, while water exchange could be happening only through the arbuscules, it is more likely that water could flow within hyphal cell wall and arrives at the root in a diffuse manner. Then it would be more difficult for a plant to associate a certain level of water benefit to a specific arbuscule and reward it accordingly. It is also difficult to imagine ways in which the plant could measure how beneficial a given fungal partner is in terms of pathogen protection and respond to it. In the case of water, it is however important to highlight that the ability of a fungus to provide water will at first order correlate with its ability to provide P and N since all these correlates with the spatial distribution of the ERM. The plant may therefore be obtaining information about other AM specific benefits by eavesdropping on the ones it can measure. There is an information bottleneck inherent to the control of AM symbiosis. While it might be decisive for the plant to orient its carbon flux to "best" partners, the information about which arbuscule corresponds to such partners is inherently hard to obtain. First because it may be in the fungal interest to not give that information easily. Second because this may vary over time. At all times, the plant investment in the symbiosis will have to bet on the future by integrating all the information obtained. Direct

proportional exchange may be an optimal way of handling that information (the partner providing most benefits now is most likely to provide most benefits later). But it might be that more complex strategies have emerged such as integrating benefits over a finite timescale or computing benefit derivative and rewarding accordingly. The control of arbuscule lifetime could be an elegant way of integrating fungal benefits over a finite timescale (1-3 days).

The microscopic determinant of trade at the fungal transport level, the supply chain problem

While the above has taken a plant-centric approach on purpose, it is important to highlight that AM fungal colony can also feature regulation mechanisms. The size asymmetry however inevitably leads to the fact that fungal transfer of nutrient to the plant mainly happen "just in time" (see 1.4.2). Vesicles and spores may be seen as ways of temporarily storing resources. However, if those resources are then to be transferred to another "more beneficial" plant partner, this calls for long range orientation of nutrient across the ERM. We will explore how the ERM performs long range orientation of lipids within the network in Chapter 4. This in turn can provide insights into the possibility that trade decisions could indeed be made microscopically at each node of the network.

Could there be no control? The source-sink hypothesis

Some studies have however questioned the idea that there could be rewards and reciprocal trade in the mycorrhizal symbisosis, especially the Ectomycorrhizal one[47, 48]. The source-sink hypothesis instead suggests that the regulation of the symbiosis is a side effect of a source-sink balance. The resource exchanged are not considered to be a cost and benefits of the symbiosis then only depend on the amount of resources received. Under that hypothesis more targeted means of regulation are rejected as highlighted by the following statements from [48]: "Whether we consider mycorrhizal relationships open to exploitation and cheating and requiring extensive regulation, or ruled by sink/source dynamics, obeying both symbiont needs and self-balancing, will deeply affect how we investigate and understand these interactions, and should be carefully considered" or "The need for rethinking C distribution to the fungal partner as not being a cost is becoming unavoidable."[48]. While the argument must be considered it is problematic for multiple reasons.

1. The first one is that it heavily relies on the discussion of the occurrence of negative MGR where the symbiosis ends up being detrimental to the plant. The authors specifically remark that "Mycorrhiza formation improves plant nutrient access by improving substrate exploration, but in the present case, M and NM plants had access to the same amount of nutrients.". In other terms, their experiment was specifically designed to avoid any effect of spatial exploration by fungal hyphae which made the occurrence of negative MGR artificially high.

2. Surplus C is also a limited notion. C is in surplus if the supply of another resource is limiting for plant growth. But investment of this C surplus in the rhizosphere (to AMF or other microorganisms) aims at overcoming these other limitations. And it is in the plant best interest to invest this "limited" C surplus in an optimal way and therefore worry about the C cost of other resource acquisition. In other terms, even if the C invested in the symbiosis is in surplus from the plant point of view, investing in the symbiosis with no control on the return on investment is still a costly C investment. That C could have been invested in different ways (to grow roots, to feed rhizosphere bacteria, to feed another AM partner.).

3. It also overlooks a dynamic component of the symbiosis. The AM "sink" is not a fixed function of time. While at early time, the C cost could be negligible from the plant point of view, the inherently quadratic nature of AM growth inevitably leads to the possibility that the sink terms exceeds the surplus.

4. The evolutionary dimension of the problem is also being overlooked in this description. It could make sense for a single plant associated with a single fungus to allocate its surplus carbon with no specific control. But considering evolutionary timescales, this would tend to promote 'cheater' phenotypes to emerge. These 'cheaters' could for example use all plant carbon to form spores, or only reward other more "careful" plant with the resources they acquire. These "cheaters" would not necessarily have direct negative MGR since their C cost would still be limited by plant C surplus and could therefore not hinder growth. However, plants interacting with them would be at a disadvantage compared to the ones that didn't allocate their carbon to these "cheaters" but to more "cooperative" partners or that would condition their C supply to a proportional P supply. At evolutionary timescale, plant with no control mechanism would simply be outcompeted by the ones that implement such control.

The above shows that the existence of "control" mechanisms regulating resource exchange in the AM symbiosis is still challenged by the community.

1.4.4 Questions

1. How do AM fungal colony spread in space over time? (Chapter 2)

2. How do these spatial dynamics impact the outcome of the symbiosis and in particular the transfer of nutrients to the plant? (Chapter 2 and 3)

3. Are any control mechanisms in place on the plant and fungal side that enforce proportionality in the bidirectional exchange of resources? (Chapter 3 and 4)

4. How does transport within the AM colony allow to match supply and demand for carbon while maintaining a coherent trade pattern? (Chapter 4)

1.4.5 Context

When I joined the team in 2021 as part of my second year of Master, Loreto Oyarte Galvez and Malin Klein were finalizing what was the first version of the automated timelapse imaging system for AM fungal colonies. The original idea was inspired by early work of Toby Kiers and motivated by the intrinsically dynamic nature of AM fungal colonies (see 1.4.2). Acquiring data at such high temporal and spatial resolution for living branching organisms had simply not been done, even less for hard to grow symbiotic fungi. In addition, we had the ability to image flows in specific parts of the colonies in higher resolution. Such multiscale data production was unprecedented.

We however lacked a systematic pipeline to extract meaningful information from this data flows. Previously, Mark Fricker and collaborators had put in place image analysis methods to extract graphs from images of branching networks[49]. My early work consisted in applying these methods to our data. There was however three challenges which I had to gradually overcome.

1. The first one was both conceptual and technical. We were dealing with a time resolved dataset, which means that we were interested in extracting dynamic information. Conceptually, we

needed to understand **what was "moving"** and **how to/at what level of detail to characterize that "movement"**. Technically, we then needed to be able extract that information from our dataset.

2. The second one was also conceptual and technical. Bidirectional flow, as we were observing ubiquitously in the fungal colony had not been reported before. This meant we lacked the concepts to think about it and the toolbox to quantify it.

3. The last one was fully technical but required a significant amount of work to overcome. The shear size of the dataset (100s of TB), meant that we could not process it in a reasonable amount of time without (i) optimizing the code runtime (ii) parallelizing the processing.

The conceptual challenges hint at the exploratory and data driven nature of the work. A simple question triggered by our limited understanding of the system would often lead us to develop new tools for analysis which in turns would generate a mass of data that spurred new questions and advanced our theoretical understanding. In that sense, conceptual and technical challenges were intimately related. We were not trying to find the right tools to justify a pre-existing theory from data. Neither were we simply trying to establish a theory from a predigested dataset.

To a large extent, we were moving in unexplored ground with often an only remotely related body of literature to inspire us, which we sometime discovered late in the research process. This important published literature that mostly deals with other kind of fungi or branching organism are referred to at the beginning of each chapter.

Bibliography

1. Gentry, T., Fuhrmann, J. J. & Zuberer, D. A. *Principles and Applications of Soil Microbiology* en. ISBN: 978-0-323-85140-4 (Elsevier, June 2021).
2. Smith, S. E. & Read, D. J. *Mycorrhizal Symbiosis* en. ISBN: 978-0-08-055934-6 (Academic Press, July 2010).
3. Etesami, H., Jeong, B. R. & Glick, B. R. Contribution of Arbuscular Mycorrhizal Fungi, Phosphate–Solubilizing Bacteria, and Silicon to P Uptake by Plant. *Frontiers in Plant Science* **12.** ISSN: 1664-462X. https://www.frontiersin.org/articles/10.3389/fpls.2021.699618 (2023) (2021).
4. Whiteside, M. D. *et al.* Mycorrhizal Fungi Respond to Resource Inequality by Moving Phosphorus from Rich to Poor Patches across Networks. en. *Current Biology* **29,** 2043–2050.e8. ISSN: 0960-9822. https://www.sciencedirect.com/science/article/pii/S0960982219304907 (2023) (June 2019).
5. Chen, E. C. H. *et al.* High intraspecific genome diversity in the model arbuscular mycorrhizal symbiont Rhizophagus irregularis. en. *New Phytologist* **220,** 1161–1171. ISSN: 1469-8137. https://nph.onlinelibrary.wiley.com/doi/abs/10.1111/nph.14989 (2020) (2018).
6. Whiteside, M. D., Garcia, M. O. & Treseder, K. K. Amino Acid Uptake in Arbuscular Mycorrhizal Plants. en. *PLOS ONE* **7,** e47643. ISSN: 1932-6203. https://journals.plos.org/plosone/article?id=10.1371/journal.pone.0047643 (2023) (Oct. 2012).
7. Ågren, G. I., Wetterstedt, J. Å. M. & Billberger, M. F. K. Nutrient limitation on terrestrial plant growth – modeling the interaction between nitrogen and phosphorus. en. *New Phytologist* **194,** 953–960. ISSN: 1469-8137. https://onlinelibrary.wiley.com/doi/abs/10.1111/j.1469-8137.2012.04116.x (2023) (2012).
8. Augé, R. M. Water relations, drought and vesicular-arbuscular mycorrhizal symbiosis. *Mycorrhiza* **11,** 3–42. ISSN: 0940-6360, 1432-1890. http://link.springer.com/10.1007/s005720100097 (2023) (May 2001).
9. Miller, R. M. & Jastrow, J. D. en. in *Arbuscular Mycorrhizas: Physiology and Function* (eds Kapulnik, Y. & Douds, D. D.) 3–18 (Springer Netherlands, Dordrecht, 2000). ISBN: 978-94-017-0776-3. https://doi.org/10.1007/978-94-017-0776-3_1 (2023).
10. Kakouridis, A. *et al.* Routes to roots: direct evidence of water transport by arbuscular mycorrhizal fungi to host plants. en. *New Phytologist* **236,** 210–221. ISSN: 1469-8137. https://onlinelibrary.wiley.com/doi/abs/10.1111/nph.18281 (2023) (2022).

11. Püschel, D., Bitterlich, M., Rydlová, J. & Jansa, J. Facilitation of plant water uptake by an arbuscular mycorrhizal fungus: a Gordian knot of roots and hyphae. en. *Mycorrhiza* **30,** 299–313. ISSN: 1432-1890. https://doi.org/10.1007/s00572-020-00949-9 (2023) (May 2020).
12. Liu, A., Hamel, C., Hamilton, R. I., Ma, B. L. & Smith, D. L. Acquisition of Cu, Zn, Mn and Fe by mycorrhizal maize (Zea mays L.) grown in soil at different P and micronutrient levels. en. *Mycorrhiza* **9,** 331–336. ISSN: 1432-1890. https://doi.org/10.1007/s005720050277 (2023) (Apr. 2000).
13. Bürkert, B. & Robson, A. 65Zn uptake in subterranean clover (Trifolium subterraneum L.) by three vesicular-arbuscular mycorrhizal fungi in a root-free sandy soil. *Soil Biology and Biochemistry* **26,** 1117–1124. ISSN: 0038-0717. https://www.sciencedirect.com/science/article/pii/0038071794901333 (2023) (Sept. 1994).
14. Watts-Williams, S. J., Smith, F. A., McLaughlin, M. J., Patti, A. F. & Cavagnaro, T. R. How important is the mycorrhizal pathway for plant Zn uptake? en. *Plant and Soil* **390,** 157–166. ISSN: 1573-5036. https://doi.org/10.1007/s11104-014-2374-4 (2023) (May 2015).
15. Garcia, K. & Zimmermann, S. D. The role of mycorrhizal associations in plant potassium nutrition. *Frontiers in Plant Science* **5.** ISSN: 1664-462X. https://www.frontiersin.org/articles/10.3389/fpls.2014.00337 (2023) (2014).
16. Borowicz, V. A. The impact of arbuscular mycorrhizal fungi on plant growth following herbivory: A search for pattern. *Acta Oecologica* **52,** 1–9. ISSN: 1146-609X. https://www.sciencedirect.com/science/article/pii/S1146609X13001045 (2023) (Oct. 2013).
17. Mauch-Mani, B., Baccelli, I., Luna, E. & Flors, V. Defense Priming: An Adaptive Part of Induced Resistance. *Annual Review of Plant Biology* **68,** 485–512. https://doi.org/10.1146/annurev-arplant-042916-041132 (2023) (2017).
18. Lutz, S. *et al.* Soil microbiome indicators can predict crop growth response to large-scale inoculation with arbuscular mycorrhizal fungi. en. *Nature Microbiology* **8,** 2277–2289. ISSN: 2058-5276. https://www.nature.com/articles/s41564-023-01520-w (2023) (Nov. 2023).
19. Smith, S. E. & Read, D. en. in *Mycorrhizal Symbiosis* 42–90 (Elsevier, 2008). ISBN: 978-0-12-370526-6. https://linkinghub.elsevier.com/retrieve/pii/B9780123705266500040 (2024).
20. Balestrini, R., Brunetti, C., Chitarra, W. & Nerva, L. Photosynthetic Traits and Nitrogen Uptake in Crops: Which Is the Role of Arbuscular Mycorrhizal Fungi? en. *Plants* **9,** 1105. ISSN: 2223-7747. https://www.mdpi.com/2223-7747/9/9/1105 (2023) (Sept. 2020).
21. Püschel, D. *et al.* Plant–fungus competition for nitrogen erases mycorrhizal growth benefits of Andropogon gerardii under limited nitrogen supply. en. *Ecology and Evolution* **6,** 4332–4346. ISSN: 2045-7758. https://onlinelibrary.wiley.com/doi/abs/10.1002/ece3.2207 (2023) (2016).
22. Kohlmeier, S. *et al.* Taking the Fungal Highway: Mobilization of Pollutant-Degrading Bacteria by Fungi. en. *Environmental Science & Technology* **39,** 4640–4646. ISSN: 0013-936X, 1520-5851. https://pubs.acs.org/doi/10.1021/es047979z (2024) (June 2005).
23. Liu, M.-Y. *et al.* Arbuscular mycorrhizal fungi inoculation impacts expression of aquaporins and salt overly sensitive genes and enhances tolerance of salt stress in tomato. en. *Chemical and Biological Technologies in Agriculture* **10,** 5. ISSN: 2196-5641. https://chembioagro.springeropen.com/articles/10.1186/s40538-022-00368-2 (2024) (Jan. 2023).

24. Wang, X., Zhao, S. & Bücking, H. Arbuscular mycorrhizal growth responses are fungal specific but do not differ between soybean genotypes with different phosphate efficiency. *Annals of Botany* **118,** 11–21. ISSN: 0305-7364. https://doi.org/10.1093/aob/mcw074 (2022) (July 2016).

25. Koch, A. M., Antunes, P. M., Maherali, H., Hart, M. M. & Klironomos, J. N. Evolutionary asymmetry in the arbuscular mycorrhizal symbiosis: conservatism in fungal morphology does not predict host plant growth. en. *New Phytologist* **214,** 1330–1337. ISSN: 1469-8137. https://nph.onlinelibrary.wiley.com/doi/abs/10.1111/nph.14465 (2021) (2017).

26. Leake, J. R. Myco-heterotroph/epiparasitic plant interactions with ectomycorrhizal and arbuscular mycorrhizal fungi. *Current Opinion in Plant Biology* **7,** 422–428. ISSN: 1369-5266. https://www.sciencedirect.com/science/article/pii/S1369526604000639 (2023) (Aug. 2004).

27. Sawers, R. J. H. *et al.* Phosphorus acquisition efficiency in arbuscular mycorrhizal maize is correlated with the abundance of root-external hyphae and the accumulation of transcripts encoding PHT1 phosphate transporters. en. *New Phytologist* **214,** 632–643. ISSN: 1469-8137. https://onlinelibrary.wiley.com/doi/abs/10.1111/nph.14403 (2023) (2017).

28. Johnson, N. C., Wilson, G. W. T., Wilson, J. A., Miller, R. M. & Bowker, M. A. Mycorrhizal phenotypes and the Law of the Minimum. en. *New Phytologist* **205,** 1473–1484. ISSN: 1469-8137. https://onlinelibrary.wiley.com/doi/abs/10.1111/nph.13172 (2023) (2015).

29. Liebig, J. F. v. & Playfair, L. P. B. *Chemistry in Its Application to Agriculture and Physiology* en (J.M. Campbell, 1843).

30. Riley, R. C. *et al.* Resource allocation to growth or luxury consumption drives mycorrhizal responses. en. *Ecology Letters* **22,** 1757–1766. ISSN: 1461-0248. https://onlinelibrary.wiley.com/doi/abs/10.1111/ele.13353 (2023) (2019).

31. Lendenmann, M. *et al.* Symbiont identity matters: carbon and phosphorus fluxes between Medicago truncatula and different arbuscular mycorrhizal fungi. en. *Mycorrhiza* **21,** 689–702. ISSN: 1432-1890. https://doi.org/10.1007/s00572-011-0371-5 (2023) (Nov. 2011).

32. Thonar, C., Schnepf, A., Frossard, E., Roose, T. & Jansa, J. Traits related to differences in function among three arbuscular mycorrhizal fungi. en. *Plant and Soil* **339,** 231–245. ISSN: 1573-5036. https://doi.org/10.1007/s11104-010-0571-3 (2022) (Feb. 2011).

33. Koch, A. M., Croll, D. & Sanders, I. R. Genetic variability in a population of arbuscular mycorrhizal fungi causes variation in plant growth. en. *Ecology Letters* **9,** 103–110. ISSN: 1461-0248. https://onlinelibrary.wiley.com/doi/abs/10.1111/j.1461-0248.2005.00853.x (2020) (2006).

34. Jakobsen, I., Abbott, L. K. & Robson, A. D. External hyphae of vesicular-arbuscular mycorrhizal fungi associated with Trifolium subterraneum L. en. *New Phytologist* **120,** 371–380. ISSN: 1469-8137. https://onlinelibrary.wiley.com/doi/abs/10.1111/j.1469-8137.1992.tb01077.x (2022) (1992).

35. Hawkins, H. J. *et al.* Mycorrhizal mycelium as a global carbon pool. *Current Biology* **33,** R560–R573. ISSN: 0960-9822. http://www.scopus.com/inward/record.url?scp=85160575900&partnerID=8YFLogxK (2023) (June 2023).

36. Smith, S. E., Smith, F. A. & Jakobsen, I. Mycorrhizal Fungi Can Dominate Phosphate Supply to Plants Irrespective of Growth Responses. *Plant Physiology* **133,** 16–20. ISSN: 0032-0889. https://doi.org/10.1104/pp.103.024380 (2023) (Sept. 2003).

37. Kiers, E. T. *et al.* Reciprocal Rewards Stabilize Cooperation in the Mycorrhizal Symbiosis. en. *Science* **333,** 880–882. ISSN: 0036-8075, 1095-9203. https://www.science.org/doi/10.1126/science.1208473 (2023) (Aug. 2011).

38. Floss, D. S. *et al.* A Transcriptional Program for Arbuscule Degeneration during AM Symbiosis Is Regulated by MYB1. en. *Current Biology* **27,** 1206–1212. ISSN: 09609822. https://linkinghub.elsevier.com/retrieve/pii/S0960982217302725 (2022) (Apr. 2017).

39. Gutjahr, C. & Parniske, M. Cell Biology: Control of Partner Lifetime in a Plant–Fungus Relationship. en. *Current Biology* **27,** R420–R423. ISSN: 0960-9822. https://www.sciencedirect.com/science/article/pii/S0960982217304293 (2023) (June 2017).

40. Alexander, T., Meier, R., Toth, R. & Weber, H. C. Dynamics of arbuscule development and degeneration in mycorrhizas of Triticum aestivum L. and Avena sativa L. with reference to Zea mays L. en. *New Phytologist* **110,** 363–370. ISSN: 1469-8137. https://onlinelibrary.wiley.com/doi/abs/10.1111/j.1469-8137.1988.tb00273.x (2023) (1988).

41. Breuillin-Sessoms, F. *et al.* Suppression of Arbuscule Degeneration in Medicago truncatula phosphate transporter4 Mutants Is Dependent on the Ammonium Transporter 2 Family Protein AMT2;3. *The Plant Cell* **27,** 1352–1366. ISSN: 1040-4651. https://doi.org/10.1105/tpc.114.131144 (2022) (Apr. 2015).

42. Zhang, Q. *et al.* Control of arbuscule development by a transcriptional negative feedback loop in Medicago. en. *Nature Communications* **14,** 5743. ISSN: 2041-1723. https://www.nature.com/articles/s41467-023-41493-2 (2023) (Sept. 2023).

43. Javot, H., Penmetsa, R. V., Terzaghi, N., Cook, D. R. & Harrison, M. J. A Medicago truncatula phosphate transporter indispensable for the arbuscular mycorrhizal symbiosis. *Proceedings of the National Academy of Sciences* **104,** 1720–1725. https://www.pnas.org/doi/full/10.1073/pnas.0608136104 (2023) (Jan. 2007).

44. Paries, M. & Gutjahr, C. The good, the bad, and the phosphate: regulation of beneficial and detrimental plant–microbe interactions by the plant phosphate status. en. *New Phytologist* **239,** 29–46. ISSN: 1469-8137. https://onlinelibrary.wiley.com/doi/abs/10.1111/nph.18933 (2023) (2023).

45. Dreyer, I. *et al.* Nutrient exchange in arbuscular mycorrhizal symbiosis from a thermodynamic point of view. en. *New Phytologist* **222,** 1043–1053. ISSN: 1469-8137. https://onlinelibrary.wiley.com/doi/abs/10.1111/nph.15646 (2023) (2019).

46. Keymer, A. *et al.* Lipid transfer from plants to arbuscular mycorrhiza fungi. en. *eLife* **6,** e29107. ISSN: 2050-084X. https://elifesciences.org/articles/29107 (2023) (July 2017).

47. Bogar, L. M. Modified source–sink dynamics govern resource exchange in ectomycorrhizal symbiosis. en. *New Phytologist* **n/a.** ISSN: 1469-8137. https://onlinelibrary.wiley.com/doi/abs/10.1111/nph.19259 (2023).

48. Corrêa, A., Ferrol, N. & Cruz, C. Testing the trade-balance model: resource stoichiometry does not sufficiently explain AM effects. en. *New Phytologist* **n/a.** ISSN: 1469-8137. https://onlinelibrary.wiley.com/doi/abs/10.1111/nph.19432 (2023).

49. Fricker, M. D. *et al.* Automated analysis of Physarum network structure and dynamics. en. *Journal of Physics D: Applied Physics* **50,** 254005. ISSN: 0022-3727. https://dx.doi.org/10.1088/1361-6463/aa72b9 (2023) (June 2017).

Chapter 2

A traveling-wave strategy

2.1 Abstract

For nearly 450 million years, mycorrhizal fungi have constructed networks to collect and trade nutrient resources with plant roots[1, 2]. Because of their dependence on host-derived carbon, these fungi face conflicting trade-offs in building networks that balance construction costs against geographic coverage and long-distance resource transport to and from roots[3]. How they navigate these design challenges is unknown[4]. To monitor the construction of living trade networks, we built a custom-designed robot for high-throughput time-lapse imaging that could track >500,000 fungal nodes simultaneously. We then measured ∼100,000 cytoplasmic flow trajectories inside networks. We found mycorrhizal fungi build networks as 'self-regulating' traveling waves: pulses of growing tips pull an expanding wave of nutrient-absorbing mycelium whose density is self-regulated by fusion. This design offers a solution to conflicting trade demands because relatively small carbon investments fuel fungal range expansions beyond nutrient depletion zones, fostering exploration for plant partners and nutrients. Over time, networks maintained surprisingly constant transport efficiencies back to roots, while simultaneously adding loops that shorten paths to potential new trade partners. Fungi further enhance transport flux by both widening hyphal tubes and driving faster flows along 'trunk routes' of the network[5]. Our findings provide the first evidence that symbiotic fungi control network-level structure and flows to meet trade demands, and illuminate the design principles of a symbiotic supply-chain network shaped by millions of years of natural selection.

2.2 Main text

2.2.1 Introduction

The arbuscular mycorrhizal (AM) symbiosis is arguably the most widespread symbiotic partnership in nature, forming in the roots of over 70% of all extant plant species[6], which in turn dominate biomass on Earth[7]. AM fungi form complex mycelial networks of filamentous hyphae that are aseptate – meaning their cells are not divided by internal walls. They form open conduits where carbon and nutrients are not only stored, but flow dynamically through cytoplasmic streaming both

toward and away from host roots[8]. These nutrient-rich networks of active transport can reach densities of 10 m/cm^3 and contribute significantly to global carbon cycling[9–11].

The diverse trade behaviours enacted by mycorrhizal fungi are well-documented, with research suggesting that fungal partners selectively move and exchange resources with host roots in ways that improve fungal access to carbon[12–15]. While progress has been made in imaging mycorrhizal networks[16] and exploring their internal cytoplasmic flows[8], the precise topology of mycorrhizal networks – and cytoplasmic flows within them – have never been quantitatively tracked across space and time. Theoretical models of AM network growth have therefore depended primarily on data at the coarser level of mycelial density[17, 18], which cannot resolve how AM fungi build and operate their networks to meet trade demands. This is surprising because spatial and temporal context of resource movement is fundamental to trade in the AM symbiosis: the fungal partner is dependent on plant roots for carbon resources in the form of sugars and fats (i.e., obligate biotroph)[19]. In return, the fungus must continuously provide nutrients (e.g., phosphorous and nitrogen) to the host by extracting and moving resources through the filamentous network[20]. The spatial expansion of the network leads to new opportunities for colonization and trade for the fungus, as the network encounters new resources and roots. Until now, difficulties in simultaneously tracking the dynamic topology of mycorrhizal networks, while measuring their internal cytoplasmic flows has prevented researchers from understanding how symbiotic fungi modulate their anatomical architecture and transport patterns to meet trade demands. To overcome these challenges, we built an imaging robot that enables time-resolved microscopy of fungal network topologies in up to 40 in-vitro root-organ-culture (ROC) plant-fungal replicates simultaneously (**Fig.** 2.1**a**, **Methods**). A typical experiment acquired 150 images per replicate every 2 hrs at 2x magnification, with image overlap of ∼20%. While this experimental configuration enables imaging of the full mycelial network graph by constraining growth to two dimensions (2-D), basic symmetry considerations suggest that our findings are relevant also for AM fungal growth in three-dimensional (3-D) soil environments (**Supplementary Discussion**). Through computational image analysis (**Supplementary Methods**), we then extracted the full network graph at every time point (**Supplementary Video 1**) and tracked every node (growing tips, hyphal branches, junctions) and every edge (hyphal segments between nodes) of the graph across time, assigning each element a unique identifier (**Supplementary Video 2**). A typical experiment tracked ∼40,000 nodes per plate and half a million nodes across replicates. This element-by-element tracking allowed us to create time-lapse videos of fungal trade routes and monitor architectural rearrangements across the symbiotic network, such as when two hyphae fused to join cytoplasm (i.e., anastomosis) and the timing/location of spore formation (**Fig.** 2.1**b**).

To image cytoplasmic flows within hyphal networks, we switched to 100x magnification and used the extracted network graphs as maps to guide targeted high-resolution video analyses (**Supplementary Video 3**). We quantified flow behavior and velocity statistics, zooming into network coordinates at specific regions of interest. From these image sequences, we constructed kymographs and extracted speeds of bi-directional flows (**Fig.** 2.1**a**, **Methods**) to ask how flow dynamics corresponded with topological features of the networks (**Fig.** 2.1**b**). This allowed us to link hundreds of thousands of individual flow trajectories to exact coordinates within the growing network.

We tracked the formation of mycorrhizal fungal networks generated by three fungal strains: *Rhizophagus irregularis* A5 (DAOM664344), *R. irregularis* C2 (DAOM664346), and *R. aggregatum*. We grew networks in two-compartment petri plates. The colonized host, in-vitro ROC Daucus carota, was restricted to the root compartment[21]. The fungal network crossed a physical bar-

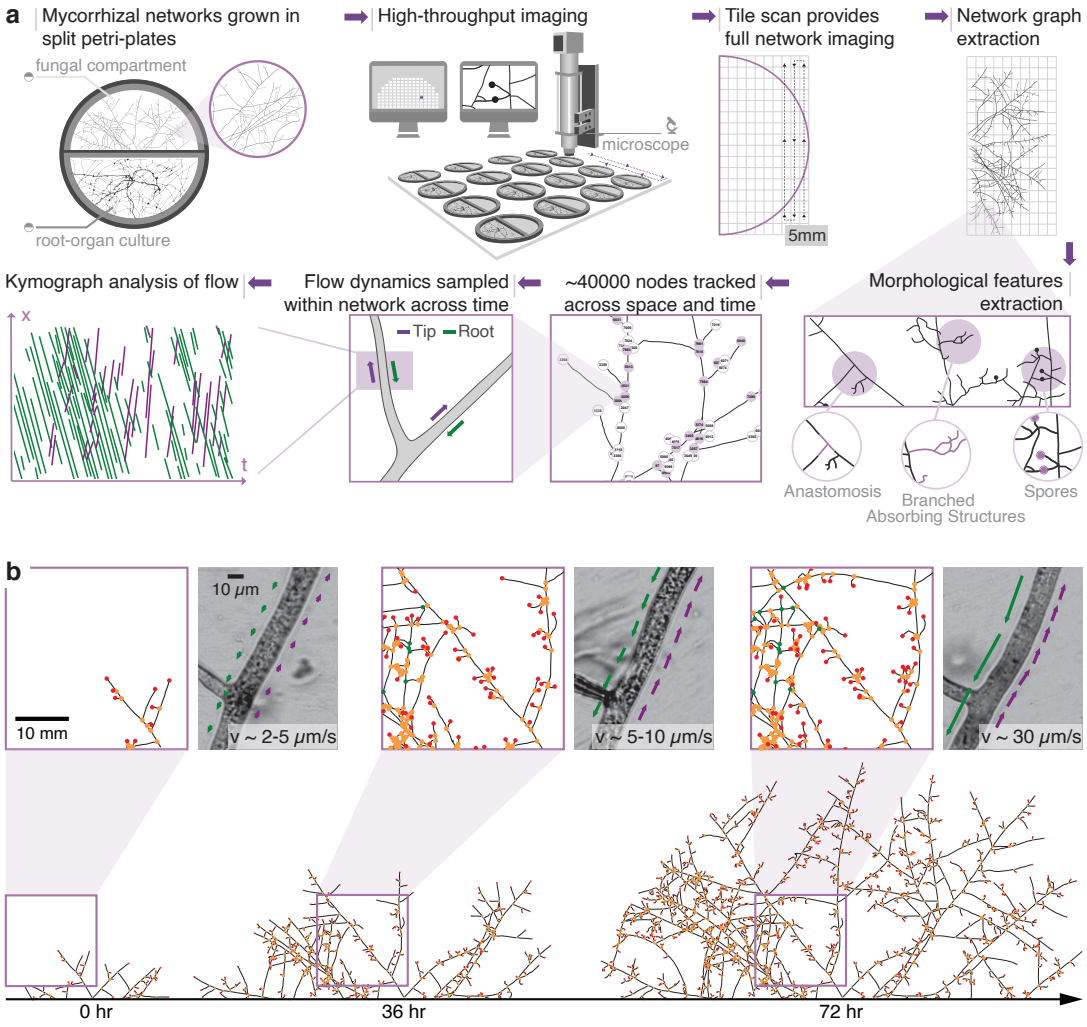

Figure 2.1: **Overview of data extraction techniques. (a)** Schematic of high-throughput imaging and analysis pipeline for extracting mycorrhizal network architecture and flow dynamics across scales. **(b)** The network skeleton and the nodes extracted from the respective graph are shown across time (tip nodes are represented by red, branch nodes by orange, and anastomosis nodes by green circles). Zoomed images indicate typical speeds of bi-directional cytoplasmic flows at three time points spanning 72 hours. Directionality and speed of flows are illustrated by arrows (larger arrows representing faster speeds), with green arrows pointing towards root and purple arrows pointing away from the root.

rier to a second compartment, inaccessible to the plant partner, lined with a permeable cellophane layer to optimize visualization, in which the fungus could access additional phosphorus (**Methods**).

From the sequence of extracted network graphs, we computed spatial density profiles of hyphae and growing tips, growth speeds at growing tips, and identified extraradical structures, including runner hyphae, anastomoses, branched absorbing structures (BAS), and reproductive spores, that reflect priorities for fungal needs as well as host demands (**Fig.** 2.1**a**).

2.2.2 Self-regulating traveling wave as a symbiotic strategy

First, we asked whether mycorrhizal fungi formed trade networks in a consistent, repeatable manner over time. We determined the network architecture of *R. irregularis* A5, tracking the full network graph as a function of time. Because the exact topology varied among replicates (**Extended Data Fig.** 2.6), we computed radially averaged spatial densities of growing tips and hyphal filaments within successive rings of equal area (**Fig.** 2.2**a**, **Methods**). We identified a simple and reproducible pattern in spatial density when the data were plotted against the distance r from the barrier crossing point (**Fig.** 2.2**b**). We found the hyphal filament density profile was plateau shaped, with a flat region toward the center (r→0) and a sloping decay to zero toward the periphery (r→∞) (**Fig.** 2.2**b**, upper). Simultaneously, the density profile of growing tips had a peaked shape that was positioned close to the decay zone of hyphal density (**Fig.** 2.2**b**, lower). Notably, the density of both hyphal filaments and growing tips had spatial profiles that were nearly invariant across time (**Fig.** 2.2**b**, left) and temporal profiles that were invariant across space (**Fig.** 2.2**b**, right), suggesting a translational symmetry.

Together, these data suggest that AM fungi explore space following a morphogenetic pattern best described as a traveling wave[22–24] – a phenomenon observed in bacteria and other microbes[25, 26], but never before documented in symbiotic fungi. AM fungi grew as a singular wave of space-filling mycelium, made up of two intimately coupled populations: (i) growing tips that 'pull' the wave as a pulse in space, and (ii) hyphal filaments that densify the space in the wake of the wave until saturating at a constant value. Consistent with this description, the shape of the wavefronts (**Supplementary Video 4**) and hyphal filament densities left in their wake (**Fig.** 2.2**c**) were constant as they translated through space. The wave speed was also independent of time (**Fig.** 2.2**d**).

To understand how the observed traveling wave pattern emerged from the underlying microscopic processes within the network, we developed a simple model of mycorrhizal network growth in space (see **Supplementary Discussion** for derivation and detailed discussion). This model, inspired by prior works on microbial colony growth[25, 27–31] and branching morphogenesis[32, 33], describes the coupled dynamics of growing tip density n (number per unit area $[mm^{-2}]$) and hyphal filament density ρ (length per unit area $[\mu m/mm^2]$):

$$\frac{\partial n}{\partial t} = b(n) - a(n,\rho) + \nabla \cdot J(n) \tag{2.2.1}$$

$$\frac{\partial \rho}{\partial t} = vn \tag{2.2.2}$$

The rate of change of tips (Eq. (2.2.1)) is governed by the rates of tip birth (due to branching $b(n)$ and tip annihilation due to anastomosis $a(n,\rho)$), and tip spatial flux $J(n)$ due to the branching random walks executed by tips, as they explore space by apical growth of existing hyphae and sub-

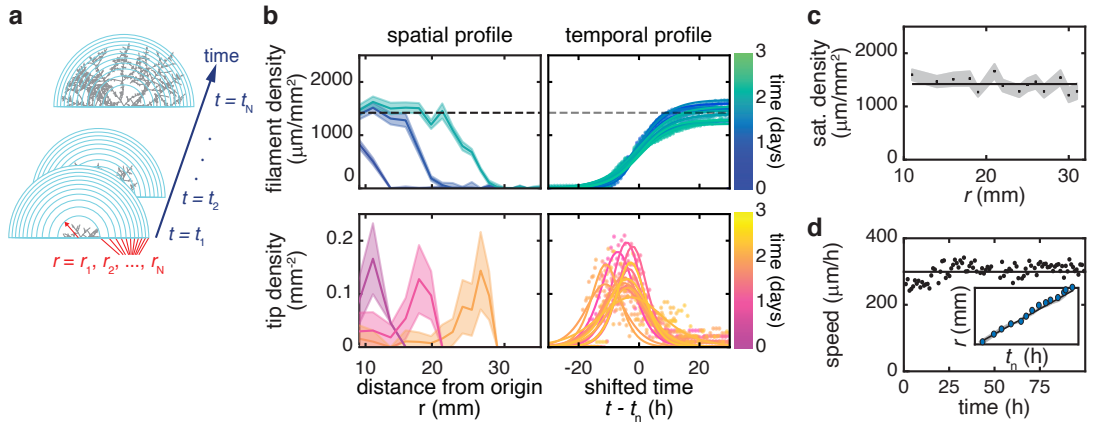

Figure 2.2: **Dynamics of hyphal-filament and growing-tip densities over time.** **(a)** Schematic illustration showing concentric rings of equal area centered at the base of the colony used for density estimates. Densities of growing tips and hyphal filaments are spatially averaged at each timestep within every ring and assigned a position corresponding to the radius $r = r_1 \dots r_N$ of the ring. Arrival times of the network at each ring $t_1 \dots t_N$ were also recorded (**Methods**). **(b)** *Left*: Spatial distribution of filament density (blue/green) and tip density (pink/orange) over three days. Shaded region corresponds to uncertainty in density estimates computed via bootstrapping (**Methods**). Color gradient from blue to green and from purple to orange correspond to day 1 to 3. *Right*: Temporal filament and tip density dynamics within each ring over time, with increasing ring radius size from small to large represented by blue to green gradient and from purple to orange, for filaments and tips, respectively. Circles are individual datapoints and solid lines are fits of sigmoid and sigmoid derivative functions (**Methods**). Time is shifted for each plot separately, by the arrival time t_n of respective densities at each ring. **(c)** Saturation density as a function of ring radius. Solid line is linear fit, and shaded region is confidence interval obtained by bootstrapping the sigmoid fit of each density curve. **(d)** Speed of growing tips over time. Black points are the average growth speed of hyphae at the front of the colony at each timestep. Black line is the average of black points. Inset: Position of the wave front over time. Blue points are data obtained from a sigmoid fit of density curves. Shaded region is bootstrapped confidence interval as obtained in **(c)**. Black line is a linear fit.

apical birth of new hyphae. The local growth rate of hyphal filaments (Eq. (2.2.2)) is determined by the local density n and speed v of growing tips.

This pair of coupled equations (Eqs. (2.2.1,2.2.2)) have solutions that can recapitulate the observed traveling-wave dynamics of mycorrhizal network growth (**Fig.** 2.2), where the wave speed c and saturating hyphal filament density ρ_{sat} are both constant (**Fig.** 2.3**a**, **Supplementary Discussion**). A sufficient condition for the existence of such solutions is that the branching and anastomosis rates are well-approximated as $b(n) = \alpha n$ and $a(n, \rho) = \beta n \rho$, respectively[20], where α and β are constants. We confirmed that our data are compatible with these relationships, finding that the

temporal profiles of $b(n)$ and $a(n, \rho)$ had shapes that closely matched those of n and $n\rho$, respectively (**Fig.** 2.3**b**), up to linear scaling factors α ($= 0.04h^{-1}$) and β ($= 23\mu m/h$), respectively.

When these conditions are met, the model further predicts that the wave speed c is just the fastest growing subpopulation of tips at the front, which effectively 'pull' the wave[23] (see **Supplementary Discussion**). Consistent with this prediction, we confirmed that the average tip growth speed $\langle v \rangle$ ($= 240\mu m/h$) obtained by tracking (**Fig.** 2.3**c**) was indeed lower than the wave speed c ($\simeq 280\mu m/h$, **Fig.** 2.2**d**), whereas the speed v_p ($\simeq 280\mu m/h$) of the 'puller' tips at the advancing wavefront (**Fig.** 2.3**c**, cyan) closely matched that faster speed of the wave front. These data demonstrate that AM fungal traveling waves are 'pulled waves' whose speed c is determined by the puller tips at the wave front (**Fig.** 2.3**a**, cyan) and the saturation density ρ_{sat} is set by the balance of branching and anastomosis (through α and β, respectively; see **Supplementary Discussion**).

These results are surprising because in typical population waves, such as those observed in bacterial colonies, microbes exhibit growth up to a density ceiling imposed by the environmental carrying capacity[25, 26, 30, 31]. By contrast, we found growth of mycorrhizal networks saturating at very low network densities (as low as $1000\mu m/mm^2$ for *R. irregularis* A5, Extended Data **Fig.**2.6,2.7**a**). We also found that the density ceilings of AM fungi observed here were an order of magnitude lower than those found for free-living (i.e. non-trading) fungi (**Extended Data Fig. 2.7b**), which tend to continue exponential growth over a similar range of increase in total network length ($(10^1 - 10^3 mm)$[34, 35]. This contrast between the growth pattern of AM fungi and free-living fungi raises an interesting question: is density saturation in these symbiotic fungi driven by environmental carrying capacity alone, or does it represent a specific growth strategy?

To address this question, we tested how the density saturation of AM fungal networks changed under different environmental conditions (**Supplementary Methods**). Despite changing both the root biomass (larger vs smaller) and root genotype (fast versus slow growing), we found no significant difference in the density ceiling of the mycorrhizal network (**Extended Data Fig.** 2.3 **a-d**, **Methods**). We also analyzed whether and how the collision of multiple fungal waves impacts the density dynamics of the merged wave, but found no change in the saturation density (**Supplementary Video 7**, **Extended Data Fig.** 2.16) To further confirm that this density was under fungal control, we grew AM fungi in the absence of a host root, replacing the in-vitro root with 0.5 mM myristic acid (**Methods**). Myristate provides a source of carbon and energy, allowing the AM fungi to grow and reproduce asymbiotically[36]. We found saturation density of the AM network did not differ whether it was grown with or without a host root (**Extended Data Fig.** 2.8 **e,f**).

We next tested whether these saturation density patterns held across networks formed by other AM fungi strains and species. If self-regulating traveling waves represent a general growth strategy for AM fungi, we would expect fungal strains to form waves, but differ in the speed and/or density of those waves. We tracked replicates of a different fungal strain, *R. irregularis* C2, and a different fungal species, *R. aggregatum*. While the timescales (i.e., wavefront speed) and exact saturation density behind the wave varied, all replicates showed a uniformly translating wavefront followed by a density profile that saturated at a low density, indicating a similar, self-regulating growth strategy (**Extended Data Figs.**2.9 and 2.10). These saturation densities correlated negatively with wave speeds, indicating a trade-off: strains that grew to a higher density were evidently slower at advancing their wavefronts in space, and vice versa (**Extended Data Fig.**2.7**a**). Taken together, these findings suggest that self-regulating traveling waves represent a general growth strategy for

AM fungi that prioritizes spatial exploration over local densification.

2.2.3 Regulated waves align plant and fungal interests

What explains this exploratory priority in the traveling-wave growth strategy of AM fungi? The answer may lie in their symbiotic lifestyle. Symbiotic trade requires that mycorrhizal fungi balance the export of nutrients to host roots with the cost of importing carbon for growing the network in search of new trade partners[3]. Self-regulating traveling waves could help balance these conflicting demands because costs associated with building exploratory tips to find new trade partners can be compensated by accompanying waves of absorbing mycelium that extract and transport nutrients back to roots in exchange for more carbon.

To test the idea, we quantified the phosphorus transported back to the host root from the expanding network. As expected, we found that total phosphorus per root increased while total phosphorus in the fungal compartment was depleted by the same amount (**Fig.** 2.3**d**). By quantifying phosphorus concentration in growth media near ($r \approx 0mm$) and far ($r \approx 40mm$) from the root compartment, we found that a spatial gradient of phosphorus depletion developed over time, until phosphorus was entirely depleted in the fungal compartment (**Extended Data Fig.** 2.11**a**). This agrees with past work using transcriptomics to demonstrate distinct spatial and temporal gene expression patterns for phosphorus absorption across hyphal networks[37].

Using these data, we expanded the travelling wave model (see **Supplementary Discussion**) to include phosphorus absorption by the network[17], showing that a phosphorus gradient forms and propagates together with the advancing wave front (**Fig.** 2.3**e**). Our model suggests that at a given saturation density, the more the fungal colony invests in spatial exploration (i.e. higher wave speed), the more phosphorus it can absorb from its environment. This is because the network can better escape its self-generated phosphorus depletion zone, leading to an overall lower carbon cost per unit of acquired phosphorus (**Extended Data Fig.** 2.11**b**,**c**). As a result, plant and fungal interests are highly aligned because relatively small carbon investments can fuel fungi to expand beyond nutrient depletion zones, fostering longer-range spatial exploration for both new roots and new nutrient patches.

Given that the carbon to fuel the fungal wave expansion is coming from host roots, we would also expect to see an expansion of intraradical colonization within the root over time. By sequentially harvesting replicates, we found that the length of intraradical hyphae significantly increased over time, closely mirroring growth dynamics of extraradical hyphae (**Extended Data Fig.** 2.12). While live-tracking of intraradical colonization is currently only possible using plant-based fluorescent protein reporters over small spatial scales, new data for *R. irregularis* on rice plants suggest that fungi form 'arbuscular fronts' that move down roots at a speed of $\sim 15\mu m/hr$[38], roughly 5% of the speed we measured for the extraradical wave front (see also [39] for arbuscular fronts formed by Glomus mosseae).

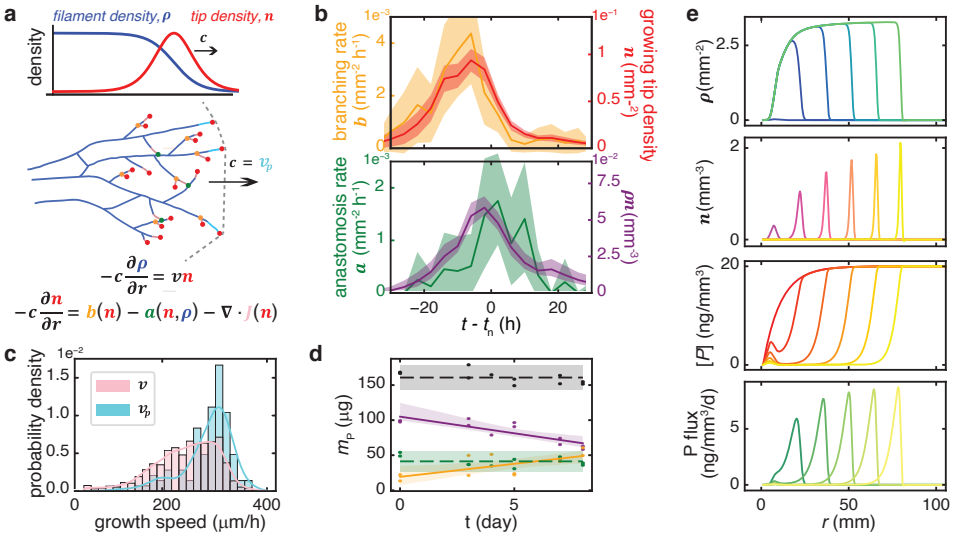

Figure 2.3: **Minimal model of a 'self-regulating' traveling wave.** (**a**) **Top.** Travelling-wave prediction of a simple model for fungal network growth. **Bottom.** This continuum model consists of two coupled partial differential equations for n (**red**, growing-tip density) and ρ (**blue**, hyphal-filament density) describing dynamics of branching at rate b (**orange**), anastomoses at rate a (**green**), and tip movement by spatial flux J (**pink**). The final velocity of the wave is described by its velocity c. **Middle.** Wave propagation is driven by fast growing hyphae that pull at the front (**red dots with cyan tails**) and densifies through growth and spatial flux of tips behind the front (**red dots with pink tails**). Branching (**orange dots**) occurs close to growing tips and tips can anastomose (**green**) when they meet an existing hypha. (**b**) Temporal dynamics of the variables from the model in the reference frame of the ring. Full line is the average over all rings, and shading corresponds to 95% confidence intervals (mean $\pm 2 \times s.e.m.$). Orange is branching rate b, red is growing tip density n, green is anastomosis rate a, purple is the product of filament and tip densities pn. (**c**) Hyphal growth speed distribution over 100 h of growth in a single plate. Pink histogram corresponds to the speed of all hyphae. Cyan histogram corresponds to the speeds of hyphae at the growing front. Lines corresponds to kernel density estimates of those histograms. (**d**) Phosphorous (P) absorbed by the spatially expanding colony is transferred to host root. P in the agar of the fungal-only compartment (**purple**) decreased over time and total P in the root (**orange**) increased, while total P in agar of the root compartment (**green**) remained constant. Black line. Points correspond to individual replicates, full lines correspond to linear fit, dashed horizontal lines show averages for the corresponding category. Shades of full lines correspond to the 95% C.I. of the linear fit obtained via bootstrapping and shades of dashed lines to (mean $\pm 2 \times s.e.m.$). (**e**) Traveling-wave model of Eqs. (1)–(2) was supplemented with and numerically integrated. Spatial profiles, from **Top to Bottom**: hyphal filament density ρ, tip density n, P concentration $[P]$, and P flux. Colour gradient corresponds to sampling at regular time intervals from $t = 0$ h to $t = 600$ h. See **Supplementary Discussion** for model details and parameters.

2.2.4 Topological changes indicate a shift to exploratory priorities over time

What is the underlying network architecture that supports these waves of carbon and phosphorus trade activity, and how does fungal architecture, including investment in structures to absorb nutrients, change over time to meet these demands? Previously, it was difficult to follow the dynamics of individual structures across the network to test how AM fungi differentially invest in nutrient absorptive capacity (through Branched Absorbing Structures, BAS[40]), spatial exploration (through growth), and reproduction (through spores). Our automated network extraction allowed for the first network-wide tracking of these structures throughout the course of network growth (**Fig.** 2.4, **Extended Data Fig.** 2.13). Consistent with self-regulated traveling-wave growth (with constant wave speed c and saturation density ρ_{sat}), we found that the total length L_{RH} of all runner hyphae edges of the network transitioned from exponential to quadratic growth ($L_{RH} \sim \rho_{sat}(ct)^2$) shortly after crossing into the fungal compartment (**Fig.** 2.4**b**). Simultaneously, the fungus constructed nutrient absorbing BAS structures at a uniform rate, throughout the course of network growth, such that ∼30% of the network length was consistently composed of BAS (**Fig.** 2.4**c**). In agreement with past transcriptomics data[37], this high and constant investment in BAS suggests these structures play a key role in mediating trade dynamics[40]. Continual investment in BAS behind exploratory tips is required for phosphorus absorption because arbuscules will collapse prematurely if insufficient phosphorus is supplied to the plant by the fungus[41, 42]. Once the BAS were established, we observed that the timing of sporulation – the onset of reproduction in AM fungi – varied among replicates, but gradually increased to an average of ≈300 spores per network at 400 h (**Extended Data Fig.** 2.13).

To construct expensive structures like spores, which are packaged with large quantities of plant-derived carbon[7], and growing tips, where biosynthetic carbon expenditures are concentrated[7], fungi must also efficiently and rapidly transport resources across the network. We therefore asked how major transport routes were distributed in space as the network matured. To quantify the relative importance of each hyphal edge for network-scale transport, we calculated its 'betweenness centrality (BC)' – a measure originally developed for communication networks – that quantifies the relative abundance of 'shortest paths' that pass through a network element[43].

We calculated and colored hyphal edges by their BC value to represent the cumulative number of shortest paths passing through them that connect nodes in the network to the root compartment (**Fig.** 2.4**a**, **Supplementary Methods**). We found that BC tended to increase along each runner hyphae in the direction toward the root – a pattern expected for tree-like networks where each successive branchpoint integrates the shortest paths from terminal nodes (i.e., hyphal tips) towards the root. The resulting distribution of BC across all network edges exhibited a long (power-law) tail (**Extended Data Fig.** 2.14**a**), characteristic of hierarchical planar networks and observed across a variety of infrastructural systems[44] (**Supplementary Discussion**). However, we also found multiple instances of hyphae with a non-monotonic pattern of BC, reflecting the presence of numerous loops created by anasotomsis events, which occurred at a nearly constant rate throughout network growth (**Fig.** 2.4**d**). These fusion events are particularly interesting for the symbiotic context because they alter network topology in ways that can lead to transport 'short-cuts' toward potential new hosts. We therefore asked whether and how these topological features of the network graph changed over time, incorporating data on hyphal fusion.

We sought to quantify the efficiency of the network's spatial layout, while accounting for resource

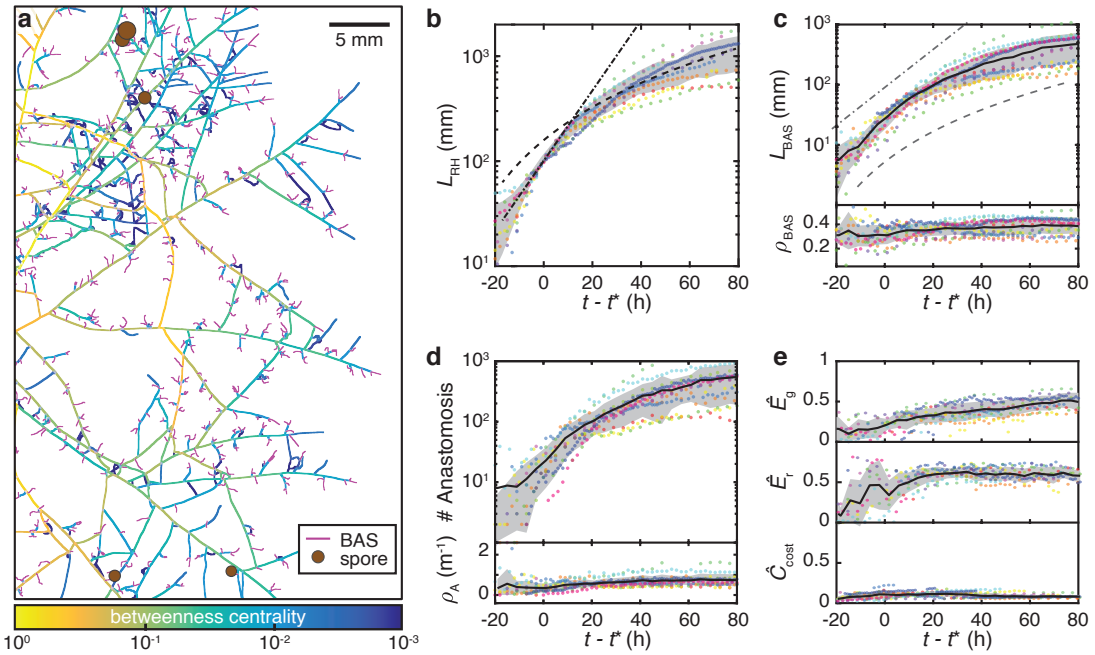

Figure 2.4: **Graph statistics of network architecture reveal a developmental strategy of symbiotic networks.** (**a**) Network graph is plotted together with BAS (magenta) and spores (brown circles). Each graph edge is colored by its betweenness centrality (BC) – the cumulative fraction shortest paths that connect every node in the AMF network to the root compartment – from lowest (blue) to highest BC (yellow). (**b**) Total runner hyphae length L_{RH} over time across samples (each color represents a replicate, $n = 12$). The black lines represent exponential (dot-dashed) and quadratic (dashed) fits, at early (< 20 h) and later (> 40 h) times, respectively. Grey region represents mean $\pm$ s.d. (**c**) Total BAS length L_{BAS} (top), and BAS length density $\rho_{BAS} = \frac{L_{BAS}}{L_{RH}+L_{BAS}}$ (bottom) versus time, with exponential-growth (dash-dotted line) and quadratic-growth (dashed line) guides for the eye. (**d**) Cumulative anastomosis events (top) and anastomosis density ρ_A (bottom), versus time. (**e**) Normalized global ($\hat{E}_g$) and root ($\hat{E}_r$) geometric transport efficiencies, and carbon cost (C_{cost}) versus time. In all plots in (**b**)-(**e**), data are from 12 sample plates (dots colored by sample), black line corresponds to the mean across all samples, the grey region represents mean $\pm$ s.d., plotted along a time axis offset by t^*, the time at which each sample's network length reached $L_{RH} = 10^2$ mm.

costs (e.g., material, energy, and time), and robustness to damage and uncertainties[4, 45–47]. We therefore computed the graph theoretical measure of 'geometric efficiency', comparing the distance d^{sp} along the shortest path between pairs of nodes to the shortest possible distance (i.e. the Euclidean distance) d^E in the physical space embedding the network[4, 45–48].

Because AM fungal networks are symbiotic, we needed to consider geometric efficiency in two contrasting contexts: (i) global efficiency (E_g), meaning transport between arbitrary pairs of nodes within the network, and (ii) root efficiency E_r) transport between network nodes and the

host root. Intuitively, these efficiency measures E_g and E_r quantify how close the shortest distance through the network is, on average, to that through a hypothetical network that connects all pairs of nodes with straight edges (**Supplementary Methods**).

From a biological perspective, however, simply maximizing these global and root efficiencies is unlikely to be the best strategy because it fails to account for associated costs. We therefore further normalized these computed efficiency measures using two 'ideal networks' that represent extreme limits in the inherent trade-off between cost and efficiency.

The first, 'Minimum Spanning Tree' (MST), minimizes the total length of edges while fully connecting a given set of nodes scattered in space. This graph represents the limit of low material cost, but is geometrically less efficient, i.e. requires longer travel distances between arbitrary node pairs[47]. The second 'Delaunay Triangulation' (DT) is an algorithm that yields a space-filling mesh network with the largest possible number of connections between nodes without crossing of edges – a maximal planar graph[47]. It represents a limit of high geometric transport efficiency because the shortest paths through the meshed network tend to be close to the Euclidian distance. DT is also robust to damage because the meshed network contains many loops[46], but these networks can be expensive in terms of building costs.

To assess how close the efficiency of the measured fungal graph is to the efficiencies of these limiting networks, we normalize both efficiency measures against those of these limiting networks to obtain their corresponding 'relative efficiencies'[49]. These are denoted as $\hat{E}_g$ for relative global efficiency and $\hat{E}_r$ for relative root efficiency (**Supplementary Methods**). Our aim was to understand if AM fungal networks tended to favor either MST and DT extremes, and whether this growth strategy changed over time for global and root efficiencies. A value closer to DT would suggest maximizing transport efficiency and robustness to damage, where a value closer to MST would suggest selection to minimize material cost.

We found that the relative root efficiency $\hat{E}_r$ (**Fig.** 2.4**e**, Top), remained stable at ≈0.5, approximately halfway between the limiting MST and DT networks. Likewise, the normalized carbon cost $\hat{C}$ for building the network (**Fig.** 2.4**e**, Bottom), which could be estimated by scaling the total network length (**Supplementary Discussion**), also remained constant, but at a level much closer to that of MST than DT. In contrast, the relative global efficiency $\hat{E}_g$ (**Fig.** 2.4**e**, Middle) gradually increased over time from ≈0.2 shortly after crossing to ≈0.5 at later times. These results mean that, like human-built transport networks[50, 51] as well as previously studied biological networks[52], mycorrhizal networks appear to strike a balance between maximizing transport efficiency (DT) and minimizing material cost (MST). Evidently, however, AM fungi navigate this trade-off in a time-dependent manner: maintaining $\hat{E}_r$ nearly constant throughout network development, while increasing E_g from a value closer to MST towards halfway between DT and MST. Together, these data suggest that as symbiotic networks start to age, their relative efficiencies shift in a manner that favor exploration for new partners over trade with existing partners.

For efficient transport, central edges (i.e. those with high BC) must accommodate a larger fraction of the flux than less central edges (with lower BC). Analogous to flows of traffic along road networks[53, 54], increased flux can be achieved in principle by: (i) increasing the cross-sectional dimensions of transport routes, (ii) the density of the flowing material, and/or (iii) the speeds of flows along those routes. We found that the radii of hyphal network edges (which determine cross-sectional dimension) were distributed broadly (**Extended Data Fig.** 2.14**b**) and significantly correlated

with BC (**Extended Data Fig.** 2.14**c**). This suggests that AM fungi modulate the width of hyphal edges in a manner informed by network architecture, with edges of higher BC having wider cross sectional areas that can support increased flux. We therefore asked how cytoplasmic flows within mycorrhizal networks were organized across space and time to accommodate resource trade, and whether those flow behaviors were correlated with network topology.

2.2.5 Modulation of bi-directional flows across the network

Arbuscular mycorrhizal fungi are unusual in that their networks are composed of one continuous cytoplasm. Resource trade with host roots also means that AM fungi need to stream nutrients in two directions – both towards and away from the host root[55]. Zooming in on the network architecture mapped by our automated imaging, we asked: how do speed statistics differ toward and away from root, and do they change with the age or position of the network as the wavefront advances?

We systematically collected high resolution, real-time videos of flows at physical coordinates across the mapped network. To avoid the potential confounding influence of added dyes, we conducted label-free imaging by brightfield microscopy (**Fig.** 2.5**a**, right). We recorded flow videos at 20-25 frames per second for a duration of 20-60 s (see **Supplementary Videos3**,**5**,**6** for examples). One or more regions of interest (ROIs) were manually defined in each video for kymograph analysis of speeds (**Fig.** 2.1**a**, **Methods**). To extract the statistics of speeds in both directions, we employed a machine-learning-based kymograph analysis of particle trajectories[56] (**Methods**). The resulting kymographs revealed a remarkably rich set of flow behaviours, including simultaneous antiparallel streams of particles within each hyphae, speeds that varied significantly across time and space, and abrupt direction switching (i.e., sign changes) of streams (**Fig.** 2.5**a**, left,**Supplementary Video 6**), including in AM fungi grown on myristate in the absence of a host root (**Supplementary Video 9**).

By quantifying over 100,000 particle trajectories, we found that the average speeds in both the tip direction $\langle u_+ \rangle$ and the root direction $\langle u_- \rangle$ were remarkably stable over 20 days (**Fig.** 2.5**b**, upper), despite increases in total network length by almost two orders of magnitude within that time frame (**Fig.** 2.4**b**). However, we did identify a significant directional bias at early times of colony development: average speeds toward the tip were ∼30% faster compared to average speeds toward the root, and this bias gradually decayed to below significance at ∼10 days (**Fig.** 2.5**b**, lower).

An open question is whether the directional bias with time reflects a change in the transport demands during the development of the network. At early times, the tip-ward bias might help meet the growth demands of the advancing front. At later times, when resources are rapidly acquired by the established BAS population, translocation back to the root becomes increasingly important, potentially reflecting developmental changes in trading requirements.

We also observed long tails in the speed distribution from each colony, with speeds often increasing transiently to greater than $20\mu m/s$. On rare occasions, we observed short-lived bursts of extremely high speeds, with particles moving between $50\mu m/s$ and $120\mu m/s$. We therefore asked whether these high flow speeds were correlated with the appearance of specific topological features of the network. By analysing the statistics of the fastest speeds observed across all regions of interest, we found a positive correlation between maximum flow speed and the total number of spores in the

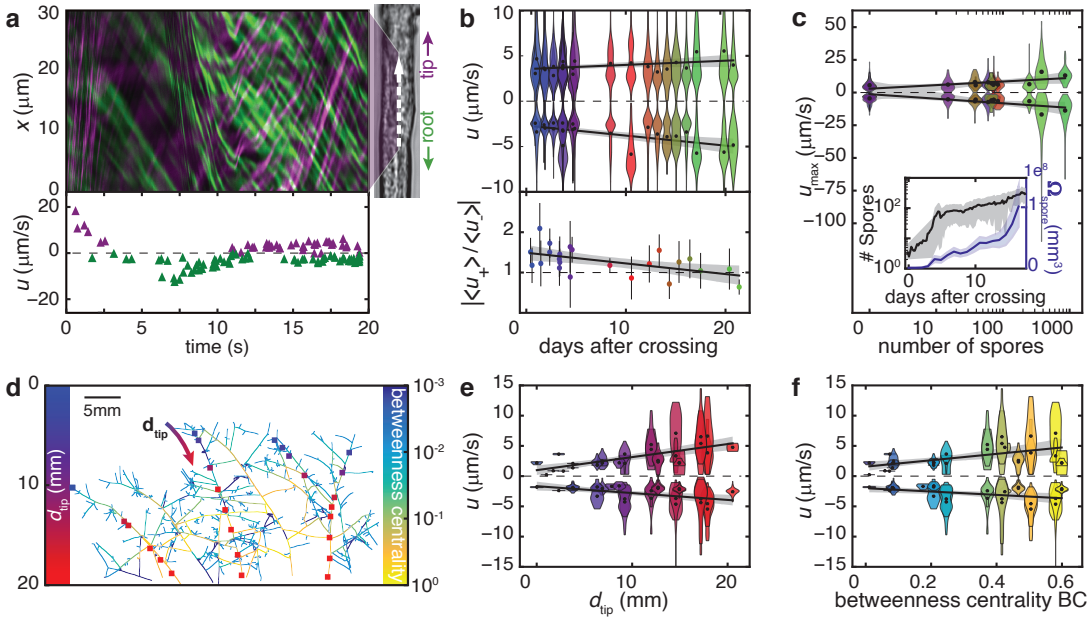

Figure 2.5: **Network architecture connects statistics of bidirectional flows to symbiotic transport requirements.** (**a**) **Top:** Example of extracted kymograph for flow trajectories with lines corresponding to moving particles coloured in purple (tip direction), and green (root direction). **Bottom:** Extracted velocities across time, with each point corresponding to a detected trajectory and purple/green colour corresponding to the tip/root direction of movement. (**b**) **Top:** Distribution of the observed velocities u over time ($u > 0$ toward tip, $u < 0$ toward root). Each violin distribution includes all velocities extracted from kymographs for each plate. Colour of the violin follows the gradient of time. Black point corresponds to the average of the positive ($\langle u_+ \rangle$) and negative ($\langle u_- \rangle$) velocity distributions for each plate. **Bottom:** Absolute ratio $\left|\frac{\langle u_+ \rangle}{\langle u_- \rangle}\right|$ showing a bias with higher average speeds toward the tip at early times. (**c**) Distribution of the observed max speeds as a function of the total number of spores. Colour of the violin are as in (**b**). **Inset:** Total number and volume of spores as a function of time. (**d**) Example of sampling for speed across a network. Squares correspond to the position sampled. Colour of the squares follows the distance to the tip d_{tip}. Colour of the edges is mapped to their betweenness centrality value (BC). (**e**, **f**). Distribution of the observed velocities as a function of d_{tip} and BC for the positions sampled in (**d**). Each violin shows the distribution of velocities obtained from one video at a given position. Colour of violin as in the color scales in (**d**). Black points correspond to positive and negative average for each video. In (**b**)-(**f**) black lines correspond to linear fit of the averages (black points). In the same figures, grey shades correspond to 95% C.I. of the linear fit obtained via bootstrapping.

network (**Fig.** 2.5**c**). Because spore number and spore volume (**Fig.** 2.5**c**, inset) both exhibited increases with time, it remains an open question whether these maximum speeds reflect absolute

spore numbers or a general allocation pattern to reproduction (i.e., fewer but bigger spores).

Having observed changes in flow speeds across time (**Fig.** 2.5**b**,**c**), we next asked whether AM fungi also modulated speeds across space. Driving active flows comes at an energetic cost that increases with speed[57, 58]. We therefore reasoned that fungi might regulate flow speeds across space in a manner that reflects contrasting demands at different network locations for high-speed transport. For example, diffusion can be sufficiently efficient for transport within a length scale L$\sim 3mm$ from growing tips (given by $L \sim 2D/v_g$, with $v_g = 300\mu m/h$ measured growth speed of tips and $D = 125\mu m^2/s$ typical of cytoplasmic diffusivity[59]). We therefore expected high-speed, active transport to be absent at growing tips within a range $\sim 3mm$ from tips, where diffusion processes should be dominant.

By systematically sampling speeds at different distances d_{tip} from the growing tips (**Fig.** 2.5**d**), we found that speeds in both directions (towards tips and towards roots) did indeed decay towards zero near growing tips (**Fig.** 2.5**e**). However, the spatial range of decay was unexpectedly long ranged, with speeds $|u|$ depending linearly on d_{tip} over the entire sampled range ($0 < d_{tip} \lesssim 20mm$, **Fig.** 2.5**e**). Whereas speed drops near growing tips could be explained by dominance of diffusion on short distances ($\sim 3mm$ from tips), why should the dependence of flow speeds across the rest of the network be so long ranged?

To answer this question, we considered the topology of the network. As noted above, increased flux through network edges of high centrality (i.e. those with high BC) enhances transport efficiency, can be achieved by increasing the density or speed of flows. Analysing the dynamics of flow velocities at different points in space revealed statistics consistent with incompressible flow, thus ruling out significant variation in fluid density across the network (**Extended Data Fig.** 2.14**e**). We therefore examined whether there was a relationship between flow speeds in each edge of the network and the edge's BC value. We found a similarly simple dependence – speeds $|u|$ in both directions were close to zero at low BC and increased systematically on average with increasing BC (**Fig.** 2.5**f**). This trend of increasing $|u|$ as a function of both d_{tip} and BC was robust over all tested samples (**Extended Data Fig.** 2.14**c**). These observations raise the compelling possibility that AM fungi modulate not only hyphal width, but also flow speeds in a manner that is informed by network topology, so as to enhance flux through 'trunk hyphae' – transport routes with higher density of shortest paths to the root. This network-scale flow modulation potentially allows the colony to respond efficiently to lipid demand at the growing tips and nutrients at the root interface.

2.2.6 Discussion

Our results represent the first systematic mapping of network topologies and internal flows across symbiotic mycorrhizal networks. We discovered that AM fungi build networks as self-regulating traveling waves. We use the term 'self-regulating' because the wave pattern contrasts with typical microbial colony growth in which waves result from environmental carrying capacities[25, 27]. Instead, AM fungal waves appear to be regulated by density-dependent hyphal fusion events, such that network growth becomes quadratic after the establishment of the wavefront at very low densities ($\sim 1000\mu m/mm^2$), a pattern not found in free-living fungi that densify exponentially to much greater densities[34, 35].

'Self-regulating' also implies the program is under fungal control. While as obligate biotrophs, the absolute amount of carbon they receive is ultimately controlled by their plant hosts, our work

suggests mycorrhizal fungi are able to precisely control how they use that imported carbon. We found traveling wave morphogenesis across all tested AM fungi (Extended Data Figs. 2.6,2.9,2.10), with strains varying in wavefront speeds and saturation densities (**Extended Data Fig.** 2.7**a**). The persistence of the traveling-wave growth across all strains tested potentially reflects an alignment of interests of plant and fungal partners: carbon payment to support exploratory tips favoring growth and new trade partnerships must be compensated with nutrients extracted by absorbing mycelium, as shown by the gradient of phosphorus depletion ultimately transported to the host root (**Fig.** 2.3**d**,**e**) .

Recent works on free-living fungi[60] and slime molds[61, 62] are revealing how microbes with branched and distributed anatomies implement diverse environmental response strategies through their network topology and morphology. Our dynamic mapping of AM fungi network graphs provides a first glimpse into how a symbiotic morphogenetic program changes across time. We found BAS density and anastomoses remain nearly constant. This ensures constant (graph-theoretical) transport efficiency towards the host root, while gradually increasing transport efficiency between arbitrary points in the network. Adding such loops could shorten paths to potential new partner root systems[46]. We also found jumps in spore production at later times, reflecting balanced investment between reproduction and growth as the network matures.

Our results represent the first systematic mapping of internal flows in mycorrhizal fungi, opening up new questions on how supply-chain dynamics for symbiotic trade are modulated during network development. We found flows were consistently and simultaneously bi-directional in most of the 1,600 high-resolution videos sampled. Strikingly, flows were faster, and hyphae were wider, along edges with higher betweenness centrality within the network, analogously to hierarchical road networks where a larger number of lanes and higher speed limits enhance flux along roads of high centrality[54]. These findings provide the first evidence that intra-hyphal flows are controlled by AM fungi in a manner informed by spatial and temporal context.

Our findings also raise a wealth of new questions. The architecture of fungal trade networks has been shaped by natural selection for over 450 million years[6]. Whether these designs can inform human-built supply chain architectures is a compelling open question[52]. To understand the flexibility and responsiveness of network design, more data are needed on how fungi control growth and flows in response to different host roots and environmental conditions. Mechanistically, more data are needed to understand what enables antiparallel fluid flows within individual hyphae, and how are local flow speeds controlled in ways that are informed by global network topology. These future studies will allow for a better understanding of how rapidly network-wide architecture and transport dynamics can be modulated under different conditions.

2.2.7 Acknowledgments

This work was supported by an HFSP Program Grant (RGP 0029) to E.T.K., H.A.S. and T.S.S. V.S. acknowledges support from ERC-Nuclear Mix (101076062). E.T.K. acknowledges support from the Jeremy and Hannelore Grantham Environmental Trust, the Schmidt Family Foundation, the Paul G Allen Family Foundation, NWO-VICI (202.012), NWO-Microp program, the Hefner Foundation, and an Ammodo Foundation grant. T.S.S. acknowledges support from NWO. We thank Dr. Ian Sanders for sharing AM fungi strains, Dr. Carlos Aguilar-Trigueros for access to published data on non-symbiotic strains, Drs. Stuart West and Sander Tans for critical reading of the manuscript, AMOLF Engineering Departments for expert assistance in design and fabrication of the imaging

setup, and all members of the Shimizu Group and Kiers Group for helpful discussions.

2.3 Material and Methods

2.3.1 Biological material and Plate Preparation

We performed experiments with Ri T-DNA transformed carrot root (Daucus carota clone DCI) organ cultures colonized by *Rhizophagus irregularis* strain A5 (DAOM664344), *R. irregularis* strain C2 (DAOM664346) (Ian Sanders, University of Lausanne, Switzerland) and Rhizophagus aggregatum. We cultivated fungal stocks on Modified Strullu-Romand (MSR) medium in association with transformed carrot root for 2-6 months until plates were fully colonized. We then used these stock cultures to inoculate sterile roots, as described below.

Each biological sample contained a root-organ culture in a split Petri plate (94 mm diameter, Greiner Bio-One). One side contained the root colonized with arbuscular mycorrhizal (AM) fungi, and the other side contained a fungus-only compartment. We designed trapezoid shaped acrylic frames to fit against the central barrier of the two-compartment split plates. These 1mm thick frames had a longer top edge (88 mm) than bottom edge (85.5 cm), and a consistent height (12 mm). The frames included a central opening (50 x 2 mm) that was located 2 mm from the top edge. This opening connected to the upper edge of the central barrier of the plate and was covered by a nylon mesh, leaving only a 50 mm wide window for the fungus (but not the root) to cross through into the second compartment. A nylon mesh (pore size 50 μm, 9 x 71 mm) was attached to the acrylic frame using UV resin such that the frame opening was fully covered by the mesh and free of resin. The resin was cured with UV light for 3 mins. The frames were then wrapped in aluminum foil and sterilized at 80°C for 72 hours.

We filled the two compartments with MSR medium. In the fungus only compartment, we used regular MSR (per 1 L: 739 mg $MgSO_4{\cdot}7H_2O$, 76 mg KNO_3, 65 mg KCl, 4.1 mg KH_2PO_4, 359 mg $Ca(NO_3)_2{\cdot}4H_2O$, 0.9 mg calcium pantothenate, 1 μg biotin, 1 mg nicotinic acid, 0.9 mg pyridoxine, 0.4 mg cyanocobalamin, 3 mg glycine, 50 mg myo-inositol, 1.6 mg NaFeEDTA, 2.45 mg $MnSO_4{\cdot}4H_2O$, 0.28 mg $ZnSO_4{\cdot}7H_2O$, 1.85 mg H_3BO_3, 0.22 mg $CuSO_4{\cdot}4.5H_2O$, 2.4 μg $Na_2MoO_4{\cdot}2H_2O$, 34 μg $(NH_4)_6Mo_7O_{24}{\cdot}4H_2O$). In the root compartment, the phosphate content of the medium was reduced to 1% (i.e. 1%P MSR) of the above-mentioned concentration (41 μg/L KH_2PO_4). We supplemented all media with 10 g/L sucrose and 3 g/L Phytagel. We verified that the addition of sucrose to the fungal compartment did not change the dynamics discussed in this paper (**Extended Data Fig.**2.15). In the plates where carbon availability was doubled, the sucrose concentration in the media in the root compartment was increased to 20 g/L sucrose.

In a laminar airflow hood, we filled one compartment of a sterile two-compartment split plate with 28 ml MSR medium. We placed an autoclaved sheet of cellophane (Hoefer™ TE73, semi-circle with trapezoidal overhang at the straight edge) on top of the solidified medium. We then folded the cellophane overhang into the empty second compartment. Next, we inserted the custom acrylic frame into the empty compartment, securing the cellophane overhang between the acrylic frame, central barrier, and the bottom of the plate. To avoid dislocation of cellophane and/or frame, we poured 5 ml 1%P MSR into the second compartment to immobilize the components. We then filled the compartment to a total of 25 ml 1%P MSR.

To quantify saturation density and internal flow velocities of AM fungi in the absence of host

roots, we used MSR medium with 0.3% (w/v) Phytagel™ as a growth substrate. For the myristate treatment, we supplied the medium with 0.5 mM myristic acid (Sigma-Aldrich; stock concentration 0.5 M in acetone). The control treatment lacking myristate (0 mM) received the same volume of acetone. After autoclaving, we filled 15 ml of medium in small petri dishes (60mm). Once fully cooled, we placed a circular sterile piece of porous cellophane (Hoefer™ TE73, 50 mm) on the surface of the medium. The 0.5 mM concentration of myristic acid ($C_{14}H_{28}O_2$) in the 15 mL of medium contributed to a total of 1.3 mg of carbon in that form, and inoculated with spores as described below.

Inoculation of fungal material on root system

In a laminar airflow hood, we transferred 2-3 cm of in vitro Ri T-DNA transformed Daucus carota root (Genotype 1 or 2) to the root compartment of the split plate. This compartment was not covered by cellophane. We then cut a circular plug containing only AM fungal mycelium and spores from fungal stock plates. We placed the inoculation plug on top of the root, covering roughly half of the root. We sealed the plates with parafilm and stored them horizontally and upright in an incubator at 25°C. For AM fungi grown with myristate, we inoculated the center of each plate with 10-15 spores in a mixture of single spores and clusters without roots. In all cases, we checked plates regularly for growth and removed any roots crossing from the root compartment into the cellophane-covered fungal compartment. The AM fungi colonized the roots in roughly 30 days, crossing into the fungus-only compartment roughly 5-6 weeks after inoculation. For AM fungi grown without roots, we used a similar time frame (2 months). We recorded the time of the first barrier-crossing event, which was set as time zero, after which we began imaging network formation.

2.3.2 Image processing

Details of image processing describing the segmentation of hyphal segments and spores as well as network graph extraction and node tracking can be found in **Supplementary Methods**.

2.3.3 Analysis

Defining Network Features

Defining the region of interest: To detect and describe all network features, we first defined the region of interest for analysis within the fully stitched image of the fungal compartment. To avoid border effects, we defined the region of interest as the area between a line that ran parallel to the central barrier of the split plate, separated by 6mm from the barrier, and a 4.5cm radius semicircle centered at the midpoint of that line within the plate.

Classifying graph edges into Branched Absorbing Structures (BAS) and Runner Hyphae (RH): We considered that a given edge of the network graph belonged to a BAS when any of these three criteria were met: (1) the length of the edge was less than 400 μm, (2) the length of the edge was less than 1000 μm and one of the two endpoints of the edge coincided with the endpoint of a hypha (i.e. a tip). (3) The average width of the edge was less than 7 μm and the product between this width and the length was less than 9,000 μm^2. These choices were inspired by the definition of branched absorbing structures according to Bago et al. 1998, with parameters tuned to achieve satisfactory BAS detection under visual evaluation. Edges that did not belong to a BAS

were designated as belonging to a RH. The total length of RH shown in Fig. 2.4**b** is therefore the total length of all edges of the network minus the total length of BAS edges.

Width estimates for BAS identification: Although the low (2x) magnification used for network extraction does preclude accurate determination of hyphal width, we found that to discriminate between runner hyphae and BAS, it was helpful to use crude width estimates obtained through the following procedure. First, transects perpendicular to the hyphal edge and of 120 pixels in extent were generated with the function profile_line of the package skimage. We then fitted a Gaussian to the resulting curve using the curve_fit function of the scipy.optimize package. Width was defined as two times the standard deviation.

Growing tip definition: Growing tips were defined as tracked nodes of degree 1 that were at least 40 pixels from their detected position in the last image frame where they were detected. Most network tips (degree 1 nodes) are non-growing BAS tips. Imperfect network alignment or extraction sometimes led to artefactual detection of growth in non-growing tips, which meant a non-zero speed was not a sufficiently robust criterion for detecting actively growing tips. It was therefore important to analyze non-growing BAS tips separately (see below).

Classifying growing tips into BAS and RH: While the classification criteria for graph edges based on hyphal filament dimensions (see above) were sufficient for accurate estimation of total RH and BAS lengths, they did yield a finite rate of classification errors that tended to be higher near growing tips (because edges near RH tips had similar dimensions to BAS edges). Those errors had little effect on total length estimation but did significantly affect the estimation of growing tip density. Accurate estimation of growing tip density thus required distinct classification criteria from those of edges. A growing tip was thus designated as belonging to a RH if its final position was at a distance greater than a threshold distance, 2.5mm, away from its initial position, and all other growing tips were designated as belonging to BAS. The threshold was set by visually assessing the classification quality. Because the model described the population of runner hyphae tips, we chose to plot in Figs. 2.2 and 2.3 the density of growing RH tips. Including all growing tips did not affect the traveling-wave dynamics discussed in the text.

Detecting anastomosis (tip annihilation) events in space and time: Anastomosis events occur when growing tips fuse with hyphal edges to create junctions across which cytoplasm is connected. Thus, every anastomosis event is also a tip annihilation event that contributes to regulating colony growth and densification behind the advancing wave front. To compute the anastomosis rate plotted in **Fig.** 2.3, we first detected anastomosis events in our tracking analysis, where they were defined as the subset of all events at which a tracked node's degree jumps from 1 to 3, whose degree never reverts back to degree 1 thereafter. The complementary subset whose degree does revert back to 1 were classified as hyphal crossing events. We recorded for each anastomosis event its position in space, defined by the pixel at which the skeletonized T-junction trifurcates, and its time, defined as the last timestep in which they were of degree 1. The anastomosis rate (in units $\mathrm{mm}^{-2}\mathrm{h}^{-1}$) within a given ring at time t was computed by dividing the number of anastomosis events occurring within that ring over a time interval $[t, t+\Delta t]$ by the area of that ring and also by Δt, the time interval between two successive frames. For the total anastomosis count (**Fig.** 2.4), the method was adjusted to study the evolving topology of the network (see Total anastomosis count).

Detecting branching events / newborn tips: Newborn tips, which result from branching events, at each timestep t were defined as growing tips that appeared for the first time at t. To

compute the branching rate plotted in **Fig.** 2.3, we first detected branching events in our tracking analysis. The branching rate (in units $\mathrm{mm}^{-2}\mathrm{h}^{-1}$) within a given ring at time t was computed by dividing the number of branching events occurring within that ring over a time interval $[t, t+\Delta t]$ by the area of that ring and also by Δt, the time interval between two successive frames.

Distance from origin and traveling wave speed: We defined the distance from origin r by approximating the polygonal convex hull of the colony as a semicircle, and computing from the convex hull area A the semicircle radius r as $r = \sqrt{\frac{2A}{\pi}}$. The accuracy of this approximation for r is limited by the degree to which the convex hull of the colony is well-approximated as a semicircle and varied across sample plates given the considerable random variation in colony shape. Inaccuracies in the estimate for r in turn lead to inaccuracies in the wave speed v estimated from the density profiles $n(r)$ and $\rho(r)$ at different times. For this reason, the growth speed of the 'puller hyphae' at the growing front v_p provides a more robust proxy for the traveling wave speed, and was used to study the stability of wave speeds in **Fig.** 2.2, **Extended Data Figs.** 2.6,2.9,2.10.

Definition of 'puller hyphae' at the growth front: At every time point t, we defined puller hyphae as those hyphae whose tip satisfies the definition for growing tips (see above), and in addition resides at the growth front at time t. Tips were defined to be at the growth front at timestep t if they were a vertex of the colony's convex hull at both timesteps t and $t+1$.

Definition of the time coordinate: In Figs. 2.2d, 2.3d and 2.5, zero on the time axis corresponds to the start time of imaging, which was initiated as soon as crossing into the fungal compartment was detected by manual examination of the pre-imaging sample pool. Because those manual examinations were carried out once every two days, on average, the zero point on these time axes is thus later than the actual crossing time by an unknown interval of up to 2 days. To compare temporal network development across samples in Figs. 2.4b-e, it was necessary to align in time the data from each sample. We therefore defined the offset time t^* as the time at which the total RH length in the fungal compartment reached 100 mm, and plotted data from all samples as a function of $t - t^*$.

Definition of the arrival time t_n at the n-th ring: The 'arrival time' t_n (used as a time offset in **Fig.** 2.2**c**) at which the traveling wave passes through the n-th ring was defined as the time at which the front of density within that ring reached half of its maximal value. To obtain t_n for the hyphal density wave, we fit a sigmoid curve of equation $\rho(t) = \frac{K_1}{1+e^{\lambda(t_n - t)}}$ to the hyphal density time series in the n-th ring, with K_1, λ, and t_n as free parameters. For the tip density wave, we fit the curve of equation $n(t) = \frac{K_2 e^{\lambda(t'_n - t)}}{(1+e^{\lambda(t'_n - t)})^2}$ with K_2, λ, and t'_n as free parameters.

Total anastomosis count: Whereas spatially resolved detection of anastomosis events for **Fig.** 2.3 achieved through tracking (see above) allowed us to estimate the rate of tip annihilation upon formation of 3-way nodes, the aim of the total anastomosis count across the entire network (**Fig.** 2.4) was to study the evolving topology of the network. As detailed in **Supplementary Methods**, a fraction of anastomoses also occurred at crossing points (i.e. degree 4 nodes) which do not lead to tip annihilation but might significantly affect the overall graph topology. We therefore used a different technique to detect anastomoses for the total-count analysis, based on graph theory. According to Euler's formula for planar graphs, there is a relationship between the number of faces (which equals the number of anastomoses), the number of nodes v and the number of edges e and the number of faces f: $v - e + f = 2$. The number of edges and the number of nodes were readily accessible from the extracted network graph. We found through high-magnification control experiments (**Supplementary Methods**) that 10% of all anastomoses computed through the

Euler formula corresponded to anastomoses at degree 4 nodes. Counting or not counting them does not substantially affect the overall picture, but we nevertheless included them in the anastomosis count (**Fig.** 2.4**c**).

Analysis of flows

Kymograph generation: We recorded transport videos at high magnification (100x), as described in **Supplementary Methods**. We captured more than 1,600 movies at 20 or 25 frames per second for a minimum duration of 20 seconds across a total of 28 biological samples (split petri plates). Within each biological sample, we recorded movies at different positions within the network (between 20 and 100 distinct positions per plate). We captured all videos within runner hyphae. We sampled flows as a function of spatial position across the network and this was done in a manner that follows particular hyphae (>90% of movies), as exemplified by the experiment of **Fig.** 2.5**d**. Because these brightfield videos are label-free, they effectively integrate information about the motion of any organelle or other biological object within the cytoplasm that produces sufficient intensity contrast. Most movies exhibited simultaneous antiparallel flows of such 'contrast objects', with some directed towards the host, i.e., the root (green arrow in **Fig.** 2.5**a**) and others toward the tip of the hypha (purple arrow in **Fig.** 2.5**a**). For kymograph analysis, we analyzed each movie by first picking a linear (one-pixel wide) region of interest of length 20 μm (white arrow in **Fig.** 2.5**a**) at the center of a straight section of the hypha to obtain at every image frame a (one-dimensional) vector of pixels $\vec{I}$. We then arrayed $\vec{I}$ at each image frame to obtain a 2D image (kymograph) where one axis (shown vertically, in the example of **Fig.** 2.5**a**) represents the spatial dimension along $\vec{I}$ (of total length 20 μm) while the other axis (horizontal in **Fig.** 2.5**a**) represents time (over the entire duration of the movie, ranging from 20 s to 60 s). Example kymographs are depicted in Extended Data **Fig.** 2.17, including kymographs from networks grown with a host in myristate (**Extended Data Fig.** 2.18). Given the label-free nature of the imaging performed, these kymographs represent a superimposition of many trajectories of individual contrast objects within the cytoplasm (detected generically as 'particles' in our speed analysis) as their position along $\vec{I}$ evolves from frame to frame.

Speed extraction: We extracted one kymograph with multiple trajectories per movie recorded, i.e., a total of more than 1,600 kymographs to sample ∼100,000 trajectories across a range of positions in space and times throughout network development. We detected from each kymograph a set of individual trajectories by using a deep learning software for automated kymograph analysis (KymoButler, Wolfram Mathematica) developed by Jakobs et al. This program works by using a fully convolutional deep neural network to identify bidirectional tracks to obtain from each kymograph a collection of particle trajectories. We imposed a minimum duration of 10 consecutive frames as a constraint on the trajectory detection algorithm to ensure that detected trajectories correspond to the actual motion of contrast objects. Very short trajectories (below 500 ms in duration) could be associated with tracking errors across image frames that give rise to erroneous (and often anomalously high) flow speeds being detected. Imposing this constraint led to robust detection of correct flow speeds up to a limit of 40 or 50 μm/s (for movies recorded at 20 or 25 fps, respectively), corresponding to the speed of an object that travels the full spatial extent of the kymograph (20 μm) in 10 image frames. We checked all kymographs manually after the automatic detection to validate our protocol and confirm the accuracy of our detected speeds. Example kymographs are represented in **Extended Data Fig.** 2.17 (with host root) and **Extended Data Fig.** 2.18 (without host root). As seen in **Extended Data Fig.** 2.17, detected trajectories demonstrated

movements in both directions (toward the tip in purple and toward the root in green) for around 3,600 trajectories per biological sample). The statistics of their average velocities are represented in the violin plots of **Fig.** 2.5**b**.

Max speed extraction: As the automatic detection of average velocities failed to capture outliers (i.e. very rapid flows larger than 40-50 μm/s, mentioned above), we performed a manual screening of all recorded movies (more than 1,600 in number) to detect the fastest flow in each direction for each movie. Once the fastest flows were identified within each movie, the maximum velocity within the movie was obtained by manually pointing at the slope of the corresponding trajectory (straight line) within the associated kymograph. We then obtained maximum velocities for each video as represented in **Fig.** 2.5**c**.

Over the entire set of over 1,600 movies investigated, only 7% of the movies (¡120 in number) included maximum-speed outliers not detected automatically by the algorithm. This relatively low incidence of undetected outliers provided additional confidence that the average speed statistics represented from the automated detection (**Fig.** 2.5**b**) are reliably representative.

Spatial mapping within the network: We next mapped the spatial position of each flow movie to the skeletonized network to enable analyses of flow velocities as a function of space, as seen in **Fig.** 2.5**d-f**. We recorded the acquisition X-Y coordinate within the sample plate for each high-magnification flow movie (using a 100x objective, image size of 141 μm x 103 μm at the sample plane), and we aligned the full set of these coordinates for each plate with the network skeleton (extracted from the stitched image of the fungal compartment obtained with a 2x objective) leading to a rough overlap. This first alignment was achieved by matching the X-Y coordinates of one particular movie (such as an easily identifiable tip) within the skeleton. We then manually performed a finer adjustment of the position of each movie within the network by comparing the exact shape of each hypha imaged with the skeleton. The maximum error for alignment was around 100 μm (of the same order of magnitude as the size of the high-magnification field of view).

Distance to the tip: The distance to the tip corresponds to the curvilinear length to the tip of the hypha to which a given video position belongs – not the closest tip including other hypha of the network. A hypha is an equivalence class on the set of edges based on the "continuity" relationship. In short, two edges belong to the same hypha if they are the trace left by the same growing tip. In practice hyphae can be recognized by a continuity in edge directionality and width at each junction. Based on visual identification we manually defined which hypha the edge in which a given video was taken belonged to and therefore which tip of the hypha to associate with it. Distances are defined by the curvilinear length along the graph through the shortest path that goes from the video position to the tip.

2.3.4 Plate harvesting and DNA extraction

The roots were harvested from the split plate using tweezers, removing any trace amounts of media at one (n=3), three (n=5), seven (n=3), twelve (n=4) and thirty (n=8) days after *R. irregularis* A5 crossed to the fungal compartment. The total wet weight of the roots was measured and split for DNA extraction and root staining to determine colonization. The roots separated for DNA extraction were placed to dry in an oven in a paper bag at 80 °C and the dry weight was measured after 72 h.

Samples were first ground using liquid nitrogen and a mortar and pestle to disrupt the cells. DNA

was extracted using the QIAGEN DNeasy® PowerSoil® kit according to manufacturer's instructions. One change was made in the duration of the first centrifugation step, lengthened from 30 sec to 3 min to better separate the supernatant. DNA was eluted into 50 μL 10 nM Tris-HCl, pH 8.5, and quantified using a Nanodrop Spectrophotometer ND-1000. For phosphorus content determination of roots and agar, see **Supplementary Methods**.

Intraradical mycelium (IRM) quantification

To quantify intraradical length, we used two methods: (i) one traditional method relying on root staining and visual quantification (i.e. Trouvelot method) and (ii) one method using droplet digital PCR (ddPCR) to calculate the length of hyphae based on counting nuclei per μm of hyphae (see **Supplementary Methods**). We used ddPCR with nuclei-specific probes which occur only once in the genome to directly quantify the total number of nuclei across the hyphae. For each plate, 4 non-template controls (NTCs) and 4 positive controls (*R. irregularis*, A5 DNA extracted from pure culture) were used to set the fluorescence amplitude threshold (high threshold) values to distinguish between the positive and negative droplet cloud. Once thresholds were set, we used the concentration (copies/μL) to calculate the length of hyphae using a modified formula from. To calculate the length of the hyphae in the roots (μm), this final value was then multiplied by the distance between nuclei as described in **Supplementary Methods**, **Extended Data Fig.** 2.19 and **Supplementary Video 8**.

2.4 Contributions

The structuration of this paper and its figures is largely the result a collaborative work together with all authors in particular Toby Kiers, Tom Shimizu, Howard Stone and Loreto Oyarte Galvez. Main text was written by Toby Kiers and Tom Shimizu. I took care of producing Figure 2.2, 2.3 and 2.5 and performed the related data analysis. I wrote the code related to network extraction and hyphal tracking including its parallelization to allow processsing of large amount of data. I wrote the corresponding methods. I took care of model integration and wrote the corresponding methods together with Tom Shimizu. I also produced and designed all External Data Figures expect 2.13 and 2.19. Detailed contributions as well as external ideas are detailed below.

Figures

- Figure 2.1 design and data was the work of Loreto Oyarte Galvez together with the help of a professional graphic designer.
- Figure 2.4 design and data related to network efficiency was the work of Loreto Oyarte Galvez.

Text

- Main text is to the most part the work of Toby Kiers and Tom Shimizu

Data acquisition

- Plate preparations was done by Malin Klein, Marije Van Son and other collaborators.

- Plate maintenance was done by Loreto Oyarte Galvez, Marije Van Son and myself
- Video acquisition was done by Loreto Oyarte Galvez and myself
- Plate harvesting and DNA extraction were the work of Marije Van Son and Bianca Turcu
- Nuclei counting allowing Intraradical Mycelium quantification was the work of Sander Van Otterdijk
- I performed the Phosphorous measurements with the help of Rob Broekman. The method was initially put in place by Loreto Oyarte Galvez and Constanza Oyarte Galvez.

Methods

- AM culture system for imaging was developed by Malin Klein and Loreto Oyarte Galvez
- Imaging set-up in both high and low resolution and the associated were build by Loreto Oyarte Galvez and the AMOLF software, electrical and mechanical engineers.
- Speed extraction from Kymographs as shown in this chapter was the work of Philippe Bourianne

Ideas

- The general idea of imaging fungal colonies both in low and high temporal and spatial resolution is from Tom Shimizu and Toby Kiers
- Looking at hyphal density in concentric rings was an initial idea of Tom Shimizu inspired by previous work on the propagation of bacterial colonies.
- We initially were suprised by the flat profile we observed in that data until we rediscovered the modelling framework of Andrea Schnepf itself inspired by the work of Leah Edelstein. We later found that similar work had been done by Edouard Hannezo for branching organisms which further inspired our discussions of the travelling wave solutions of the equation.

2.5 List of Supplementary Videos

Supplementary Video 1: Extracted skeleton of the network development over the first 112 hours. Colour of each segment corresponds to time of appearance.

Supplementary Video 2: Tracking of nodes in a region of space. Node colour corresponds to their label, maintained over time. Edge colour corresponds to label, maintained over time when the two end nodes are constant. Scale bar is 1 mm.

Supplementary Video 3: Example high magnification video of flow trajectories of *Rhizophagus irregularis* A5. Scale bar is 10μm.

Supplementary Video 4: Traveling wave of hyphal filaments and tip densities. Blue is filament density and red is tip density. Shaded region corresponds to uncertainty in density estimates computed via bootstrapping.

Supplementary Video 5: Example high magnification video of flow trajectories of Rhizophagus irregularis A5. Videos correspond to kymographs of Extended Data Fig. 2.17. Scale bar is 10μm.

Supplementary Video 6: High magnification video associated with Fig. 2.5. Scale bar is 10μm.

Supplementary Video 7: Example colliding wave videos corresponding to Extended Data Fig. 2.16. Scale bar is 1cm.

Supplementary Video 8: Imaging of nuclei in fixed mycelia of the strain *Rhizophagus irregularis* A5. Scale bar is 20μm corresponding to Extended Data Fig. 2.19

Supplementary Video 9: High magnification video of flow in hyphae of Rhizophagus irregularis in the absence of host root with carbon supplied as myristate corresponding to Extended Data Fig. 2.18

2.6 Supplementary Methods

2.6.1 Timelapse Imaging

After the fungal network entered the fungus-only compartment, we placed each replicate into the sample rack of our custom-built, high-throughput imagining robot. This allowed us to generate high-resolution images of the fungal network every 1, 2 or 4 hours, for ∼15 days, and every 8 hours for the next 30 days. The imaging platform was temperature controlled (25 °C) in a dark enclosed environment. Our optical system integrated an illumination light source, lenses, and camera, which translated across the samples, allowing imaging of up to 40 plates in parallel. Our customized microscope was composed of a 2x objective lens (Thorlabs TL2X-SAP - 2X 0.1 NA Super Apochromatic) coupled through a tube lens (f=200mm) to a 12MP CMOS camera (Basler acA4112-30um) with a pixel size 1.725um small enough to achieve Nyquist sampling of the optical resolution, which we estimated according to Rayleigh criterion at $0.61\lambda/\text{NA} \approx 3.7\mu m$, given the objective's numerical aperture (NA= 0.1) and illumination wavelength ($\lambda \approx 600nm$). The objective, tube lens, and camera were mounted altogether on a Thorlabs KMTS25E/M motorized stage, which was used for focusing. For illumination, we used red LEDs (TOPLED® - Enhanced Optical Power LED (HOP 2000)), a customized arranged in a 2x2 square array with a spacing such that the array covered a 15x15mm2 area. To collect and diffuse the light, we placed an aspheric condenser lens with diffuser (ACL2520U-DG15-A, Thorlabs) between the sample and LEDs.

The entire microscope (comprising the light source, objective, camera, intervening optical elements, and focusing stage) was mounted on an X-Y motorized linear stage with stepper motors (NEMA23L IP65 Servotronix) driven by a customized motor controller. The range of travel of this stage was 0.5m in the X-direction and 1.0m in the Y-direction, which was sufficient to cover the entire 8x5 array of plates on the sample rack. This system allowed us to generate a fully-tiled image (1.2 Gigapixels) of the fungal compartment composed of a matrix of 10x15 images (5x7mm2 each) with a 20% overlap, at every time point.

2.6.2 Image Processsing

All the code used for image processing is available in this GitHub repository

Image stitching

For each timestep, we stitched together the network images using the ImageJ Stitching plug-in Grid/Collection Stitching Plugin[63]. In this program, stitching is achieved by aligning images by utilizing cross-correlation of the intensity pattern between neighbouring images. To correct for heterogeneities in the illumination, the background of every image is first subtracted using a "rolling ball" algorithm with a ball radius of 15 px[64].

Network extraction

Our network extraction strategy was inspired by methods developed for fungal colonies by Heaton et al. (see [65] for mathematical details). Briefly, we first removed the background using the same rolling ball algorithm as above, then enhanced edges using the bowler hat algorithm[66] and used anisotropic smoothing to maintain connectivity of the network[67]. Edge enhancement algorithms tend to put lower weight on junction points with the risk of losing connectivity. Anisotropic smoothing allowed us to make sure junction points stay connected by expending edges slightly in following along their own local orientation. After these steps, we hysteresis-thresholded the images using the `apply_hysteresis_threshold` function of the skimage module of Python[68]. The high threshold is set to the minimum between the pixel value 90 and the 99.5th percentile of pixel values. The low percentile is set to be the maximum between a pixel value of 20 and the 93rd percentile of pixel values. We then stitched the resulting thresholded images together using the stitching parameters found during image stitching. The result was thinned out to a one pixel wide skeleton using the `ximgproc.thinning` routine of the cv2 package of Python[69].

We manually adjusted all the parameters of the extraction (i.e. edge enhancement, anisotropic smoothing, thresholding) once for all plates of the same strain. The aim was to maximize the extraction quality with a focus on maintaining connectivity and on minimizing the detection bias between thicker and thinner edges. Pixel level segmentation precision and recall were not considered a good metric to evaluate the quality of network extraction since it overlooks the importance of connectivity. We therefore evaluated the precision and recall of edge detection. An edge was considered to be correctly detected if both of its endpoint nodes were positioned correctly and were of the right degree. To extract these metrics, we compared the extracted graph to the raw images of a given plate in randomly selected regions and counted manually the number of false-positive and false-negative detections of graph edges. The precision of edge detection (i.e. true positives divided by the sum of true positives and false positives) was estimated to be 0.93, while recall (true positives divided by the sum of true positives and false negatives) was estimated to be 0.96.

Network overlay

Due to differences in the image-stitching parameters and/or imperfections in the repeatability of the imaging robot's relative positioning of the optics on the sample, networks at different timesteps did not always fully overlap. We therefore had to identify the correct translation and rotation to align extracted networks. For the overlay, we used the "Coherent Point Drift" (CPD) algorithm8, using randomly selected subset of points from the skeleton. Because it relies on the relationship between different points more than on individual "nearest neighbour" routines, the algorithm is good at roughly matching structured shapes even when they are heavily shifted relative to each other and with a fair amount of noise. Using Python/C++ implementation in the cycpd package[70] with a sufficiently high number of random points taken from the skeleton (1% of all points of the skeleton),

the computation was tractable, and a first rough overlay was obtained with this routine. The second routine to more finely adjust the translation and rotation used the iterative closest point algorithm (ICP)[71] . Here, we employed a Python/C++ implementation of the package Open3d[72] on the subset of points from the skeleton corresponding to junctions.

Graph generation

Using a custom algorithm based on pixel neighbouring relations in the skeleton, we transformed the pixel skeletons to a graph format where all junctions and apexes become "nodes" of the graph and branches between them become "edges". Pixels of the skeleton that had 0, 1 3 or 4 neighbours were therefore considered "nodes" and two nodes were connected by an "edge" if they were connected by a consecutive series of neighbouring skeleton pixels with no intervening nodes among them.

Node tracking

After transformation to a graph, we employed two postprocessing steps to identify and track every unique node over time and space. First, we removed the small unconnected components not belonging to the fungal colony. We computed a score based on the total length of each connected component. We then removed all those below 1 mm. This was chosen because most of these connected components would reach such a size within a few timepoints if they really corresponded to fungal material.

Second, to ensure consistent node identification at junctions, we introduced steps to confirm degree 3 and degree 4 nodes. Degree 3 nodes correspond to branching or to anastomosis points. Degree 4 nodes were found in the network when two hyphae crossed, or because of a rarely occurring double branching event at a single location. Because the skeleton was only one pixel wide, the degree 4 nodes were sometimes detected as two very close degree 3 nodes.

To solve the problem leading to incorrect node identification, we reassigned any detected pairs of degree 3 nodes that were within 30 pixels of each other as a single degree 4 node. Next, we assumed that nodes of degree 3 or more were static across frames, apart from a small movement (¡10px) due to noise of the skeletonization process and imperfect alignment of successive image frames. Therefore, for each node at a given time t we considered the nearest neighbouring node at time t+1 as "biologically identical" and assigned them the same label. Sometimes ambiguity would arise because two nodes at time t have the same nearest-neighbour node at time t+1. In those cases, we linked the node of time t with that node at time t+1 lying nearest to the position of this ambiguous node at time t.

In general, degree 1 nodes are more difficult to track since they are effectively moving from apical extension. For each degree 1 node at time t, the algorithm first identified the closest edge at time t+1 and set it as the current edge. Then it selected one of the two nodes of that edge based on the direction of tip growth. Direction of tip growth was defined based on the orientation of the edge connecting to that degree 1 node at time t. The selected node was set to be the current node. Then the algorithm operated recursively. If the current node was of degree 1, the algorithm stopped and established identity between that node of time t+1 and the initial one at time t. Otherwise, it compared the angles between the current edge and other edges that connect to the current node. The edge that subtended the smallest deflection angle relative to the current edge was selected. That angle was then compared with the angle between the selected edge and all other edges joined at the

junction. If any of those deflection angles were smaller than the angle between the current edge and the selected edge, then the algorithm stopped. We established identity between the current node and the node that was of degree 1 at timestep t and that now, at time t+1, became of degree 3 or more (i.e. the apex anastomosed). Otherwise, the other endpoint node of the selected edge became the current node, and the selected edge became the current edge. This algorithm could correctly track hyphal tip when crossing over an already existing hyphal filament. Indeed, this kind of event creates a degree 4 junction where the path of lowest deflection angle followed by the algorithm would continue across the junction. To evaluate performance, we selected randomly growing tips and visually assessed that more than 98% of them were correctly tracked over two timesteps. We found that the main runner hyphae were generally more reliably tracked over several timepoints compared to the small, branched absorbing structures.

Spore extraction

We extracted spore number and biovolume from images using the SimpleBlobDetector function in OpenCV 7. The function was set up to detect blobs with a minimum area of 500 pixels and a maximum area of 50000 pixels. We set the minimum circularity to 0.4 to ensure that only round or elliptical blobs were detected. Before running the SimpleBlobDetector function, we removed the background of the image to simplify the detection process. We applied this function to each image individually, saving the position and radius (from which volume was computed) of each individual spore. We then tracked individual spores across timepoints by minimizing the distance between center points.

All code related to network and spore extraction and node tracking can be found in this GitHub repository.

2.6.3 Spatial averaging

Definition and use of rings for density mapping

At each timestep, we first separated the full colony graph into its connected component subgraphs (sets of nodes that have at least one path between them through the graph). The number of such connected subgraphs can be greater than one because crossings into the root compartment can occur more than once on a single plate. Such disjoint networks were not the most common occurrence, but also not rare. However, when they did occur, disjoint subgraphs tended to join with one another through anastomosis within a few time steps, to yield a single connected graph.

We then generated polygons (or multiple polygons in the case of multiple subgraphs) connecting the leading apexes of the network graph(s). Mathematically, these polygons correspond to the convex hull of each graph. We then selected a subset of these convex hulls at successive time points to define a set of rings (polygonal annuli) of approximately equal area. In the case of multiple subgraphs, each ring was discontinuous and went around each of the crossing front. Hyphal filament density ρ was calculated by dividing the total length of graph edges lying within each ring by the ring area. We calculated the growing tip density n by dividing the total number of growing tips lying within each ring by the ring area (see below for exact procedure of computing ring area, hyphal length, and growing tip numbers.)

We also tested an alternative scheme in which rings of equal width (rather than equal area) were used to compute density. We confirmed that there were no qualitative differences in results, namely

the emergence of the traveling-wave pattern of density dynamics, and no significant quantitative differences in traveling wave parameters (the saturating density ρ_{sat} and wave speed c).

Hyphal length definition

In a given region of interest (ROI), we defined length as the sum of the curvilinear length of all edges of the network graph contained within that region. We computed curvilinear length of an using the list of pixels of the skeleton composing the edge and added the Euclidian distance between successive pixels after down sampling the total list of pixels by taking one out of every ten skeleton pixels. We multiplied the resulting length in pixel units by 1.725μ m/pixel corresponding to the pixel size projected onto the sample plane at the (2x) magnification of the optical system.

Area definition

We defined the area of a given region by using the area function of the Python shapely module[73]. For the total colony area, we first computed the area of each connected component subgraph using the polygon defined by the convex hull of the set of nodes composing that subgraph. We then summed over all these subgraph areas to obtain the total colony area.

2.6.4 Microscopic network connectivity

Connectivity of overlapping hyphae (degree 4 nodes)

We typically detected nodes of the 2D network that corresponded to two hyphae overlapping without tip annihilation during crossing as degree 4 nodes. Such events were not rare. Assessing visually these degree 4 nodes at high magnification revealed that at early time they would usually not correspond to an actual biological connection (i.e., with a cytoplasmic continuity). However, after about a week, we found these junctions fused, either at points of direct contact between existing walls, or via small hyphal side branches that emerged to connect the two overlapping hyphae. Observing a total of 128 positions corresponding to overlapping hyphae at higher (50x,10x) magnification and confirming cytoplasmic continuity by imaging the flows, we estimated that about 34% of all these points could be considered "fused".

Connectivity of anastomosis and crossing points

To confirm connectivity of anastomosis point detected in 2x magnification, we randomly sampled degree 3 nodes that were suspected to be anastomosis points. Imaging of the flows in higher magnification further confirmed whether or not there was complete cytoplasmic continuity. Out of 18 such suspected anastomosis points, 17 displayed cytoplasmic continuity. This led to the conclusion that when a degree 1 node corresponding to a growing tip, detected at 2x magnification, became a degree 3 node by ceasing its growth at a position occupied by an existing hyphal filament, it corresponds to an actual anastomosis event.

2.6.5 Phosphorus measurement

Agar and root preparation

We calculated phosphorus concentrations in fungal and root compartments by first removing cellophane from the fungal agar, and then cutting the agar into equal sized pieces (up to 18 pieces). Each agar cube corresponded to a spatial position either away or close to the root. We cut the root compartment agar into two pieces and carefully separated the root from the root agar. We weighed each agar piece and placed it in a Teflon cylinder, and we placed each root in a kraft envelope. We put the Teflon cylinders and envelopes in the oven at 70°C for two days to dry. After drying, we weighed roots and placed them in a Teflon cylinder.

Digestion

We added 0.5 ml of digestion mixture (HNO3/HCl 4:1) to the Teflon cylinders using a repeating pipette and left the cylinders open for 30 mins to release gases. We then placed the closed cylinders in a destruction oven at 140°C with the temperature limit set to 160°C for 7 hours. We opened the cylinders, added 2 ml of demiwater using a dispenser and transferred the contents of the cylinder to a test tube. We left the test tubes in a fume cupboard for at least one day to release acid fumes and covered them with plastic foil before placing them in the cold room for a week.

Spectrophotometric determination of phosphate content

The phosphate estimation was based on the formation and reduction of phosphomolybdate. Following the method of[74], we pipetted 150μL of the solution obtained after digestion in test tubes and added 4mL of colour reagent. The colour reagent was prepared in a 1L water solution with 13.33mL concentrated H2SO4, 1.14g ammonium heptamolybdate, 1.00g ascorbic acid and 0.026g of potassium antimony. The test tubes were left for 30 mins for the colour to form. We measured absorbance at 880nm in a spectrophotometer using plastic cuvettes. Because P is known to be bound/adsorbed by soluble aluminium, iron, and manganese at low pH[75], we calculated that $\sim$2μg/mL of P was inaccessible in root and fungal compartments, which we used as our baseline in Ext. Data. Fig. 2.11.

2.6.6 Estimating carbon cost

In order to estimate the carbon cost of the colony in Fig. 2.4e, we first estimated the total carbon in each edge linking node i and node j. To estimate its biovolume, we approximated it to be a cylinder of radius $r = 5\mu m$ and therefore defined its volume $V_{i,j}$ to be $V_{i,j} = \pi r^2 L_{i,j}$ where $L_{i,j}$ is the length of the edge. To then estimate the total carbon in each edge, we assumed fixed ratios true for most biological material. The first one is the ratio of dry mass to wet mass p_{dry} which is generally estimated to be 21% for fungi[76]. The second one is the ratio of carbon in dry mass p_{carbon} that we set to 50%[77]. The third element is the cell density d_{cell} which is generally estimated to be around 1.1 g/cm^3[76]. Such ratios could theoretically be expected to be different for AMF. They could also differ between edges and within the phylogeny. But these "living cells" averages are a good first-order approximation and don't affect the general conclusion discussed within the scope of this paper.

The mass of carbon contained in the edge is therefore $m_{i,j,C} = V_{i,j} d_{\text{cell}} p_{\text{dry}} p_{\text{carbon}}$.

Carbon cost was finally estimated to be $\xi_{ij} = \frac{m_{i,j,C}}{\text{CUE}} = \gamma L_{i,j}$ where CUE is the carbon use efficiency i.e. the proportion of carbon incorporated in biomass and not respired of all the carbon used. We used an average CUE for soil microorganisms of 50%[78] as this does not affect the general trend shown in that figure. We therefore obtain

$$\xi_{ij} = \gamma L_{ij}$$

where

$$\gamma = \frac{\pi r^2 d_{\text{cell}} p_{\text{dry}} p_{\text{carbon}}}{\text{CUE}}.$$

We then could estimate the network-wide carbon cost of the network by summing over all the edges: $C = \sum \xi_{ij}$. For 1 m of colony length, this typically means the typical carbon mass of hyphae is approximately 3 μ g and the total carbon used to grow this biovolume is $\sim$6 μ g.

We then normalized this network-wide carbon cost with respect to its counterparts for the limiting networks $\hat{C} = \frac{C - C_{\text{MST}}}{C_{\text{DT}} - C_{\text{MST}}}$, where C_{DT} is the cost for Delaunay triangulation and C_{MST} is the cost of the minimum-spanning tree.

To estimate the carbon cost of phosphorus absorbed in Ext. Data Fig. 2.11c, we considered L to be the integral over space of hyphal density. Because of the 3d embedding and cylindrical symmetry, it therefore represents hyphal length per root length. Total mass of P and C are then given per unit length. The carbon cost of phosphorus was finally estimated to be

$$\pi = \frac{m_C}{m_P} \times \frac{1}{\text{CUE}}$$

with m_P the mass of P as defined in section 4.2.5.

2.6.7 Intraradical colonization quantification

Counting nuclei

We added the concentration (copies/μL) from both FAM and HEX channels (MAT3 and MAT6 loci due to the heterokaryotic status of the A5 strain used) and we used the final value to calculate the total AM fungal nuclear content in the roots using a modified formula from Kokkoris et al.[79].

$$\text{final value} = (\text{QuantaLife value} \cdot \frac{\text{RV}}{\text{SQ}} \cdot \text{EQ})$$

Where the QuantaLife value is the additive value of the copies/μL from the software for the two channels, RV is the volume of the reaction, SQ is sample DNA quantity used in the reaction, and EQ is the quantity of DNA extracted.

Total length of intraradical hyphae

Fixation and nuclear staining in intraradical mycelium To be able to translate the number of nuclei to intraradical mycelium (IRM) length, we used a protocol to fix AM fungal mycelia of R. irregularis A5, followed by nuclear staining. This allowed for quantification of average number of nuclei per μm of hyphae. As in experiments above, we harvested fungi grown in split plates.

We harvested replicates across different time points to allow for variation in the fungal life stage. Before harvest, each Petri plate was stored for at least 2 days at 4°C to slow down cytoplasmic flows and avoid disturbance in the nuclei distribution during fixation. The growing network on top of the cellophane was then fixed and DAPI stained to visualize the nuclei. Specifically, the network was fixed by slowly applying PFA 4% in 1x PBS (100 mM KHP04, pH=7.4) with a syringe pump (Fusion200, ChemYX) at a flow rate of 50.000 μL/hour for 3 mins. The syringe tip was connected to the cellophane with IBIDI silicone tubing (IBIDI ref:10842). Then, the network was incubated for 45 minutes submerged in a thin layer of 4% PFA at RT. After fixation, the PFA was removed by reversing the direction of the syringe pump at the same flow rate. Lastly, the network was DAPI-stained by adding DAPI (5 μg/mL) at a flow rate of 50.000 ul/hour for 3 mins and incubating at room temperature for 10 mins. The DAPI was removed reversing the direction of the syringe pump at the same flow rate. Pieces of cellophane containing network were cut out and placed on glass slides. The pieces were covered by glass square coverslips for imaging.

Nuclear visualization Cellophane cutouts were imaged using an Olympus BX63, a wide-field epifluorescence microscope, equipped with Ultrasonic stage and UPlanSApo 60× 1.35 NA oil-immersion objective (Olympus). Lumencore SOLA FISH light source, a Hamamatsu ORCAFusion sCMOS camera (6.5 μm pixel size, 2304 x 2304 pixels) mounted using U-CMT C-Mount Adapter, and zero-pixel shift filter set: F36-500 DAPI HC Brightline Bandpass Filter. The software used to control the microscope was CellSens Dimension 2.3 Build 18987. Per image position, field of view (fov), tens to hundreds DAPI (exposure time 5 ms) planes, depending on the thickness of the hyphal network, were taken with a spacing of 0.3 μm between each plane. Images were taken with a 60x objective.

Image analysis To obtain calculations for density of nuclei per hyphal length, we performed a segmentation analysis, analysing 8,14 and 15 fields of view (fovs) for replicates 1-3. For the analysis, firstly the nuclei in the 8 fovs of the first replicate were manually annotated in the python image viewer 'Napari'. These 8 images and nuclear masks were divided into 144 × 144× number of zplane crops. Crops that contained at least 3 nuclei (202 crops in total) were kept for training in a 3D StarDist model[80]. Default settings for data augmentation and training were used (see Notebook 1_training – AMF.ipynb). Next, this trained model was used to predict the nuclear mask for the images in replicates 2 and 3 (see Notebook 2_prediction – AMF.ipynb). The predicted nuclear masks were manually corrected using Napari[81]. Next, cell masks of the overall network were created by manually annotating a maximum projected image of the DAPI channel for every field of view. To calculate, the length of the hyphal network these cell masks were skeletonized using the `medial_axis` function from scikit-image morphology library[82]. These skeleton masks were checked in the Napari-viewer and corrected manually if necessary. Lastly, the nuclear density per area and length were calculated and plotted by dividing the number of nuclei by the length of the skeleton mask per FOV using the notebook "Calculate_Nuclear_Density.ipynb". Knowing the average number of nuclei per μ m of hyphae allows us to calculate the total IRM using the nuclear count values originated from the ddPCR analysis (Ext. Data. Fig. 2.19, Supplementary Video 8)

2.6.8 Graph metrics

Betweenness Centrality

Betweenness centrality $BC(e)$ of an edge e of the graph is the sum of the fraction of pairwise shortest paths that pass through it. It can be computed specifying two (possibly overlapping) groups of nodes, "source nodes" S and "target nodes" T, the set of pairs between which defines the ensemble of shortest paths. More specifically, $BC(e) = \sum_{(s \neq t)} \frac{\sigma_{st}(e)}{\sigma_{st}}$ where σ_{st} is the number of shortest paths between nodes $s \in S$ and $t \in T$ and $\sigma_{st}(e)$ is the number of those paths that pass through the edge e, and the summation is over all nonidentical pairs of nodes between S and T. The resulting quantity $BC(e)$ indicates how 'central' the edge e is, on average, for the transport of resources between nodes in S and T. For mycorrhizal networks, a meaningful choice for source nodes S are those nodes directly proximal to the root compartment, and for target notes T, those nodes where carbon resources from the roots are consumed for growth. Note that $BC(e)$ is a symmetric measure in the sense that it is invariant under swapping S and T. Thus, their designation as "source" and "target" is arbitrary, and $BC(e)$ values computed for AM fungal networks (Figs. 2.4a,2.5d) are equally relevant for both carbon transport towards growing tips, and for transport of phosphorous and other nutrients back to the root. We computed betweenness centrality using the `edge_betweenness_centrality_subset` function of the Python networkx library[83] on the graph formed by the network.

We manually selected the set of source nodes S as those nodes immediately proximal to the root compartment. We then selected as target nodes T all the degree 1 nodes of the network other than those in S. For shortest path calculations, we provided curvilinear length of edges as weights to the program, so that shortest paths were detected based on the physical (rather than topological) distance along the network graph. We then set the parameter "normalized" to "True" which means the final result is normalized by $2/(n_S n_T)$, where n_S is the number of source nodes and n_T is the number of target nodes. For each plate, we further normalized betweenness centrality by the highest centrality observed in the network. The latter normalization allowed the betweenness centrality of edges belonging to networks of different sizes to be of comparable magnitude. We noted that these normalizations did not affect the trend described in Figs. 2.5 and Ext. Data Fig. 2.4.

Global and root efficiency

To quantify the geometric efficiency of the network graph layout for transport, we computed the 'network efficiency' measure originally proposed by Latora & Marchiori[45], which compares the distance d^{SP} along the shortest path between pairs of nodes to the shortest possible distance d^{E} in the physical space embedding the network.

To consider the transport demands for symbiotic trade, we computed geometric efficiency for two contrasting contexts: (i) transport between arbitrary pairs of nodes within the network, and (ii) transport between network nodes and the plant host. In both cases, the relevant nodes for considering transport are the terminal nodes T, which we define as the set of all nodes corresponding to growing tips (at which nutrients are consumed to build the network) and attachment sites of BAS (through which absorbed nutrients flow into the network), as well as the root nodes R, which we define as the set of all nodes corresponding to sites of crossing from the root compartment (through which C flows into the network). Because only the fungal compartment is visible with our optical system, we define a node connecting both compartments as any node in a 5mm distance near the

physical barrier in the plate (see Biological Material and Plate Preparation section).

For transport between arbitrary locations of the network, we average over all pairs of nodes in the joint set $P = T \cup R$ to obtain the *global efficiency*, defined as

$$E_g = \frac{1}{\frac{1}{2}N_p(N_p-1)} \sum_{i,j \in P, i \neq j} \frac{d_{ij}^E}{d_{ij}^{SP}}$$

, where the sums run over all $N_p(N_p-1)/2$ node pairs with N_p is the number of nodes in P. For transport between the root and the terminal nodes, we average over all root-terminal node pairs to obtain the *root efficiency*, defined as

$$E_r = \frac{\sum_{i \in T, j \in R} \frac{1}{d_{ij}^{SP}}}{\sum_{i \in T, j \in R} \frac{1}{d_{ij}^{E}}}$$

, where the sums run over all $N_T \times N_R$ node pairs with N_T and N_R the number of nodes in T and R, respectively.

Both efficiency measures E_g and E_r are effectively normalized by the set of shortest possible (i.e., Euclidean) distances such that $0 \leq (E_g, E_r) \leq 1$. Intuitively, this normalization quantifies how close the shortest paths through the network are, on average, to the shortest possible paths (i.e. Euclidean distances) through the physical space in which the network is embedded.
Biologically, simply maximizing the efficiencies is unlikely to be the best strategy because of associated costs. As an extreme example, a totally connected network with $N(N-1)/2$ straight edges between all of N its nodes will maximize both efficiency measures $(E_g, E_r) = 1$, but the large number of edges means the material cost of building the network will also be very high. We therefore further normalized these computed efficiency measures using those for two ideal networks (explained also in the Main Text) that represent limiting cases of efficiency priorities, the "Minimum spanning tree (MST)" and "Delaunay triangulation" (DT), which correspond to graphs with the minimal and maximal limits, respectively, for both efficiency and cost given a fixed set of nodes[4, 45, 49, 84]. We therefore defined analogues to [49] the *relative efficiencies* as $E_g = (E_g^{MST} - E_g^{DT})/(E_g^{MST} - E_g^{DT})$ and $E_r = (E_r^{DT} - E_r^{MST})/(E_r^{DT} - E_r^{MST})$, where E_g^{MST} and E_r^{MST} are the efficiencies for MST and DT graphs, respectively. This normalization results in efficiencies between zero and unity $(0 \leq E_g^r, E_r^g \leq 1)$, with $E_g^r = 0$ corresponding to the efficiency of an MST network for the measured set of nodes, and $E_g^r = 1$ corresponding to that of a DT network for the same set of nodes.

2.6.9 Transport imaging

Imaging system

We built a customized microscope system to acquire high-magnification videos of cytoplasmic flows inside the mycorrhizal hyphae, with the imaging-path optical system identical to that used for low-magnification network imaging (objective, 200mm tube lens and a Basler acA4112-30um CMOS camera, mounted on a Thorlabs KMTS25E/M motorized stage). However, we used a different objective lens (100X Nikon CFI60 TU Plan Epi ELWD). A 1 W red fiber optic LED light source (Product ID: 4165, Adafruit Industries) for illumination through an LED reflector assembled with a Fresnel lens to collect and diffuse the light before the beam reached the sample. The sample stage

was customized X-Y motorized linear stage, with stepper motors (NEMA23 IP20, Servotronix) driven by an Arduino Uno Rev3 micro-controller. With this setup, every video could be related to a specific coordinate in the fungal network.

For transport imaging, we mounted the sample plate on the X-Y motorized stage, which allowed accurate positioning at specific, recorded, coordinates of the network. These recorded coordinates of the movies within the network could then be used to locate the specific nodes and edges within network graph (see below) for correlative analysis between flow velocities and the geometric / topological observables of the network (Fig. 2.5e-f). At each position with recorded coordinates, we acquired high-resolution (100x magnification) videos at 20-25fps for 30 seconds, with at least 3 repetitions per position. We removed the lid of the sample plate at the time of imaging to maximize image quality.

Spatial mapping of videos in the network

We mapped the spatial position of each flow movie to the skeletonized network to enable analyses of flow velocities as a function of space, as seen in Fig. 2.5e-f. We recorded the acquisition X-Y coordinate within the sample plate for each high-magnification flow movie (using a 100X objective, image size of $141\mu m \times 103\mu m$ at the sample plane). We aligned the full set of these coordinates for each plate with the network skeleton (extracted from the stitched image of the fungal compartment obtained with a 2X objective) leading to a rough overlap. This first alignment was achieved by matching the X-Y coordinates of one movie (such as an easily identifiable tip) within the skeleton. We then manually performed a finer adjustment of the position of each movie within the network by comparing the exact shape of each hypha imaged with the skeleton. The maximum error for alignment was around $100\mu m$ (of the same order of magnitude as the size of the high-magnification field of view).

Fourier filtering of kymographs

In order to distinguish the traces of particles moving in opposite directions, we implemented in python a method from the software KymographClear[85]. We first tile the kymograph together with flipped version of itself. Then the tiled image is Fourier transformed. Pairs of diagonally opposing (upper left, bottom right/upper right, bottom left) quadrants as well as the central line of the image's Fourier spectrum are then set to zero to generate two images in this Fourier space. We then reverse Fourier transform the resulting images and only keep the central tile to obtain the two (backward/forward) kymographs. This method was used to generate the kymograph shown in Fig. 2.5a.

Hyphal radius determination

Hyphae radii were measured manually using Icy. For each "edge" (hypha segment from one intersection to another) we drew two lines across the hypha that would span its whole external diameter, which includes the hyphal cell wall. The raw measurements in pixels were then converted into μm in the data table using a coefficient of $0.0345\mu m$/pixel. The mean difference between pairs of measures is $0.39\mu m$ without removing outliers.

2.7 Supplementary discussion

2.7.1 Dimensionality (2-D vs 3-D) and geometry of Mycorrhizal growth

Our experimental configuration enabled imaging of the full mycelial network graph by confining growth of the mycorrhizal network to two dimensions (2-D), whereas growth in real-world soil habitats unquestionably occurs in three-dimensional (3-D) space. Yet, basic symmetry considerations suggest that the radial traveling-wave range expansions we observe in this 2-D experiment are relevant also for mycorrhizal growth in 3-D environments. Extraradical growth of mycorrhizal networks radiate outward from the plant root – a one-dimensional object – and hence the biologically relevant spatial context obeys cylindrical symmetry – an assumption made also in other modeling studies that have addressed data from 3-D soil environments[17, 18]. Our 2-D measurements thus approximate growth patterns along a cross section of a cylinder surrounding the host root, and therefore can be expected to capture salient features of mycorrhizal growth relevant also in 3-D.

2.7.2 Model for travelling-wave growth of Mycorrhizal fungi

General model description

The advancing wavefront of hyphal density observed in growing mycorrhizal networks is reminiscent of traveling waves observed in range expansion phenomena in growing colonies of bacteria and other microbes[25, 27–31]. In the case of bacteria, properties of the wave-like migrating front have been explained using variants of the Fisher-Kolmogorov (FK) model of population range expansion[22–24]. The FK model is the canonical framework for modeling the propagation of traveling wave fronts in both biological population dynamics[22, 24] and physical pattern formation[23], and is described by just one equation:

$$\frac{\partial n}{\partial t} = D\nabla^2 n + kn\left(1 - \frac{n}{n_{\text{sat}}}\right) \tag{2.7.1}$$

Describing the dynamics of the local population density $n(r,t)$ at position r in d-dimensional space. Its time rate of change $\frac{\partial n}{\partial t}$ is determined by the sum of two contributions on the right-hand side. The first term $D\nabla^2 n$ with diffusion coefficient D and ∇^2 the Laplace operator accounts for diffusive spreading of the population due to underlying random motion of individuals. The second term $k(n\left(1 - \frac{n}{n_{sat}}\right))$ accounts for logistic growth, characterized by growth rate k and saturation density n_{sat}. Given appropriate initial conditions, this equation has traveling-wave solutions of the form $n(r,t) = n(r')$ where the spatial profile of the density $n(r')$ in a reference frame moving at constant speed c along the r-direction (such that $r' = r - ct$) becomes invariant in time, and the orientation r of that r-direction is determined by the initial conditions. Thus, the FK model explains traveling waves that arise when individuals of a growing population execute a random walk in space. In intuitive terms, the macroscopic density wave results from successive advances into virgin territory via random motion of individuals, followed by growth up to a density ceiling, typically due to resource limitation.

However, the canonical FK model cannot be applied directly to fungal networks because it fails to capture an essential feature of branched, filamentous growth. In fungi, the population of growing tips can be considered random walkers that explore space through apical growth and branching. These growing tips can interact not only with one another but also with the hyphal filaments they

lay down as they move. Inspired by related works on branching morphogenesis in fungal[18, 32] and other[33] networks as well as traveling-wave pattern formation[23], we propose a simple model that generalizes the FK framework to capture the traveling-wave dynamics we observe in mycorrhizal networks (Fig. 2.3).

As in the FK framework, we set up a continuum mean-field model that approximates the growth and movement of the underlying population of proliferating random walkers – here the growing tips – in terms of their spatial density, $n(r,t)$ (with units of number per d-dimensional volume, e.g., $[mm^{-d}]$). To represent the hyphal filaments laid down by growing tips, we introduce an additional variable $p(r,t)$ to represent their spatial density (with units of filament length per d-dimensional volume, e.g., $[\mu m/mm^d]$).

If individual hyphal tips grow at speed v, each tip deposits a cumulative hyphal length of $v\Delta t$ in its path over a time interval Δt. Now, in a region of size $(v\Delta t)^d$ with a growing tip density n, the number of tips will be $N = n \times (v\Delta t)^d$, and the hyphal density will increase by $\Delta p = Nv\Delta t/(v\Delta t)^d$. Dividing through by Δt and taking the limit $\Delta t \to 0$ gives a dynamical equation for the hyphal density within the continuum approximation:

$$\frac{\partial \rho}{\partial t} = vn \tag{2.7.2}$$

Note that the mean-field approximation applied here does not explicitly consider possible variation in growth speed across individual tips of the population, and hence if the growth-speed variance is non-zero (as is the case in our experimental data), v is taken to be the average speed of growing tips.

The calculation for growing tip density requires considerations of, along with the creation and annihilation of tips, the directional movement of tips into and out of every point in space. The latter is accounted for by their net spatial flux $\mathbf{J}(n)$ (a vector pointing in the direction of net movement, with units of number per time per area in d-dimensional space), and at every point in space, new tips are created due to branching at a rate $b(n,\rho)$ (tip creation events per unit time per unit volume), existing tips are annihilated due to anastomosis at a rate $a(n,\rho)$ (tip annihilation events per unit time per unit volume) and can increase or decrease depending on the divergence of the spatial flux $\mathbf{J}(n)$:

$$\frac{\partial n}{\partial t} = b(n,\rho) - a(n,\rho) - \nabla \cdot \mathbf{J}(n) \tag{2.7.3}$$

The joint system described by equations 2.7.2 andn 2.7.3 describes the coupled dynamics of growing tips and hyphal filaments), which are explained in the following section 2.7.2 these equations demonstrate traveling wave solutions in a similar manner to the original FK model (Eq. (2.7.1)), as we discuss in further detail in the section 2.7.2.

Expressions for $b(n,\rho)$ and $a(n,\rho)$

In our experiments on AM fungi, we found that new tips always emerge in the vicinity of another growing tip. This means the rate of branching events is not directly dependent on the hyphal filament density but rather on the tip density, i.e., $b(n,\rho) = b(n)$. Assuming the simplest case of linear dependence, we set $b(n) = \alpha n$, with α the branching rate per unit time.

For the anastomosis rate $a(n, \rho)$, it is natural to assume a dependence on both densities n and ρ because such fusion events must depend on the rate of collision between tips and hyphal filaments. For tips growing at speed v, assuming the orientation distribution of hyphae is uniform, the probability of colliding with an existing filament between t and $t + dt$ is $\rho v dt$. Assuming every time a tip meets an existing filament, it has a probability p_f of fusing to yield an anastomosis event, the probability for a tip to undergo anastomosis between t and $t + dt$ is $p_f \rho v dt$. Then in a region of tip density n the density of anastomosis events occurring between t and $t + dt$ can be written $a(n, \rho)dt = np_f \rho v dt$. Dividing through by dt and defining the rate parameter $\beta \equiv p_f v$, we obtain $a(n, \rho) = \beta n \rho$.

We note that this simple form for $a(n, \rho)$ proportional to both n and ρ is useful for gaining analytical insight (see 2.7.2, below) and for approximate agreement with experimental data (Fig. 2.3b), but its derivation above depends on the assumption of a uniform orientation distribution, which is not fully realistic. In particular, near the expanding front where hyphal densities are low, the relative angles between hyphae and growing tips are not fully randomized because the angular distribution of new branches is not uniform (Extended Data Fig. 2.20b) and most tips have undergone only one or two branching events from the radially expanding runner hyphae. Relaxing the assumption of uniform hyphal orientation in full generality would require a more detailed model that explicitly represents filament orientation as an additional dimension of the densities. For our purposes of understanding the observed traveling wave phenotypes, however, we show below that choosing a slightly modified form for $a(n, \rho)$ such as $a(n, \rho) = \beta n \rho^2$ (which phenomenologically accounts for the observation that orientations are not fully randomized in regions of low filament density ρ) can yield substantially improved agreement with data (see 2.7.3, below).

While the derivation of these terms is subject to assumptions, the section 0 details the evidence within our experimental data that support these specific choices for $a(n, \rho)$ and $b(n, \rho)$.

Traveling wave solutions of the model yield "pulled waves"

Traveling waves are defined by a density profile that is invariant in a moving coordinate. In our experiment, the density was computed along a radial coordinate r, so we seek solutions that give asymptotically time-invariant density profiles $n(r, t) = n(r')$ and $\rho(r, t) = \rho(r')$ in a transformed radial coordinate $r' = r - ct$ where c is the speed of the traveling wavefront. With this transformation, the dependence of n and ρ on time is removed, and Eqs. 2.7.2 and 2.7.3 become:

$$-c\frac{\partial \rho}{\partial r} = vn \tag{2.7.4}$$

$$-c\frac{\partial n}{\partial r} = b(n, \rho) - a(n, \rho) - \nabla \cdot J(n) \tag{2.7.5}$$

where we have renamed the transformed spatial coordinate back to r (i.e. $r' \to r$) for notational simplicity. Solutions of Eqs. (2.7.4) and (2.7.5) are thus traveling-wave solutions, and as with the FK model (Eq. (2.7.1)), the conditions for existence for such solutions are not very restrictive. In particular, as also noted above, traveling wave solutions can be found regardless of the specific choice for $J(n)$, from fully advective, or advective-diffusive, to fully diffusive with constant wave speed c and saturating hyphal filament density ρ_{sat} (see Extended Data Fig. 2.21 for example simulations demonstrating traveling waves for each of these three choices). Indeed, as long as certain conditions

are met for the branching and anastomosis terms and $b(n,\rho)$ and $a(n,\rho)$, the only requirement on $J(n)$ is that it is non-zero. Perhaps not surprisingly, however, the specifics of $J(n)$ do directly affect the wave speed c, a point we discuss in detail within section 2.7.3, below.

One of the simplest choices of $b(n,\rho)$ and $a(n,\rho)$ that can yield traveling wave solutions is the proportional forms $b(n,\rho) = b(n) = \alpha n$ and $a(n,\rho) = \beta n\rho$, respectively[23, 32, 33]. This choice effectively reduces the dynamics of tip birth and annihilation in Eqs. (2.7.5) and (2.7.4) to a form of coupled logistic growth,

$$b(n,\rho) - a(n,\rho) = \alpha n\left(1 - \frac{2\rho}{\rho_{sat}}\right), \tag{2.7.6}$$

where the negative feedback on growth comes not directly through n but rather through ρ, whose growth in turn is determined by n. Thus, the tip density n increases exponentially at the branching rate α when the local hyphal filament density is low ($\rho \ll \rho_{sat}/2$), but its value peaks at intermediate filament density (where $\rho = \rho_{sat}/2$), and finally decays again to zero as the filament density approaches its saturation value ($\rho \to \rho_{sat}$). The saturation towards ρ_{sat} is independent of the choice of flux term $J(n)$. The value of ρ_{sat} can be obtained by substituting the tip density in Eq. (2.7.4) by its expression stated in Eq. (2.7.5) and integrating, which yields $\rho_{sat} = \frac{2\alpha}{\beta}$.

A well-known property of the FK model (Eq. (2.7.1)) is that its traveling-wave solutions are examples of "pulled waves", meaning that the speed c of the advancing wavefront is determined solely by the local dynamics at the wave front, and not by processes behind the front. Mathematically, sufficient conditions for obtaining a pulled wavefront in FK-type models is that the terms accounting for growth and/or annihilation allow growth to proceed exponentially near zero density (mathematically speaking, corresponding to a linear instability) but eventually terminates at a finite saturation density.

The logistic growth expression in the FK model clearly satisfies this condition, as do the above choices for $b(n,\rho)$ and $a(n,\rho)$ in our model (Eqs. 2-3). Thus, traveling wave solutions for our model with the above choice for $b(n,\rho)$ and $a(n,\rho)$ also yield pulled-wave solutions.

The speed of a pulled wave is determined by dynamics at the front[23], which in turn requires some finite outward flux (i.e. $J(n) > 0$, where $J(n) = \mathbf{J}(n)\cdot\hat{\mathbf{r}}$ is the flux in the radial r-direction indicated by unit vector $\hat{\mathbf{r}}$) to continue to advance. Therefore, if the population of growing tips are heterogeneous with respect to their outward growth velocities, the model predicts that the subpopulation with the fastest outward (radial) velocity will dominate over others and determine the wave speed. Because of exponential growth, even if this subpopulation of fastest hyphae is small, their effects on densification are amplified exponentially through branching. In this way, therefore, they can pull the entire density wave even if the bulk of the tip population propagates slower. Variation in outward radiating speed can arise not only due to variation in the speed of growth (which is substantial, as seen in Fig. 2.3c), but also due to variation in the orientation of growth. Because the tip population effectively executes a random walk-through successive branching events, there is always a small subpopulation of tips growing in the radially outward direction of wave propagation. In general, the wave speed will be dictated by the speed of those leading "puller tips" lying at the growing front and with the fastest outward growth speeds.

In summary, our model (Eqs. 2-3) yields traveling wave solutions with pulled wavefronts. Whereas the saturation density is determined by the balance of branching and anastomosis terms $b(n,\rho)$ and $a(n,\rho)$, the wave speed is determined primarily by the flux term $J(n)$.

Evidence from experiments and parameter fitting

We tested these ideas with our microscopic tracking data. The tracking data allowed us to identify all branching and anastomosis events during network growth since the network grew on a plane. We estimated the average rates of change in their spatial density $b(n)$ and $a(n,\rho)$ at a given position as the wave passes by computing the temporal density profile of these events through the same spatial averaging and time translation scheme used to obtain the temporal profiles of n and ρ (see Fig. 2.2b, right). By overlaying the temporal profiles of $b(n)$ and $a(n,\rho)$ with those of n and $n\rho$ respectively, we found good agreement in their shape up to linear scaling factors $\alpha(=0.04h^{-1})$ and $\beta(=23\mu m/h)$ respectively (Fig. 2.3b).

Consistent with traveling-wave solutions of the model being "pulled waves" (see section 2.7.2, above), the observed wave speed ($c \approx 280\mu m/h$) closely matched that of the subpopulation of tips at the advancing front (Fig. 2.3c, cyan, $\langle v_p \rangle \approx 280\mu m/h$), which was in turn faster than the average speed of the remainder of the growing tip population (Fig. 2.3c, pink; $\langle v \rangle \approx 240\mu m/h$). Together with the proportionality between the branching and anastomosis event density profiles and of n and $n\rho$ respectively, noted above, these data provide support for our model with coupled logistic growth (specifically, the choice $b(n) = \alpha n$ and $a(n,\rho) = \beta n\rho$) as a basis for an AM fungal traveling wave.

Modeling P absorption

To model the absorption of phosphorous (P) by the traveling AM fungal wave, we need to consider both the absorptive flux of P through the hyphal membrane and diffusion of P through the medium. Following the methods developed in ref. [17], at any point in time and space, the amount of phosphorous (P) acquired by the colony is a function of the local P concentration and of the hyphal surface area. Approximating hyphal filaments as cylinders of radius r, when the local filament length density is ρ, the density of surface area density is $s = 2\pi r\rho$. The flux ϕ_P of P into the hyphae is assumed proportional to s but a saturating function of P-concentration (as in an enzymatic reaction), such that

$$\phi_P = \frac{sV_{\max}[P]}{[P] + K_m} \tag{2.7.7}$$

with K_m the Michaelis-Menten constant for absorption. The dynamics of P-concentration in the medium is then determined by the balance of this depleting flux $-\phi_P$, which depletes P from the medium, and the diffusive flux $D\nabla^2[P]$, yielding the following partial differential equation (PDE):

$$\frac{\partial[P]}{\partial t} = D_P\nabla^2[P] - \phi_P \tag{2.7.8}$$

where D_P is the diffusion coefficient of P in the medium.

Soil specific P dynamics P dynamics in agar differ from what can be observed in a real soil. P in soil is in most case reversely bound to soil particles and only a small fraction is in solution. The equilibrium between the liquid fraction concentration C_L and the solid fraction C_S concentration can be represented with the following relations $b_pC_L = C_S$ where $b_p \approx 200$ represents the phosphorous buffer power of the soil [17].

The above equations must therefore be adapted to account for that effect. First the P concentration experienced by transporters at the hyphal surface is C_L and equation. The expression for ϕ_P must therefore be adapted to be

$$\phi_P = \frac{sV_{\max}[P]/b_p}{[P]/b_p + K_m} \tag{2.7.9}$$

where $[P] = C_S$ represents the total P bound on soil particles. Then neglecting the diffusion of P on solid surfaces, one can rewrite

$$\frac{\partial[P]}{\partial t} = D_P\nabla^2([P]/b_p) - \phi_P \tag{2.7.10}$$

This means the diffusion is effectively slowed down by a factor $b_p = 200$ which corresponds to the general consensus for the movement of adsorbed species and specifically Phosphorous in soils [86, 87]

Model parameter for Fig. 2.3e and Ext. Data Fig. 2.11b,c For Fig. 2.3e and Ext. Data Fig. 2.11b,c, we numerically integrated the set of three PDEs comprising the traveling wave model Eqs. (2.7.2,2.7.3) together with the P absorption model Eq. (2.7.7) as explained in 2.7.4. We chose $J(n) = -nv_d\hat{\mathbf{r}} + D\nabla n$ and parameters $\alpha = 0.039$ h^{-1}, $\beta = 22\mu$m/h and $D = 0.0008$ mm^2/h so that $v_d \approx v_{\text{wave}}$ and we could more easily vary wave speed.

P absorption parameters were from refs. [17] for AM fungi: $r = 5\mu$m for the (average) hyphal radius, $V_{\max} = 2\times10^{-5}\mu\text{mol}\cdot\text{cm}^{-2}\cdot\text{s}^{-1}$ and $K_m = 3\times10^{-4}\mu$mol/cm^3 for P uptake, and $D_P = 10^{-5}$cm^2/s which is the diffusion coefficient of a small molecule in water. As initial conditions we used a uniform P-concentration $[P]_0 = 0.02\mu$g/mm^3, which corresponds to medium concentration of P in soils[88]. We also chose $b_p = 239$ as proposed in [17]. For the spatial flux term in Eq. (2.7.3), we chose other equation parameters such that $v_{\text{wave}} = 250\mu$m/h.

Initial condition were $\rho(r,0) = 0$, $n(r,0) = n_{max}e^{-\lambda(r-r_0)^2}$ where $n_{max} = 0.3mm^{-3}$, $\lambda = 0.2mm^{-2}$ and $r_0 = 7mm$ and $[P](r,0) = [P]_0(1 - e^{-\lambda_2(r-r_0^{(P)})})$ where $\lambda_2 = 0.1mm^{-1}$ and $r_0^{(P)} = 1mm$. The later profile for P concentration was chosen to reflect the existence of a P depletion zone around the plant root.

2d and 3d embedding

In the case of modelling of P absorption as shown in Fig. 2.3e and Ext. Data Fig. 2.11b,c, our goal was to represent the consequences in real soil of the observed colony propagation dynamics. We therefore we used 3d concentration of P and 3d embedding corresponding to cylindrical coordinates with cylindrical translational symmetry for the tip and hyphal density. This had the only consequence of changing the final units in which those were expressed which allowed to connect them to P absorption. This choice however didn't change the overall dynamic. For those figures we therefore used a buffer parameter $b_p = 239$ as explained in 2.7.2. For all other figures (Ext. Data Fig. 2.21,2.22), we wanted to represent the dynamics in our system with agar and therefore used a 2d embedding.

Total mass of P absorbed m_P as shown in Ext. Data Fig. 2.11b was calculated using the integral over space and time of ϕ.

Conclusion

In summary, our analysis combining both microscopic and macroscopic observables provided agreement that AM fungal traveling waves are generated by an underlying branching random walk, in which coupled logistic growth due to branching and anastomosis is pulled by tips of runner hyphae that radiate outwards at a speed v_p greater than the rest of the tip population, leaving in their wake a hyphal network of constant, saturating density ρ_{sat}.

Notably, saturation density ρ_{sat} in our model is determined by the rate parameters α and β for branching and anastomosis, respectively. Therefore, in contrast to typical population waves, such as those of bacterial colonies modeled by the FK model, our model suggests the constant density level behind the traveling wavefront of AM fungi is set not by the carrying capacity of the environment, but rather a morphogenetic program of the fungal network itself. In this sense, the AMF traveling wave is *self-regulating*[89].

It is also worth noting that only a small subpopulation of fast-growing tips is sufficient to "pull" the wave of mycelial network expansion at their growth speed. Because of this, somewhat counter-intuitively, the speed c of traveling-wave range expansion can be substantially greater than that of the typical growing tip $\langle v \rangle$, as we discuss in more detail below in section 2.7.3. Expanding the model to account for soil 3d environment and phsphorous absorption dynamics yields interesting insights into the functionality of AMF colony propagation. Finally, we note that while the aim of the simple model described here (Eqs. 2-3) and in the Main Text (Eqs. 1-2) is to provide conceptual and analytical insight, it is also interesting to ask whether further refinements of the model can yield deeper mechanistic insights. To that end, we present below in section 2.7.3, more detailed discussions of quantitative and mechanistic considerations, as well as suggested directions for future modeling efforts.

2.7.3 Further discussion of the model, its refinement, and alternative models

Choice of $\mathbf{J}(n)$

One possible choice for $\mathbf{J}(n)$ is to consider that growing tips move in a purely persistent manner: $\mathbf{J}(n) = nv$, where $v(\mathbf{r}, t)$ is the local tip growth velocity (a vector field over the spatial coordinate $\mathbf{r}$). This form has been proposed in previous studies of fungal colonies[18, 32]. Here, v is essentially a uniform outward-oriented velocity field, $\mathbf{v} = v\hat{\mathbf{r}}$, where v is the speed and $\hat{\mathbf{r}}$ is the unit vector in the outward radial direction[32]. This choice appears at first sight quite appropriate for modeling AM fungal growth where the movement of individual growing tips is directionally highly persistent with little or no decorrelation of orientation. However, this uniform-velocity approximation for $\mathbf{J}(n)$ leads to somewhat unphysical predictions. Although mathematically, the resulting system of Eqs 2-3 can yield traveling wave solutions, the existence conditions for those solutions require $c > v$, meaning the wave speed must exceed the speed of growing [32], which is physically implausible. Furthermore, the wave speed is dependent on initial conditions, and obtaining a traveling wave solution requires in addition that the shape of the initial density profile is an exponential distribution, the spatial decay length of which affects the wave speed over an indefinite distance, which is again unphysical. A purely advective $\mathbf{J}(n)$ is therefore an unsuitable choice for describing our experimental observations.

Another possible choice for $\mathbf{J}(n)$ is as a purely diffusive flux: $\mathbf{J}(n) = -D\nabla n$ where D is a diffusion

coefficient. For a hyphal network, the microscopic parameters that determine D are those of the temporal autocorrelation functions of growth speed and orientation, as well as the branching angle distribution of hyphal tips. This choice of $\mathbf{J}(n)$ leads to the same spatial flux term as in the classical FK model (Eq. (2.7.1)). Moreover, a recent study of branching morphogenesis in mammalian mammary glands[33] also used this as the spatial flux term in a model very similar to Eqs. 2-3. Such a choice is partially justified in our system as evidenced by the fact that the direction chosen at birth of a new hypha subtends a randomly distributed angle with average $\langle\theta\rangle \approx 70^\circ$ relative to the growth direction of the parent hypha. Traveling-wave solutions with this choice for $\mathbf{J}(n)$ yields a wave speed given by $c = 2\sqrt{D\alpha}$ for the coupled system of Eqs. 2-3, equivalent to that for the well-known FK model solution[22–24]. However, to match the wave speed of our system, one must select a value for the parameter D, which, when combined with other parameters directly measured in our system, predicts a width for the peak of growing tip density (27mm at half height) that is well beyond what is observed in our system (6mm at half height). We therefore conclude that a purely diffusive $\mathbf{J}(n)$ also fails to sufficiently describe traveling waves of AM fungi.

Finally, one can further generalize $\mathbf{J}(n)$ to combine both advective and diffusive components: $\mathbf{J}(n) = nv_d\hat{\mathbf{r}} - D\nabla n$. This choice means that there exists a moving reference frame traveling along $\hat{\mathbf{r}}$ at a "drift speed" v_d, within which the movement of tips is correctly described as purely diffusive. Velocity differences across the growing tip population can emerge not only from growth speed variations/fluctuations but also from orientation randomization due to branching. Indeed, an individual tip's velocity can be positive or negative within this moving reference frame, depending on whether its velocity vector $\mathbf{v}$ projected along the outward radial direction $\mathbf{v}\cdot\hat{\mathbf{r}}$ is greater or less than v_d.

The wave speed c for the traveling-wave solution for Eqs. 2-3 with this advective-diffusive flux for $\mathbf{J}(n)$ can be solved for analytically[33]. Given that the speeds of pulled waves are determined only by dynamics of the linear instability at the front[23], we introduce an ansatz $n(r) = Ke^{\lambda r}$ describing the leading profile of the growing tip wavefront along the coordinate r along the propagation direction ($r \equiv \mathbf{r}\cdot\hat{\mathbf{r}}$). Inserting this ansatz for $n(r)$ and $\mathbf{J}(n) = nv_d\hat{\mathbf{r}} - D\nabla n$ into Eq. 5 and linearizing, one obtains the following eigenvalue equation,

$$D\lambda^2 + (c - v_d)\lambda + \alpha = 0$$

which yields the solution,

$$\lambda = \frac{-(c - v_d) \pm \sqrt{(c - v_d)^2 - 4D\alpha}}{2D}$$

A necessary condition for a stable wavefront is that λ is real and negative. This leads to the conclusion that c must satisfy $c \geq v_d + 2\sqrt{D\alpha}$. Numerical simulations show that the wave speed selected is precisely the minimum: $v_d + 2\sqrt{D\alpha}$. This means that given a fixed α, different combinations of v_d and D can yield the same wave speed. These parameters can then be adjusted to match the observed width of the tip density peak. Within this framework, the value of v_d can be interpreted to reflect an average velocity of propagation of tips projected onto the wave propagation direction, and hence there is nothing unphysical about a wave speed greater than v_d. In simulations we find adjusting D to match the experimentally observed wave speed while constraining v_d and α to experimentally determined values yields a peak width for the n density (6mm at half height) close to that of experiments. This agreement provides confidence in the advective-diffusive $\mathbf{J}(n)$ providing a reasonable approximation for tip spatial flux in AM fungal traveling waves.

In addition to yielding good agreement with the macroscopic density dynamics of AM fungal growth, the choice of an advective-diffusive approximation for $\mathbf{J}(n)$ can be further motivated by features of the observed microscopic parameters. First, we found that the growth of individual hyphae after birth is highly directionally persistent (leading to an approximate lower bound for the persistence length $\ell_p \gtrsim 10$ cm), thus motivating an advective component to the flux. Second, the orientation changes upon the birth of a new hypha were randomly distributed, with an average angle $\langle\theta\rangle \approx 70°$ relative to the orientation of the parent hypha, motivating the diffusive term. Third, we also noted the broad distribution of growth speeds that hyphae can adopt, which can contribute further to the diffusive term. However, we emphasize that the advective-diffusive flux $\mathbf{J}(n)$ also remains an imperfect approximation. In particular, for the diffusion approximation to hold accurately, one requires a separation of scales between the diffusive dynamics approximated by the flux term $-D\nabla n$ and the underlying random walk. Yet given the extremely long persistence length of individual hyphae ($\ell_p \gtrsim 10$ cm), the effective persistence length of the tip population's branching random walk L_p will be dominated by orientation randomizations upon branching and will be of the order of the inter-branch interval, i.e. $L_p \sim v/\alpha$, which (given our measured values for v and α) is of order ~ 6 mm, comparable to the width of the growing tip pulses. Thus, there is no clear separation of scales, and hence any interpretation of fitted parameters D and v_d in terms of microscopic parameters such as the tip growth speeds and branching statistics will require adequate care. Because of these limitations, we discuss in the following section one additional alternative formulation of a mean-field model that does allow an explicit representation of the important microscopic parameter v_p, which we found (see above, and Figs. 2-3) to be the determinant of the propagation speed c of AM fungal waves.

Other models

An alternative formulation to describe explicitly puller and average hyphae consists in adding a third term to the system of equations explicitly describing a puller population of density n_p. This population moves with a purely advective flux $\mathbf{J}(n_p) = n_p v_p \hat{\mathbf{r}}$ at a higher speed than the rest of the "normal" population that has density n. A tip from the "normal" population can become puller with a rate K_1 and puller can transition to a "normal" state with a rate K_2 and moves via an advective-diffusive flux $\mathbf{J}(n) = n v_d \hat{\mathbf{r}} - D\nabla n$. These rates can be interpreted to represent multiple underlying phenomena. Firstly, a change of orientation through branching or limited directional persistence of growth that can direct hyphae towards or away from the direction of propagation of the wave. Secondly, the broadly variable speeds observed across individual tips within the population of hyphae. This leads to a system of three equations:

$$\begin{cases} \frac{\partial n}{\partial t} = \alpha n - K_1 n + K_2 n_p - \beta n \rho - \nabla \cdot (n v_d \hat{\mathbf{r}}) + D\nabla^2 n \\ \frac{\partial \rho}{\partial t} = n s + n_p v_p \\ \frac{\partial n_p}{\partial t} = \alpha n_p + K_1 n - K_2 n_p - \nabla \cdot (n_p v_p \hat{\mathbf{r}}) \end{cases}$$

Numerical simulations confirm that this model gives rise to a traveling wave with a wave speed very close to (albeit slightly below) that of growth speed v_p of puller tips. Interestingly, the difference between the speed of the wave and the one of puller hyphae is dependent on the values of α, K_1, and K_2. While this formulation still includes a term that depends on the diffusion approximation, it does allow for an explicit representation of the puller hyphae population and their growth speed v_p, which our analysis (see above) and experimental data (Figs. 2.2,2.3) revealed to be the key microscopic parameter determining the AM fungal wave speed.

As an extension to this approach, one could relax the assumption of two discrete populations and explicitly model the underlying space of possible speeds and orientations as additional dimensions to the continuous space in which population densities are defined, such that the density then becomes an explicit function of its orientation ϕ and its speed v, i.e. $n = n(\mathbf{r}, \phi, v, t)$. Within this higher-dimensional space, branching formulated as jump Markov processes between orientation and speed states[89] could circumvent the diffusion approximation and may be a promising direction for future modeling endeavors.

These two formulations have some degree of equivalence with the advection-diffusion formulation discussed above but they allow to explicitly describe the puller hyphae population which facilitates the interpretation of the terms opening the possibility of observing them microscopically.

Refinement of morphogenetic model to match the observed saturation density

The saturation value for the filament density ρ_{sat} predicted by our model $\left(\frac{2\alpha}{\beta} = 3.5 \text{ mm}^{-1}\right)$, is of the same order of magnitude as that observed in our experiments (≈ 1 mm^{-1} for runner hyphae only; see Fig. 2.2b,c) and yet the exact values are unmatched by a few-fold. Although the aim of the simple model presented in the main text is to provide conceptual and analytical insight, it is interesting to ask what mechanistic factors might account for this quantitative discrepancy. In this section, we present an analysis of multiple factors that could contribute to this discrepancy, to iteratively refine both the model itself and the data analysis for calibrating model parameters.

Firstly, our extraction of the density-dependent rate coefficient for anastomosis β from tracking data (Fig. 2.3b, lower) could be too simplistic. That analysis detected anastomoses by looking for events in which the collision of a growing tip, a degree 1 node of the network, with a hyphal filament, an edge of the network, produces a new degree 3 node. However, we did also observe numerous examples of anastomoses that form through a more complex series of events that could have been missed by this analysis. Specifically, we found that even when growing tips did not immediately produce anastomosis upon collision and continued growth after crossing with the hypha with which they collide, hence producing a degree 4 node, they would stop growth after a few hundred micrometers beyond the point of crossing. Follow-up observations at higher magnification revealed that hyphal fusion can occur at those crossing points. While such "overshoot anastomosis" events were not detected by our tracking analysis (Fig. 2.3b, lower), it is possible to account for them by adding an additional parameter – a density dependent "stopping" rate coefficient β_s – which we can estimate from experimental data through the same linear scaling analysis of density profiles in the reference frame of the wave that we used to extract α and β (see above, and also section 2.7.5 below). This analysis resulted in the value $\beta_s = 9\mu$m/h.

Secondly, one can observe that the density-profile matching between $b(n)$ and αn as they are observed in experiments (Fig. 2.3b, upper) is slightly imperfect with branching decaying faster than tip density. This suggests that the branching rate could also have a weak (and negative) density dependence, contributing to another modulation of β. By matching the residuals $\alpha n - b(n) = \beta_b n \rho$ we get $\beta_b = 7\mu$m/h. Modifying $b(n)$ and $a(n)$ with these two additional density-dependent parameters leads to a total density-dependent feedback parameter $\beta_{\text{tot}} = \beta + \beta_s + \beta_b$, which results in a prediction $\rho_{sat} = \frac{2\alpha}{\beta_{\text{tot}}} = 2$ mm^{-1}, which is closer to the experimentally observed value but still off by $\sim$ 2-fold.

Thirdly, it is also noticeable from Fig. 2.3b (lower) that the front of the density product $n\rho$ arrives

slightly ahead of that of anastomosis-event density. This discrepancy could arise, for example, from geometric effects in 2-D, because the new tips generated just behind puller tips at the growing front will tend to be oriented outward into virgin territory (because the average branching angle is < 90 degrees), and hence have no chance of colliding with any existing hyphae to produce anastomoses. Such effects can be modeled phenomenologically by generalizing the coefficient β to allow it to depend explicitly on the filament density ρ, i.e. $\beta = \beta(\rho)$. Given that filament density ρ is always lowest at those front regions where we observe a relative paucity of anastomosis events, $\beta(\rho)$ should be an increasing function of ρ. Taking the simplest possible linear form $\beta(\rho) = \beta'\rho$, where β' is a positive constant (with units of length squared per unit time, e.g. [mm^2/h]), we obtain an expression for the anastomosis rate that depends quadratically, rather than linearly on ρ, as $a(n, \rho) = \beta(\rho)n\rho = \beta' n\rho^2$. This modification does not qualitatively alter the traveling wave behavior – the resulting equations still satisfy the conditions of a pulled wave – but does lead to a different expression for the saturation density on the branching and tip annihilation rates, $\rho_{sat} = \sqrt{\frac{3\alpha}{\beta'}}$.

Combining all of the above, we considered the possibility that the density-dependent stopping and branching coefficients discussed above can similarly depend on ρ, i.e. $\beta_s = \beta_s(\rho) = \beta'_s\rho$ and $\beta'_b = \beta_b(\rho) = \beta'_b\rho$, respectively. Then, all three of these density-dependent contributions (anastomosis, stopping, and branching attenuation) became proportional to $n\rho^2$ instead of $n\rho$, so that the combined branching and annihilation terms could be written $b(n) - a(n, \rho) = \alpha n - \beta'_{\text{tot}} n\rho^2$, with $\beta'_{\text{tot}} = \beta' + \beta'_s + \beta'_b$. We found that experimental data for the anastomosis rate, stopping rate, and branching attenuation were very well matched by proportional fits to $n\rho^2$, with the constants of proportionality yielding estimates for β', β'_s, and β'_b, respectively. Using the sum of these parameters as β'_{tot} yields for the saturating density model solution $\rho_{sat} = \sqrt{\frac{3\alpha}{\beta'_{\text{tot}}}} = 1.3$ mm^{-1}, which is in very close agreement with the measured value (≈ 1 mm^{-1}). We also note that this modified model with $n\rho^2$-dependence robustly yields traveling wave solutions with almost the same wave speed c as that of the same model with $n\rho$-dependence.

In summary, we have demonstrated how the simple model of AM fungi traveling waves presented in the Main Text can be iteratively refined to achieve better quantitative agreement with the observed data. Although full quantitative explanation of the data would likely require a more detailed model that explicitly accounts for the variability in microscopic variables such as hyphal orientations and growth speeds, we have shown that many of the quantitative observables within the experimental data can be captured by slightly generalizing the simplest mean-field model of Eqs. 2-3. Overall, we found better agreement with experimental data (with the same number of parameters), when the density-dependent rates of anastomosis, stopping (a proxy for overshoot anastomosis), and branching attenuation were all assumed proportional to $n\rho^2$, rather than $n\rho$. It is interesting to ask what mechanism might account for this quadratic dependence on the hyphal filament density ρ. As noted above, for the anastomosis rate (and by extension the related rate of stopping), the correlation between density and the degree of angular randomization must be a contributing factor. However, for the attenuation of the branching rate, it is not obvious how the growth orientation could play a significant role. It would seem more likely that the effective dependence of the branching propensity depends on some sensing of the local hyphal density, perhaps through some chemical cue that is either secreted or depleted by hyphal filaments. Exploring these possibilities through further experimental and modeling efforts would be a promising line of future inquiries.

2.7.4 Numerical simulations of traveling-wave models

The system of partial differential equations (PDEs) for each model described in Supplementary Text were numerically integrated using the Python dolfinx package based on the FEniCS project's computational framework[90] to translate the PDE model into efficient finite element C++ and Python code. A polar coordinate system was used to express explicitly the gradient and Laplacian operators. In that coordinate system and with the expressions $b(n,\rho) = b(n) = \alpha n$, $a(n,\rho) = \beta n\rho$ and $J(n) = nv_d\hat{v} - D\nabla n$, equation (2) and (3) become:

$$\frac{\partial \rho}{\partial t} = vn \tag{2.7.11}$$

$$\frac{\partial n}{\partial t} = \alpha n - \beta n\rho - \frac{1}{r}\frac{\partial}{\partial r}(rnv_d) + D\frac{1}{r}\frac{\partial}{\partial r}\left(r\frac{\partial n}{\partial r}\right) \tag{2.7.12}$$

Time was discretized using a first order upwind scheme to avoid instabilities due to the advection term. The equations were reformulated in their weak form with Dirichlet boundary conditions by multiplying (7) and (8) by two test functions and integrating second-order derivative by parts. Space was divided in a mesh of 200 cells and time was divided in 900 elements.

We set initial conditions for the tip density to be a Gaussian whose height and width was manually adapted to accelerate the convergence towards the travelling wave solution. In the case of a purely advective flux, we used exponentially decaying initial conditions as described in the caption of Extended Data Fig. 2.21. The solve function of the dolfinx package was used to integrate the equations between each timestep. Notebooks to reproduce these numerical simulations can be found on the dedicated repository at https://github.com/Cocopyth/model_integration.

2.7.5 Linking modelling and experimental parameters

Parameter extraction from curve proportionality

The parameters in the continuous model represented proportionality factors between various quantities, such as n, ρn, the anastomosis rate, and the branching rate, among others. To obtain accurate estimates of these factors, we computed the average of the temporal dynamics associated with these quantities in the reference frame of successive rings (as shown in Fig. 2.3b, right).

We then extracted fit these average time series within a window width 40 h, centred at the point of their common peak (0h for ρn, anastomosis rate, and all quantities shown in Extended Data Fig. 2.22a-c). This windowing was necessary to avoid the near-zero values of these time series, where noise would otherwise become dominant to corrupt estimates of extracted proportionality factors. We then obtained the proportionality factor by minimizing the mean square fitting error within this window by linear regression.

Stopping rate

To extract stopping rate as shown in Extended Data Fig. 2.22c we first detected stopping events in our tracking analysis, where they were defined as the subset of all events at which a tracked node's gets closer than $70\mu m$ from its final position but stays of degree 1. We recorded for each

stopping event its position in space, defined as its final position, and its time, defined as the last timestep where it was further away than $70\mu m$ from its final position. The stopping rate (in units mm^-2hr^-1) within a given ring at time t was computed by dividing the number of stopping events occurring within that ring over a time interval $[t, t + \Delta t]$ by the area of that ring and also by Δt, the time interval between two successive frames.

Total hyphal density

In the versions of the model presented in Extended Data Fig. 2.21a,b,c and Extended Data Fig. 2.22d, the modelling assumptions do not represent branched absorbing structures (BAS) that have different dynamics of growth and branching from those of runner hyphae (RH). Parameter extraction must therefore be done considering only tips and hyphal filaments that belong to runner hyphae for parameters to accurately represent the growth dynamics of this subpopulation. This is why in order to extract parameters from Fig3.b and Extended Data Fig. 2.22a/b/c, we used RH density for the quantity ρ and RH tip density is used for the quantity n.

The total hyphal density as shown in Fig. 2.2 can then be extrapolated using the constant density of BAS shown in Fig. 2.4b. Specifically, since BAS represent 30-40% of the total hyphal length, we can multiply the runner hypha density by a factor of 1.4-1.6 to obtain the total hyphal density.

2.7.6 Bootstrap resampling uncertainties

Fig. 2.2b

We obtained uncertainty estimates for hyphal and growing tip density by splitting each ring in which densities were computed into a set of 10,000 rectangles of equal area, computing the densities in each of the rectangular area separately, and estimating the standard deviation of the mean density by bootstrap resampling (sampling with replacement) 100 times over the set of rectangular area densities. The shade shown corresponds to two times the standard deviation of the bootstrap resampling.

Fig. 2.2d,e

Shaded region is confidence interval obtained by bootstrap resampling 1000 the sigmoid fit of each density profile in each ring referential. A function $\rho(t) = K_1 \frac{1}{1+e^{\lambda(t_n - t)}}$ was fitted to the resampled hyphal density timeseries in the n-th ring, with K_1, λ, and t_n as free parameters. The grey region in c,d shows an interval around the mean value of K_1, $t_n \pm 2$ times the standard error of the bootstrap estimates of these parameters.

2.7.7 Ring dynamics average

Fig. 2.3b, extended data Fig. 2.22a,b,c

Shades correspond to 2 times the standard error of the dynamics in all rings ($n_{\text{ring}} = 15$).

2.7.8 Histograms

Fig. 2.3c

Number of speeds recorded for the pink and cyan histograms are $n_{\text{pink}} = 1645$ and $n_{\text{cyan}} = 103$.

2.7.9 Violin plots

Fig. 2.5b,c,e,f

All violin plots have been plotted using the violinplot of the matplotlib library of Python with the parameter show_extrema set to false.

Fig. 2.5b,c

In total $\sim 75,000$ trajectories from $\sim 1,200$ videos were used.

Fig. 2.5b

Number of trajectories and videos used for each violin are shown in the table below.

Days	Counts trajectories tip	Counts trajectories root	Counts Videos
0.4	464	494	12
0.6	989	387	29
1.4	527	516	13
1.5	306	555	7
2.3	774	941	22
2.4	686	1092	19
3.3	402	872	23
3.3	969	1160	24
3.4	1678	1060	54
3.4	1553	2332	50
4.4	592	1084	24
4.4	673	865	18
4.6	1475	1842	52
8.4	4959	4594	158
10.6	677	614	22
12.4	1817	1823	22
13.3	825	1546	20
14.4	517	1365	13
15.3	1223	1284	22
16.4	1034	987	26
17.5	2468	1373	53
20.4	2689	2342	73
21.4	9595	8414	284

For each video, we computed an average positive and negative speeds. The lower panel error bars show two times the standard deviation of the ratios of average positive and negative speeds for all videos divided by the square root of the video count.

Fig. 2.5c

Number of trajectories and videos used for each violin are shown in the table below.

Spores	Counts trajectories tip	Counts trajectories root	Counts Videos
0	96	96	96
0	57	57	57
0	133	133	132
0	24	24	24
15	58	58	58
38	32	32	32
39	22	22	21
60	55	55	55
67	32	32	31
72	54	54	54
73	177	177	177
84	27	27	27
249	333	333	332
380	81	80	81
857	59	59	59

Fig. 2.5e,f

In total 824 trajectories from 24 videos were used. Number of trajectories used for each violin are shown in the table below. Each violin corresponds to one video.

BC	Counts trajectories tip	Counts trajectories root	Counts video
0.0110	1	0	1
0.0110	3	2	1
0.0586	1	0	1
0.0726	1	0	1
0.0736	2	1	1
0.0819	4	116	4
0.0851	68	70	2
0.1753	0	4	1
0.2076	122	100	4
0.2082	5	10	1
0.2463	106	260	4
0.3719	78	114	4
0.4163	180	128	4
0.4251	2	79	1
0.4668	138	206	4
0.5049	100	170	4
0.5805	70	150	4
0.5992	12	136	4

dtip	Counts trajectories tip	Counts trajectories root	Counts video
0.0	3	2	1
1.0	1	0	1
1.7	1	0	1
2.3	2	1	1
2.8	1	0	1
3.8	4	116	4
6.3	122	100	4
6.9	68	70	2
7.9	0	4	1
8.6	5	10	1
9.2	106	260	4
12.0	78	114	4
12.7	138	206	4
14.6	70	150	4
14.9	12	136	4
17.2	180	128	4
17.9	100	170	4
20.5	2	79	1

2.7.10 Linear fits

All linear fits shown in Fig. 2.5 were shown using the regplot function of the seaborn package[91]. It computes the regression line and shows a 95% confidence interval as a shaded area around this regression line.

2.7.11 Immotile Fraction in flow-speed analysis

For the flow-speed analyses on myristate plates, (Extended Data Fig. 2.18), we excluded immotile objects, which we defined as trajectories demonstrating displacements indistinguishable from diffusion. We excluded extracted speed below a threshold of $0.8\mu m\, s^{-1}$ corresponding to the average speed of a one pixel wide (r=35nm) particle diffusing for $\Delta t = 20s$ (video length) in water ($D = \frac{k_b T}{6\pi\eta r}, v = \sqrt{\frac{D}{\Delta t}}$). This leads to excluding about 50% of the speeds in the case of myristate indicating that flows were less active in that case.

[35]

2.8 External Data Figures

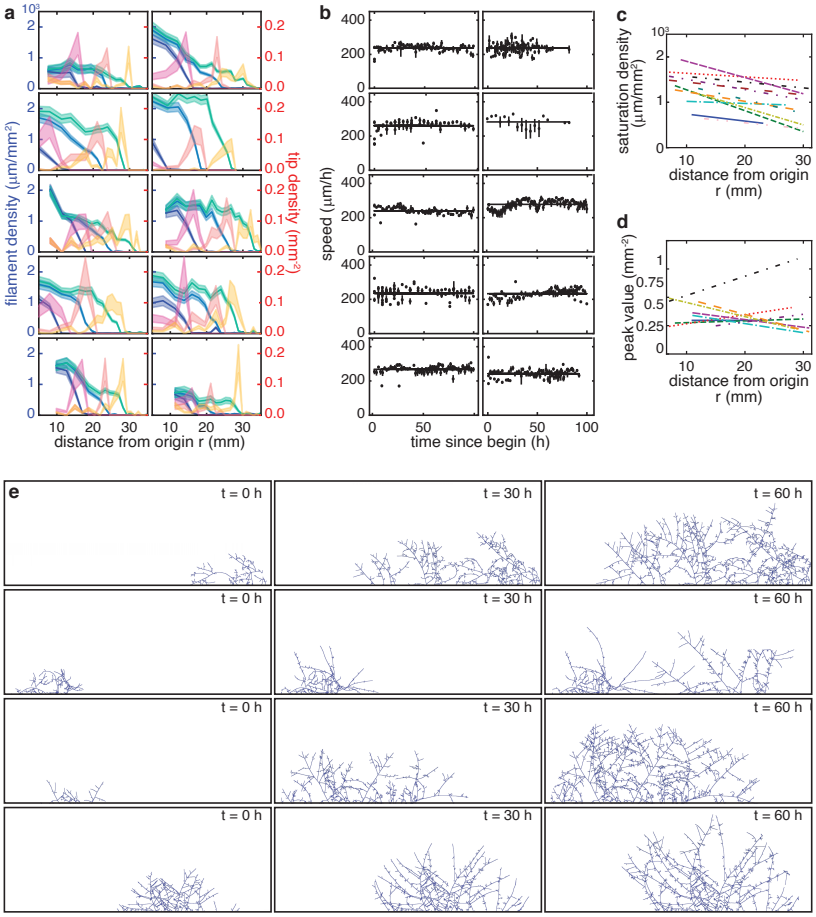

Figure 2.6: **Replicates of *R. irregularis* A5 plates show consistent traveling wave pattern.** **(a)** Spatial distribution of filament density (blue) and tip (red) density over three consecutive days (color gradient, with dark colors going to lighter from day one to three). Shaded region corresponds to uncertainty in density estimates computed by extrapolating the ones obtained for the plate in the main text. Profile shown at regular intervals separated by 30 hours, while distance from origin is computed under the assumption of half circular colonisation of the plate. **(b)** Speed of growing tips at the front over time. Black points are the average hyphal growth speed at the front of the colony at each timestep. Error bars represent 95% C.I. Black line is the average of black points. **(c)** Saturation density as a function of ring radius. Each line corresponds to the linear fit across saturation value obtained by fitting a sigmoid to density curves for each replicate. **(d)** Growing tip density peak value as a function of ring radius. Each line corresponds to the linear fit across peak values obtained by fitting the derivative of a sigmoid to growing tip density curves for each replicate. **(e)** Additional examples of extracted networks. Each row represents different timepoints of the same replicate. Scale bar is 1 mm.

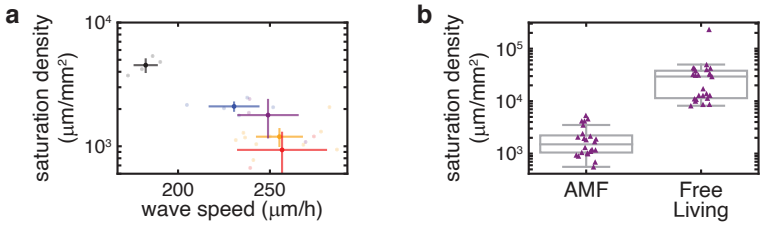

Figure 2.7: **Saturation density varies across AM fungal genotypes but is invariably lower than that of free living fungi (a)** AM fungal networks demonstrate a speed-density trade off, with saturation density and wave speed depending on fungal strain. On the same host root genotype, different fungal strains grow differently, with some strains growing sparse but fast networks, while others grow slower, denser networks. Scatter plot of saturation density and wave speed for all replicates. Data shown for *R. irregularis* A5, grown under control conditions (blue) or with root grown under double the amount of carbon in root compartment (purple), *R. irregularis* C2 grown under control conditions (orange) or with root grown under double the amount of carbon in root compartment (red), *R. aggregatum* (black). **(b)** Saturation density (μm^2) of AM fungi is substantially lower than free living fungi. Saturation density of AM fungi (n=23) vs saturation density in data from non-chord-forming, free-living fungi as reported in Aguilar-Trigueros et al.[35] (n=25). The box represents the interquartile range (IQR), with the central line indicating the median. The whiskers extend from the box to the minimum and maximum values within 1.5 times the IQR.

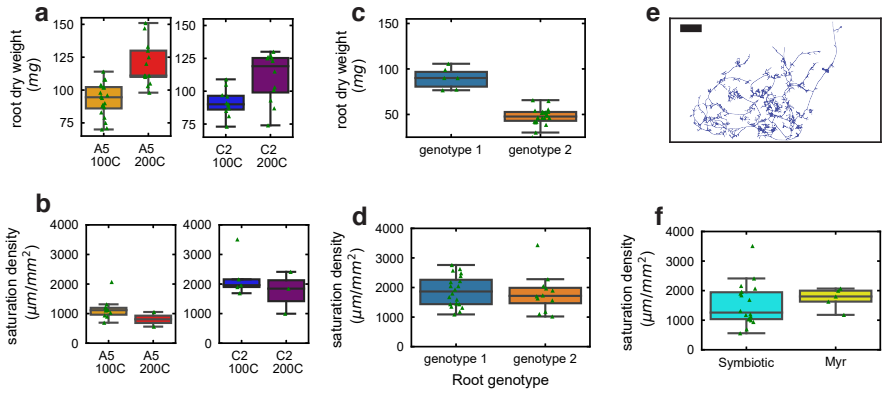

Figure 2.8: **AM fungi consistently regulate network structure despite changes in carbon supply, root genotype, or even absence of a host root with carbon supplied as myristate.** **(a)** Comparison of root dry weight under control conditions (**100C**) and when carbon concentration for root compartment is doubled (**200C**) in replicates grown on root genotype 1 together with *R. irregularis* A5 (left) and *R. irregularis* C2 (right). **(b)** No difference in saturating hyphal density of *R. irregularis* A5 (left) and *R. irregularis* C2 (right) under control conditions (**100C**) and when carbon concentration for root compartment are doubled (**200C**). **(c)** Carrot root genotype 1 (blue box) and genotype 2 (orange box) differ in root dry weight after 45 days of growth (**d**) Despite being grown on different root genotypes, *R. irregularis* C2 networks reached the same saturating hyphal density. **(e)** Network image of *R. irregularis* C2 grown in myristate in the absence of a host root after ∼14 days of growth. Scale bar: 1mm. **(f)** *R. irregularis* C2 networks reached similar hyphal density after ∼14 days of growth, regardless of whether they are grown with or without a host root when supplied with myristate (**myr**). Saturating hyphal density of AM fungi (n=23) vs hyphal density of AM fungi grown in a myristate medium (n=5). In all figures, triangles correspond to individual replicates.

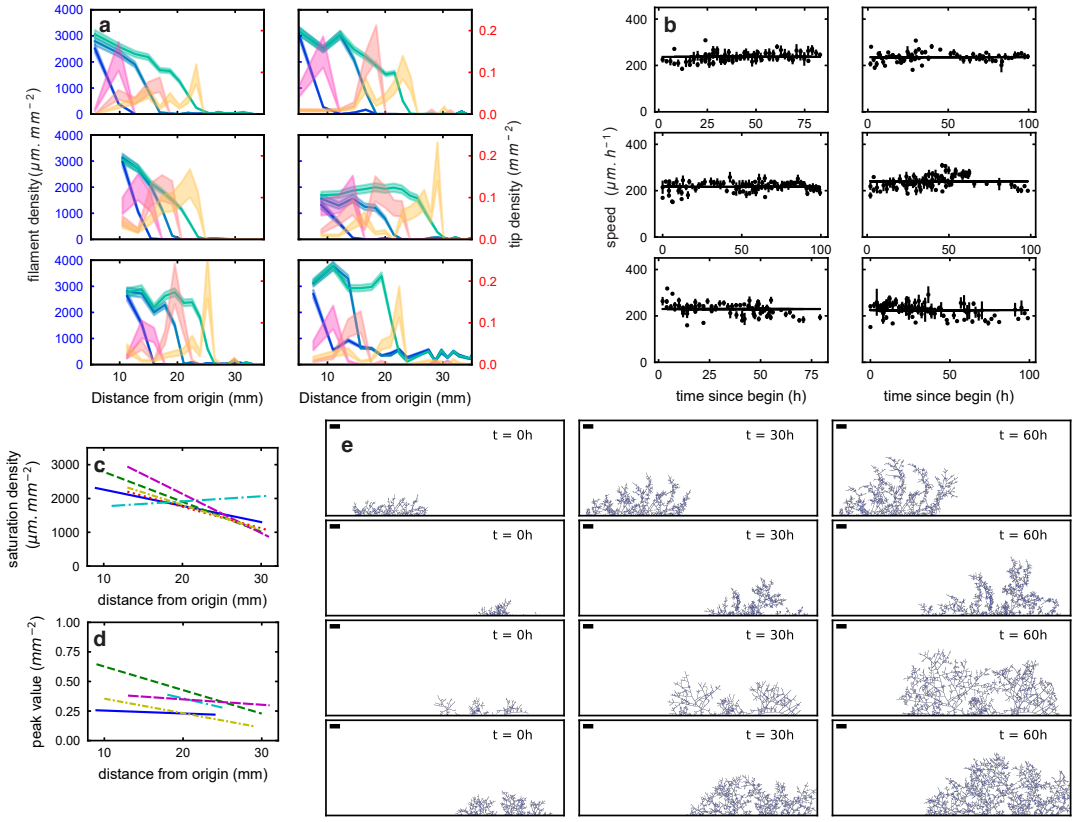

Figure 2.9: **Replicates of *R. irregularis* C2 plates show consistent traveling wave pattern.** **(a)** Spatial distribution of filament density (blue) and tip (red) density over three consecutive days (color gradient, with dark colors going to lighter from day one to three). Shaded region corresponds to uncertainty in density estimates computed by extrapolating the ones obtained for the plate in the main text. Profile shown at regular intervals separated by 30 hours, while distance from origin is computed under the assumption of half circular colonisation of the plate. **(b)** Speed of growing tips at the front over time. Black points are the average hyphal growth speed at the front of the colony at each timestep. Error bars represent 95% C.I. Black line is the average of black points. **(c)** Saturation density as a function of ring radius. Each line corresponds to the linear fit across saturation value obtained by fitting a sigmoid to density curves for each replicate. **(d)** Growing tip density peak value as a function of ring radius. Each line corresponds to the linear fit across peak values obtained by fitting the derivative of a sigmoid to growing tip density curves for each replicate. **(e)** Additional examples of extracted networks. Each row represents different timepoints of the same replicate. Scale bar is 1mm.

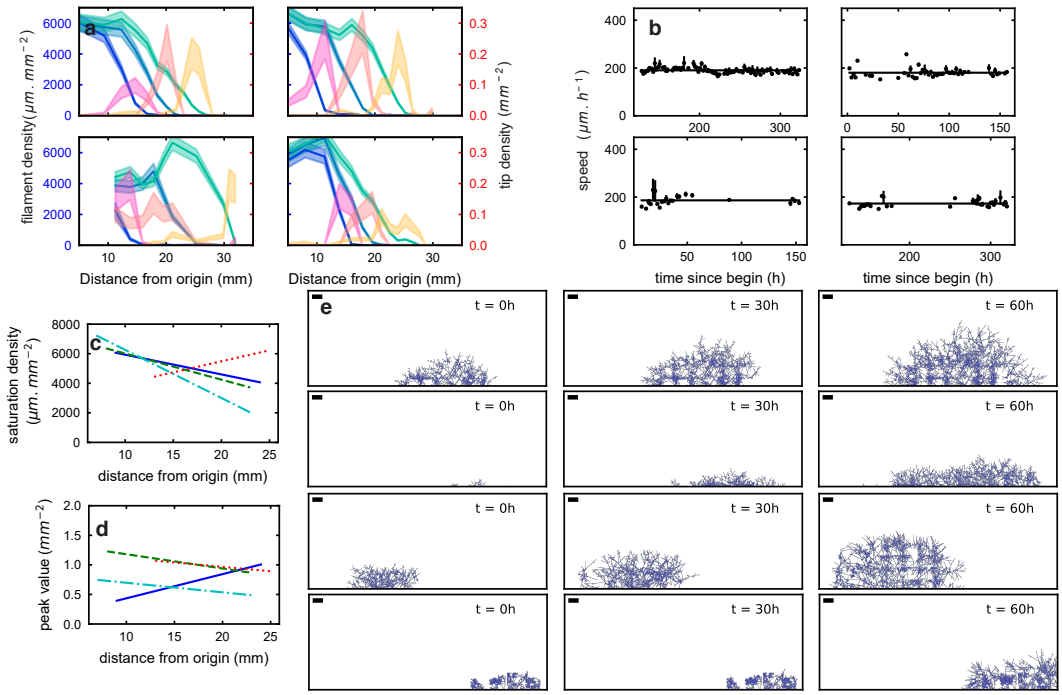

Figure 2.10: **Replicates of *R. aggregatum* plates show consistent traveling wave pattern.** **(a)** Spatial distribution of filament density (blue) and tip (red) density over three consecutive days (color gradient, with dark colors going to lighter from day one to three). Shaded region corresponds to uncertainty in density estimates computed by extrapolating the ones obtained for the plate in the main text. Profile shown at regular intervals separated by 30 hours, while distance from origin is computed under the assumption of half circular colonisation of the plate. **(b)** Speed of growing tips at the front over time. Black points are the average hyphal growth speed at the front of the colony at each timestep. Error bars represent 95% C.I. Black line is the average of black points. **(c)** Saturation density as a function of ring radius. Each line corresponds to the linear fit across saturation value obtained by fitting a sigmoid to density curves for each replicate. **(d)** Active tip density peak value as a function of ring radius. Each line corresponds to the linear fit across peak values obtained by fitting the derivative of a sigmoid to growing tip density curves for each replicate. (e) Additional examples of extracted networks. Each row represents different timepoints of the same replicate. Scale bar is 1mm. *R. aggregatum* forms very thin and densely packed hyphae. The segmentation of this strain can be sensitive to illumination. Non-uniform illumination can cause non-uniform detection of these hyphae which explains the checkboard pattern observed in some plates.

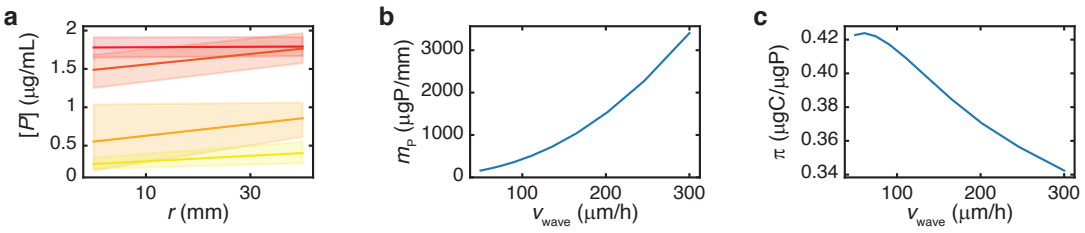

Figure 2.11: **Pattern of spatial phosphorus (P) absorption aligns with regulated fungal wave growth. (a)** Concentration of agar in fungal compartment of root organ cultures measured at 4 times points starting after fungal network crosses into fungal-only compartment (red = 0 days, dark orange = 3 days, light orange = 6 days, yellow = 9 days). $r = 0\,mm$ corresponds to cross-over point where fungal colony enters fungal-only compartment and $r = 40\,mm$ corresponds to the opposite end, where P depletion will take the longest to form. By 9 days (yellow line), P is almost completely depleted from the agar in the fungal-only compartment. **(b)-(c)** The data of **(a)** were used to parameterize the model of P depletion by the fungal traveling wave defined in Supplementary Discussion 2.7.2. **(b)** Total phosphorous captured by the colony per unit length of root over 600h of colony propagation (see Fig. 3e for spatial profiles) as a function of wave speed v_{wave}. At a fixed saturation density, the more the fungal colony invests in spatial exploration (i.e., the higher the wave speed), the more phosphorous it can absorb from its environment. This is because it can better escape its self-generated P depletion zone. **(c)** Carbon cost for the phosphorous captured by the colony over the same 600h interval. The cost is defined as the total carbon cost of growth divided by the total amount of P acquired over the duration of traveling-wave growth. Carbon cost is calculated in the same manner as was done for experimental data, as explained in Supplementary Discussion 2.6.6.

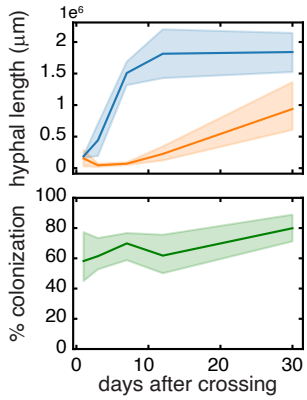

Figure 2.12: **Intraradical growth and colonization increase concurrently with extraradical growth.** Temporal variation of (**Top**) total extraradical hyphal length in um x10^6 (ERM, blue), total intraradical mycorrhizal length (IRM, orange) as measured by ddPCR, and (**Bottom**) per cent colonization (green), as measured using Trouvelot method. AM fungal networks were grown and harvested destructively over 30 days. Lines connect the means at 1, 3, 7, 12 and 30 days after crossing, shaded regions correspond to 95% confidence interval computed as mean $\pm 2 \times s.e.m.$ at each timepoint. For details of ddPCR and Trouvelot, see Methods.

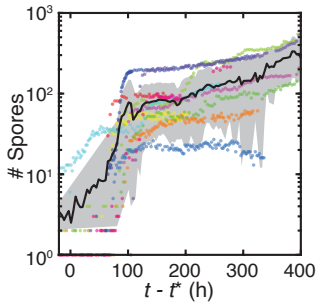

Figure 2.13: **Total number of spores across the network jumps rapidly at variable times, and then grows more gradually.** Data from the same 12 sample plates (dots colored by replicate) as in Fig. 2.4b-e. Black line corresponds to the mean across all samples and the grey region represents mean ± s.d., plotted along a time axis offset by t', the time at which each sample's network length reached $L_{RH} = 10^2$ mm.

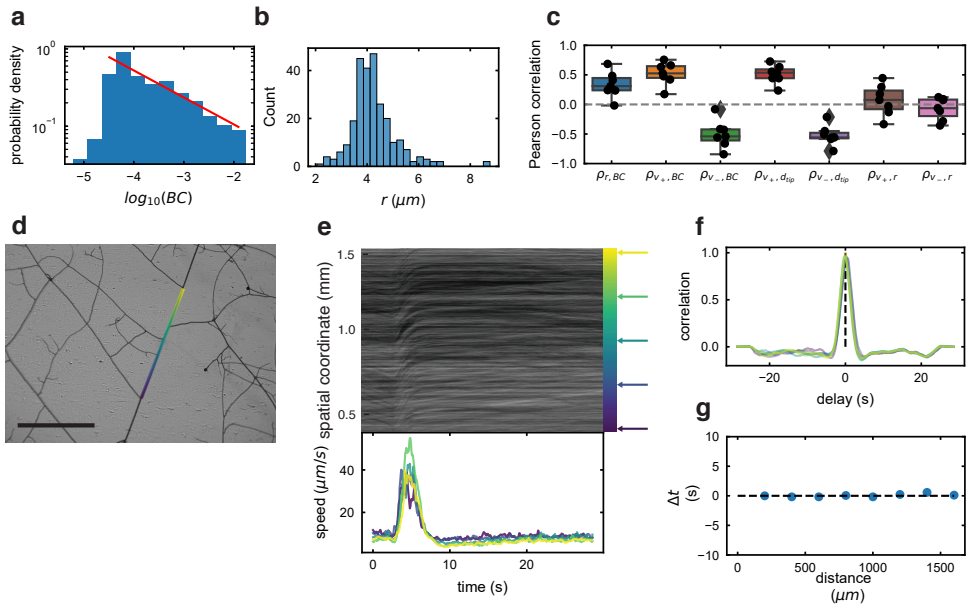

Figure 2.14: **Flow statistics correlate Betweenness Centrality (BC) hierarchy and indicates incompressibility.** **(a)** Length-weighted distribution of hyphal BC across the entire network demonstrates a long-tailed power-law distribution $P(BC) \sim BC^{-\gamma}$ with $\gamma \approx 0.3$, indicating hierarchical order. **(b)** Distribution of hyphal radius extracted from high-resolution videos. **(c)** Correlation between measured edge observables: radius r, betweenness centrality BC, distance to tip d_{tip}, the speed towards tip v_{tip}, and speed towards root v_{root}. Each dot represent the Pearson correlation coefficient computed over all edges belonging to a replicate plate sample ($n = 7$) Box represents interquartile range (IQR), with central line indicating median. Whiskers extend from box to minimum and maximum values within 1.5 times IQR. **(d)** Flow speeds are highly correlated across space and time with no detectable lag, consistent with incompressible flow. **(e)** Kymograph (**Top**) and speed time series (**Bottom**) of flows within the coloured hyphal segment in **(d)**, for a 30 s interval in which rapid changes in flow speed were observed. Arrows indicate spatial position for speed time series of matching colour. **(f)** Cross-correlation of speed time series at $x = 1.2$ mm in **(e)** against all other speed time series in **(e)**. All curves were nearly identical, peaking at a high cross-correlation value centred at a delay close to zero. **(g)** Cross-correlation delay At corresponding to the peak position of each curve in **(f)**, as a function of the distance along the hypha, was very close to zero and demonstrated no dependence on distance, consistent with incompressible flow.

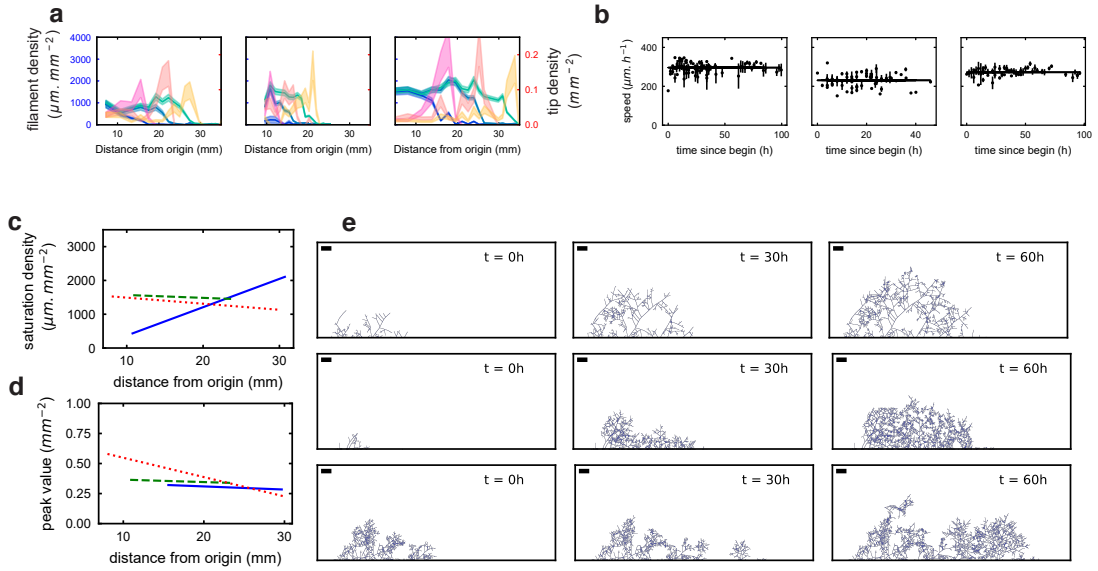

Figure 2.15: **Travelling wave dynamics do not differ between the sucrose and no sucrose treatments in the fungal compartment (a)** Spatial distribution of filament density (blue) and tip (red) density over three consecutive days (color gradient, with dark colors going to lighter from day one to three). Shaded region corresponds to uncertainty in density estimates computed by extrapolating the ones obtained for the plate in the main text. Profile shown at regular intervals separated by 30 hours, while distance from origin is computed under the assumption of half circular colonisation of the plate. **(b)** Speed of growing tips at the front over time. Black points are the average hyphal growth speed at the front of the colony at each timestep. Error bars represent 95% C.I. Black line is the average of black points. **(c)** Saturation density as a function of ring radius. Each line corresponds to the linear fit across saturation value obtained by fitting a sigmoid to density curves for each replicate. **(d)** Growing tip density peak value as a function of ring radius. Each line corresponds to the linear fit across peak values obtained by fitting the derivative of a sigmoid to growing tip density curves for each replicate. **(e)** Additional examples of extracted networks. Each row represents different timepoints of the same replicate. Scale bar is 1mm.

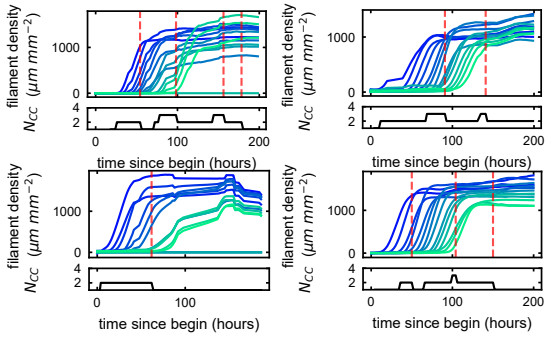

Figure 2.16: **Quantitative analysis of colliding waves in plates with multiple crossing events (Supplementary Video 7).** The position of the four panels within the 2x2 array above reflects the position of the corresponding video within the Supplementary Video 7. Within each panel, the upper subpanel shows a family of density time series, one for each successive concentric rings of increasing radius, represented by blue to green gradient (blue=small, green=large). No effects on the density time series are observed upon collision events (red lines), which are detected as decreases in the number of connected components N_{cc} waves (lower subpanel) representing the number of disjoint waves that have yet to collide. This outcome is consistent with our model: when waves collide, networks continue to cover the available space until the tips anastomose into an existing network upon reaching saturation density.

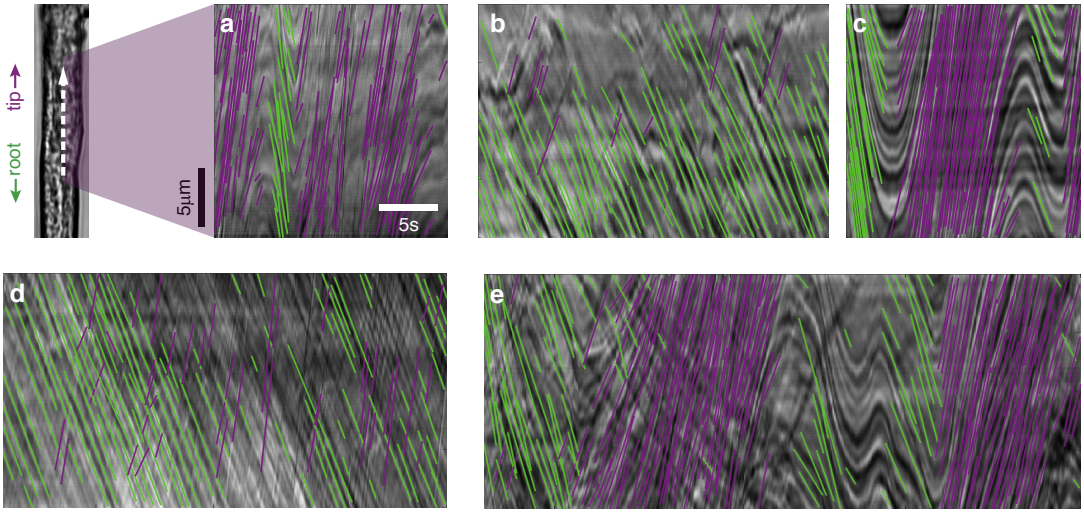

Figure 2.17: **Example kymographs showing the automatic detection of flow velocities across different ages.** Representation of five kymographs from five different biological samples of *R. irregularis* of age: **(a)** 1 day, **(b & c)** 4 days, **(d)** 5 days and **(e)** 11 days after crossing. Vertical axis represents space (20 μm) while horizontal axis represents time (from 20 s to 60 s). Averaged velocities automatically detected are represented by colored straight lines. Scale bars in **(a)** are valid for all panels. Trajectories in both directions, towards the tip (purple) and the root (green), were detected in most of the 1600 videos acquired. The density of detected trajectories fluctuated substantially across samples (as seen by the differences between **(a)** and **(b)** for instance). Flow patterns across time were also diverse – for example, the reversal events prominent in **(a)**, **(c)**, **(e)** are not observed in **(b)** or **(d)**. Corresponding videos can be found in Supplementary Video 5.

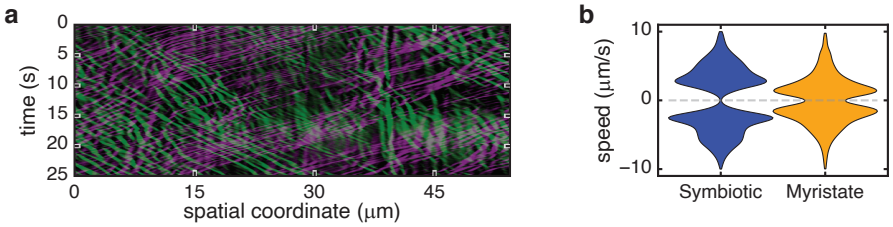

Figure 2.18: **Flow patterns inside networks of *R. irregularis* strain A5 when grown in the absence of a host root. (a)** Example kymograph from a video of flows of a *R. irregularis* network grown on myristate rather than with a host root shows bidirectional movement. Lines correspond to moving particles colored in purple (tip direction), and green (spore direction). **(b)** Distribution of observed velocities in two directions measuring flows from symbiotic context in which networks are connected to host roots (blue, $N = 71009$) and distribution of flow speeds observed in 86 positions from 7 replicates of networks grown in non-symbiotic context with myristate (orange, $N = 2450$). In both cases, we excluded the immotile fraction of tracked objects, defined as those demonstrating displacements indistinguishable from diffusion (see Supplementary Notes).

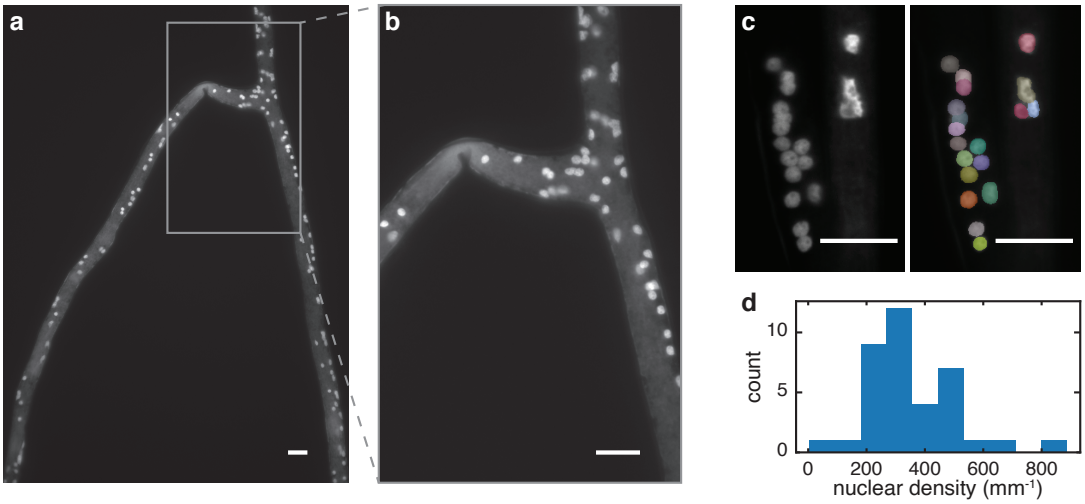

Figure 2.19: **Methodology for quantifying nuclear density Nuclear imaging and segmentation for the extraradical hyphae for *R. irregularis* A5, using DAPI (4',6-diamidino-2-phenylindole) blue-fluorescent DNA dye.** Scale bars indicate 10 μm. **(a)** Shows an example of the distribution of DAPI stained nuclei in the extraradical hyphae, while **(b)** is an enlarged crop image at the extraradical hyphae intersection (see Supplementaru video 8). **(c)** Panels show the segmented nuclear masks – a process to automatically recognize nuclei and calculate their distribution and density. Unique colours are automatically attributed to each nucleus via the trained StarDist model. **(d)** Number of nuclei per millimetre of extraradical hyphal length as measured by DAPI staining.

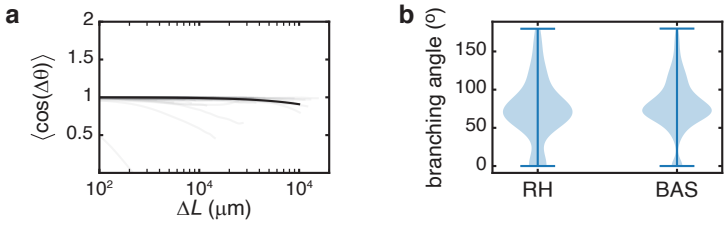

Figure 2.20: **Individual hyphal filaments grow with high directional persistence but form branches over a distribution of angles. (a)** For each individual hyphal filament, persistence of the growth direction is shown by plotting the average cosine of the angular deviation $\cos(\Delta\theta(\Delta L))$ computed for different lags in length ΔL. Under the assumption that the expectation value of the cosine of the angle falls off exponentially with distance we have $\cos(\Delta\theta(\Delta L)) = e^{-\Delta L/\ell_p}$, where ℓ_p is the persistence length of the growing filament and the averaging is done over all the starting positions along the hypha. Grey lines show the decay of $\cos(\Delta\theta(\Delta L))$ as a function of ΔL for each individual hypha ($n_{\text{hyphae}} = 118$). The median persistence length of all hyphae is $\ell_p \approx 10$ cm. The corresponding median decay $e^{-\Delta L/\ell_p}$ is shown as a thick black line. Note that given that the orientation correlation $\cos(\Delta\theta(\Delta L))$ barely decays over the entire tested range, these persistence lengths estimated from exponential fits should be interpreted with care, and likely represent lower bounds on the true persistence length. **(b)** Distribution of absolute branching angle of new-born runner hyphae (RH, $n = 71$) and new-born branched absorbing structures (BAS, $n = 881$). Angles above 100° can be an artefact of the extraction. On average RH branch at an angle of 73° from the initial growth direction and BAS branch at an angle of 80°. These two values are not statistically significantly different.

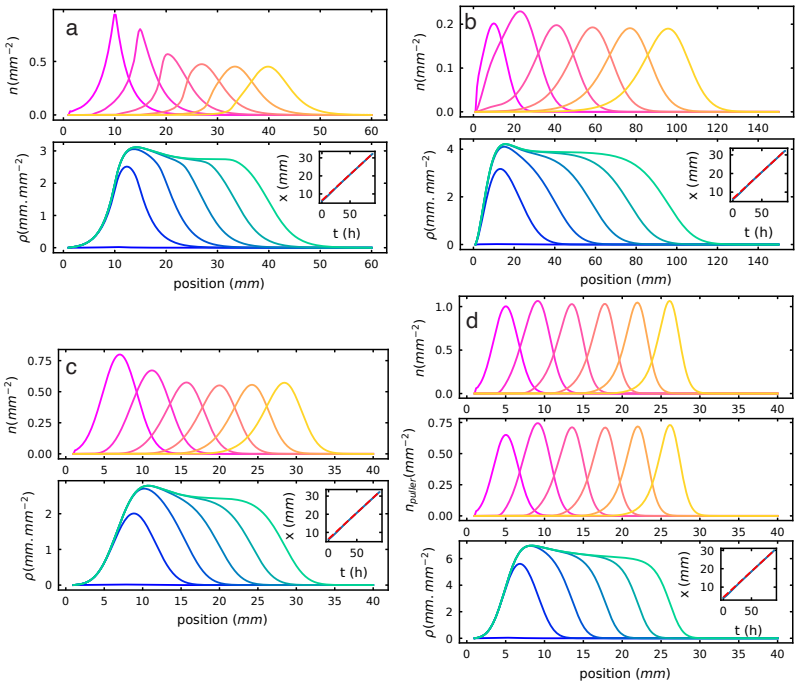

Figure 2.21: **Numerical simulations of model variants with different assumptions about the spatial flux $J(n)$ underlying the wave speed.** **(a)** Numerical integration of model with $J(n) = -n\nu r$ with $\nu = 0.039h^{-1}$, $v_a = 235\mu m/h$, $\beta = 22\mu m/h$, $s = 200\mu m/h$. Simulated wave speed was $c = 330\mu m/h$. Color gradient corresponds to sampling at regular time interval from $t = 0$h to $t = 120$h. Initial condition was $p(r, 0) = 0$ and $n(r, 0) = n_{\max}e^{-\lambda x - x_0}$ where $n_{\max} = 1mm^{-1}$, $\lambda = 0.4mm^{-1}$ and $x_0 = 10mm$. **(b)** Numerical integration of model with $J(n) = D\nabla n$ with $\alpha = 0.039h^{-1}$, $\beta = 22\mu m/h$, and $D = 0.55mm^2/h$, $s = 200\mu m/h$. Simulated wave speed was $c = 280\mu m/h$. Color gradient corresponds to sampling at regular time interval from $t = 0$h to $t = 400$h. **(c)** Model integration for $J(n) = -n\nu af$ with $\alpha = 0.039h^{-1}$, $v_a = 235\mu m/h$, $\beta = 22\mu m/h$, $D = 0.02mm^2/h$ and $s = 200\mu m/h$. Simulated wave speed was $c = 280\mu m/h$. Color gradient corresponds to sampling at regular time interval from $t = 0$h to $t = 90$h. **(d)** Model integration for $J(n) = -n\nu af$ with $\alpha = 0.039h^{-1}$, $v_a = 220\mu m/h$, $\beta = 22\mu m/h$, $s = 220\mu m/h$, $K_1 = 0.25h^{-1}$, $K_2 = 0.40h^{-1}$ and $v_p = 300\mu m/h$. Simulated wave speed was $c = 280\mu m/h$. In all case, the equations integrated are 2.7.2 and 2.7.3 from Supplementary discussion, color gradient corresponds to sampling at regular time interval from $t = 0$h to $t = 90$h. Insets show the position of the peak of tip density over time. Blue line is the result from model integration. Red dashed line corresponds to a linear fit, the slope of which gives the speed of the wave. See Supplementary Discussion section 2.7.3

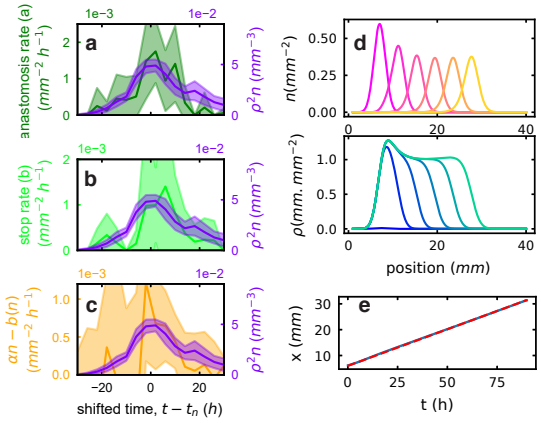

Figure 2.22: **raveling wave model with refined density control accurately predicts saturating density (a)-(c)** Average temporal profile in the reference frame of the ring for density-dependent processes relevant to the exact calculation of predicted saturation density as explained in Supplementary Discussion 2.7.3. Shaded regions correspond to 95% confidence interval computed as mean $\pm 2 \times s.e.m.$ across all rings ($n_{\text{ring}} = 15$). Magenta is the product of the square of hyphal density and growing tip density $p^2 n$. **(a)** shows anastomosis rate, **(b)** shows the rate of tip annihilation when tips stop growing shortly after crossing over another hypha – the precursor of "overshoot anastomoses". **(c)** shows the residuals $an - b(n)$ with the proportionality factor extracted through the linear scaling analysis of Fig. 3b. Non-zero residuals in **(c)** suggest there is a weak but significant component of density-dependent branching that plays a role in saturation density control. Mathematically, this density dependent component of branching can be represented as a contribution to the density dependent tip annihilation (Supplementary Discussion 2.7.3). Combining these three processes and assuming a tip annihilation rate of the form $a(n, p) = \beta n^2$ yields $\beta = 0.075\text{mm}^2.h^{-1}$. Plugging into the solution of the model yields $\rho_{\text{sat}} = \sqrt{3/\beta} = 1.3\text{mm}^{-1}$, which is very close to the experimentally observed value (1mm^{-1}). **(d),(e)** This finding is further supported by simulations that show that the choice of a different density dependence for the tip annihilation term does not affect the existence and speed of the travelling wave. All the parameters and figure specificities correspond to the one shown in Extended Data Fig. 2.21c. Only the parameter $\beta_{\text{tot}} = 0.075\text{mm}^2.h^{-1}$ and the tip annihilation term were changed during integration See Supplementary Discussion 2.7.3

Bibliography

1. Genre, A., Lanfranco, L., Perotto, S. & Bonfante, P. Unique and common traits in mycorrhizal symbioses. eng. *Nature Reviews. Microbiology* **18,** 649–660. ISSN: 1740-1534 (Nov. 2020).
2. Parniske, M. Arbuscular mycorrhiza: the mother of plant root endosymbioses. eng. *Nature Reviews. Microbiology* **6,** 763–775. ISSN: 1740-1534 (Oct. 2008).
3. Wipf, D., Krajinski, F., van Tuinen, D., Recorbet, G. & Courty, P.-E. Trading on the arbuscular mycorrhiza market: from arbuscules to common mycorrhizal networks. eng. *The New Phytologist* **223,** 1127–1142. ISSN: 1469-8137 (Aug. 2019).
4. Bebber, D. P., Hynes, J., Darrah, P. R., Boddy, L. & Fricker, M. D. Biological solutions to transport network design. *Proceedings of the Royal Society B: Biological Sciences* **274,** 2307–2315. ISSN: 0962-8452. https://www.ncbi.nlm.nih.gov/pmc/articles/PMC2288531/ (2023) (Sept. 2007).
5. Ganin, A., Kitsak, M., Marchese, D., Keisler, J. & Seager, T. Resilience and efficiency in transportation networks. *Science Advances* **3,** e1701079 (Dec. 2017).
6. Brundrett, M. C. & Tedersoo, L. Evolutionary history of mycorrhizal symbioses and global host plant diversity. en. *New Phytologist* **220,** 1108–1115. ISSN: 1469-8137. https://onlinelibrary.wiley.com/doi/abs/10.1111/nph.14976 (2024) (2018).
7. Bago, B. *et al.* Translocation and Utilization of Fungal Storage Lipid in the Arbuscular Mycorrhizal Symbiosis. *Plant Physiology* **128,** 108–124. ISSN: 0032-0889. https://doi.org/10.1104/pp.010466 (2023) (Jan. 2002).
8. Bago, B., Pfeffer, P. E., Zipfel, W., Lammers, P. & Shachar-Hill, Y. Tracking metabolism and imaging transport in arbuscular mycorrhizal fungi. Metabolism and transport in AM fungi. en. *Plant and Soil* **244,** 189–197. ISSN: 1573-5036. https://doi.org/10.1023/A:1020212328955 (2024) (July 2002).
9. Hawkins, H. J. *et al.* Mycorrhizal mycelium as a global carbon pool. *Current Biology* **33,** R560–R573. ISSN: 0960-9822. http://www.scopus.com/inward/record.url?scp=85160575900&partnerID=8YFLogxK (2023) (June 2023).
10. Miller, R. M., Jastrow, J. D. & Reinhardt, D. R. External hyphal production of vesicular-arbuscular mycorrhizal fungi in pasture and tallgrass prairie communities. en. *Oecologia* **103,** 17–23. ISSN: 0029-8549, 1432-1939. http://link.springer.com/10.1007/BF00328420 (2023) (July 1995).

11. Camenzind, T. & Rillig, M. C. Extraradical arbuscular mycorrhizal fungal hyphae in an organic tropical montane forest soil. en. *Soil Biology and Biochemistry* **64,** 96–102. ISSN: 00380717. https://linkinghub.elsevier.com/retrieve/pii/S0038071713001430 (2023) (Sept. 2013).
12. Argüello, A. *et al.* Options of partners improve carbon for phosphorus trade in the arbuscular mycorrhizal mutualism. en. *Ecology Letters* **19** (ed Maherali, H.) 648–656. ISSN: 1461023X. https://onlinelibrary.wiley.com/doi/10.1111/ele.12601 (2023) (June 2016).
13. Noë, R. & Kiers, E. T. Mycorrhizal Markets, Firms, and Co-ops. en. *Trends in Ecology & Evolution* **33,** 777–789. ISSN: 01695347. https://linkinghub.elsevier.com/retrieve/pii/S0169534718301782 (2023) (Oct. 2018).
14. Van 't Padje, A., Werner, G. & Kiers, T. Mycorrhizal fungi control value of phosphorus in trade symbiosis with host roots when exposed to abrupt 'crashes' and 'booms' of resource availability. *New Phytologist* **229** (Oct. 2020).
15. Kiers, E. T. *et al.* Reciprocal Rewards Stabilize Cooperation in the Mycorrhizal Symbiosis. en. *Science* **333,** 880–882. ISSN: 0036-8075, 1095-9203. https://www.science.org/doi/10.1126/science.1208473 (2023) (Aug. 2011).
16. Cardini, A. *et al.* HyLength: a semi-automated digital image analysis tool for measuring the length of roots and fungal hyphae of dense mycelia. en. *Mycorrhiza* **30,** 229–242. ISSN: 1432-1890. https://doi.org/10.1007/s00572-020-00956-w (2024) (May 2020).
17. Schnepf, A. & Roose, T. Modelling the contribution of arbuscular mycorrhizal fungi to plant phosphate uptake. en. *New Phytologist* **171,** 669–682. ISSN: 1469-8137. https://onlinelibrary.wiley.com/doi/abs/10.1111/j.1469-8137.2006.01771.x (2024) (2006).
18. Schnepf, A., Roose, T. & Schweiger, P. Growth model for arbuscular mycorrhizal fungi. *Journal of The Royal Society Interface* **5,** 773–784. https://royalsocietypublishing.org/doi/10.1098/rsif.2007.1250 (2024) (Dec. 2007).
19. Keymer, A. *et al.* Lipid transfer from plants to arbuscular mycorrhiza fungi. en. *eLife* **6,** e29107. ISSN: 2050-084X. https://elifesciences.org/articles/29107 (2023) (July 2017).
20. Luginbuehl, L. H. & Oldroyd, G. E. D. Understanding the Arbuscule at the Heart of Endomycorrhizal Symbioses in Plants. en. *Current Biology* **27,** R952–R963. ISSN: 0960-9822. https://www.sciencedirect.com/science/article/pii/S0960982217307790 (2023) (Sept. 2017).
21. Van't Padje, A. *et al.* Temporal tracking of quantum-dot apatite across in vitro mycorrhizal networks shows how host demand can influence fungal nutrient transfer strategies. en. *The ISME Journal* **15,** 435–449. ISSN: 1751-7370. https://www.nature.com/articles/s41396-020-00786-w (2023) (Feb. 2021).
22. Kolmogorov, A., Petrovskii, I. & Piscunov, N. A study of the equation of diffusion with increase in the quantity of matter, and its application to a biological problem. *Byul. Moskovskogo Gos. Univ.* **1,** 1–25. http://books.google.com/books?id=ikN59GkYJKIC&lpg=PP1&dq=A.N.%20Kolmogorov%3A%20Selected%20Works&client=firefox-a&pg=PA242#v=onepage&q=&f=false (2023) (1937).
23. Van Saarloos, W. Front propagation into unstable states. en. *Physics Reports* **386,** 29–222. ISSN: 0370-1573. https://www.sciencedirect.com/science/article/pii/S0370157303003223 (2023) (Nov. 2003).

24. Fisher, R. A. The wave advance of advantageous genes. en. *Annals of Eugenics* **7,** 355–369. ISSN: 20501420. https://onlinelibrary.wiley.com/doi/10.1111/j.1469-1809.1937.tb02153.x (2023) (June 1937).

25. Hallatschek, O., Hersen, P., Ramanathan, S. & Nelson, D. R. Genetic drift at expanding frontiers promotes gene segregation. *Proceedings of the National Academy of Sciences* **104,** 19926–19930. https://www.pnas.org/doi/full/10.1073/pnas.0710150104 (2024) (Dec. 2007).

26. Hallatschek, O. *et al.* Proliferating active matter. en. *Nature Reviews Physics* **5,** 407–419. ISSN: 2522-5820. https://www.nature.com/articles/s42254-023-00593-0 (2024) (July 2023).

27. Gandhi, S. R., Yurtsev, E. A., Korolev, K. S. & Gore, J. Range expansions transition from pulled to pushed waves as growth becomes more cooperative in an experimental microbial population. *Proceedings of the National Academy of Sciences* **113,** 6922–6927. https://www.pnas.org/doi/abs/10.1073/pnas.1521056113 (2023) (June 2016).

28. Fu, X. *et al.* Spatial self-organization resolves conflicts between individuality and collective migration. en. *Nature Communications* **9,** 2177. ISSN: 2041-1723. https://www.nature.com/articles/s41467-018-04539-4 (2023) (June 2018).

29. Warren, M. R. *et al.* Spatiotemporal establishment of dense bacterial colonies growing on hard agar. *eLife* **8** (eds Neher, R. A., Barkai, N. & Neher, R. A.) e41093. ISSN: 2050-084X. https://doi.org/10.7554/eLife.41093 (2023) (Mar. 2019).

30. Gude, S. *et al.* Bacterial coexistence driven by motility and spatial competition. en. *Nature* **578,** 588–592. ISSN: 1476-4687. https://www.nature.com/articles/s41586-020-2033-2 (2024) (Feb. 2020).

31. Narla, A. V., Cremer, J. & Hwa, T. A traveling-wave solution for bacterial chemotaxis with growth. *Proceedings of the National Academy of Sciences* **118,** e2105138118. https://www.pnas.org/doi/abs/10.1073/pnas.2105138118 (2023) (Nov. 2021).

32. Edelstein, L. The propagation of fungal colonies: a model for tissue growth. *Journal of Theoretical Biology* **98,** 679–701. ISSN: 0022-5193. https://www.sciencedirect.com/science/article/pii/0022519382901461 (2024) (Oct. 1982).

33. Hannezo, E. *et al.* A Unifying Theory of Branching Morphogenesis. eng. *Cell* **171,** 242–255.e27. ISSN: 1097-4172 (Sept. 2017).

34. Dikec, J. *et al.* Hyphal network whole field imaging allows for accurate estimation of anastomosis rates and branching dynamics of the filamentous fungus Podospora anserina. en. *Scientific Reports* **10,** 3131. ISSN: 2045-2322. https://www.nature.com/articles/s41598-020-57808-y (2023) (Feb. 2020).

35. Aguilar-Trigueros, C. A., Boddy, L., Rillig, M. C. & Fricker, M. D. Network traits predict ecological strategies in fungi. en. *ISME Communications* **2,** 1–11. ISSN: 2730-6151. https://www.nature.com/articles/s43705-021-00085-1 (2023) (Jan. 2022).

36. Sugiura, Y. *et al.* Myristate can be used as a carbon and energy source for the asymbiotic growth of arbuscular mycorrhizal fungi. *Proceedings of the National Academy of Sciences* **117,** 25779–25788. https://www.pnas.org/doi/abs/10.1073/pnas.2006948117 (2024) (Oct. 2020).

37. Kameoka, H., Maeda, T., Okuma, N. & Kawaguchi, M. Structure-Specific Regulation of Nutrient Transport and Metabolism in Arbuscular Mycorrhizal Fungi. *Plant and Cell Physiology* **60,** 2272–2281. ISSN: 0032-0781. https://doi.org/10.1093/pcp/pcz122 (2024) (Oct. 2019).

38. McGaley, J., Schneider, B. & Paszkowski, U. The AMSlide for noninvasive time-lapse imaging of arbuscular mycorrhizal symbiosis. en. *Journal of Microscopy,* jmi.13313. ISSN: 0022-2720, 1365-2818. https://onlinelibrary.wiley.com/doi/10.1111/jmi.13313 (2024) (May 2024).

39. Kobae, Y. & Hata, S. Dynamics of Periarbuscular Membranes Visualized with a Fluorescent Phosphate Transporter in Arbuscular Mycorrhizal Roots of Rice. *Plant and Cell Physiology* **51,** 341–353. ISSN: 0032-0781. https://doi.org/10.1093/pcp/pcq013 (2024) (Mar. 2010).

40. Bago, B., Azcon-Aguilar, C., Goulet, A. & Piche, Y. Branched Absorbing Structures (BAS): A Feature of the Extraradical Mycelium of Symbiotic Arbuscular Mycorrhizal Fungi. *The New Phytologist* **139,** 375–388. ISSN: 0028-646X. https://www.jstor.org/stable/2588307 (2024) (1998).

41. Alexander, T., Meier, R., Toth, R. & Weber, H. C. Dynamics of arbuscule development and degeneration in mycorrhizas of Triticum aestivum L. and Avena sativa L. with reference to Zea mays L. en. *New Phytologist* **110,** 363–370. ISSN: 1469-8137. https://onlinelibrary.wiley.com/doi/abs/10.1111/j.1469-8137.1988.tb00273.x (2023) (1988).

42. Gutjahr, C. & Parniske, M. Cell Biology: Control of Partner Lifetime in a Plant–Fungus Relationship. en. *Current Biology* **27,** R420–R423. ISSN: 0960-9822. https://www.sciencedirect.com/science/article/pii/S0960982217304293 (2023) (June 2017).

43. Freeman, L. C. A Set of Measures of Centrality Based on Betweenness. *Sociometry* **40,** 35–41. ISSN: 0038-0431. https://www.jstor.org/stable/3033543 (2023) (1977).

44. Kirkley, A., Barbosa, H., Barthelemy, M. & Ghoshal, G. From the betweenness centrality in street networks to structural invariants in random planar graphs. en. *Nature Communications* **9,** 2501. ISSN: 2041-1723. https://www.nature.com/articles/s41467-018-04978-z (2024) (June 2018).

45. Latora, V. & Marchiori, M. Efficient Behavior of Small-World Networks. *Physical Review Letters* **87,** 198701. https://link.aps.org/doi/10.1103/PhysRevLett.87.198701 (2023) (Oct. 2001).

46. Katifori, E., Szöllősi, G. J. & Magnasco, M. O. Damage and Fluctuations Induce Loops in Optimal Transport Networks. *Physical Review Letters* **104,** 048704. https://link.aps.org/doi/10.1103/PhysRevLett.104.048704 (2023) (Jan. 2010).

47. Barthélemy, M. Spatial networks. en. *Physics Reports* **499,** 1–101. ISSN: 03701573. https://linkinghub.elsevier.com/retrieve/pii/S037015731000308X (2023) (Feb. 2011).

48. Cardillo, A., Scellato, S., Latora, V. & Porta, S. Structural properties of planar graphs of urban street patterns. *Physical Review E: Statistical Physics, Plasmas, Fluids, and Related Interdisciplinary Topics* **73.** ISSN: 1539-3755 (June 2006).

49. Papadopoulos, L. *et al.* Comparing two classes of biological distribution systems using network analysis. en. *PLOS Computational Biology* **14,** e1006428. ISSN: 1553-7358. https://journals.plos.org/ploscompbiol/article?id=10.1371/journal.pcbi.1006428 (2023) (Sept. 2018).

50. Louf, R., Jensen, P. & Barthelemy, M. Emergence of hierarchy in cost-driven growth of spatial networks. eng. *Proceedings of the National Academy of Sciences of the United States of America* **110,** 8824–8829. ISSN: 1091-6490 (May 2013).

51. Popović, M., Štefančić, H. & Zlatić, V. Geometric Origin of Scaling in Large Traffic Networks. *Physical Review Letters* **109,** 208701. https://link.aps.org/doi/10.1103/PhysRevLett.109.208701 (2024) (Nov. 2012).

52. Tero, A. *et al.* Rules for Biologically Inspired Adaptive Network Design. *Science* **327,** 439–442. https://www.science.org/doi/10.1126/science.1177894 (2024) (Jan. 2010).

53. Cui, Y., Yu, Y., Cai, Z. & Wang, D. Optimizing Road Network Density Considering Automobile Traffic Efficiency: Theoretical Approach. EN. *Journal of Urban Planning and Development* **148,** 04021062. ISSN: 1943-5444. https://ascelibrary.org/doi/10.1061/%28ASCE%29UP.1943-5444.0000780 (2023) (Mar. 2022).

54. Yerra, B. M. & Levinson, D. M. The emergence of hierarchy in transportation networks. en. *The Annals of Regional Science* **39,** 541–553. ISSN: 1432-0592. https://doi.org/10.1007/s00168-005-0230-4 (2024) (Sept. 2005).

55. Whiteside, M. D. *et al.* Mycorrhizal Fungi Respond to Resource Inequality by Moving Phosphorus from Rich to Poor Patches across Networks. en. *Current Biology* **29,** 2043–2050.e8. ISSN: 0960-9822. https://www.sciencedirect.com/science/article/pii/S0960982219304907 (2023) (June 2019).

56. Jakobs, M. A., Dimitracopoulos, A. & Franze, K. KymoButler, a deep learning software for automated kymograph analysis. *eLife* **8** (eds Bassereau, P., Malhotra, V., Urbach, J. & Danuser, G.) e42288. ISSN: 2050-084X. https://doi.org/10.7554/eLife.42288 (2023) (Aug. 2019).

57. Murray, C. D. The Physiological Principle of Minimum Work. *Proceedings of the National Academy of Sciences* **12,** 207–214. https://www.pnas.org/doi/10.1073/pnas.12.3.207 (2023) (Mar. 1926).

58. Marbach, S., Ziethen, N., Bastin, L., Bäuerle, F. K. & Alim, K. Vein fate determined by flow-based but time-delayed integration of network architecture. *eLife* **12** (eds Seminara, A. & Walczak, A. M.) e78100. ISSN: 2050-084X. https://doi.org/10.7554/eLife.78100 (2023) (Mar. 2023).

59. Verkman, A. S. Solute and macromolecule diffusion in cellular aqueous compartments. English. *Trends in Biochemical Sciences* **27,** 27–33. ISSN: 0968-0004. https://www.cell.com/trends/biochemical-sciences/abstract/S0968-0004(01)02003-5 (2023) (Jan. 2002).

60. Fukasawa, Y., Savoury, M. & Boddy, L. Ecological memory and relocation decisions in fungal mycelial networks: responses to quantity and location of new resources. en. *The ISME Journal* **14,** 380–388. ISSN: 1751-7370. https://www.nature.com/articles/s41396-019-0536-3 (2023) (Feb. 2020).

61. Kramar, M. & Alim, K. Encoding memory in tube diameter hierarchy of living flow network. *Proceedings of the National Academy of Sciences* **118,** e2007815118. https://www.pnas.org/doi/abs/10.1073/pnas.2007815118 (2023) (Mar. 2021).

62. Chen, S. & Alim, K. Network topology enables efficient response to environment in Physarum polycephalum. en. *Physical Biology* **20,** 046003. ISSN: 1478-3975. https://dx.doi.org/10.1088/1478-3975/accef2 (2023) (May 2023).

63. Preibisch, S., Saalfeld, S. & Tomancak, P. Globally optimal stitching of tiled 3D microscopic image acquisitions. *Bioinformatics* **25,** 1463–1465. ISSN: 1367-4803. https://www.ncbi.nlm.nih.gov/pmc/articles/PMC2682522/ (2023) (June 2009).

64. Sternberg. Biomedical Image Processing. *Computer* **16,** 22–34. ISSN: 1558-0814 (Jan. 1983).

65. Heaton, L. *et al.* Analysis of fungal networks. en. *Fungal Biology Reviews. Hyphal networks: mechanisms, modelling and ecology* **26,** 12–29. ISSN: 1749-4613. https://www.sciencedirect.com/science/article/pii/S1749461312000024 (2023) (Apr. 2012).

66. Sazak, Ç., Nelson, C. J. & Obara, B. The multiscale bowler-hat transform for blood vessel enhancement in retinal images. en. *Pattern Recognition* **88,** 739–750. ISSN: 0031-3203. https://eprints.gla.ac.uk/171475/ (2023) (Apr. 2019).

67. Long, Y. *et al.* Cellular Heterogeneity in Pressure and Growth Emerges from Tissue Topology and Geometry. en. *Current Biology* **30,** 1504–1516.e8. ISSN: 0960-9822. https://www.sciencedirect.com/science/article/pii/S0960982220302001 (2023) (Apr. 2020).

68. Van Der Walt, S. *et al.* scikit-image: image processing in Python. en. *PeerJ* **2,** e453. ISSN: 2167-8359. https://peerj.com/articles/453 (2023) (June 2014).

69. Bradski, G. *The Opencv Library* (Nov. 2000).

70. Anthony. *Cython-CPD* May 2023. https://github.com/gattia/cycpd (2023).

71. Besl, P. & McKay, N. D. A method for registration of 3-D shapes. *IEEE Transactions on Pattern Analysis and Machine Intelligence* **14,** 239–256. ISSN: 1939-3539 (Feb. 1992).

72. Zhou, Q.-Y., Park, J. & Koltun, V. *Open3D: A Modern Library for 3D Data Processing* Jan. 2018. http://arxiv.org/abs/1801.09847 (2023).

73. Gillies, S. *et al. Shapely* Jan. 2023. https://github.com/shapely/shapely (2023).

74. Murphy, J. & Riley, J. P. A modified single solution method for the determination of phosphate in natural waters. *Analytica Chimica Acta* **27,** 31–36. ISSN: 0003-2670. https://www.sciencedirect.com/science/article/pii/S0003267000884445 (2023) (Jan. 1962).

75. Etesami, H., Jeong, B. R. & Glick, B. R. Contribution of Arbuscular Mycorrhizal Fungi, Phosphate–Solubilizing Bacteria, and Silicon to P Uptake by Plant. *Frontiers in Plant Science* **12.** ISSN: 1664-462X. https://www.frontiersin.org/articles/10.3389/fpls.2021.699618 (2023) (2021).

76. Bakken, L. R. & Olsen, R. A. Buoyant densities and dry-matter contents of microorganisms: conversion of a measured biovolume into biomass. eng. *Applied and Environmental Microbiology* **45,** 1188–1195. ISSN: 0099-2240 (Apr. 1983).

77. Bar-On, Y. M., Phillips, R. & Milo, R. The biomass distribution on Earth. en. *Proceedings of the National Academy of Sciences* **115,** 6506–6511. ISSN: 0027-8424, 1091-6490. https://pnas.org/doi/full/10.1073/pnas.1711842115 (2024) (June 2018).

78. Manzoni, S., Taylor, P., Richter, A., Porporato, A. & Ågren, G. I. Environmental and stoichiometric controls on microbial carbon-use efficiency in soils. en. *New Phytologist* **196,** 79–91. ISSN: 1469-8137. https://onlinelibrary.wiley.com/doi/abs/10.1111/j.1469-8137.2012.04225.x (2024) (2012).

79. Kokkoris, V., Pogiatzis, A. & Hart, M. M. Contrasting common measures of arbuscular mycorrhizal fungal root colonization. en. *Journal of Microbiological Methods* **167,** 105727. ISSN: 01677012. https://linkinghub.elsevier.com/retrieve/pii/S016770121930658X (2024) (Dec. 2019).

80. Weigert, M., Schmidt, U., Haase, R., Sugawara, K. & Myers, G. *Star-convex Polyhedra for 3D Object Detection and Segmentation in Microscopy* in (2020), 3666–3673. https://openaccess.thecvf.com/content_WACV_2020/html/Weigert_Star-convex_Polyhedra_for_3D_Object_Detection_and_Segmentation_in_Microscopy_WACV_2020_paper.html (2024).

81. *napari: a multi-dimensional image viewer for Python* https://zenodo.org/records/8115575 (2024).

82. *scikit-image: Image processing in Python* July 2023. https://github.com/scikit-image/scikit-image (2023).

83. Hagberg, A., Swart, P. J. & Schult, D. A. *Exploring network structure, dynamics, and function using NetworkX* English. Tech. rep. LA-UR-08-05495; LA-UR-08-5495 (Los Alamos National Laboratory (LANL), Los Alamos, NM (United States), Jan. 2008). https://www.osti.gov/biblio/960616 (2023).

84. Latora, V. & Marchiori, M. Economic small-world behavior in weighted networks. en. *The European Physical Journal B - Condensed Matter and Complex Systems* **32,** 249–263. ISSN: 1434-6036. https://doi.org/10.1140/epjb/e2003-00095-5 (2023) (Mar. 2003).

85. Mangeol, P., Prevo, B. & Peterman, E. J. G. KymographClear and KymographDirect: two tools for the automated quantitative analysis of molecular and cellular dynamics using kymographs. *Molecular Biology of the Cell* **27,** 1948–1957. ISSN: 1059-1524. https://www.ncbi.nlm.nih.gov/pmc/articles/PMC4907728/ (2023) (June 2016).

86. Bieleski, R. L. Phosphate Pools, Phosphate Transport, and Phosphate Availability. en. *Annual Review of Plant Physiology* **24,** 225–252. ISSN: 0066-4294. https://www.annualreviews.org/doi/10.1146/annurev.pp.24.060173.001301 (2024) (June 1973).

87. Darrah, P. R. & Staunton, S. A mathematical model of root uptake of cations incorporating root turnover, distribution within the plant, and recycling of absorbed species. en. *European Journal of Soil Science* **51,** 643–653. ISSN: 1365-2389. https://onlinelibrary.wiley.com/doi/abs/10.1046/j.1365-2389.2000.00331.x (2024) (2000).

88. Zhan, X. *et al.* Changes in Olsen Phosphorus Concentration and Its Response to Phosphorus Balance in Black Soils under Different Long-Term Fertilization Patterns. en. *PLOS ONE* **10,** e0131713. ISSN: 1932-6203. https://journals.plos.org/plosone/article?id=10.1371/journal.pone.0131713 (2024) (2015).

89. Edelstein-Keshet, L. & Ermentrout, B. Models for Branching Networks in Two Dimensions. *SIAM Journal on Applied Mathematics* **49,** 1136–1157. ISSN: 0036-1399. https://www.jstor.org/stable/2102010 (2024) (1989).

90. Scroggs, M. W., Dokken, J. S., Richardson, C. N. & Wells, G. N. Construction of Arbitrary Order Finite Element Degree-of-Freedom Maps on Polygonal and Polyhedral Cell Meshes. en. *ACM Transactions on Mathematical Software* **48,** 1–23. ISSN: 0098-3500, 1557-7295. https://dl.acm.org/doi/10.1145/3524456 (2023) (June 2022).

91. Waskom, M. L. seaborn: statistical data visualization. en. *Journal of Open Source Software* **6,** 3021. ISSN: 2475-9066. https://joss.theoj.org/papers/10.21105/joss.03021 (2023) (Apr. 2021).

Chapter 3

Spatial dynamics shape resource exchange

3.1 abstract

The outcomes of the arbuscular mycorrhizal (AM) symbiosis exhibit wide variation, influenced by the specific plant and fungal identities, along with soil conditions. Predicting these outcomes remains challenging due to the complexity and dynamic nature of the symbiotic process. In this process, plants allocate a portion of their photosynthetically fixed carbon to their AM fungal partners. The fungi use this carbon to expand their nutrient-absorbing network in the soil. The quantity of nutrients subsequently transported to the plant then influences the plant's future carbon allocation decisions to the fungal colony, affecting the fungal potential to secure additional nutrients.

In our research, we have precisely measured the plant's carbon investment in the extraradical mycelium and the AM phosphorus absorption ability over time. We find a direct proportionality between the rate of carbon transfer by the plant to the fungus and the rate of phosphorus transfer from the fungus. The proportionality coefficient remains constant across various fungal strains associated with the same plant host, despite these strains exhibiting a wide range of traits.

Incorporating this enforced proportionality into a model of AMF propagation sheds light on how mycorrhizal traits, the plant's control of the symbiosis, and soil characteristics interact to shape the overall outcome of the symbiotic relationship. This is pivotal for reevaluating previous experimental data on AM symbiosis across different scenarios and in developing new hypothesis that can be empirically tested.

3.2 Introduction

The symbiosis between Arbuscular Mycorrhizal (AM) fungi and their host plants represents one of the clearest examples of a biological trading market. Plants provide AM fungi with carbon in the form of sugars and fats, in exchange for phosphorous (P) and other nutrients provided by fungal

partners. This trade symbiosis helped facilitate the colonisation of land by plants 400 million years ago. Today, it is fundamental to both global ecosystem productivity and the regulation of the Earth's climate. Over 70% of all plant species rely on AM fungi for nutrients, with fungi providing up to 80% of the phosphorus (P) required for plant growth [1]. In return, plants allocate an average 6% of photosynthetically fixed carbon (C) to the AM partner [2].

While the importance of nutrient trade between AM fungi and plants is well recognized, resource trade can be highly context dependent depending upon both biotic and abiotic conditions in ways that we do not understand. This makes the outcomes of the symbiosis, like the total quantity of phosphorous transferred by the fungal partner to its host, difficult to predict. Specifically, fungal strains differ in the amounts of phosphorous that they supply to their host plants [3–6]. This has been linked to differences in fungal traits and/or fungal trading strategies over space and time [7, 8]. Concurrently, plants appear to adjust the amount of carbon that they supply to fungi, in response to how much phosphorous they are supplied [9, 10]. However, the mechanisms and strategies underlying this variation is not clear. Do plants have fixed trading rules, or do they vary trade depending upon nutrient availability or the fungi that that they are interacting with? Are plants transferring an initial amount of carbon to their fungal partner to allow them to grow and then later adjust their carbon supply depending on the amount of phosphorous they receive? Does the amount of phosphorous provided by fungi reflect variation in the extent to which they are cooperators or cheaters?

Past work has quantified cost-benefit ratios of different AM fungal strains using fungal biomass at time of harvest as a proxy for plant carbon cost per unit of phosphorus transferred. However, this approach fails to dynamically track how fungi utilize plant carbon to build their network and obtain phosphorus for trade. Without tracking the physical blueprint of the fungal network, it is impossible to quantify AM fungal phosphorus absorption ability over time to understand if there is: (i) a consistent correlation between rate of carbon transfer by the plant and the rate of phosphorus transfer from the fungus (i.e., reciprocal exchange), and (ii) whether this correlation varies across strains or remains constant. Dynamically tracking the network over time provides a direct blueprint of how different fungal strains use plant carbon to grow and reproduce. It can provide an estimate for the rate at which the network is acquiring resources for trade with the host, and whether the trade is driven by reciprocal exchange patterns.

Historically, quantifying trade networks over time has been challenging because of limitations in the methods that can be used to follow precise changes in fungi morphology. The ability of a fungal colony to absorb solutes, like phosphorus, from the environment is dependent on its total membrane area. Simultaneously, the building costs of network construction will be linked to the total biovolume of network. However, both membrane area and biovolume are direct functions of hyphal radius, which has been difficult to accurately measure and track over time. Past work has estimated AM fungal hypha radii to be anywhere from 0.6 to 9μm[11], but no direct measures over time and over whole networks have ever been acquired.

Here, we developed an imaging pipeline that allowed us to quantify the radius of all hyphae in a growing AM fungal colony, resulting in roughly 1 million hyphal radius measures per network time-lapse. Using an imaging robot that enabled time-resolved microscopy of fungal network topologies for in-vitro root-organ-culture (ROC) plant-fungal replicates, we grew networks in two-compartment petri plates. The colonized host was restricted to the root compartment, while the fungal network crossed a physical barrier to a second compartment lined with a permeable cellophane layer to

optimize visualization. We combined this high-resolution imaging data with direct measurements of phosphorus depletion across the network. This allowed us to dynamically track how AM fungi utilize plant-derived carbon to acquire fungal phosphorus and determine if there is proportionality between the rate of carbon transfer by the plant and the rate of phosphorus transfer from the fungus. We precisely quantified these dynamics for multiple plant-fungus-P concentration combinations to describe in what way fungal dynamics could differ in those situations. Finally, we modelled the impact of those differences on the trade of ressources.

3.3 Results

3.3.1 Extracting radius reveals temporal, spatial and genetic variation

First, we asked how the absorbing capacity of AM fungal networks changed over time by measuring hyphal radius from three different AM fungal strains over a 5-6 day period. We trained a Convolutional Neural Network to obtain hyphal radius from low magnification images of AM colonies (Fig. 3.1A). Approximately 1000 positions from 6 fungal networks were selected and imaged both in low and high resolution. We manually measured hyphal radius on the high resolution (50x) image. Transects orthogonal to the hyphae at those positions were automatically extracted from the low-resolution (2x) image at the video position. We then used the former as labels and the latter as features to train a two-layer Convolutional Neural Network. The Convolutional Neural Network was evaluated on an independent test set (RMSE=0.71, R^2 =0.64) confirming that the model could reliably be used to predict hyphal radius from new data (Fig. 3.1B, SI Fig. 3.6).

We then used the model to visualize hyphal radii for all the edges of the fungal networks (Fig.3.1C). We found that it varied widely from 1 μm for the thinnest Branched Absorbing Structures (key sites for nutrient uptake) to 6-7 μm for the thickest runner hyphae. On top of this spatial variation, we observed that runner hyphae tended to increase in radius over time, changing on average from 3 to 5 μm over 100 hour (Fig. 3.1D). We confirmed that this temporal variation was not an artefact of the Convolutional Neural Network model by manually measuring a subset of edges over multiple days (SI Fig. 3.7). Fungal hyphae are generally believed to grow by accumulation of material at the hyphal tip. It is to our knowledge the first time that such hyphal widening is being reported.

Next, we asked if the distribution of hyphal radius varied across the AM fungal strains, focusing on Rhizophagus irregularis A5, C2 and C3, Rhizophagus aggregatum, and Rhizophagus clarum and used the Convolutional Neural Network to predict the radius of all network edges. Those genotypes were chosen because their network growth pattern differed significantly. We found that the size distribution varied widely even within one species, with Rhizophagus aggregatum allocating proportionally less of its biovolume to thicker hyphae (Fig. 3.1E).

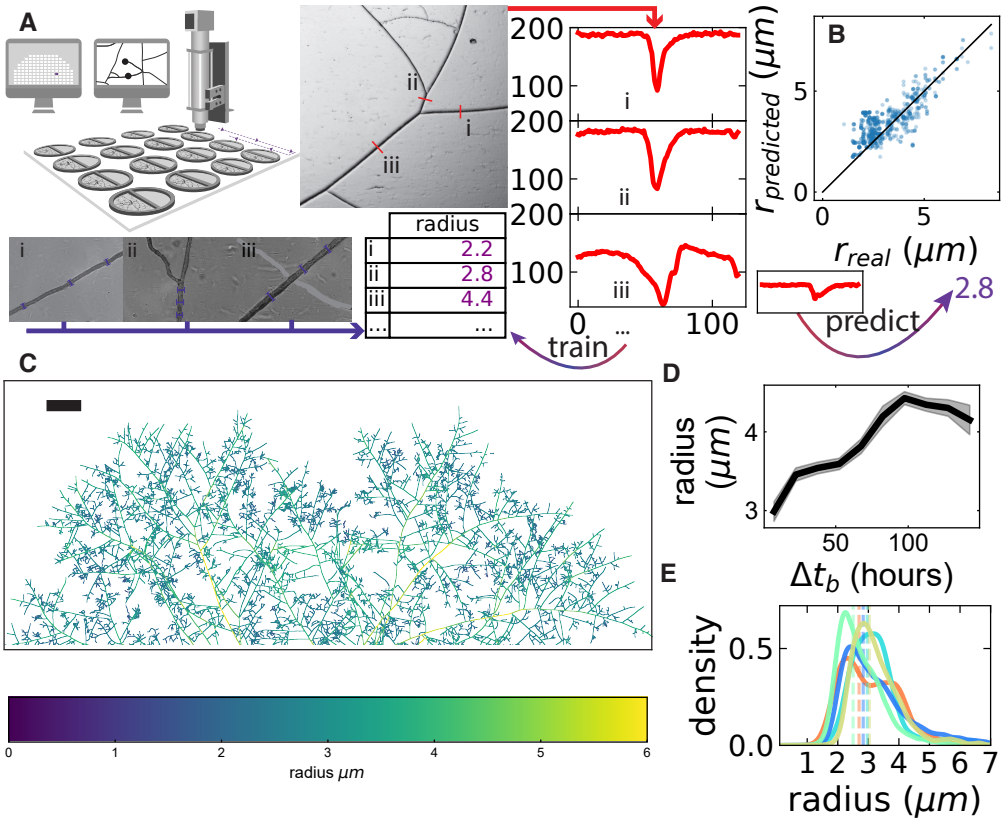

Figure 3.1: **Hyphal radius variation in space, time and across genotypes as revealed by Convolutional Neural Network.** **(A)** Description of the dataset generation and training scheme. Images are acquired in low and high magnification at different location in the network. Hyphal radius is manually measured on the high magnification images and orthogonal 120 px transect are extracted from the low magnification images. A Convolutional Neural Network is trained to predict the measured radius from the extracted transect. **(B)** Evaluation of the trained neural network on an independent dataset that has not been used for training (RMSE=0.76, R2 =0.60). Black line is the identity function, blue points are individual predictions from the independent dataset. **(C)** Network graph where each edge colour is mapped to the radius value estimated with the trained Convolutional Neural Network. **(D)** Temporal variation in radius of a selection of (n=13) major hyphae of the network as a function of the time since their emergence after branching. Black line corresponds to average and grey shade to 95% confidence interval. **(E)** Kernel density estimator of the weighted distribution of the radius of all edges at final timestep for different fungal strains and species: *R. irregularis* A5 (cyan, n=8), C2 (blue, n=19) and C3 (red, n=2), *G. aggregatum* (green, n=4), *G. Clarum* (orange, n=4). Distributions are weighted by edge volume (length $\times$ radius^2) to represent the contribution of hyphae of different radiuses to total biovolume. Dashed line correspond to effective mean radius $r_{\text{eff}} = \sqrt{\frac{\sum L_i r_i^2}{\sum L_i}}$ so that:$r_{\text{eff}}^2 \sum L_i = \sum L_i r_i^2$

3.3.2 Fungal carbon constraint is being relaxed over time

To investigate the consequence of this differing radius allocation over time and space on carbon cost of the colony, we used hyphal density and speed measurements from the image pipeline. At each timestep and for each replicate, we computed the instantaneous carbon density of the colony d_{carbon} and its propagation speed v_{wave} (Fig. 3.2A). This was inspired by previous research showing that AM colony growth is best described as a travelling wave, with pulses of growing tips pulling an expanding wave whose density is self-regulated by fusion. In line with this research, we found that fungal networks that expanded faster (larger v_{wave}) tended to grow sparser (smaller d_{carbon}). Conversely, slower growing strains grew denser on average.

To further investigate this speed-density trade-off, we asked whether the pattern was robust across different host roots for two of the fungal strains. We chose two different genotype of carrot root (later referred as genotype 1 and 2) for which preliminary experiments suggested that the associated fungal colonies differed in their growth patterns. We found that while the speed of network growth was strongly affected by this change of treatment, it did so in a way that conserved the trade-off (SI Fig. 3.8). Specifically, colonies grown with genotype 2 carrot root expanded spatially faster than the ones grown with genotype 1 carrot root but R. *irregularis* A5 was still sparser than R. *irregularis* C2.

The existence of a trade-off between exploration (speed) and exploitation (density) suggests that AM fungal networks face resource limitation. Unlike free-living filamentous fungi, AMF rely entirely on their root host for their carbon nutrition. We therefore estimated how much carbon was spent by the fungal colonies on hyphal growth at each timestep. We found that the rate of carbon expenditure Φ_C increased over time for all strains observed (Fig. 3.2B), suggesting that this constraint is being relaxed as the colony develops further. To determine what was driving the gradual relaxation of the growth constraint, we quantified the decrease of phosphorus concentration in the environment. This allowed us to test the hypothesis that, as the colony developed, so did its ability to absorb P and consequently its supply of C from the host.

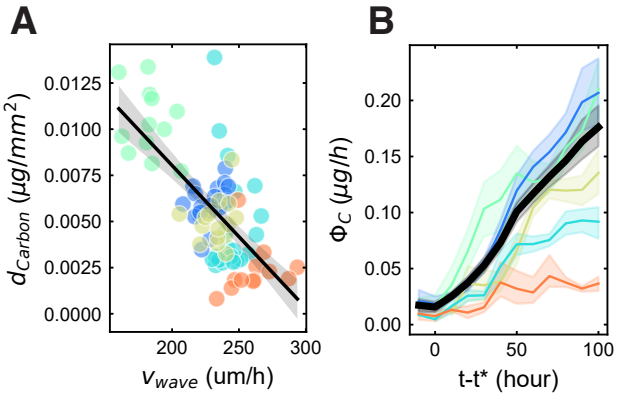

Figure 3.2: **Carbon expenditure pattern of various fungal strains (A)** Travelling wave observables. d_{carbon} represents the instantaneous hyphal carbon density and v_{wave} represents the instantaneous wave speed. Each small circle corresponds to an independent median of those parameters over 10 hours for all plates of the same strain ($n = 7 - 11$). Black line represent bootstrap regression on all datapoints. Grey shade correspond to 95% C.I. of the linear fit obtained via bootstrapping. **(B)** Carbon spent by the growing network in hyphal structures per hour as a function of time. Black line and shade represent average and 95% confidence interval of all replicates' dynamics. Coloured lines correspond to average and 95% confidence over all replicates for one strain. Average and 95% confidence interval (mean $\pm 2\times$ s.e.m.) are computed over 10-hour time intervals. For all plots, colour correspondence and number of replicates are the following: *R. irregularis* A5 (cyan, n=8), C2 (blue, n =19) and C3 (red, n=2), *G. aggregatum* (green, n=4), *G. Clarum* (orange, n= 4).

3.3.3 Fungal P supply grows with colony surface area

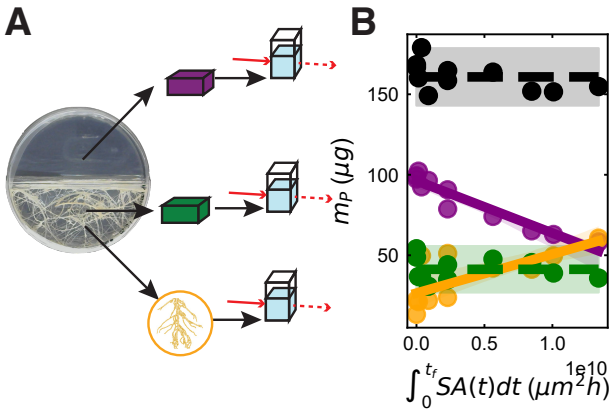

Figure 3.3: **Phosphorous depletion and transfer by the growing colony.(A)** Illustration of the experimental method used for measurement of phosphorus mass in the agar of the fungal compartment (purple), the agar of the root compartment (green) and the root (orange) **(B)** Total mass of phosphorous found in the agar of the fungal compartment (purple), the agar of the root compartment (green) and the root biomass (orange) as a function of the temporal integral of total colony surface area. Black line and dots correspond to the total mass of P measured in the three compartments for each replicate. Points correspond to individual replicates, full lines correspond to linear fit, dashed horizontal lines show averages for the corresponding category. Shades of full lines correspond to the 95% C.I. of the linear fit obtained via bootstrapping and shades of dashed lines to (mean $\pm 2\times$ s.e.m.). Coefficient of determination for the linear fits (R^2) are 0.91 (purple), 0.51 (orange)

Using spectrophotometric assays, we measured the mass of phosphorus in the agar of the root compartment, the fungal agar compartment, and the root (Fig. 3.3A, method). Next, we estimated the total surface area of the colony at each point in time until harvest using extracted hyphal radius from our imaging pipeline. This was motivated by the assumption that absorption of P by the fungal colony is limited only by the amount of P transporters. Assuming those transporters are present on the hyphal surface at a constant density, then the rate of P absorption should closely follow the total hyphal surface area $S(t)$ yielding the following equation for the total mass of phosphorus in the agar of the fungal compartment P_{agar}.

$$\frac{dP_{agar}}{dt} = -F_{max} S(t) \tag{3.3.1}$$

Where F_{max} is a constant that depends on the surface density of P transporters and their affinity. Integrating equation (1) over time yields:

$$P_{agar}(t) = P_{agar}(0) - F_{max} \int_0^t S(t)\, dt \tag{3.3.2}$$

We found that the mass of P ($P_{agar}(t)$), left in the fungal agar compartment at a given point in time was linearly decreasing with the integral over time of total surface area $S(t)$ (Fig. 3.3B) which allowed us to extract $F_{max} \approx 3\,\mathrm{ng \cdot mm^{-2} \cdot h^{-1}}$. This key parameter is fundamental to the plant-fungal symbiosis as it determines the rate at which a given network will absorb P from its environment. For example, a network that totalizes 1 m of hypha and of average radius 3 μm would extract about 1 μg of P every day.

A similar expression as the one shown in equation 3.3.1 had been proposed in previous models of P absorption by AMF:

$$\frac{d[P]}{dt} = -\tilde{F}_{max} s(t) \frac{[P]}{[P] + K_m} \tag{3.3.3}$$

where $[P]$ represents the concentration of P in solution and $s(t)$ is a volumetric density of hyphal surface area. Our experimentally derived formula corresponds to the regime where the Michaelis-Menten constant K_m is small compared to the temporal change in solute concentration (see SI 3.6.8). In those earlier studies, estimates of F_{max} were obtained by fitting AMF propagation and absorption models to soil P concentration and fungal density measurements assuming hyphal radius to be 5 μm for all hyphae. Our direct estimate $F_{max} = 3\,\mathrm{ng \cdot mm^{-2} \cdot h^{-1}}$ closely matches the one from those earlier studies, although they overestimated the hyphal radius which probably led to an underestimation of F_{max}.

We also found that the decrease in P_{agar} was associated with a proportional increase in the amount of P in the root P_{root}. We also verified that the amount of P in the root agar was not significantly changing meaning that all the increase of P_{root} could be attributed to the symbiosis (Fig. 3.2B). These data suggest that the P absorbed by the fungal colony is being rapidly transferred to the host root, and doesn't remain inside the fungal hyphae. This result was further confirmed by estimates of P concentration in fungal hyphae. If no phosphorus was transferred to the root, approximately 50% of the dry fungal biomass would be phosphorus (SI Fig. 3.9). Yet, the highest observed concentration of phosphorus in AM fungal hyphae is only approximately 4% of its dry weight [12].

Overall, our results suggest that: (1) the rate of P absorption by the colony can be approximated by $\Phi_{P,abs} = F_{max} S(t)$ at sufficiently early time and at our high concentration of P; (2) most of the P absorbed by the colony $\Phi_{P,abs}$ was transferred to the root; (3) the rate of P transfer from the fungal colony to the root host $\Phi_{P,trans}$ could well be approximated by $\Phi_{P,trans} = \Phi_{P,abs}$. In other words, the rate of P transfer to the root can directly be obtained by measuring total fungal surface area from images.

3.3.4 Simultaneous quantification reveals proportionality between C used for growth and P supply to the plant

We then asked if there was a relationship between the rate of phosphorous transfer (Φ_P) and the rate of carbon expenditure by the fungus (Φ_C). We found that these two rates were linearly correlated with a slope of approximately 3 Carbon for 1 Phosphorous (Fig.3.4A). A correlation between these two quantities is expected since both the rate of biovolume growth and the total surface area are growing over time. In addition, we found that the slope of the correlation did not differ between the different fungal strains (Fig.3.4B) despite wide variation in carbon density of the colony d_{carbon} and

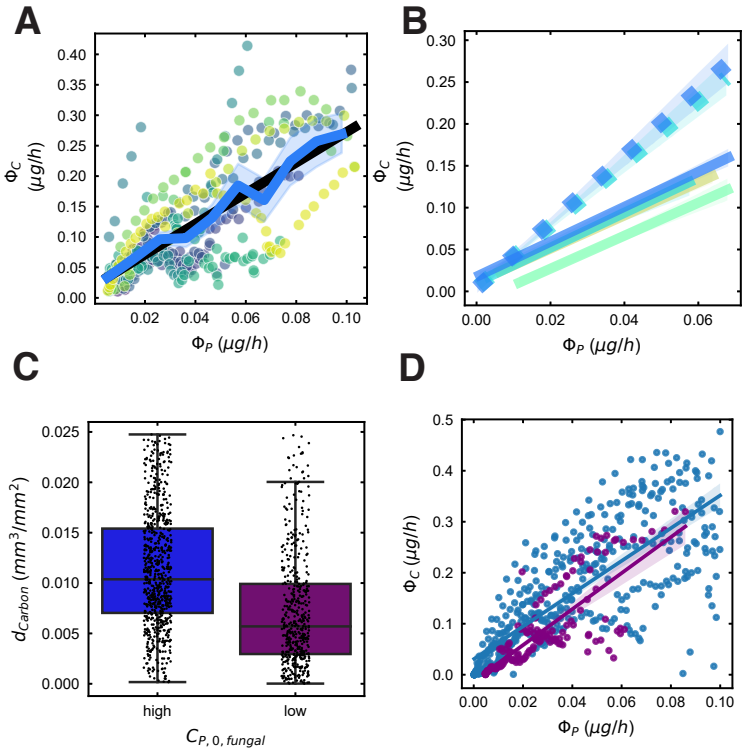

Figure 3.4: **Carbon expenditure and Phosphorous proportionality across treatments. (A), (B), (D)** Carbon expenditure rate (φ_C) as a function of Phosphorous acquisition rate (φ_P). **(A)** *R. irregularis* strain C2 with genotype 2 carrot root. Each point corresponds to a measurement of φ_C and φ_P at one timestep for one replicate, each replicate is shown in a different colour. Blue line shade corresponds to binned average 95% C.I. over regular φ_P intervals. Black line corresponds to linear fit over the blue points.**(B)** For *R. irregularis* A5 (cyan; $n_{\text{genotype 1}} = 8$, $n_{\text{genotype 2}} = 6$),C2 (blue; $n_{\text{genotype 1}} = 19$,$n_{\text{genotype 2}} = 11$), *G. aggregatum* (green, $n = 4$), *G. Clarum* (orange, $n = 4$) associated with genotype 2 (dashed line) and genotype 1 (full line). *R. irregularis* C3 is not shown because its sparsity did not allow to to fully establish the proportionality. Lines correspond to linear fit as obtained in (A), shades to the 95% C.I. of the linear fit obtained via bootstrapping. **(C)** Instantaneous carbon density (d_{carbon}) at high ($1.4\mu g/mL$) and low ($0.6\mu g/mL$) available phosphorous concentrations in the fungal compartment for *R. irregularis* C2 grown with genotype 2 carrot root. Each point corresponds to a measurement of d_{carbon} at one timestep for one replicate. The box represents the interquartile range (IQR), with the central line indicating the median. The whiskers extend from the box to the minimum and maximum values within 1.5 times the IQR. Number of replicates in the high and low P treatment are respectively 11 and 6. **(D)** φ_C as a function of φ_P for *R. irregularis* strain C2 colonies grown at high (blue) and low (purple) P concentrations. Lines and points are as in **(A)**.

its propagation speed v_{wave} (Fig. 3.2A, SI Fig 3.8). We also observed that the root identity could strongly affect this relationship (Fig.3.4B). When grown with root genotype 2, in both fungal strain A5 and C2, the proportionality coefficient between Φ_P and Φ_C increased compared to genotype 1. The two fungal strains however still had the same coefficient of proportionality despite the fact that their traits significantly differed (SI Fig. 3.8). Collectively, our results suggest that there is a consistent correlation between the rate of carbon transfer by the plant and the rate of phosphorus transfer from the fungus (i.e., reciprocal exchange), and this correlation remains constant across different strains but can vary between host roots.

Lastly, we altered phosphorus availability, to see if the correlation between the rate of carbon transfer and the rate of phosphorus transfer was held consistent, even under low phosphorus conditions. Our hypothesis was that, because of the lower P availability, the fungal ability to invest C would be limited. It would therefore either decrease its fungal carbon density or its propagation speed. We decreased the amount of P available to the fungal colony by about half and found that the fungal density was significantly reduced as expected (Fig.3.4C). However, we observed that the wave speed was not strongly affected by the change in P concentration (SI Fig. 3.8). This change in the travelling wave parameters could likely be explained by the fact that the lower P availability reduced the rate of P absorption. We therefore adapted expression (2) to account for a concentration dependence of P absorption (Method).

$$\Phi_P = F_{max} S(t) \frac{[P]}{[P] + K_m} \tag{3.3.4}$$

Using this new formulation, we asked if the relationship between Φ_P and Φ_C was affected by the change in concentration. We found that the slope of the correlation (slope = 3 C/P) was equivalent to the slope of the correlation under higher P concentration (Fig.3.4D).

The ratio of $\simeq$ 3 C/P observed in Fig.3.4A, B, D also directly suggests that the flux of carbon in one direction and of phosphorus in the other are of similar orders of magnitudes which directly calls for the need for bidirectional transport and more generally for advanced ways of routing resources within the network. The latter interest in transport is even further prompted by the comparison of mass of phosphorus absorbed by the network throughout its growth and the mass of the network itself (SI Fig. 3.9) that suggest that the network would need to flush its own mass of phosphorus towards the root in a few days.

Our data support the hypothesis that the rate of C provision by the root host is roughly proportional to Φ_P, regardless of fungal strain, host or environmental conditions. This supports a conceptual model of resource exchange in which: (1) at all times, the rate of C provision by the root host is proportional to Φ_P; (2) at all times, the fungal colony is investing all the carbon available in growth.

3.3.5 P absorption shape colony growth and symbiotic outcome

Can this conceptual model of resource exchange quantitatively explain the speed-density trade-off, as well as the context dependence of plant response to different AM strains? Building on previous work on the propagation of fungal colonies, we implemented a partial differential equation version of this conceptual model (method). In short, based on the above observations, we assumed the wave speed was a fixed parameter of a strain-root association. We also proposed that faster

expanding strains would have to pay extra cost per unit hyphal length built. This can be justified by introducing some cost of transport in the colony [13]. Faster expanding strains must transport carbon from the plant over longer distances. The observation that faster expanding strains tend to invest more in wider hyphae that are more costly (Fig. 3.1E) is consistent with the idea that fast expansion would come at a higher carbon cost. We therefore introduce a drag parameter γ that represents the importance of the extra carbon costs of fast expansion. When $\gamma = 0$ there is no extra cost while when $\gamma = 1$, the extra cost grows linearly with the expansion speed. We finally proposed that the fungal colony would dynamically adapt its branching frequency to match the proportionality between the rate of phosphorous transfer (Φ_P) and the rate of carbon expenditure by the fungus (Φ_C).

To test our model, we parameterised it with data from our strains and examined the predicated patterns of growth. We observed that slower strains (Fig. 3.5A, left) were predicted to grow denser than the faster ones (Fig. 3.5A, right). Consistent with our previous finding about fungal travelling waves, the colony propagated in space at a fixed speed (Fig. 3.5B). The rate of phosphorous transfer (Φ_P) and the rate of carbon expenditure by the fungus (Φ_C) were indeed maintained proportional (Fig. 3.5C) thanks to the dynamically evolving value of the branching rate α (Fig. 3.5D). The model also yields consistent predictions concerning the decrease in fungal density at lower P availability (SI Fig. 3.10). Using a realistic parametrization, our model also recapitulated quantitatively the exploration-exploitation trade-off, predicting the range of variation of saturation densities (Fig. 3.5E).

What is the functional significance of the exploration-exploitation trade-off, and can it explain some of the context dependence of the AM symbiosis? To answer this question, we simulated the growth of fungal colonies of varying wave speed at different initial P concentration $[P]_0$. We found the colony providing the highest average rate of phosphorous transfer (Φ_P) depended on $[P]_0$ (Fig. 3.5F). Specifically, at higher $[P]_0$, the slowest colonies that invest in dense growth without paying extra transport costs can better capture the available P. In contrast, at low $[P]_0$, faster colony can better escape their self-generated depletion zone leading to an overall better ability to capture P (Fig. 3.5A, bottom panels). There is then an optimal propagation speed at each initial concentration of phosphorous $[P]_0$ (Fig. 3.5F).

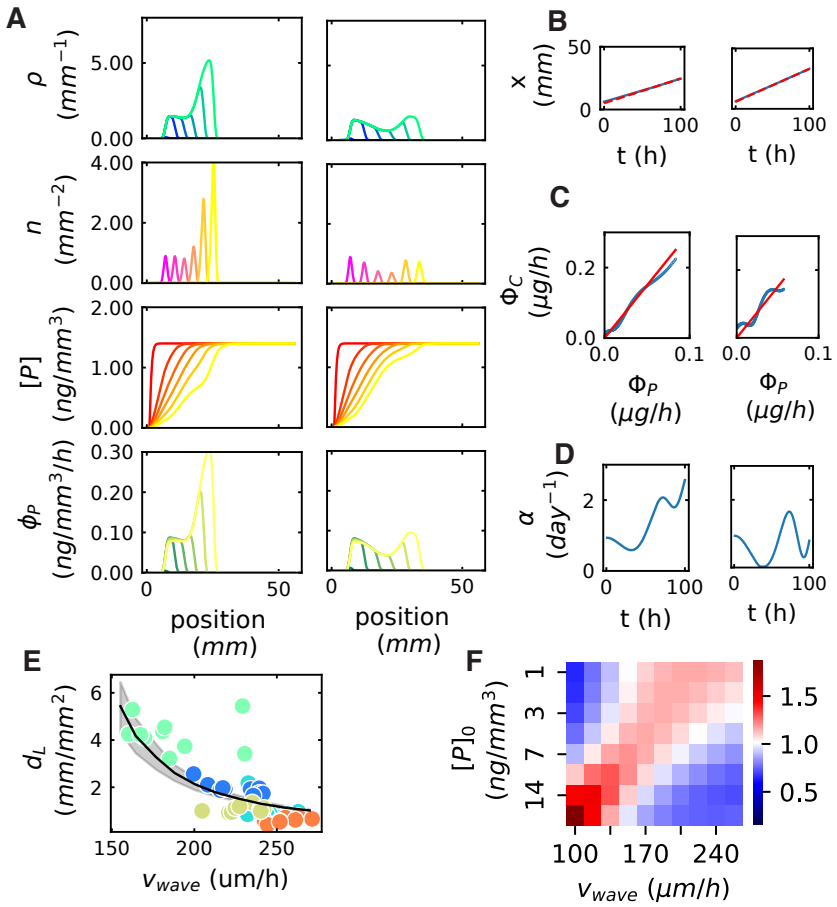

Figure 3.5: **Numerical simulations of model at varying wave speed. (A)** Model integration with $v_0 = 170\mu$m/h. (left) Model integration with for $v_0 = 260\mu$m/h (right): Colors gradients correspond to sampling at regular time interval from $t = 0$h to $t = 100$h. **(B)** Position of the peak of tip density over time. Blue line is the result from model integration. Red dashed line corresponds to a linear fit which slopes give the speed of the wave. **(C)** φ_C as a function of φ_P. Red line corresponds to $\varphi_C = \pi_0\varphi_P$, blue line corresponds to model outputs. **(D)** α as a function of time. For **(B)**, **(C)** and **(D)** left and right are as in **(A)**. **(E)** Model prediction versus experimental observations. Each small circle corresponds to an independent median of hyphal length density d_L and wave speed v_{wave} over 10 hours for one plate. Black line link the mean density observed at final timestep of PDE simulations using v_{wave} as a colony growth parameter. Black shade corresponds to 95% C.I. of spatial density profile observed at final timestep **(F)** P absorption advantage as a function of wave speed v_{wave} and initial concentration C_0. Colour corresponds to the relative increase in P absorption compared to the average of the line for a given concentration. Integration parameters are detailed in (Method 3.6.9)

.

3.4 Discussion

Our high-resolution growth data has shown the importance of fungal spatial dynamics for reciprocal resource exchange patterns. Specifically: (1) colony growth is constrained by resource exchange, such that carbon can only be obtained by trading P; (2) a network's ability to obtain P from the environment is determined by its past growth. The potential of a fungal network to absorb P increases with its total surface area laid down in region of not-yet depleted P.

Our results suggest that the optimal fungal growth strategy depends upon the availability of P in the soil. At low P, the whole P pool is rapidly depleted and cannot be refilled by slow diffusion, then only the faster expanding colonies will be able to escape their self-generated P depletion zone rapidly enough. In contrast, at high P, investment in hyphal surface area production can be privileged over spatial expansion. Because slow expansion allows to avoid extra carbon cost associated with fast expansion (long range transport, lower carbon use efficiency), the slower colonies are able to provide P to their host plant at a higher rate. Differences across different fungal strains therefore appear to represent growth strategies that are optimised to different environments rather than different degrees of cheating.

It is difficult for a fungal colony to effectively probe the surrounding P concentration. In soils, the P dissolved in water solution only represents a small fraction of the total P pool. When dissolved P is absorbed by the fungus from the water phase, it is quickly replaced by exchangeable P adsorbed on soil particles. The P concentration in the liquid phase as "seen" by the fungus represents 0.5-1% of the total P that can rapidly desorb from the soil solid phase[14, 15]. The lack of information about total P has can be read out from the liquid phase concentration justifies the existence of different strategies.

Our work shows the significance of the coupled spatial dynamics of fungal colonies and phosphorous. This is important for both design and interpretation of AM related ecological studies. When designing an experiment, it is important to note that spatial dynamics of networks will differently affect the outcome if plants are regularly and uniformly fertilized versus if the initial concentration is set and unchanged. When observing two fungal densities at a final timepoint and a set point in space, one may observe one fungal strain being denser than another. But this does not straightforwardly means that the denser strain necessarily cost more carbon or provided more phosphorous, only the integrated spatial dynamics can yield such a statement.

Our findings and model can help build experimentally testable hypothesis. For example, at high P availability, slower colonies should proportionally provide more P to their host plant compared to faster ones, while the inverse should be true at low $[P]_0$. In previous pot experiments with full plants in different P fertilization treatments it was found that *R. irregularis* did provide more P to the host plant than *G. aggregatum* with the difference between the two strains becoming insignificant with higher P fertilization [16]. However, fertilization was provided uniformly at regular time intervals which, as pointed out above, limits the spatial dynamics effect discussed in this paper.

Our data cannot rule out other more complex conceptual models of reciprocal resource exchange, especially under natural conditions in which AM fungi have been shown to provide a diversity of other benefits. It is however remarkable that we found a constant of proportionality as in principle, many growth dynamics could lead to the rate of phosphorous transfer (Φ_P) and the rate of carbon expenditure by the fungus (Φ_C) not being proportional to each other, or to the proportionality relationship to differ between strains grown with the same root. This is further highlighted by

the fact that changing the root host is sufficient to obtain significantly different proportionality relationships.

Our work also shows the functional significance of hyphal radius to understand resource exchange. At first approximation, as far as resource absorption is concerned, thinner structures are preferable. Indeed, the cost of a hypha grows as a square of its radius. Its ability to absorb nutrients from the environment grows linearly. In other terms for a hypha of radius r, if we call ξ the cost of the hypha and η its absorption potential, we have $\xi \propto r^2$ and $\eta \propto r$. Minimizing the absorption costs inherently leads to minimizing the ratio $\eta/\xi = 1/r$. This minimization objective tends to reduce hyphal radius. This principle is well illustrated by the fact that root hairs and AM fungal hyphae tend to be a lot thinner than roots. Even among fungal hyphae the absorptive Branched Absorbing Structures tend to be thinner (Fig. 3.1C). However, the observation that hyphal radius varies over time and space, highlights the fact, that optimizing the absorption cost is not the only optimization objective. The observation that faster developing colonies tend to invest more in thicker hyphae (Fig. 3.1E) suggests that fast colony propagation requires investment in thick runner hyphae to allow the transport of carbon to the colony margin and the transfer of P back to the root host. The constraint induced by the necessity of transport inside the colony is a clear avenue for future investigation.

Our result provide a simplified vision of AM symbiosis as the propagation of a hyphal density wave that can absorb phosphorous from the environment. The propagation of the wave is constrained by trade with the host plant and must satisfy at all time the proportionality between the carbon cost of new growth and the P absorption from the already existing network of filaments. This leaves only the wave speed as a free parameter describing the fungal strategy. Variation in that one parameters together with the initial P concentration distribution already yields a wide range of potential outcome to the symbiosis. It is a first order contribution that does not exclude other potentially advanced cheating or cooperating strategies.

3.5 Contributions

This work was done more independently than chapter 2. I had the initial idea of the paper structure. I wrote the large majority of the code, all the text and designed figures with exceptions that are presented below.

Figures

All the work presented here is my work.

Text

All the work presented here is my work. Main text benefited from active contribution and feedback from Stuart West and Toby Kiers.

Data acquisition

As for chapter 2, I participated in plate maintenance. For the data shown in this chapter, I performed plate harvest (root weighing and phosphorus measurements) myself with the help of

Rob Broekman.

Methods

- The model used for radius estimation was the work of Felix Kahane and Kai-Kai Lin performed during their internship under my supervision. It benefited from further contributions of Antoine Babu, which internship I also supervised who labeled additional edges to help creating the test dataset and show explicitly hyphal radius widening.
- The ability to plot full network with color coded edge is the work of Felix Kahane.
- The method used to measure P concentration in our plate was initially put in plate by Constanza Madriaga with the help of Loreto Oyarte Galvez

Ideas

- The modelling framework for P dynamics took inspiration from the work of Andrea Schnepf.
- The considerations about how a growing fungal colony must be consuming energy/lipid was inspired by work of Mark Fricker and Luke Heaton

3.6 Method

3.6.1 Sample Preparation

Plate Preparation

General Recipe We used modified Strullu-Romand (MSR) medium[17] solidified with (3g/L) Phytagel and 10g/L sucrose (Carl Roth). The MSR medium in this study contained final concentrations of 739 mg/L $MgSO_4.7H_2O$, 76 mg/L KNO_3, 65 mg/L KCl, 4.1 mg/L KH_2PO_4, 359 mg/L $Ca(NO_3)_2.4H_2O$, 0.9 mg calcium pantothenate, 1 μg/L biotin, 1 mg/L nicotinic acid, 0.9 mg/L pyridoxine, 0.4 mg/L cyanocobalamin, 3 mg/L glycine, 50 mg/L myo-inositol, 1.6 mg/L NaFeEDTA, 2.45 mg/L $MnSO_4.4H_2O$, 0.28 mg/L $ZnSO_4.7H_2O$, 1.85 mg/L H_3BO_3, 0.22 mg/L $CuSO_4.4.5H_2O$, 2.4 μg/L $Na_2MoO_4.2H_2O$, and 34 μg/L $(NH_4)Mo_7O_{24}.4H_2O$.

In the root compartment, the phosphate content of the medium was reduced to 1% of the above-mentioned concentration (41 μg/L KH_2PO_4) to stimulate mycorrhizal colonization of the roots. In the fungal compartment, we applied either a High P treatment using the full MSR medium as described above, or a Low P treatment in which KH_2PO_4 was removed entirely.

Low and High P Treatment We adjusted the phosphorus content in the MSR to create a Low P and High P treatment. For the Low P treatment, we excluded KH_2PO_4 from the medium. Phytagel, the gelling agent used in this study, however also contains P in a concentration we cannot change. In preliminary experiments, we estimated the concentration of P in the phytagel to be 27 μmol/g. The fungal compartment was composed of 28mL of MSR medium. Based on the above concentrations, this means the fungal compartment contained 96 μg P in the high P treatment and 70 μg P in the low P treatment corresponding respectively to respective concentrations of 3.4 μg/mL and 2.5 μg/mL.

We observed that the concentration of P in the root compartment did not seem to significantly decrease over time (Fig 3b). Also, observations over longer timescales ($\geq$ 10 days) showed that the concentration in the fungal compartment seemed to plateau around similar but slightly higher value as the root P concentration after its initial decrease. P is known to be bound/adsorbed by soluble aluminum, iron, and manganese at low pH[18]. pH in our plate was around 5 meaning that potentially a large proportion of the P we could measure was in fact not available to the plant or fungus. The slightly lower plateau concentration in the root compartment could be due to a change in pH due to the root presence. Based on measurement of root compartment plateau P concentration and fungal compartment plateau concentration at time $\geq$ 10 days, we estimated that 2 μg/mL of P were inaccessible. 0 concentration of P as shown in therefore correspond to 0 concentration "seen" by fungus and root but 2 μg/mL of P measured with our method. Concentration "seen" by the fungus are therefore 1.4 μg/mL in the high P treatment and 0.6 μg/mL in the low P treatment.

Assembly of Mesh Frames Frames were designed slightly trapezoid to fit next to the central barrier of two-compartment split plates (Greiner Bio-One) with a longer top edge (88 mm) than bottom edge (85.5 mm), and a consistent height (12 mm). They include a central opening (50 x 2 mm) distanced 2 mm from the top edge. This opening connects to the upper edge of the central barrier of the plate, therefore extending the central barrier at the outsides of the plates. The fungus could cross through the opening into the second compartment. To slow down the root from crossing over, the opening was covered with nylon mesh.

Acrylic frames were cut using a laser cutter. Nylon mesh (pore size 50 μm, 9 x 71 mm) was attached to the acrylic frame using UV resin in such a manner that the frame opening was fully covered by the mesh and free of resin. The resin was cured with UV light for 3 min, the frames then wrapped in aluminum foil and sterilized at 80°C for 72 hours.

Two-compartment Split Plate Preparation In a laminar airflow hood, one compartment of a sterile two-compartment split plate (94 mm diameter, Greiner Bio-One) was filled with 28 ml MSR medium. An autoclaved sheet of cellophane (Hoefer™ TE73, semi-circle with trapezoidal overhang at the straight edge) was placed on top of the solidified medium and the cellophane overhang was folded into the empty second compartment. A custom acrylic frame was inserted into the empty compartment, securing the cellophane overhang between the acrylic frame, central barrier, and the bottom of the plate. To avoid dislocation of cellophane and/or frame, 5 ml 1%P MSR was poured into the second compartment to immobilize the components. The compartment was then filled to a total of 25 ml 1%P MSR.

Inoculation In a laminar airflow hood, 2-3 cm of in vitro Ri T-DNA transformed root were transferred to the split plate compartment not covered by cellophane ('root compartment'). A circular plug containing only mycelium and spores was cut from the AMF stock plate (2-6 months). Roots were carefully removed if necessary. The inoculation plug was placed on top of the root, covering not more than half of the root. The plates were sealed with parafilm and stored horizontally and upright in an incubator at 25°C.

Plate Maintenance Plates were controlled regularly for fungal and root growth. Any root crossing from the root compartment into the cellophane-cover fungal compartment were pulled back or removed.

Fungal and Plant Strains Used

Fungal Strain All experiments were performed with *Rhizophaghus irregularis* strains A5, C2, C3 (Ian Sanders' lab, Lausanne, Switzerland), *Glomus aggregatum* and *G. clarum* (Ian Sanders' lab, Lausanne, Switzerland). All AMF were cultivated on regular MSR medium associated with Ri T-DNA transformed carrot root for 2-6 months until plates were fully colonized.

Root Strain All experiments were performed with two different root organ culture of Ri T-DNA transformed carrot root. Ri T-DNA transformed carrot root "EU" (referred to as as genotype 1 in main text) originated from a lab in Europe and exact genetic background information cannot be traced back. Ri T-DNA transformed carrot root "CA" (referred to as as genotype 2 in main text) originated from Canadian Collection of Arbuscular Mycorrhizal Fungi and was derived from Clone P68.

3.6.2 Phosphorus Measurements

See 2.6.5.

3.6.3 Timelapse imaging and network segmentation

See 2.6.1 and 2.6.2. Important to note that the rate of false negative tends to be higher for very thin edges especially when focus conditions are not ideal. Such an effect was however estimated to be of small magnitude for most strains. In the case of G. aggregatum, a higher proportion of very thin edges were not detected. However, such thin edges contribute less in proportion to total surface area or biovolume which means this bias doesn't affect our main results significantly.

3.6.4 High resolution imaging

See 2.6.9. The objective used was 50x instead of 100x but the rest of the system was identical.

3.6.5 Estimation of hyphal radius from low resolution imagess

Label dataset generation

Fungal networks grown in normal conditions (see 3.6.1) were imaged in the timelapse imaging system (see 2.6.1). Right after a round of imaging, we transferred the plates to the high-resolution imaging microscope. We then imaged in high resolution different position of the network and recorded their network position. The focus was made to position the optical plane in the centre of the hypha. This was done on the basis that the cell wall should look thinnest and the moving interior should be the widest. The whole operation was done in less than 2 hours. Images were then labelled using the software `labelme`. We drew three lines across the hypha that would span its whole external diameter. This external diameter included the hyphal cell wall. The person labelling had previous experience changing the focus of the imaging system and could therefore establish with little ambiguity what part of the imaged hypha corresponded to the interior moving part and what part should be attributed to the dark thick cell wall. In general the dark thick cell wall would never contribute more than 10-20% of the total diameter which is in line with previous estimates of hyphal cell wall thickness for AMF[19]. For each hyphal segment, we assigned the diameter corresponding

to the mean of the three measurements. By repeating several independent measurements along several edges on these high resolution image, we estimated the standard deviation of the manual estimate to be of 0.3μm. This variation was either due to the difference in appreciation of the exact boundaries of the hyphae on the high resolution image or to effective biological variation of the hyphal radius along an edge in a single field of view.

Feature dataset generation

The networks were segmented and skeletonized (see 2.6.2). For each edge that had been imaged in higher magnification and labelled, we manually identified the corresponding edge of the network. Transects perpendicular to the skeleton and of size 120 pixels were generated with the function `profile_line` of the package `skimage` [20]. We selected the transect that was the closest to the position of the labelled image to use as a feature.

Data augmentation

For part of the dataset, we varied the focus over 0.1 to 0.2mm above and below the "optimal focus" for images and varied illumination. Each label from high magnification was therefore associated with multiple features corresponding to the different focus. In some other datasets, we extracted multiple transects close to the high magnification labelled image and associated them with the same label. This data augmentation procedure was done to help the model generalize over different focus and illumination settings. We also added transect corresponding to regions of the image empty of any hypha and a zero radius corresponding values in order to limit the overestimation of thinner hyphae.

CNN Model

Final dataset The final dataset, following data augmentation consisted of 3182 elements, which were divided into training, validation, and testing sets. Specifically, 90% of the data (approximately 2,546 samples) was used for training and validation, while the remaining 10% was kept for final testing, resulting in 292 samples for the test set. The test set consisted in a combination from entirely independent timesteps and plates from the rest of the dataset. This means, none of the data corresponding to the plate at that timestep was "seen" during training and completely new plates were included in this test set. We resampled the test set so it would follow the same distribution as the training set and comparison of errors would be comparable. To do so, we calculated the frequency distribution over 20 bins of the training set and sampled with replacement from the full test set. The distributions of the training/validation and resampled test sets are shown in SI Fig. 3.6A,C. Values ranged from 0 to 8 in both cases.

Hyperparameter tuning We used keras Bayesian Optimization tuner to explore the hyperparameter space. We set the max number of trials to 20 and the number of initial points to 50. The following parameters were adapted.

Convolutional Layers

- Number of Convolutional Layers: Ranges from 1 to 4. The default setting is 2. This determines how many convolutional layers will be added to the model.

- Filters: For each convolutional layer, the number of filters can range from 32 to 256, with a step of 32.
- Kernel Size: The kernel size for each convolutional layer is selectable in a range from 10 to 20 with a step of one. This range was specifically chosen to allow the different hyphal shape to be within the receptive field of the kernel.
- Regularization: Applies L1 regularization on the kernel, activity, and bias with a logarithmic range from 1e-5 to 1e-1 for each, allowing the model to potentially reduce overfitting by penalizing large weights.

Pooling Layers

- Pooling: Can be "MaxPooling" (MP), "AveragePooling" (AP), or "No pool". This choice dictates whether to downsample the feature maps and by which method.
- Pooling Size and Padding: For "MP" or "AP", the pooling layer's size ranges from 1 to 4 with step 1, and padding can be either 'valid' or 'same', impacting the downsampling behavior and the spatial dimensions of the output.

Batch Normalization

- Inclusion: A boolean indicating whether a Batch Normalization layer is added, aimed at stabilizing and accelerating training by normalizing the inputs of activation functions.

Dropout

- Rate: Applied after each dense layer, with a range from 0 to 0.5 in steps of 0.1. This is used to prevent overfitting by randomly setting a fraction of input units to 0 at each update during training.

Dense Layers

- Number of Dense Layers: Ranges from 1 to 4, with a default of 2. This defines how many fully connected layers are added towards the end of the model.
- Units in Dense Layers: For each dense layer, the number of units can range from 8 to 256, with a step of 32. This determines the dimensionality of the layer's output space.

Learning Rate

- Learning Rate: Used by the Adam optimizer, with a logarithmic range from 1e-5 to 1e-1. The learning rate is crucial for controlling the rate at which model weights are updated during training.

Through Bayesian Optimization, these hyperparameters are systematically explored to identify the combination that results in the best performance on the validation set, as measured by the mean absolute error metric.

3.6.6 Architecture

Our final model, implemented using the `Keras` framework, is a sequential convolutional neural network designed for processing one-dimensional data. The architecture is summarized as follows:

- Input Rescaling Layer: The first layer is a Rescaling layer that normalizes the input data. Convolutional Layers:
- The first convolutional layer (`conv_1`) consists of 128 filters with a kernel size of 20 and a stride of 1. It employs the ReLU (Rectified Linear Unit) activation function to introduce non-linearities. This layer is configured with L1 kernel regularization to prevent overfitting by encouraging sparsity in the learned features.
- The second convolutional layer (`conv_2`) also has 128 filters but with a kernel size of 11, maintaining a stride of 1 and using the ReLU activation function. Similar to the first convolutional layer, it includes L1 kernel regularization.
- Batch Normalization: Following the convolutional layers, a Batch Normalization layer is employed to stabilize and accelerate the learning process. This layer normalizes the activations of the previous layer at each batch, maintaining the mean activation close to 0 and the activation standard deviation close to 1.

Dropout Layers:

- The first dropout layer is applied after batch normalization with a dropout rate of 20%. It randomly sets a fraction of input units to 0 at each update during training, which helps in preventing overfitting.
- The second dropout layer follows the first dense layer, with a slightly higher dropout rate of 30%, providing further regularization.
- Flattening Layer: A Flatten layer is used to convert the two-dimensional output of the preceding layers into a one-dimensional array, making it suitable for input into the dense layers. Dense Layers:
- A dense layer with 232 units follows, employing the ReLU activation function. This layer, like the convolutional layers, uses L1 regularization for both kernel and bias. The final output layer has a single unit with a linear activation function, suitable for regression tasks or binary classification.

The total trainable parameters of the model amount to 2,886,097, with an additional 256 non-trainable parameters, leading to a total of 2,886,353 parameters. This architecture is designed to effectively capture the complex patterns in one-dimensional input data, balancing the need for model expressiveness and the risk of overfitting through careful regularization and dropout strategies.

Training

Final Training Procedure The model was trained using the Adam optimizer with an initial learning rate of 1e-4. The loss function used was mean squared error on the difference between radius squared. We made this choice to avoid underestimation of high radiuses that represented a small proportion of the dataset. The batch size for training was set at 32, and the model was trained for a maximum of 120 epochs. During training, an EarlyStopping callback was employed to prevent overfitting. This callback monitored the validation mean absolute error, with a patience of 20 epochs and a minimum delta of 1e-3 for the first training phase. After the initial training phase, the learning rate was reduced in two subsequent phases to fine-tune the model: In the second phase, the learning rate was set to 1e-5 with the same batch size and number of epochs. The

EarlyStopping callback's patience was reduced to 10 epochs. In the third phase, the learning rate was further reduced to 1e-6, retaining the same batch size, number of epochs, and EarlyStopping configuration as in the second phase. This stepwise reduction in the learning rate is a form of learning rate annealing, which helps in fine-tuning the model parameters and potentially improving the model's performance on the validation set.

Evaluation

Independent Test Set Evaluation We reserved an independent test set for final evaluation. The model was trained on the entire training set using the final model and learning rates optimized through hyperparameter tuning. It was then used to make predictions on the test set. The performance was assessed using the same RMSE and R^2 metrics.

Comparison with Linear Regression To benchmark the performance of our neural network model, we compared its results with those from a simple linear regression model. The linear regression model was trained on the same training set and evaluated on the same independent test set. The performance metrics (RMSE and R^2) were calculated in the same manner as for the neural network model.

Results

- The null model consisting in taking the average of the training set and using it as a prediction yielded a RMSE of 1.5μm on the resampled test set.
- The linear regression model, used as a baseline, yielded an RMSE of 0.79μm and an R^2 of 0.58 on the resampled test set. The neural network model demonstrated a RMSE of 0.67μm and a R^2 of 0.78 on validation set.
- On the independent resampled test set, the neural network model achieved an RMSE of 0.70 μm and an R^2 of 0.66.
- The distribution of residuals on the training and test sets show that large radius may tend to be underestimated, and smaller radius overestimated. (SI Fig.3.6 B,D).

These results indicate that:

- The neural networks does better than the baseline and the simple linear model
- The RMSE of 0.76 on the test set means that the model predicts a radius value with a 95% confidence interval of +-1.5 μm.
- This error is quite large compared to the typical values of radius. But two points need taking into consideration. When estimating total hyphal surface and volume as it is done in this publication, if radius measurements are (i) independent and (ii) unbiased, error should cancel out. This means that even a large error on radius extraction will translate only in a small relative error on total hyphal surface or biovolume. (i) is justified by the fact that each hyphal radius measurement is taken (ii) is not entirely justified given the uneven distribution of residuals, but we can estimate the overall impact of such systematic error.

- The estimated standard deviation of our manual hyphal radius measurement was 0.3μm. This is about 2 times smaller than the RMSE on the test set, which means the neural network is not so far from the maximum precision it could achieve.
- During prediction, multiple transects are used for each edge, and the median of the predicted radius for these transects is used as the edge radius. This tend to mitigate error at the edge level.

Estimating integrated error We estimated the impact of all sources of error (uneven distribution of error along the radius spectrum and quadratic error accumulation) by resampling our radius estimates adding a noise model corresponding to the test set radius dependent RMSE (SI Fig.3.6D). We specifically divided radiuses in 8 classes from 0 to 8μm. Then for each edge, we calculated its radius as predicted by the model and added an error sample from the residual distribution for that class (assumed gaussian with mean and standard deviation obtained from the test set data). We followed this procedure on 38 mature networks and found that the total biovolume estimate was affected by a few percent (always inferior to 8%, average 5%). We therefore decided to ignore this source of error in subsequent calculations of 95% confidence interval. The biological variability is indeed of larger amplitude than the uncertainty of biovolume extraction due to imperfect radius extraction.

3.6.7 Carbon cost and phosphorous absorption calculations

Carbon

Total Colony Carbon For a given edge e, of length L as measured by segmentation (see 2.6.3), and radius r as estimated with the CNN model (see 3.6.5), we approximated each edge to be a cylinder and therefore its volume V to be $V = \pi r^2 L$.

Given the active transport observed in fungal hyphae, they can hardly be seen as passive tubes empty of cell material. Hyphae must therefore be seen as "living cells". The mass of a cell is composed by the summed weight of proteins, RNA, DNA, lipids etc... Together they generally account for 30% of the cell mass. The rest being water. All these organic molecules have a fixed ratio of carbon in mass that is generally around 50% [21].

We used this reasoning to estimate the total carbon in each edge assuming fixed ratios true for most biological material. The first one is the ratio of dry mass to wet mass p_{dry} which is generally estimated to be 21% for fungi [22]. The second one is the ratio of carbon in dry mass p_{carbon} that we set to 50% [21]. The third element is the cell density d_{cell} which is generally estimated to be around 1.1 g/cm^3 [22]. Such ratio could theoretically be expected to be different for AMF. They could also differ between edges and within the phylogeny. But these "living cells" averages are a good first-order approximation.

The mass of carbon in each edge is therefore:

$$m_C = V d_{cell} p_{dry} p_{carbon}$$

We followed a similar principle to compute the mass of carbon in each spore. We first computed the volume of each spore from its radius estimated with classical image analysis techniques (2.6.2).

Given the lack of spore specific ratios, we used the same ones as for hyphae. The limitations of such an approach are discussed below.

Total colony carbon $M_C(t)$ was computed by summing the volume of all individual edges composing the network and all the spores at each point in time (see 2.6.6).

Carbon Density To compute the carbon density, we calculated the change in area ΔA and in total colony carbon ΔM_C over a time interval Δt. The carbon density was then defined as:

$$\rho_C = \frac{\Delta M_C}{\Delta A}$$

In the case of Fig. 3.2A we choose $\Delta t = 10h$.

Carbon Investment Flux Carbon investment flux was defined as:

$$\Phi_C = \frac{\Delta M_C}{\Delta t} \times \frac{1}{CUE}$$

where CUE is the carbon use efficiency i.e. the proportion of carbon incorporated in biomass and not respired of all the carbon used. We used an average CUE for soil microorganisms of 50% [23]. It is important to note that CUE reported in the literature can encompass variable definitions and measurement methods. We didn't find any specific estimates for Arbuscular Mycorrhizal Fungi that would match our criteria. In nutrient poor Boreal forests, CUE of ectomycorrhizal fungi (EMF) was found to vary between 3 and 15% [24]. We however expect AMF CUE to be significantly higher since, on the contrary to EMF, they invest no carbon in substrate decomposition. While our estimate of CUE for AMF is uncertain, it is important to note that it does not affect the main conclusion of the paper since a different CUE, if it is not strain specific, will not break the observed proportionality between P absorption by AMF and C use but simply change the proportionality factor.

Limitations

- **Variations in Cell Wall Thickness and Lipid Density:** The estimate above does not consider variations in cell wall thickness or lipid density inside the cells which can vary from hypha to hypha [19, 25]. Further refinements can include such considerations, but we expect the carbon ratio of cells to be close to the one used in this study.
- **Maintenance Cost, Carbon Recycling, and Spores:** At the timescale considered (4-5 days) we considered that some more complex carbon dynamics could be neglected. All the different possible carbon costs for a growing fungal colony are nicely summarized and quantified in [13].
    - ⋆ First, we neglected the carbon cost associated with cell maintenance. This cost, although of smaller magnitude, is proportional to total network length, while the cost associated with growth is proportional to the derivative of the total length. It has been estimated for fungi that the time over which the metabolic cost of maintaining a fungal volume is equal to the number of joules embodied in that volume was about 30 days for fungi [13]. At the timescale considered it is therefore valid to consider the maintenance cost negligible.

- ⋆ We also neglected the cost associated with transport of resources within the colony. This was motivated by the following calculation. Assuming all the cytoplasm is moving at $v_0 = 3\mu m$ in $L = 1m$ of colony of radius $R = 3\mu m$. The hydraulic resistance associated with the colony is $R_h = \frac{8\mu L}{\pi R^4}$ where $\mu = 1g.m^{-1}.s^{-1}$ is the viscosity of the cytoplasm and the flux through the pipe is $\Phi \approx \pi R^2 v_0$. The energy dissipation power is then of the order of $P_{transport} = R_h \Phi^2 = 8\pi\mu L v_0^2$ which does not depend on R. We can therefore evaluate that $P_{transport} = 226 \times 10^{-15} W \approx 0.2 \times 10^{-6} \mu W$. In comparison, we estimate that the growing colonies can consume $\phi_C \approx 0.2\mu g/h$ of carbon. This carbon is in the form of lipids/palmitic acid which energy density is about $d_E = 37MJ/kg$. The Power requirement for growth can therefore be estimated to $P_{growth} = d_E \phi_C \approx 2\mu W$. At first approximation, the energetic cost of transport therefore seems negligible compared to the energetic cost of growth.
- ⋆ Fungi can also recycle cell material. To generate the dataset used for machine learning, we sampled multiple positions in the fungal network over several days. At the timescale considered, we didn't observe hyphal cytoplasm retracting except for thin Branched Absorbing Structures (BAS) around the end of that timescale. It was previously estimated that full BAS lifecycle consisted in 7 days for formation followed by 5 weeks until full retraction [19]. Our observation of BAS lifecycle to be somewhat faster than this (some hyphae starting to retract after just 5 days). Interestingly the timescale of BAS retraction seems to coincide with the one of P depletion. We however decided not to include this effect in our calculation since 1) BAS constitute 30% of total hyphal length (see 2.4) but are thinner than the rest of the hyphae. We expect they constitute no more than 10-15% of total hyphal volume 2) While some BAS could indeed start to retract over a similar timescale as the one of our experiments, it was clearly not the case for most of them, so we expect the overall amount of recycling to be negligible at the timescales considered.
- ⋆ Finally, while spores are expected to hold more carbon since they are meant to store carbon, we didn't use spore specific ratios to compute total network carbon. At the timescales considered, spores only constitute a small fraction of total volume. We therefore expect this inaccuracy to be negligible.

- **Carbon investment flux in the root compartment:** We're not observing the hyphal growth in the root compartment. It is however likely that, because phosphorous is already depleted in that compartment (see 3.6.7), the hyphal growth is also negligible.

Phosphorous Absorption

Total Network Surface For a given edge, its surface is defined assuming a cylindrical shape $s = 2\pi r L$. To get the total surface of the network we summed the surfaces of all edges.

Figure 4D We first estimated that the initial concentration in the low P treatment was 0.6 $\mu g/mL$ (see 3.6.1). We then divided the plate in 18 regions over 4 rows from the bottom of the plate. In each region, we estimated automatically the total fungal surface area. In each region the absorption rate was proportional to the total surface area until the concentration of P reached 0. Then it was set to 0. The total colony absorption rate was the sum of the absorption rate in all the regions. In this approach the concentration-absorption rate curve is a step function that goes

directly to 0 at 0 concentration. This is because (i) the 8mm thick agar acts as a buffer (ii) K_m is thought to be very small compared to $[P]$ over the range of value considered (except 0) (see 3.6.8). Therefore, the transition time from a regime where P absorption is simply proportional to surface area to a regime where it becomes proportional to $[P]$ is below the timescales of our sampling rate. In the second regime, it becomes quickly negligible compared to other absorption rates in other regions. We neglected diffusion for a similar reason, because of the agar buffer, diffusion from one region to another was negligible because concentration in the agar at one point in space remained close to the initial concentration at all time until it dropped directly to 0 making the diffusion fluxes negligible compared to the absorption fluxes.

Limitations

- **BAS and Runner Hyphae:** Estimates of structure specific expression of P absorption genes showed higher relative expression of P-transporters in BAS [26]. The normalisation is however done on volume and not surface, and it is unclear from these results whether the transporter density on the surface of BAS hyphae should be considered higher. We therefore decided not to make any distinction between different hyphal structures beyond their radii.
- **Hyphal Septation:** As explained in 3.6.7, at the timescales considered, we decided not to consider the possibility that some subpart of the hyphal network could retract and septate and therefore not contribute to P absorption.
- **Root compartment absorption:** We only observe hyphae present in the fungal compartment (upper half). However, hyphae that could be absorbing phosphorous can also be present in the root compartment. We do not account for those in our estimates. This is however justified by the fact that at the moment where hyphae are crossing in the fungal compartment, phosphorous is generally already depleted in the root compartment (see Fig.3.3 and 2.6.5).

3.6.8 Supplementary discussion on modelling P absorption

The general formula for absorption of a solute by an AMF colony growing on agar is given by the following:

$$\frac{d[P]}{dt} = -\tilde{F}_{max} s(t) \frac{[P]}{[P] + K_m} \tag{3.6.1}$$

Where $s(t)$ is the total surface area of the colony divided by the total volume of agar, $[P]$ represents the concentration of P in solution, $\tilde{F}_{max}$ is a constant representing the maximal influx rate into mycorrhizal hyphae and K_m is the Michaelis-Menten constant of mycorrhizhal hyphae.

In our experiment, the fungal colony is experiencing an initial concentration $[P]_0 = 1.4\mu g/mL$ which is well above the typical Michaelis-Menten constant for plant root cells ($K_m = 0.17\mu g/mL$) which itself is considered to be superior to the one of AM hyphae [14].

For $[P] \gg K_m$ we have $\frac{[P]}{[P]+K_m} \approx 1$ and the equation for P concentration simplifies to $\frac{d[P]}{dt} = -\tilde{F}_{max} s(t)$. Using the notations from main text, $F_{max} = \tilde{F}_{max}$

In addition to this effect, although the P concentration in the agar is relatively low, the fact that the fungal colony is constrained to 2d growth means that the $\approx 9mm$ thick agar acts as a buffer.

Similarly to 2.7.2, we can represent that buffer effect by including a buffer power parameter $b_p = 9mm$ which we can use to rewrite 3.6.1 as

$$\frac{d[P]}{dt} = -\tilde{F}_{max}\frac{\sigma(t)}{b_p}\frac{[P]}{[P]+K_m}$$

where $\sigma(t)$ is the 2d hyphal surface area density. The later can be rewritten as

$$\frac{d[P]_s}{dt} = -\tilde{F}_{max}\sigma(t)\frac{[P]_s/b_p}{[P]_s/b_p+K_m} \tag{3.6.2}$$

where $[P]_s = b_p[P]$ represents the surface concentration of P.

Small variations in surface concentration of P are then damped by the buffer. It is correct to consider that as long as variation in surface concentration remain inferior to $K_m b_p$ then $\frac{[P]_s/b_p}{[P]_s/b_p+K_m} \approx cste$ and we can rewrite

$$\frac{d[P]_s}{dt} = -F_{max}\sigma(t)$$

where $F_{max} = \tilde{F}_{max}\frac{[P]_s/b_p}{[P]_s/b_p+K_m}$. Which itself can be rewritten as

$$\frac{dP_{agar}}{dt} = -F_{max}S(t) \tag{3.6.3}$$

where $S(t)$ is the total surface area of the colony.

In conclusion, in both the case (i) $[P] \gg K_m$ and (ii) $K_m b_p \gg \Delta[P]_s$ it is correct to write the depletion of P in the form of equation 3.6.3.

Another consideration from equation 3.6.2 is the fact that because of the buffer, the transition to the regime where using equation 3.6.3 is incorrect is steep and is is a reasonably good approximation to consider that then $[P] \approx 0$. The final consideration is the fact that the diffusion of the surface P concentration is also slowed down by the buffer effect and it is correct within our agar plate to consider it negligible.

High and Low P modelling of absorption In the high P treatment ($1.4\mu g/mL$), the surface concentration $[P]_s$ is typically of the order of $11ng/mm^2$. The highest surface density of length for R. irregularis A5 is of the order of $1.5mm/mm^2$ which for an average radius of $3\mu m$ (Fig. 3.1) corresponds to a surface density of hyphal surface area of $\sigma =\approx 0.03$. Considering our measured $F_{max} = 3ng.mm^{-2}.h^{-1}$, the typical time of depletion is $\Delta t \approx 120h$ which justifies our choice of neglecting the effect of depletion in the high P treatment since all data shown corresponded at max to the first 100 hours of growth.

In the low P treatment ($0.6\mu g/mL$), the typical depletion time was 50 hours and the effect of depletion could not be ignored which explains why the additional P concentration dependence was added. Due to the buffer effect of the agar thickness, that dependence was later simplified to a bimodal system with $\frac{[P]_s/b_p}{[P]_s/b_p+K_m}$ equal either to 0 or 1 for the precision of our measurement and our time resolution.

3.6.9 Model of colony propagation with feedback

Model equations

General Framework The general framework is the same as explained in 2.7.2 and 2.7.2

Carbon Cost and Colony P Absorption By integrating over space, we can define the colony P absorption per unit length flux as:

$$\Phi_P(t) = \iint \phi_P(t) = \iint s\frac{V_{max}[P]}{[P]+K_m}dV.$$

At any point in time and space, the amount of carbon used for colony growth is proportional to the amount of newly built biovolume. Newly built length is $\frac{\partial \rho}{\partial t}$ and newly built biovolume is then $\pi r^2 \frac{\partial \rho}{\partial t}$ with r an effective radius computed as the square root of the length-weighted average cross-section. The proportionality factor M_C between this newly built biovolume and the amount of carbon used is the product of four parameters: cell density d_{cell}, the ratio of dry to wet mass p_{dry}, the ratio of carbon in dry mass p_{Carbon}, and the inverse of carbon use efficiency $\frac{1}{1-p_{respired}}$ so that

$$M_C = \frac{d_{cell}p_{dry}p_{Carbon}}{1-p_{respired}}.$$

By integration over space, we can define the colony carbon building cost Φ_C as

$$\Phi_C(t) = \iint \phi_C(t) = \iint M_C \pi r^2 \frac{\partial \rho}{\partial t}dV.$$

Expressions for $b(n,\rho)$ and $a(n,\rho)$ As in 2.7.2, we set $b(n) = \alpha n$, with α the branching rate per unit time and $a(n,\rho) = \beta n \rho$ with β an anastomosis rate parameter.

Price driven adaptation The ratio $\pi(t) = \frac{\Phi_C(t)}{\Phi_P(t)}$ is the instantaneous "price" of Phosphorous in carbon units. We assume that the colony adapts its growth parameter to match an average objective price π_0. Specifically, we assumed that the branching rate α is changing over time in order to reach the objective. This is motivated by the fact that branching in fungi is thought to be the consequence of vesicle accumulation at the tips beyond a maximum threshold. In other terms, when the supply of vesicles exceeds their capacity to be incorporated into the existing tip, they accumulate leading to the formation of a new tip [27]. Assuming carbon availability is the limiting factor for vesicle production, it is therefore possible that AM adapt to shortage or abundance of carbon by adapting their branching rate. Since the saturation density is a growing function of α, at a fixed propagation speed, increasing Φ_C tends to increase together with α. We therefore assumed that, when the average recent "price" $\bar{\pi}(t_0) = \frac{1}{\Delta T}\int_{t_0-\Delta t}^{t0} \pi(t)dt$ overshoots π_0, α is reduced. Such an integral formulation was chosen to damp oscillatory behaviour due to adaption of branching rate overshooting the objective price and we chose $\Delta t = 10h$.

We added one last closing equation to the system:

$$\frac{d\alpha}{dt} = k_2 \left(1 - \frac{\bar{\pi}}{\pi_0}\right). \tag{4}$$

With k_2 a rate parameter homogeneous to the inverse of time squared. k_2 can be chosen to be time dependent in order to maximize the reaching of the price objective. Such a form is entirely subject to a number of hypotheses. The main conclusions of the research are however not affected by the specific form of the adaptation as long as it allows the price to match the ideal price on average (Fig. 3.5C).

Accounting for radius differences We observed that slower growing colonies tended to have smaller effective mean radius r_{eff} (Fig. 3.1E). This suggests that the hyphal radius r used for model integration should also vary with speed. The sparse nature of the data (only 5 strains/species sampled throughout the phylogeny) makes it difficult to give a precise functional form to this dependence. Given that $\pi(t) \propto r$, we decided to implement this difference by multiplying $\pi(t)$ by a factor $\left(\frac{v}{v_0}\right)^{\gamma}$ with v_0 an average speed $v_0 = 250\mu m/h$ and γ a parameter indicating the strength of the effect. $\gamma = 0$ corresponds to the first order approximation that radius does not depend on the speed while higher γ corresponds to stronger dependence. Under that form, it is homogeneous to a "drag" factor which sets that faster growing colonies will tend to pay more metabolic cost per unit growth. This is analogous to the general idea that microbes will tend to have a higher carbon use efficiency at slower growth rate in a resource rich environment where maintenance costs are negligible. The "drag" factor can finally be seen as representing a transport cost within the colony, faster colonies having to pay a higher price (as is represented by their higher average radius) because they must transport more matter on longer distances. We generally chose $\gamma = 1$ to quantitatively reproduce our experimental results as shown in Fig. 3.5. As seen in Fig. 3.1E and Fig. 3.2A, while slower *G. Aggregatum* that grow at $v \approx 170\mu m/h$ have an mean effective radius $r_{agg} = 2.5\mu m$, the faster *R. irregularis* A5 have a growth speed $v \approx v_0 = 250\mu m/h$ and a mean effective radius $r_{A5} = 3\mu m$. The extra price of *R. irregularis* A5 hyphae is $\left(\frac{r_{A5}}{r_{agg}}\right)^2 \approx 1.5 \approx \frac{v_0}{v}$. With $\gamma = 0$, slower growing colonies will always provide less P than faster growing ones.

The effect of change in radius distribution on P absorption was considered negligible and we didn't account for it. Indeed, while the change in mean biovolume effective radius (corresponding to the square root of the mean length-weighted cross sectional area) is significant, the change in the mean surface area effective radius (mean length-wieghted radius) is smaller (≈ 1.2 factor between the smallest and largest one).

Model integration

Model integration is the same as explained in 2.7.4.

General model parameters We chose $J(n) = -nv_d\hat{\mathbf{r}} + D\nabla n$ and parameters $\alpha = 0.039$ h^{-1}, $\beta = 22\mu$m/h and $D = 0.00008$ mm^2/h so that $v_d \approx v_{\text{wave}}$ and we could more easily vary wave speed.

P absorption parameters chosen were $r = 3\mu$m for the average hyphal radius as shown in Fig. 3.1. Change in hyphal radius accross strains was accounted for with the γ parameter (see 3.6.9). We

chose $V_{\max} = 3.25 \times 10^{-3} \mu g \cdot mm^{-2} \cdot h^{-1}$ as found Fig. 3.3 and $K_m = 1 \times 10^{-3} \mu mol/cm^3$ as proposed by [14], and $D_P = 10^{-5} cm^2/s$ which is the diffusion coefficient of a small ion in water.

Figure 3.5A-E and SI Figure 3.10 In those figures, the goal was to reproduce the conditions of the fungal agar plate. We therefore chose a semi 2d embedding where tip and hyphal densities were expressed per unit area and the full agar depth was represented using a buffer parameter b_p (see 3.6.8). The concentration of phosphorous was chosen to correspond to the one in the agar.

Initial condition were $\rho(r,0) = 0$, $n(r,0) = n_{max} e^{-\lambda/(r-r_0)^2}$ where $n_{max} = 0.3mm^{-1}$, $\lambda = 0.2mm^{-1}$ and $r_0 = 7mm$ and $[P](r,0) = [P]_0(1 - e^{-\lambda_2(r-r_0^{(P)})})$ where $\lambda_2 = 0.1mm^{-1}$ and $r_0^{(P)} = 1mm$.

We chose $\pi_0 = 3$, $k_2(t) = k_2(0)\frac{t}{\tau}$ with $tau = 50h$ and $k_2(0) = 8 \times 10^{-3} h^{-2}$ and $b_p = 8.8mm = \frac{28mL}{\pi(4.5cm)^2}$ (see 3.6.1).

Space was divided in a mesh of 262 cells from 0 to $56mm$ and time was divided in 200 elements from 0 to $100h$.

For Figure 3.5A-E we chose $[P]_0 = 1.4\mu g/mL$ and varied v_d as shown in the legend and figure axis. For SI Figure 3.10 we chose $v_d = 200\mu m/h$ and we varied $[P]_0$ from $0.3\mu g/mL$ to $1.5\mu g/mL$

Figure 5F In this figure, the goals was to reproduce the conditions of a real soil to discuss the impact of the difference in spatial dynamics on P absorption and trade, we therefore chose a 3d embedding with cylindrical symmetry.

Initial condition were $\rho(r,0) = 0$, $n(r,0) = n_{max} e^{-\lambda/(r-r_0)^2}$ where $n_{max} = 1mm^{-1}$, $\lambda = 0.1mm^{-1}$ and $r_0 = 7mm$ and $[P](r,0) = [P]_0(1 - e^{-\lambda_2(r-r_0^{(P)})})$ where $\lambda_2 = 0.1mm^{-1}$ and $r_0^{(P)} = 1mm$.

We chose, $k_2(t) = k_2(0)\frac{t}{\tau}$ with $tau = 50h$ and $k_2(0) = 8 \times 10^{-2} h^{-2}$ and $b_p = 239$.

We varied v_d over the interval $[100\mu m/h, 260\mu m/h]$ sampling uniformly 10 times. We varied $[P]_0$ over the interval $[1\mu g/mL, 20\mu g/mL]$ sampling over a logarithmic scale 10 times. Because we varied $[P]_0$ over such a large interval, we decided to adapt slighlty π_0 so colonies could still develop when P was very scarce. We chose $\pi_0 = 2\left(\frac{[P]_0^{(0)}}{[P]_0}\right)^{1.2}$. This was necessary to keep fungal density to stay within reasonable bounds over the timescale observed, too high a price at high P concentration leading to exploding densities and too low price at low P concentration leading to vanishing densities. This is also reasonable since, although we did not observe it within the limited range of P concentration value of our experiment, the price could in theory be adapting to the availability of phosphorous.

Space was divided in a mesh of 393 cells from 0 to $84mm$ and time was divided in 400 elements from 0 to 200.

3.7 Supplementary Figures

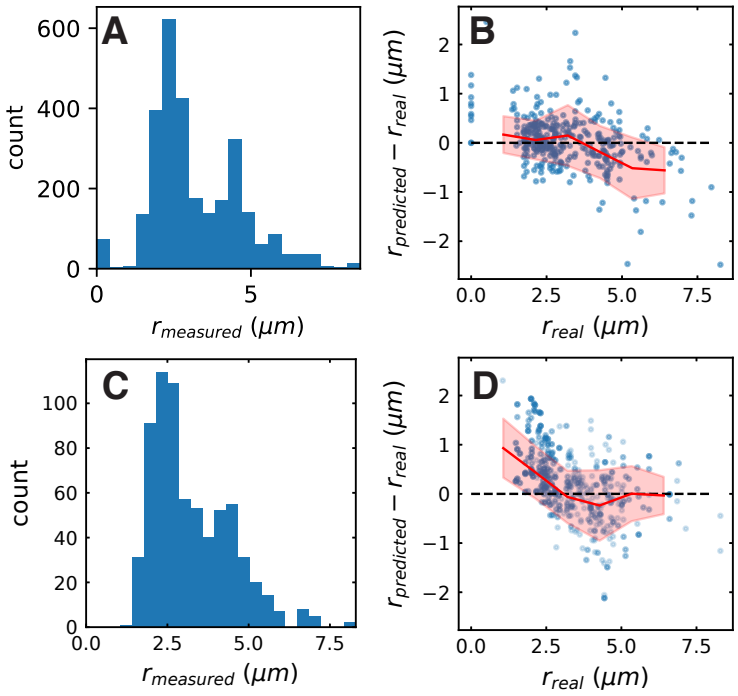

Figure 3.6: **Training and test set distribution and model performance on validation and test sets.** (**A**) Training + validation set distribution. (**B**) Residual of the model prediction on the validation set. (**C**) Test set distribution after resampling. (**D**) Residuals of the model prediction on the resampled test set. For (**B**) and (**D**), blue points correspond to individual predictions from the set. Radiuses were separated in 8 classes from 0 to 8µm. For each class, the mean residual and the standard deviation were computed. Red line links the mean residual for each class and red shade shows the 95% C.I. for each class (mean ± 2 × s.e.m.).

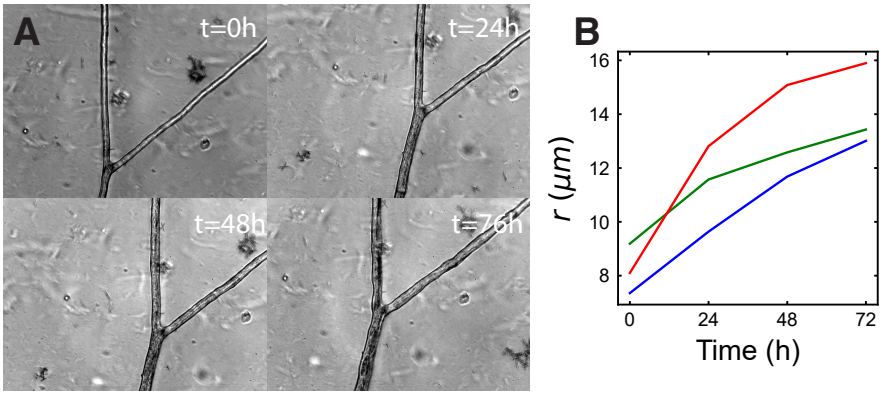

Figure 3.7: **High resolution imaging shows hyphal widening. (A)** High resolution images of the same Y-shaped intersection over 4 days. **(B)** Average of measured radius of the three edges of the intersection over time (Bottom : red, upper-left: green, upper-right: blue)

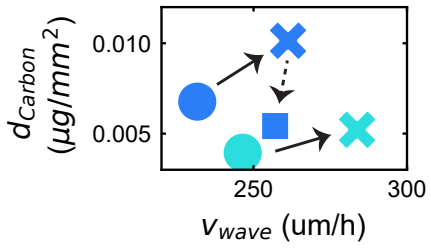

Figure 3.8: **Effect of changing root host and environment on travelling wave parameters.**Travelling wave observables. d_{carbon} represents the instantaneous hyphal carbon density and v_{wave} represents the instantaneous wave speed. Symbols circles are median of those parameters for each strain. Dark blue corresponds to strain C2 and cyan blue to strain A5. Circles correspond to carrot root genotype 1 and high P environment in the fungal compartment, crosses correspond to carrot root genotype 2 and high P environment, square correspond to carrot root genotype 2 and low P environment. Arrows are guide for the eye. Continuous arrow corresponds to a change from genotype 1 to genotype 2, dashed arrow corresponds to a change from high to low P environment.

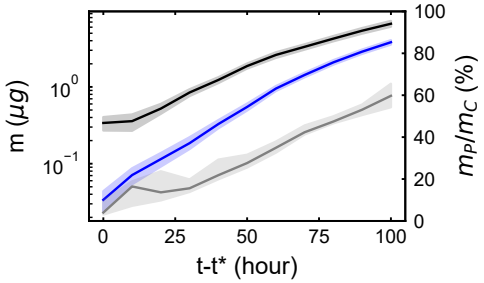

Figure 3.9: **Mass stoichiometry of fungal hyphae under the hypothesis of no transfer to the plant.** Estimates of total carbon mass (black), total absorbed phosphorous mass (blue) and ratio of the two (grey) as a function of time. Absorbed phosphorous mass is estimated from the measured temporal dynamic of network surface area. Thick lines correspond to average of all replicates over 10 hour time intervals, shades correspond to 95% C.I. over the same interval (mean $\pm 2\times$ s.e.m.).

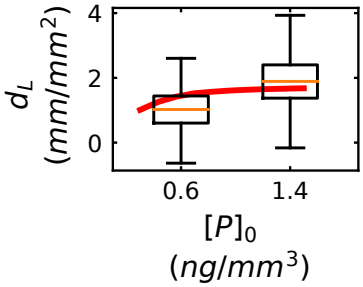

Figure 3.10: **Dependence of fungal density on initial P concentration at a fixed speed.** Boxplot show distribution of hyphal length density in a similar maner as in Fig. 3.4C but the length density d_L is shown instead of the carbon density d_{carbon}. Red line links the mean density observed at final timestep of PDE simulations for varying $[P]_0$ as explained in 3.6.9

.

Bibliography

1. Smith, S. E. & Read, D. J. *Mycorrhizal Symbiosis* en. ISBN: 978-0-08-055934-6 (Academic Press, July 2010).
2. Hawkins, H. J. *et al.* Mycorrhizal mycelium as a global carbon pool. *Current Biology* **33,** R560–R573. ISSN: 0960-9822. http://www.scopus.com/inward/record.url?scp=85160575900&partnerID=8YFLogxK (2023) (June 2023).
3. Pearson, J. N. & Jakobsen, I. Symbiotic exchange of carbon and phosphorus between cucumber and three arbuscular mycorrhizal fungi. en. *New Phytologist* **124,** 481–488. ISSN: 1469-8137. https://onlinelibrary.wiley.com/doi/abs/10.1111/j.1469-8137.1993.tb03839.x (2024) (1993).
4. Smith, S. E., Smith, F. A. & Jakobsen, I. Mycorrhizal Fungi Can Dominate Phosphate Supply to Plants Irrespective of Growth Responses. *Plant Physiology* **133,** 16–20. ISSN: 0032-0889. https://doi.org/10.1104/pp.103.024380 (2023) (Sept. 2003).
5. Lendenmann, M. *et al.* Symbiont identity matters: carbon and phosphorus fluxes between Medicago truncatula and different arbuscular mycorrhizal fungi. en. *Mycorrhiza* **21,** 689–702. ISSN: 1432-1890. https://doi.org/10.1007/s00572-011-0371-5 (2023) (Nov. 2011).
6. Koch, A. M., Antunes, P. M., Maherali, H., Hart, M. M. & Klironomos, J. N. Evolutionary asymmetry in the arbuscular mycorrhizal symbiosis: conservatism in fungal morphology does not predict host plant growth. en. *New Phytologist* **214,** 1330–1337. ISSN: 1469-8137. https://nph.onlinelibrary.wiley.com/doi/abs/10.1111/nph.14465 (2021) (2017).
7. Thonar, C., Schnepf, A., Frossard, E., Roose, T. & Jansa, J. Traits related to differences in function among three arbuscular mycorrhizal fungi. en. *Plant and Soil* **339,** 231–245. ISSN: 1573-5036. https://doi.org/10.1007/s11104-010-0571-3 (2022) (Feb. 2011).
8. Koch, A. M., Croll, D. & Sanders, I. R. Genetic variability in a population of arbuscular mycorrhizal fungi causes variation in plant growth. en. *Ecology Letters* **9,** 103–110. ISSN: 1461-0248. https://onlinelibrary.wiley.com/doi/abs/10.1111/j.1461-0248.2005.00853.x (2020) (2006).
9. Jakobsen, I., Abbott, L. K. & Robson, A. D. External hyphae of vesicular-arbuscular mycorrhizal fungi associated with Trifolium subterraneum L. en. *New Phytologist* **120,** 371–380. ISSN: 1469-8137. https://onlinelibrary.wiley.com/doi/abs/10.1111/j.1469-8137.1992.tb01077.x (2022) (1992).

10. Kiers, E. T. *et al.* Reciprocal Rewards Stabilize Cooperation in the Mycorrhizal Symbiosis. en. *Science* **333,** 880–882. ISSN: 0036-8075, 1095-9203. https://www.science.org/doi/10.1126/science.1208473 (2023) (Aug. 2011).

11. Dodd, J. C., Boddington, C. L., Rodriguez, A., Gonzalez-Chavez, C. & Mansur, I. Mycelium of Arbuscular Mycorrhizal fungi (AMF) from different genera: form, function and detection. en. *Plant and Soil* **226,** 131–151. ISSN: 1573-5036. https://doi.org/10.1023/A:1026574828169 (2024) (Nov. 2000).

12. Hammer, E. C., Pallon, J., Wallander, H. & Olsson, P. A. Tit for tat? A mycorrhizal fungus accumulates phosphorus under low plant carbon availability. *FEMS Microbiology Ecology* **76,** 236–244. ISSN: 0168-6496. https://doi.org/10.1111/j.1574-6941.2011.01043.x (2023) (May 2011).

13. Heaton, L. L. M., Jones, N. S. & Fricker, M. D. Energetic Constraints on Fungal Growth. *The American Naturalist* **187,** E27–E40. ISSN: 0003-0147. https://www.journals.uchicago.edu/doi/full/10.1086/684392 (2021) (Dec. 2015).

14. Schnepf, A. & Roose, T. Modelling the contribution of arbuscular mycorrhizal fungi to plant phosphate uptake. en. *New Phytologist* **171,** 669–682. ISSN: 1469-8137. https://onlinelibrary.wiley.com/doi/abs/10.1111/j.1469-8137.2006.01771.x (2024) (2006).

15. Darrah, P. R. & Staunton, S. A mathematical model of root uptake of cations incorporating root turnover, distribution within the plant, and recycling of absorbed species. en. *European Journal of Soil Science* **51,** 643–653. ISSN: 1365-2389. https://onlinelibrary.wiley.com/doi/abs/10.1046/j.1365-2389.2000.00331.x (2024) (2000).

16. Wang, X., Zhao, S. & Bücking, H. Arbuscular mycorrhizal growth responses are fungal specific but do not differ between soybean genotypes with different phosphate efficiency. *Annals of Botany* **118,** 11–21. ISSN: 0305-7364. https://doi.org/10.1093/aob/mcw074 (2022) (July 2016).

17. Declerck, S., Strullu, D.-G. & Fortin, J. A. *In vitro culture of mycorrhizas* en. *Soil biology* **4.** ISBN: 978-3-540-24027-3 (Springer, Berlin [etc.], 2005).

18. Etesami, H., Jeong, B. R. & Glick, B. R. Contribution of Arbuscular Mycorrhizal Fungi, Phosphate–Solubilizing Bacteria, and Silicon to P Uptake by Plant. *Frontiers in Plant Science* **12.** ISSN: 1664-462X. https://www.frontiersin.org/articles/10.3389/fpls.2021.699618 (2023) (2021).

19. Bago, B., Azcon-Aguilar, C., Goulet, A. & Piche, Y. Branched Absorbing Structures (BAS): A Feature of the Extraradical Mycelium of Symbiotic Arbuscular Mycorrhizal Fungi. *The New Phytologist* **139,** 375–388. ISSN: 0028-646X. https://www.jstor.org/stable/2588307 (2024) (1998).

20. Van Der Walt, S. *et al.* scikit-image: image processing in Python. en. *PeerJ* **2,** e453. ISSN: 2167-8359. https://peerj.com/articles/453 (2023) (June 2014).

21. Bar-On, Y. M., Phillips, R. & Milo, R. The biomass distribution on Earth. en. *Proceedings of the National Academy of Sciences* **115,** 6506–6511. ISSN: 0027-8424, 1091-6490. https://pnas.org/doi/full/10.1073/pnas.1711842115 (2024) (June 2018).

22. Bakken, L. R. & Olsen, R. A. Buoyant densities and dry-matter contents of microorganisms: conversion of a measured biovolume into biomass. eng. *Applied and Environmental Microbiology* **45,** 1188–1195. ISSN: 0099-2240 (Apr. 1983).

23. Manzoni, S., Taylor, P., Richter, A., Porporato, A. & Ågren, G. I. Environmental and stoichiometric controls on microbial carbon-use efficiency in soils. en. *New Phytologist* **196,** 79–91. ISSN: 1469-8137. https://onlinelibrary.wiley.com/doi/abs/10.1111/j.1469-8137.2012.04225.x (2024) (2012).

24. Hagenbo, A. *et al.* Carbon use efficiency of mycorrhizal fungal mycelium increases during the growing season but decreases with forest age across a Pinus sylvestris chronosequence. en. *Journal of Ecology* **107,** 2808–2822. ISSN: 1365-2745. http://besjournals.onlinelibrary.wiley.com/doi/abs/10.1111/1365-2745.13209 (2021) (2019).

25. Bago, B. *et al.* Translocation and Utilization of Fungal Storage Lipid in the Arbuscular Mycorrhizal Symbiosis. *Plant Physiology* **128,** 108–124. ISSN: 0032-0889. https://doi.org/10.1104/pp.010466 (2023) (Jan. 2002).

26. Kameoka, H., Maeda, T., Okuma, N. & Kawaguchi, M. Structure-Specific Regulation of Nutrient Transport and Metabolism in Arbuscular Mycorrhizal Fungi. *Plant and Cell Physiology* **60,** 2272–2281. ISSN: 0032-0781. https://doi.org/10.1093/pcp/pcz122 (2024) (Oct. 2019).

27. Harris, S. D. Branching of fungal hyphae: regulation, mechanisms and comparison with other branching systems. en. *Mycologia* **100,** 823–832. ISSN: 0027-5514, 1557-2536. https://www.tandfonline.com/doi/full/10.3852/08-177 (2024) (Nov. 2008).

Chapter 4

Lipid transport drives bidirectional flows

4.1 Abstract

The plant-mycorrhizal symbiosis is fundamental to terrestrial ecosystems and is responsible large flows of nutrients at the planetary scale. In this symbiosis, two distinct organisms are trading phosphorus (P) against energy in the form of carbon (C). Yet, the mechanism behind the bidirectional transport of ressources within their microscopic hyphae has not been entirely elucidated.We imaged transport dynamics of nutrient flows in high resolution in different position of a growing networks. We find that carbon is most probably moving across the network on an oriented network of molecular motor filaments. Our findings also suggest a tight coupling between network growth, internal carbon (lipid) transport dynamics, and bidirectional fluid movement within the network. The movement of lipid in the closed pipe system inherently produces a backflow of cytoplasmic fluid which may be responsible for the movement of phosphorus. Our model provides a possible explanation to the observed proportionality in resource exchange between the two organisms.

4.2 Introduction

The symbiosis between Arbuscular Mycorrhizal (AM) fungi and their host plants has existed for 400 million years. This requires robust mechanisms to ensure the stability of the symbiosis. Indeed, the symbiosis can be a many to many interactions which means that plant can interact with multiple independent fungal colonies and one fungal network can interact with multiple plant hosts. Without selective orientation of nutrients towards partners that engage in a proportional effort of nutrient provision, plant or fungal "free ride" phenotypes reaping the benefits of the symbiosis while evading the costs may emerge.

The fungal partner forms a network in the soil using plant derived carbon. It absorbs phosphorous that is then transported back to the plant. This means carbon needs to be constantly shipped to the growing edge of the colony away from the plant while phosphorous needs to be transported

back in the other direction. The mechanisms that could explain such bidirectional transport in a network of open pipes is so far unknown.

When a fungal colony is attached to a single plant host, we observed in the past that the fungal use of carbon for growth was proportional to the flux of phosphorous towards the plant (see Chapter 3). In addition, it has been observed in the past that, when a single AM network was connected to two different plant hosts that differed in their carbon supply, more phosphorous was directed toward the plant that provided more carbon [1].

In Chap. 2 we quantified flow speed in both directions in networks of different ages. However, a dye-free approach was used which made it impossible to determine exactly what was moving. Without staining lipids and/or phosphorous, it is difficult to understand the organisation of resource flow across the network and the underpinning mechanisms. Resource specific staining can shed light on the exact distribution of resource flux within the network. Using Nile Red staining, it was found that lipid density could vary along hyphae and reach more than 25% of the hyphal volume[2]. But the mechanism underlying lipid movement is so far unkown.

In Chap. 2 we have also found that flow speed seems to be modulated over time and location within the network. The finding was interpreted through a traffic analogy, and we found correlation between betweenness centrality, a typical transport network metrics, and flow speeds. This correlation however lacked a direct physical underpinning explaining how such a relationship between global metrics and flows could emerge mechanically. Because AM fungi are coenocytic, the colony can be represented as a hydraulic network of connected pipes with varying radii. The hydraulic coupling between all the elements of the network could generate spatial correlation in ways that can be physically framed. Such a mechanical framework for growing AM colonies is still missing.

What mechanisms explain the bidirectional transport of resources in the colony and its modulation over space and time? How can the transport mechanisms in place maintain a form of bidirectional transport in which the magnitude of resource flux in opposite directions are maintained proportional? How can flows of phosphorous be organized to orient preferentially towards the host that provides the most carbon resource?

To answer these questions, we acquired image data at two different spatial and temporal resolutions to quantify flow speed in specific edges of growing networks over multiple days. At high spatial and temporal resolution, we acquired brightfield videos of transport dynamics within single hyphal edges over multiple days. Using Nile red, a neutral lipid specific fluorescent dye, we also characterized and quantified the movement of carbon in those same edges. At a low spatial and temporal resolution, we obtained timelapses of growing networks that were transformed into their equivalent mathematical graph. We asked how this low-resolution observation of network growth could explain mechanistically and quantitatively the high-resolution observations.

4.3 Results

4.3.1 Asymmetric bidirectional speeds

Fungal networks grow through the extension of fungal tips away from the host plant root. Over time, this constructs elongated branched structures called hyphae. Over the length of a hypha, the network's topological context can vary widely (Fig. 4.1a). Near the hyphal tip, the network

is close to a tree with very few loops. As one moves further away from the tip, the number of growing hyphae that depend on the main hyphal branch progressively increases. At the other end of the hypha, the densified networks shows many example of anastomosis (fusion between a hyphal tip and a hyphal segment). This leads to the creation of loops allowing many alternative paths towards the root. We asked how this change in topological context affected the speed observed in the network in the two directions at different point in time. We extracted the speed in both directions.(method, SI Fig.4.5) from 40 flow videos acquired in high resolution along the hyphal transect (SI Fig. 4.7). Those videos were taken over three consecutive days. We observed that the speed towards the tip did not significantly vary in space and time and stayed close to $3\mu m/s$ (Fig. 4.1b). In the tip-to-root direction however, the speed varied between 2 and $6\mu m/s$. In space, however the variation did not seem to be monotonic. While there seemed to be a general tendency for a decrease when getting close to the tip, there was also examples of increasing speed, sometime in abrupt ways (Fig. 4.1c). Over time, there seemed to be a general tendency for the absolute speed in the tip to root direction to increase. In summary, while speed of movement in one direction was mostly constant in space and time, in the other directions we observed much more temporal and spatial variation.

We asked if that asymmetry could be due to the difference in cell components that would be moving in the two directions and therefore their mechanisms of movement. We stained neutral lipids using Nile Red fluorescent dye [3] and imaged the same positions as in brightfield (Fig. 4.1d, upper, SI video 1). We observed that most of the lipid movement seemed to be going in only one direction. This was further confirmed by Fourier filtering of the kymograph[4], which decomposes the raw kymograph into two directional components, one representing the signal moving away from the root and another representing the signal moving towards the root. The fluorescent trace left by lipids moving towards the tip is visibly more intense. These orientationally filtered kymographs also reveal that the movement of lipid results in straight lines of constant intensity. This is indicative of movement of lipid that is persistent. At this temporal and spatial scale, there is no evidence of lipid particles switching direction randomly as in a random walk underlying diffusive motion (Fig. 4.1d, lower). We also observed that lipids were moving at a speed close to $3\mu m/s$ which corresponded to the speed observed in brightfield in that direction. Such filtering finally allowed us to establish the general direction of lipid flux in an automated way in all videos (Methods). We found that in most cases, the net flux of lipid was moving in the direction of the tip (Fig. 4.1e).

We wanted to know how general was the observation that the speed observed in the network were asymmetrically distributed over the two possible directions. In order to assign a direction to each edge of the network, we used the lipid flux direction that we could determine from the fluorescence video. We associated one speed with the speed of particles moving in the same direction as the lipid flux, and the other to the particles moving in the other direction. This procedure was performed on the whole dataset comprising 6 developmental timepoints from 2 different plates and a total of $\sim$ 2000 edges (SI Fig.4.7). We found that the distribution of particle speeds moving in the lipid direction was narrow and peaked around a value of $3\mu m/s$ (Fig. 4.1f). The speed distribution in the other direction was wider with a long tail at higher speed going up to $\sim 8\mu m/s$.

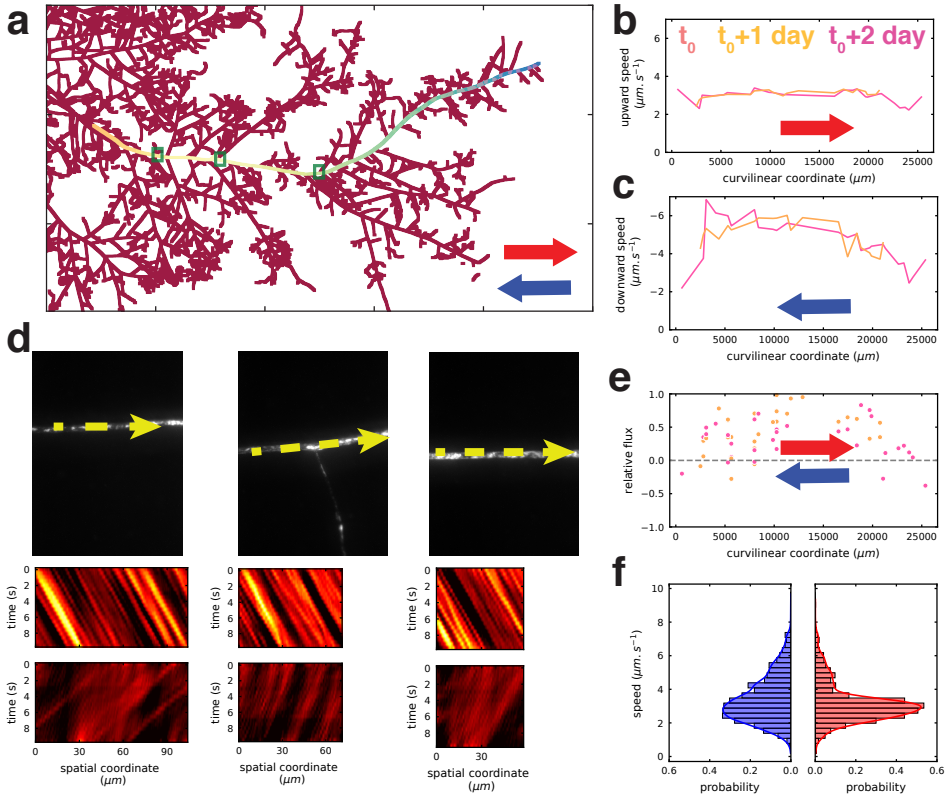

Figure 4.1: **Bidirectional speed and lipid flux over a hyphal transect. (a)** Network graph where a hyphal transect has been highlighted. Green boxes indicate example video position shown in **(d)**. Color gradient along the transect indicates curvilinear abscise. **(b)** and **(c)** Measured speed of particles moving from left to right **(b)** and from right to left **(c)** in brightfield movies at different points along the transect. **(d)** First image of Nile red fluorescence video (top) corresponding to the kymograph (bottom). Yellow arrow indicates the observed direction of the flux. First row of kymograph shows particle moving from left to right while second row of kymograph shows particles moving from right to left as obtained by Fourier filtering (Method). **(e)** Observed relative flux along the transect. Positive relative flux correspond to flux moving from left to right. In **(b)**, **(c)** and **(e)**, different colours correspond to successive timepoints over two days. **(f)** Distribution of speeds observed in brightfield movies in the direction of the lipid flux (red) and in the other direction (blue). Data from all positions where videos in fluorescence were taken was used **(n=1000).**

4.3.2 Lipid transport across the colony

The results presented in the previous section strongly suggested that lipids were moving in a persistent manner at a fixed speed ($\sim 3\mu m/s$) in a global direction that could be characterized as "away from the root" or "toward the tips". However, this description was potentially ambiguous in a network with loops and many different tips growing in different directions at different speed and in different direction. We wanted to characterize more precisely how the growth of different tips could collectively contribute to the movement of lipid. To do so, we represented the growing colony as a temporal graph where each edge has an activation time corresponding to its time of first appearance. We call N the set of all graph nodes and E the set of all graph edges. This allowed the growth between two time steps to be established in a spatially resolved manner (Fig. 4.2a,Method). For each growing node $k \in N$ we could establish the total newly built biovolume from that node ΔV_k . The demand for carbon at each node ΔC_k was proportional to that newly built biovolume.

That carbon had to be supplied from the root compartment. This was represented by adding one additional "source" node to the network which demand we set to a negative value $S_{source} = -\sum_{k\in N} \Delta C_k$. The "source" node was connected to the nodes of the network closest to the plant (see methods) through zero length junctions. In some cases, because of loops created through anastomosis, there were multiple possible paths from the "source" node to a node with non-zero carbon demand. We assumed the flux of carbon would distribute over those paths in a way that minimized a hydraulic-like energy dissipation. We assigned to each edge $(i, j) \in E$ a hydraulic like resistance $D_{i,j}$ associated with energy dissipation, in analogical way to hydraulic resistance we set $D_{i,j} = \frac{8\mu L_{i,j}}{\pi R_{i,j}^4}$ where $L_{i,j}$ is the length of the edge, $R_{i,j}$ is its radius and μ is a viscosity that is treated as a constant in the global energy minimization. With a flux of carbon from i to j $\phi_{i,j}$ the power dissipation is then set as $D_{i,j}\phi_{i,j}^2$. We minimized the objective function $\sum_{(i,j)\in E} D_{i,j}\phi_{i,j}^2$ under the constraint that for all nodes k, $\sum_{i\in N} \phi_{i,k} = \Delta C_k$ (Methods). This allowed us to estimate, in each edge of the network, an expected direction and lower bound of lipid flux required for the observed tip growth (Fig. 4.2b).

We then compared these expected lipid fluxes with the one observed in each edge. We found that in 70% of the cases, the direction of lipid flux could be predicted by our model. This percentage increased to more than 80% when we considered only points in the network where both the modelled and measured absolute flux were high (Fig. 4.2c).

Hyphal extension as shown in Fig. 4.2a, in addition to consuming carbon, is also associated with the creation of new network volume. The corresponding demand for water has been shown to be the mechanism driving flows in colonies of other (non-mycorrhizal) fungal species [5, 6]. In those systems, the movement of matter within the network was well explained by the free movement of water in the network of pipes with set sources and sinks. We wanted to test that hypothesis in our system. Because volume creation and carbon demand are proportional, we used the same approach as for carbon simply replacing the source and sink magnitude ΔC_k with ΔV_k. We kept a similar global source node corresponding to a water reservoir. The calculation in this case yields the exact volumetric flow rate $Q_{i,j}$ in the hydraulic equivalent of the network. The speed $v_{i,j}$ was then set as $v_{i,j} = \frac{Q_{i,j}}{\pi R_{i,j}^2}$. We found that this model failed to explain the speed in the direction predicted by the model (Fig. 4.2d). Such a model also does not explain the existence of fluid movement in the other direction. Indeed, the fluid flow always follows the pressure gradient and can therefore not be bidirectional. Finally, as shown shown in Fig. 4.1b,f and 4.2e, the flow speed in the modelled and

observed direction of lipid flux is narrowly peaked around the value $v_0 = 3\mu m/s$. In addition to not being able to predict a speed of the right order of magnitude, the growth induced mass flow model does not yield such a peaked distribution (Fig. 4.2e). The peaked distribution instead strongly suggests, that the movement of lipid within the AM fungal colony is an active process driven by the movement of molecular motors on tracks walking at fixed speed. Speed of known molecular motors can indeed typically be in the range $2 - 6\mu m/s$ for the faster ones [7]. This hypothesis is further motivated by the qualitative observation that the movement of lipid in the colony follows well established tracks (SI Video 2).

Is moving lipids at such high speed necessary to match supply and demand while avoiding saturating hyphae with lipids? To answer that question, we set the speed of all lipids to be $v_0 = 3\mu m/s$ and used the value of lipid fluxes we estimated from growth data to estimate the lipid volume fraction $\theta_{i,j} = \frac{\phi_{i,j}}{v_0 \pi R_{i,j}^2}$ in each edge of the network required to explain the observed growth. We found that as we moved away from the hyphal tip, that fraction gradually increased over 10mm and reached value as high as 4% (Fig. 4.2f). The decrease further from the tip was due to a decrease in flux which itself was due to the multiplication of alternative paths towards the root when moving closer to it. Similar spatial variation over similar lengthscales has been previously established in *R. irregularis* [8]. However the magnitude of the the maximum volume fraction was estimated in that earlier research to be $\sim 20\%$. This could explain why active transport mechanisms at high speed is necessary to allow expansion of the colony at sufficient rate while avoiding overloading hyphal edges.

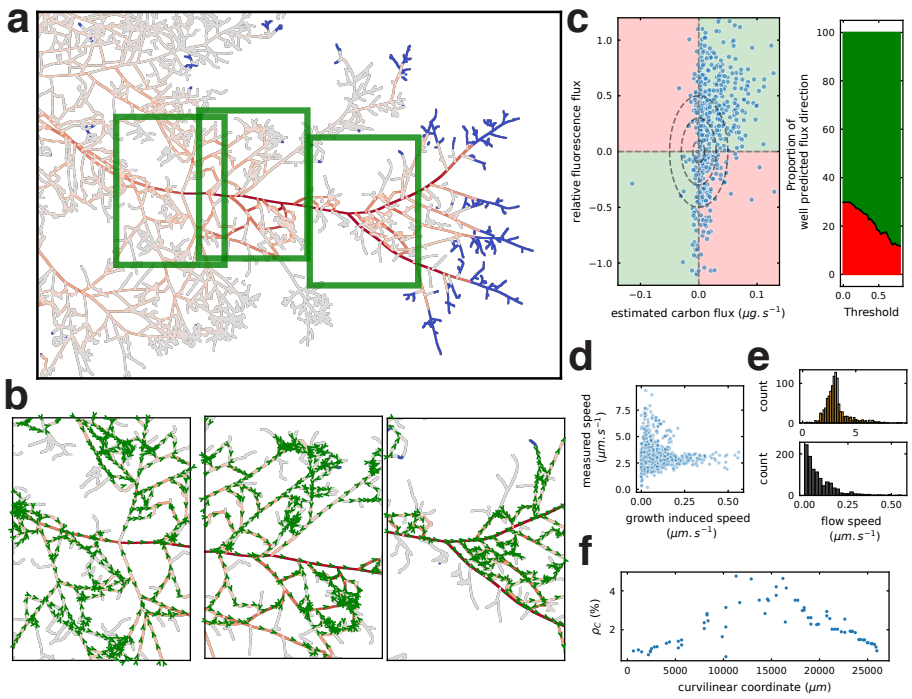

Figure 4.2: **Demand of carbon for growth creates carbon flux at the colony scale** . **(a)** Network graph where regions that have grown between and have been highlighted in blue. Tones of red intensity correspond to the estimated density of lipids in the hyphal volume (see methods). **(b)** Zoom in on regions indicated by green rectangles in **(a)**. Tones of red intensity follow same color mapping as in **(a)**, green arrows correspond to the estimated direction of movement of the lipid flux (see methods). **(c)** Comparison of estimated and observed flux directions. On the left, each blue points corresponds to an observation at one timepoint of one replicate at one position where fluorescence video was taken. Negative and positive carbon flux correspond to left-right orientation as shown in Fig. 4.1. On the right, the proportion of well predicted flux direction of carbon (points in green quadrants) as opposed to ill-predicted flux direction (points in red quadrant) is shown as a function of a threshold corresponding to a weighted distance from the (0,0) coordinate in the right plot. Dashed line ellipses represent the setting of the threshold with increasing values 0.1, 0.3 and 0.5. For a given threshold, only the points outside of the ellipse are kept to compute the proportion of well predicted flux direction. **(d)** Measured speed in the estimated lipid flux direction against estimated growth induced speed (methods). Each point corresponds to one edge of one brightfield movie at one timepoint for one replicate. **(e)** Measured (orange) and growth-induced modelled (black) distribution of speeds in the estimated growth-induced flow direction for brightfield movies across all samples (n=1330). **(f)** Density of lipids in percentage of volume occupation along the curvilinear abscise described in Fig.4.1

.

4.3.3 Lipid generated backflow

Even our estimate of 4% of cytoplasm filled with lipids suggest that a significant proportion of hyphal volume is filled with lipids. Such proportion could easily lead to clogging if all lipids coalesce into a single phase. How is then this large fraction of neutral lipid packaged within the cytoplasm? The minimal unit of lipid packaging is generally thought to be membrane bound lipid droplets. Such lipid droplets are generally kept from coalescing by coating [9]. The ensemble of those lipid droplets can then form an emulsion with a set lipid volume fraction. The emulsion phase, because of the repulsive strength between the different lipid droplets can have different rheological properties than the rest of the cytoplasm [10]. We assume this emulsion is phase-separated from the bulk cytoplasm. We thought this large flux of a lipid emulsion throughout the aseptate mycellium could trigger large movement of cytoplasmic fluid both in the direction of the lipid due to viscous friction, and in the other direction because of the incompressibility of the fluid in the case where no water could flow out of the hyphae. This led us to propose the following conceptual model. Lipid droplets form a water-oil-like emulsion of higher viscosity that coats uniformly the internal surface of the hyphal pipe. We assumed the speed profile across the thickness of the emulsion layer was uniform at v_0, which could be explained by the emulsion having an effective viscosity that is much higher than the bulk cytoplasm. (Fig. 4.3a, upper). The emulsion is made of a volumetric proportion p_{lipid} of lipids and $(1 - p_{lipid})$ of water. This effectively creates an inner pipe where water can freely flow. That inner pipe is of smaller radius R_B and can let a net flow of water B pass through it. By solving the Navier-Stokes equation in the inner pipe, setting boundary conditions to be v_0 at the border of the inner pipe one can determine the radial speed profile $u(r)$ in cylindrical symmetry to be

$$u(r) = v_0 + \frac{2(B - \pi R_B v_0)(R_B^2 - r^2)}{\pi R_B^4} \tag{4.3.1}$$

The flow of water through the inner pipe can be written as:

$$B = \Xi - \pi R^2 \theta \frac{1 - p_{lipid}}{p_{lipid}} v_0 \tag{4.3.2}$$

where Ξ is the net flow of water through the whole pipe. Interestingly, when one assumes $\Xi = 0$ as would be the case in a closed pipe system, we have:

$$u(0) = -v_0 \left(1 + 2\frac{\theta(1 - p_{lipid})}{p_{lipid} - \theta}\right) \tag{4.3.3}$$

This result suggests a possible explanation for the bidirectional movement that we observe. For all values of of θ and p_{lipid}, we have $u(0)$ which is of opposite sign compared to v_0. It also suggests possible explanation for the spatial and temporal variation of speeds. The spatial variation of θ (Fig. 4.2f) indeed directly contributes to the magnitude of the backflow speed.

A direct consequence of such a conceptual model is that a single pipe insulated at both ends where the movement of lipid is maintained will still exhibit bidirectional flows. We therefore isolated a segment of ∼1mm of hypha from the rest of the network by physically cutting the neighbouring edges. Preliminary experiments had shown that severing the hyphae in that way led to a temporary spilling of cytoplasm that quickly stopped because of some physical clotting. A similar clotting

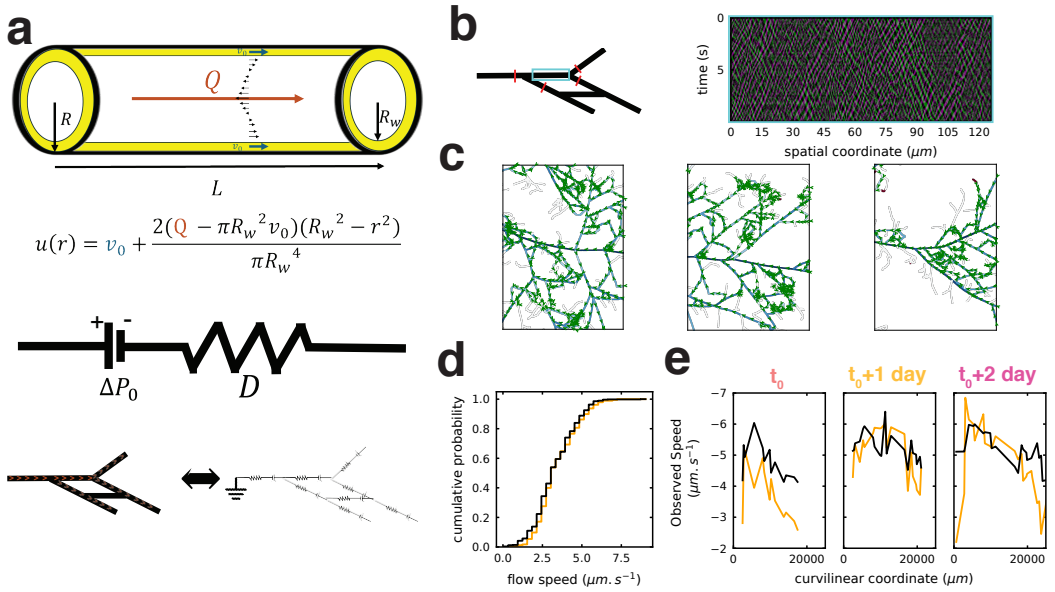

Figure 4.3: **Lipid movement induced backflow.** **(a)** Schematic representation of surface induced backflow in a single pipe of radius . Lipid movement forces speed at the surface to a set speed v_0. If total water flux through the inner pipe of radius R_B is ϕ then the flow profile through the pipe can be obtained by integrating Navier-Stokes equations in cylindrical coordinates with such boundary conditions. The pressure gradient that builds up because of lipid movement can be represented as voltage generator in an electrical equivalent of the pipe. The whole network can then be represented by its hydraulic circuit equivalent. **(b)** (left) Graphical representation of the experiment consisting in separating and individual edge from the rest of the network. (right) Example kymograph in single edges than have been separated from the network by cutting. Lines correspond to moving particles coloured in purple (lipid direction), and green (other direction). **(c)** Zoom in on regions indicated by green rectangles in (Fig. 4.2a). Tones of blue intensity follow speed intensity; red arrows correspond to the estimated direction of movement of the water backflow (see methods). **(d)** Measured (orange) and modelled (black) cumulative probability distribution of speeds in the estimated water flux direction for brightfield movies across all samples (n=1330). **(e)** Measured (orange) and estimated (black) speed in brightfield movies at different points along the transect represented in Fig. 4.1. The three pannels from left to right correspond to successive timepoints.

phenomenon upon hyphal injury was recently reported in another (non-mycorrhizal) fungal species to involve a shear sensitive protein called gellin [11]. We then observed fluid movement inside the isolated edge at high resolution (Fig.4.3b, SI video 3). We found that fluid was still moving and that flow was still bidirectional. Flow speed was of similar magnitude (3μm/s) in both directions. This observation provides further evidence against the idea that a significant proportion of fluid movement could be explained by growth induced mass flow. We indeed observed fluid movement

of similar magnitude than in the full network while our isolated segment did not show any growth. Our model is instead fully compatible with the maintenance of bidirectional fluid movement in the disconnected hypha. According to our model, after cutting, the active entrainment of the lipid suspension phase could be maintained at its fixed speed (3μm/s). Because the isolated hypha is clotted at both ends, it is reasonable to assume that the net water flux through the whole pipe Ξ is zero. Further with the extra assumption that the volume fraction of the lipid suspension is negligible we directly obtain from equation 4.3.3 that speed in the opposite direction should also be maintained and should be close to v_0. Analysis of the kymograph revealed that speed in both directions is indeed close to $3\mu m/s$.

Our conceptual model seemed well validated by the data at an individual pipe level. However, we wanted to know what its consequences would be at the network level. Could it explain the observed variation of speed in space and time? When establishing the speed profile through the pipe, we were also able to derive the pressure gradient along the idealised hyphal pipe. For a pipe of length L the expression for the pressure drop was analogous to an electrical voltage drop where a voltage generator and a resistor would be put in series (Methods). Because fluid movement happens at low Reynold numbers in our system and the entrance length in each individual hyphal pipe is close to its diameter, the approximation of infinite length cylinder we did to derive flow profile in a single pipe is still justified in the network context. A network of connected pipes is then analogous to a network of these individual circuit element (method, Fig. 4.3a, lower).

Such an electrical circuit equivalent of the network can be solved with linear algebra using Kirchkhoff's law at each intersection, and requiring that the sum of pressure drops around loops in the network is zero (Methods). As in the case of growth induced mass flow discussed above in 4.3.2, we set the sink magnitude at each node to correspond to newly created volume ΔV_k and added a global source node. This allowed us to predict in each edge what would be the net volumetric rate of fluid movement Ξ and then the direction and magnitude of flow speed in the inner tube of each edge of the network (Fig. 4.3c). We found that our model capture salient features of the bidirectionality of flow observed across all edges. Speed was larger in those central hyphae where lipid density was also higher which was explained by the larger proportion of the pipe volume occupied by the lipid suspension moving at v_0 and dragging water with it (4.3.3). In the tree-like parts of the network the net volumetric flow of water through the whole pipe Ξ is close to zero because the amplitude of growth induced mass flow is negligible (Fig. 4.2d,e). Then the movement of water in and around the suspension of lipid droplets can only be compensated by faster speeds in the opposite direction in the inner pipe.

Could our conceptual model at the network level explain quantitatively the variation of speeds observed throughout the networks (Fig.4.1f)? To answer that question, we first plotted the cumulative distribution of observed and modelled flow speeds for all edges observed in high magnification (Fig.4.3 d). We found that the model could overall explain well the distribution of speeds from 1.5 to 6 $\mu m/s$. Speeds slower than v_0 were explained by the existence of loops in the network which led to a net circulation of water through some of the pipes going sometime in the same direction as lipid flux. According to equations 4.3.2 and 4.3.1, when Ξ is large enough and positive, B can also be positive and larger than $\pi R_B v_0$ which can lead to absolute speed being lower than v_0. Over the length of a hypha, our model could explain the gradual increase of flow speed when moving away from the tip as well as sudden decrease which seemed to coincide with entering regions with multiple alternative paths due to anastomoses to the root (Fig.4.3e). Our model could also explain the increase of flow speed over time at specific locations (Fig.4.3e).

Our simple physical model can therefore explain a wide variety of our experimental observations. At the single hypha level it provides an explanation for bidirectional fluid flow. At the growing network level, it is compatible with the observed non-trivial spatio-temporal variations in flow speeds. Such a physical explanation of bidirectional transport in AM fungal networks has direct consequences on symbiotic trade. Because it is the movement of lipids that generates the fluid flow in the reverse direction, the proportionality of resource exchange could emerge directly from this physical coupling.

4.3.4 From bidirectional flows to bidirectional trade

To understand the relationship between this mechanism of bidirectional transport and trade, we built a simplified representation of a network connected to two plant host that could differ in their carbon supply. The network consisted of 8 nodes. Each host plant was connected to the network by one edge. The two plants play the role of water reservoirs and therefore are considered to be at equal ground potential in the equivalent circuit. The network is symmetric, and we set an equal carbon demand at two sinks that represent growing tips. (Fig. 4.4a). We then solved the corresponding system of bidirectional flow equations (Methods) for this simplified network to find the distribution of carbon and water fluxes.

We started with the situation in which the carbon supply from the two plants is equal. This is equivalent to the case where a single fungal network is connected to a single plant. We wanted to know whether the lipid movement induced backflow could explain the proportionality of resource exchange. We assumed that the concentration of phosphorous in the water of the inner tube was constant and varied the input carbon flux. We found that, under that assumption, the carbon flux from the plant and the phosphorous flux from the fungal colony were maintained proportional (Fig. 4.4b). To obtain a proportionality factor of $1/3$ $\mu g\mathrm{P}/\mu g\mathrm{C}$, as had been found earlier (see Chapter 3), we had to set the P concentration to $\approx 1.9 mol/L$ which is much larger than the concentration typically found in plant cells of 5-20$mmol/L$[12].

We then asked how the ratio p of the two plants' carbon inputs ϕ_A an ϕ_B defined as $p = \frac{\phi_A}{\phi_A+\phi_B}$ affected the ratio of phosphorous brought back to them. We initially set all the radii of the network hyphae to be equal to $3\mu m$. In this case, we found the plant that provided the least carbon tended to obtain the majority of the phosphorous flux (Fig. 4.4c). This was explained by the circulation of net water flow in the main loop that connected the two plant hosts. The water entrained with the lipids of the plant providing most carbon was circulated back along the path of least resistance. In the edge connected to the plant providing least carbon, the inner radius was maximal because the proportion of the cross section occupied by lipids was minimal. Therefore the effective hydraulic resistance was lower in that edge and the net flow of water went preferentially to that plant. This somewhat counter-intuitive mechanism works against the possibility that the regulation of trade when a fungal colonies is confronted with multiple plant host could be mechanically mediated.

The situation is however different when an element of radial adaptation is introduced. It was observed before (3) that the radii in growing fungal colonies adapt over time. Our data suggests that hyphae supporting the most carbon flux also tend to have larger cross section (SI Fig. 4.8). The apparent approximately linear relationship between these two elements inspired us to examine how such radial adaptation could affect the distribution of backflow. We therefore set the radius of the last edge connecting to the plant host in our simplified network so that the hyphal cross section would depend linearly on the lipid flux. With that additional element, we found that the ratio of

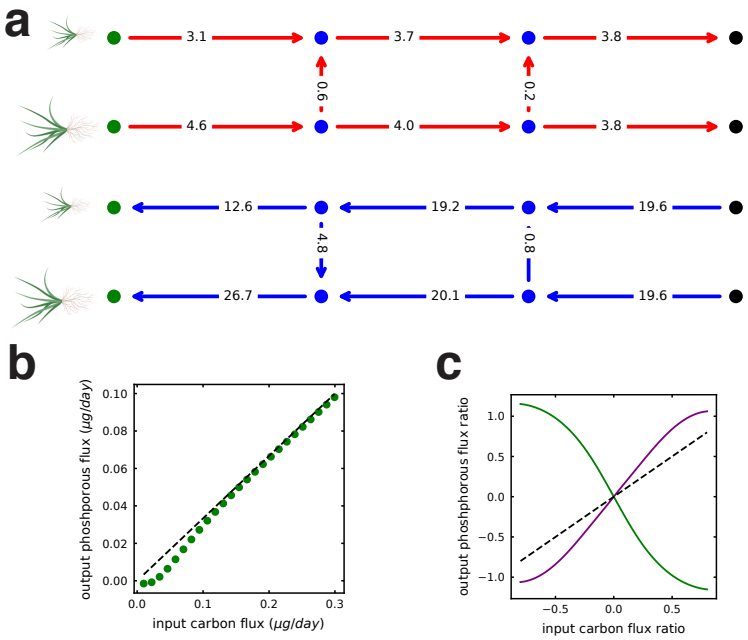

Figure 4.4: **Hydraulically induced proportionality of resource exchange.** **(a)** Representation of the network used for simulations. Green points are source nodes that represent connection to two different root host. Blue points are nodes of the inner part of the network. Black points are growing tips that are consuming carbon for grotwh. (upper) The red graph represents the flux of lipid. The blue graph represents the flux of water in the inner tube. Arrows represent the direction of the flux and the number represent its intensity in$\mu m^3/s$. The values shown are computed with the model of bidirectional movement. The ratio of input carbon flux was 0.4. For the edge connected to the plants, the cross section was chosen to be proportional to the lipid flux (Methods).**(b)** Model computed phosphorous flux for different values of input carbon flux. The ratio of plant carbon supply was set to 0.5 to represent a single plant. Lipid density was estimated to be $1.1g.cm^{-3}$ and the phosphorous concentration in the water phase was $\approx 2mol/L$. Green points corresponds to model outputs and black dashed line is a guide for the eye indicating a slope of $1/3\mu g\mathrm{P}/\mu g\mathrm{C}$. **(c)** Model computed ratio of phosphorous flux towards the two different root hosts for different ratios of input carbon flux. Black dashed line is 1:1 line used as a guide for the eye, green line corresponds to model outputs when all the radii were set to $3\mu m$, purple line corresponds to the case where the radius of the last edge connecting to the plant host was set so that the ratio of the cross section occupied by lipids would be maintained constant.

phosphorous flux towards the two plant hosts recovered the expected positive dependence on the ratio of lipid input (Fig. 4.4c). This can be analytically understood from equation 4.3.2 and the expression for the lipid volume fraction θ which yields for each edge $B = \Xi - \frac{1-p_{lipid}}{p_{lipid}}\phi$ where ϕ is the flux of carbon, Ξ is the net flow of water through the whole pipe and B is the backflow in the

inner pipe. With radial adaptation, Ξ contribution to backflow B does not work as much against the ϕ induced backflow.

4.4 Discussion

Our results suggest that lipids are preferentially moving in a direction that is informed by fungal growth. They also are strongly support the idea that this movement of lipid could be actively driven by molecular motors moving in one direction on polar cytoskeletal filaments. This network of filaments inside the fungal network is mathematically equivalent to a weighted oriented graph where the weight of a given edge can represent the number of cytoskeletal filaments allowing molecular motor movement. It is unclear how this oriented network organises to maintain an intensity and polarity coherent with growth.

Each edge of the network has a growth inherited orientation that is associated with the polarity of tip extension. It is likely that part of the network of transport filament simply orients in the direction of tip growth at the moment of its creation and persists in that direction over longer timescales.

One way of thinking about the system is that it is mainly supply driven. While in this paper our approach was to estimate what the flux of carbon was in each edge of the network from growth observation, it is possible that from the fungal point of view, things work the other way around. Growth would mainly emerge from the network's underlying molecular motor track organisation. This has the advantage of solving an informational bottleneck. If a tip grows at one end of the network, how is the information about its carbon demand transmitted to the root-fungal interface where that carbon will eventually come from? Instead of needing information transmission to match supply and demand and orient carbon fluxes accordingly, fungal tips could grow and branch according to the carbon supply of the existing network of molecular motor tracks. Indeed, the net flux of lipid across the colony could be entirely determined by its orientation (track direction) and intensity (number of parallel tracks assuming tracks are saturated with motors) as well as by the plant supply (source). Growth might then simply be occuring at a rate limited by the network-determined supply of lipids.

Some abrupt topological changes like anastomosis or the colony abandoning growth in a specific region of space however could require a reorganisation of the cytoskelal filaments. It is unclear how that reorganisation is modulated in a way that allows to maintain a flux of carbon that is coherent with the general fungal growth strategy. Depending on the timing of reorganisation, it is also likely that the flux of lipid moving on microtubules will not always follow Kirchhoff law at some intersection. Because lipids are incompressible and cannot accumulate at a node, this means that they will be recirculated in the internal cytoplasmic flow. This phenomenon could explain the observation that lipids can also move in two directions in fungal hyphae.

We see that bidirectional resource movement and trade could be largely mechanically mediated. Such a control mechanism has the advantage of being robust because the proportionality of flow is embedded in the physical properties of the system and therefore does not require additional biological control. In our model, the path taken by the phosphorous in the network is however strongly dependent on its relative cumulative hydraulic resistance and therefore on edge radii. We observed in Chapter 3 that edge radii could increase over time. Our results suggest that such radial

adaptation could constitute a flow control mechanism. We however never observed hyphal external radii diminishing. Full control would probably require an additional ingredient of radial shrinking.

In our model, we assumed that water could not flow out of hyphae except at the hyphal-root interface. It is however likely that ERM hyphae are covered with aquaporins that let water in and out. In that case any kind of water potential gradient between the inside and outside of the hyphae could produce influx or outflux of water at any point of the network. The resulting system would be analogous to the xylem-phloem system of plants. In that case the sugar loaded phloem generate an influx of water from the xylem. This in turn generates a net flux of water through the phloem. Any kind of osmolyte that would be produced inside the fungal network could very well drive a similar osmotic pump changing the overall flow distribution in the network. While we can not exclude such effects to play a role in the transport of resources within the AM colony, it is not incompatible with the mechanism of bidirectional flow described in this paper. Whatever the contribution of other mechanisms is, our results strongly suggest that lipid movement results in some fluid flow in the opposite direction. And such backflows must be playing a significant role in the full picture of AM fungal flows. The framework developped here can also be flexibly expanded to include the effect of other kinds of carbon demand like spore growth or hyphal maintenance. By adding current generators at different places in the network to represent influx or outflux of water due to water potential mediated flow of water through aquaporin, it is also possible to account for additional transport mechanisms.

4.5 Contributions

This work was done more independently than chapters 2 and 3. While the main building blocks of the model emerged slowly through active discussions with other collaborators, I combined all the ingredients and found the way of solving the network problem with its electrical circuit equivalent. I wrote the large majority of the code, text and designed figures with exceptions that are presented below.

Figures

All the figures presented are my work.

Text

- Methods presenting temporal graph extraction is work by Amin Hamzaoui
- Main text benefited from feedback of Max Kerr Winter, Christophe Godin and Toby Kiers

Data acquisition

- Daan Te Rietmole helped for acquiring 20% of the high magnification data shown in this work.

Methods

- Methods related to Nile red imaging were initially put in place by Jaap Van Krugten who himself took inspiration of the work of Berta Bago. Those methods were further improved and developed by Rachael Cargill and Jaap Van Krugten. I adapter them to be able to image plates over multiple days by ensuring minimal disturbance of the growing network.
- High and low magnification imaging setups were put in place by Loreto Oyarte Galvez with the help of the AMOLF software, mechanical and electrical engineering teams.
- By investigating in details experimental sources of noise during flow imaging, in particular the role of evaporation, Thomas Clerc and Simon Van Staalduine helped significantly reduce the variability in results from flow imaging.
- The methods related to temporal graph construction were built by Amin Hamzaoui during his internship under my supervision. Original idea was taken from the plant root imaging community.
- I initially put in place the methods for automated high magnification video analysis in particular speed and flux extraction. They were the combination of an idea of Tom Shimizu and work by Jaap Van Krugten who himself was using methods developed by Erwin Peterman. Those toools were further improved by Simon Van Staalduine during his internship under my supervision. He also enabled the method to run in parallel on large datasets at once by generalizing the parallelization scheme designed for low magnification timelapses. The methods was validated by Daan Te Rietmole. During his internship under my supervision, he manually annotated a subset of kymographs to compare the speed extracted that way to the automated one.

Ideas

- Idea that simultaneously imaging colony growth and internal flows would shed light on AM trade initially originated from Toby Kiers and Tom Shimizu.
- Simon Van Staalduine and Daan Te Rietmole helped providing first insights into the complexity of the bidirectional speed datasets. Their work was the foundation on which I could built this story and guided the intuition I had when running further analysis.
- The initial idea that lipid movement in the colony could be producing the bidirectional movement we observed was a long-standing intuition that emerged over discussions with Howard Stone, Toby Kiers, Tom Shimizu and Vasilis Kokkoris.
- I understood more clearly how to properly frame that intuition after a discussion with Denis Bartolo, Alexis Poncet and Camille Jorge.
- Further work on my own as well as discussions with Howard Stone, Tom Shimizu, Christophe Godin and Gauthier Legrand clarified progressively how to properly set-up the circuit equivalent representation.
- Work in parallel with Loreto Oyarte Galvez and Rachel Cargill brought up the idea that the lipid phase could be considered a separate water-oil emulsion with specific rheological

properties leading to the volume of water moving at the speed of lipids being greater than the volume of lipid only.

4.6 List of Supplementary Videos

Supplementary Video 1: Example video in brightifield then with Nile Red Fluorescence imaging in a given position.

Supplementary Video 2: Example video with Nile Red fluorescence imaging where one can clearly see that lipid movement seem to happen on well defined tracks within the hypha.

Supplementary Video 3: Zoomed in brightfield video showing internal fluid movement in a hypha isolated from the rest of the network.

Supplementary Video 4: Synthetically generated video as explained in 4.7.2 that displays bidirectional particle movement.

4.7 Methods

4.7.1 Timelapse Imaging

See 2.6.1 and 2.6.2.

4.7.2 Video Acquisition

See 2.6.9. The objective used was 50x instead of 100x but the rest of the system was identical. The excitation light was

Nile red staining

Nile red dye was used to follow neutral lipids inside the hyphae. Nile red dye associates with lipids that are free, they are not inside a membrane. The addition of dye was done in the biosafety cabinet by opening the plates and adding 3-10 droplets of 3 μl Nile red dye solution around the growing network (depending on its size). The solution was diluted 10 times before adding it to the plate.

In preliminary tests, we observed that the staining location (staining the center of the colony or around its periphery) did not seem to affect the general direction or speed of the lipids we observed. However, staining at the periphery did seem to result in larger fluorescence signal which in turn allowed us to limit the intensity of excitation light and therefore phototoxicity. Growing hyphae did not seem to specifically avoid the zone where droplets of stain were added and we think that growing tips are where endocytosis is mostly happening which explains better absorption of the dye when those regions were stained. In addition, if the direction of flux observed was mostly due to uneven staining, staining at the growing tips should have worked against the conclusions that we draw in this publication. We therefore decided to stain the colony by surrounding its periphery with droplets of dye and letting the dye diffuse and the fungus grow over these regions.

Sampling strategy

All data from main figures (except Fig. 3b) originates from two plates of *R. irregularis* A5 and one plate of *R. irregularis* C2. Each plate was stained with Nile red (see above) before the first day of imaging then left in the timelapse imaging setup overnight. They were then imaged over 3-6 successive days for 1-2 hours each day before being put back in the timelapse imaging set-up. The lid was kept closed. We did the brightfield videos using the same light as the one used in the timelapse imaging set-up where we know this doesn't affect growth. We observed in preliminary experiments that fluorescence imaging did seem to affect growth and therefore kept fluorescence excitation intensity and time to their minimum. Each fluorescence video was 10-20s long and the fluorescence light was turned off immediately after the recording. Growth observed in the timelapse imaging platform did not seem to be affected by the imaging sessions. Hyphal growth speeds were similar to the ones observed in conditions without staining.

We focused on 2-3 "main hyphae" per plate which would usually span the whole plate at last timepoints. This was however not always possible to predict from the start of the experiment, so we occasionally had to switch hyphae over the multiple days of experiments. We generally imaged at every intersection along the hypha therefore capturing the flows in all the branches emerging from a junction. We also added, when intersections were sufficiently far from each other, videos away from intersections along those main hyphae. All networks at the time of imaging with video position are shown in SI Fig. 4.7.

Network cut

The high-resolution imaging system was also adapted with a manipulatable needle attachment, positioning a 0.3 x 12mm disposable needle (Henke-Sass Wolf) at an oblique angle above the surface of the plate. Three fine adjustment screw knobs (Thorlabs) allowed for up/down, left/right, and forward/back manipulation of the needle as needed.

Upon cutting, the needle was lowered down against the cellophane on the far site of the hypha, pulled backwards across the hypha to slice it, then raised up away from the cellophane.

Synthetic video generation

Synthetic ideos were generated to test the validity of our flux and speed extraction methods. We represented fluorescent lipid droplets as bright moving Gaussian spots within a rectangular frame. We initialized the video specifying the size of the rectangle, speeds of spots moving to the left and right, number of spots, and their size. Initial positions for the spots were randomly determined, and Gaussian distributions were generated to represent each spot.

For each time step, the positions of the moving spots were updated by shifting their positions based on the specified speeds. Right-moving spots were shifted to the right, left-moving spots to the left, and stationary spots remained unchanged. The frames for right-moving and left-moving spots were combined with the stationary spots using a weighted average. Finally, noise was added to each frame to simulate realistic variability. The process was repeated for the desired number of time steps to produce the video.

The corresponding kymograph was obtained by averaging over each column of the rectangular frame at each timestep.

4.7.3 Kymograph Operations

Video segmentation and graph generation

For each video, we first generated a segmented image where each pixel would be set to 1 if it belonged to the hypha and 0 otherwise.

For brightfield video, we took the first 300 frames and for each pixel computed the standard deviation of that pixel intensity and its average over those frames. Pixels belonging to a hypha are expected to have higher coefficient of variation (standard deviation divided by mean) since the cell material moves either because of cytoplasmic movement or because of diffusion. The standard deviation and average maps were then convoluted by a 20x20 blurring kernel using the function `cv2.blur` from OpenCV. We then divided the standard deviation map by the mean intensity map to obtain coefficient of variation (CV) maps. That image was itself again blurred by a 20x20 kernel to maximize the connectivity of the graph obtained at later steps. We then computed the binned distribution of intensity of the CV map over 40 bins ranging from min to max value and took the derivative of the resulting histogram. The abscise of the minimum of the derivative (corresponding to a sudden drop in the distribution) was used as a threshold to separate the pixels in the CV that belonged to hyphae to the ones that belonged to the background. The result was thinned out to a one pixel wide skeleton using the `skeletonize` function of `skimage.morphology` package of Python.

Kymograph generation

Using a custom algorithm based on pixel neighbouring relations in the skeleton, we transformed the pixel skeletons to a graph format where all junctions and apexes become "nodes" of the graph and branches between them become "edges". Pixels of the skeleton that had 0, 1, 3 or 4 neighbours were therefore considered "nodes" and two nodes were connected by an "edge" if they were connected by a consecutive series of neighbouring skeleton pixels with no intervening nodes among them. Each edge pixel sequence is then used to generate perpendicular lines along the edge at a 1-pixel distance from each other. Perpendicular lines of 17μm (240 pixels in 50x magnification without binning) were generated symmetrically to the central line of the hypha. The pixel values in this line were averaged to generate the mean intensity value at that length position along the hypha. Placing these intensity values next to each other in a line produces the first horizontal line in a kymograph. This process is then repeated for each frame in the video. In the resulting kymograph, moving particles are represented as lines and each line's slope is correlated to the speed of that particle. The choice of the length of the transect over which to average (17μm) was made so it would exceed the maximum diameter of all hyphae. Overshooting the diameter of most hyphae did not have effect on further analysis since no movement of particles could be observed outside of the hyphae. The only effect of including background in the transect was that it decreased contrast but both the Fourier filtering (see 4.7.3) and the speed extraction (see 4.7.3) were unaffected by contrast.

Kymograph filtering

Because particles move in both directions within each hypha, it was important to separate particle tracks that would cross over each other. To this end, each kymograph was first put through a Fourier directional filter, as described in the supplemental for KymographClear [4]. In short...

Speed extraction

Speed extraction of these kymographs was done using structural tensor analysis as described in Spatio-Temporal Image Processing [13]. For each pixel, a window of pixel size $w \in \mathbb{N}$ around the center pixel, is used to assess the local structure of the kymograph. For this window, the local structure is described by a structure tensor operator:

$$J = \begin{pmatrix} J_{xx} & J_{xy} \\ J_{xy} & J_{yy} \end{pmatrix}$$

where each component is calculated using a discrete partial derivative operator along the coordinate p, described as D_p:

$$J_{pq} = D_p I \cdot D_q I$$

where the dot multiplication denotes pixel-wise multiplication. In the speed analysis, Sobel filters are used along the x and y direction. An additional smoothing operator is also used in the original description, which has been forgone in this analysis. After solving an eigenvalue problem with this structure tensor, the image orientation

$$\theta = \frac{1}{2} \tan^{-1} \left(\frac{2J_{xy}}{J_{xx} - J_{yy}} \right)$$

and the coherency of the speeds that are found

$$C = \frac{\sqrt{(J_{xx} - J_{yy})^2 + 4J_{xy}^2}}{J_{xx} + J_{yy}}$$

can be readily extracted from this window. Speed coherency is a measure between 0 and 1 that gives an indication how anisotropic the structure of a given image is. This measure is used in the analysis to threshold for orientations that have a coherency higher than 0.95.

For each kymograph, this analysis is done with multiple window sizes, typically $w \in [3, 15]$. This is because particle size within the kymographs vary, and the goal is to capture the speeds of small and large particles alike. This means that for i amount of window sizes, each pixel will have i amount of orientations and coherencies. We select the orientation associated with the highest coherency.

The separated kymographs then underwent the above-described speed analysis independently, leading to the creation of two 'speed fields', describing the velocities in both directions. The speed fields of the kymograph in Figure 1 can be seen in Figure 2. Velocity is calculated with the image orientation $O(x, t)$ at each pixel:

$$v = \frac{\Delta x}{\Delta t} \tan\left(O(x, t)\right)$$

with Δx and Δt being the spatial and temporal resolution of the video respectively.

We then only kept extracted speeds at pixels where the associated coherency was ≥ 0.95.

Flux estimate

In order to estimate relative flux in a kymograph obtained from a fluorescence video we first generated the kymographs corresponding to one and the other direction as explained in 4.7.3. We then computed the speed at each pixel as explained in 4.7.3 keeping only speed with coherency above 0.95. For each direction then computed the average speed of the whole kymograph and multiplied it by the average intensity of the whole kymograph. This way of averaging was justified by the fact that in all videos, we observed flow speeds in both directions that were constant over time (see SI Fig. 4.5a). Obtaining an estimate of the flux in the two directions ϕ^+ and ϕ^-. The relative flux was then estimated as:

$$\phi_{relative} = \frac{\phi^+ - \phi^-}{\phi^+ + \phi^-}$$

Using a set of 200 randomly generated artificially generated videos (see 4.7.2) where we knew the actual relative flux, we verified that this method gave an estimate of the flux with the right sign 85% of the time.

4.7.4 Network Operation

Temporal graph construction

Once the spatial graph for each time step have been computed, the goal is to merge them into one temporal graph which edges have the attribute *activation time*, denoting the time step at which the edge appeared. The edges represent the same thing as in 1.4. At each intersection of hyphae, of degree not equal to two, a node is created. And, edges are what link nodes together. Hence, they represent a portion of an hyphae. Hyphae are the long, branching, filamentous structures forming the fungus.
It is possible to create the temporal graph because once a hypha is created, it never disappears. Thanks to this, the temporal graph can almost be created by adding activation time to each edge of the final spatial graph.
But in reality, it takes several time steps for an edge to grow fully. So an edge doesn't have a well defined activation time. To avoid this problem, and also improve activation time tracking, each edge is divided into segments of length, l, where l should be way smaller than the growing rate. Hence, a segment is a portion of an edge, which is a portion of an hypha. And adjacent edges can be stick together to form back the edge they originated from.

Activation time setting Once the edges are segmented, an activation time for each segment needs to be set. It is done iteratively. First, a center for each segment is set and the activation time is set to the final graph time step. Then the algorithm look into the previous graphs iteratively, from last to first, to see if there is an edge is closer than a settled threshold, t, to each segment center. If this the case for a segment, s, the activation time for this segment is set to be the iterated graph time step. And the center is also set to be the closest point to the segment in the iterated graph. Moreover, the attributes from the closest edge, such as the width at this time step, are also conserved in the attributes of the segments.

Activation time fixing and hyphae creation Once the previous steps are done, the result is a graph with small edges having an *activation time*. The small edges can be group by their initial edge and ordered. It results in ordered activation times. To avoid tracking problems on the borders of each initial edges, median filters are used on each initial edges activation times at the borders. Because hyphae are growing in only one direction, the activation times in each group are monotone. To fix those non activation monotone initial edges, first a median filter is applied to the activation times of each initial edges. And then, if the median filter is not sufficient, the activation times are flatten iteratively from the sides to the center, until it is monotone or flat.
Another constraint, is that a group of initial edges ordered forming an hypha also have monotone activation times. Making the hypothesis that, at each intersection, at most one of the edge is not forming an hypha with another edge, initial edges can be group together into hyphae(at a degree 3 intersection, there is one hypha and one lonely edge; at a degree 4 intersection, there is two hyphae). At each intersection, the edge with the smallest activation time is selected. If there are multiple edges in this case, then the pair of those edges that have their angle closest to 180° are put in the same group. Else edges with the second smallest activation time is selected. If there is only one, the two edges are put in the same group. If there are two or more edges, the edge that has the angle with the first edge closest to 180° is put in the same group as the first edge. The process is repeated with the remaining edges at the intersection until there is less then one edge left.
Once initial edges are grouped together, activation times are also fixed to be monotone through each hypha. A median filter is applied to fix the non time monotone hyphae. If some hyphae are still not time monotone, they are break into multiple hyphae that are time monotone.

Radius setting One interesting attribute to monitor is the radius of the hyphae. The radius are tracked on the graph created at each time step. With the help of a machine learning model, a width value is attributed to each edge (i.e. $2 * radius$). The input of the machine learning model are the transverse intensity, in the original picture of the graph, of an edge. It then output a value which correspond to the width of the edge. The training dataset was built by measuring hundreds of width by hand.
Then, during the iterative process, as described above each segment of the temporal graph, built from the graph created at each time step, have an attribute width for each time step, from the moment it was considered "activated".

Carbon and volume sink node estimation

AMF use carbon from their host root to grow. An hyphae growing correspond to a carbon supply to its tip. We set the following conversion factor between newly built hyphal volume and carbon consumption $\alpha_C = p_{dry} \times p_C \times d_{cell}/CUE$. In that later expression, p_{dry} is the ratio of dry mass to wet mass, p_{carbon} is the ratio of carbon in dry mass , d_{cell} is the cell volumetric mass and CUE is the carbon use efficiency of hyphal growth. Therefore, an hyphae growing of volume, $V_g (= \pi * length * \frac{width^2}{4})$, corresponds to a volume of carbon, V_c:

$$V_c = \alpha_C * V_g$$

Using the activation times of the temporal graph, the graph at time step t and $t+1$ can be computed. The difference between the two graphs results in multiple connected graphs. For each connected

graph, "growing extremities" i.e. nodes that are both in the graph at time step t and the connected graph are selected. It results that all the carbon, that was used to create the connected graph, needed to pass through those nodes between time step t and $t+1$. This amount can be calculated via the above formula and the widths and lengths of the edges of the connected graph. When there is only one node at the intersection, the volume of carbon can be directly attributed to this node. If there are multiple nodes, which shouldn't not happen with small time step, the volume is equally shared between the nodes.

Carbon source/hydraulic ground setting

To select a set of nodes that would be used as a carbon source and a hydraulic ground for a given timestep, we first selected all the nodes that were present at that timestep. To do so, we looked for the minimum activation time of edges connected to that node in the temporal graph and defined this minimum activation time as the time of appearance of the node. The position of the resulting nodes formed a point cloud which y position was associated with the distance to the root compartment. We separated the point cloud in 20 columns of equal width from the minimum to the maximum x position. Within each column, we selected the point with smallest y position and added the corresponding node to a list that would later be used to represent the connections to the root.

It is difficult from the images, to determine which hyphae of the network in the fungal compartment connect to the root compartment. It is also impossible to know whether this connections in-between compartments correspond to actual connections to parts of the network that are connected to plant root cells. The choice of connecting all those nodes to a single ground via a zero resistance edge (see 4.7.5) mitigates the influence of the specific choice of sink nodes as long as it is sufficiently well distributed.

Video edge matching

Each edge of the graph of each flow video was matched to a corresponding edge of the graph extracted from the timelapse. During imaging, we wrote down on an image of the full network the positions at which each video was taken. Then, to match the coordinate system from the high and low magnification imaging, we first selected a subset of 4-10 videos from each imaging session where a junction had been imaged and then manually found the corresponding junction of the low magnification graph using the initial image with manual annotation as a guide. This allowed us to find the correct translation, rotation, and dilation matching the two coordinates systems. Then, because exact edge matching required precise overlay of the graphs, for each video we selected the low-resolution graph edges that were at a distance of less than 170μm from the centre of the video. We then found the rotation and translation that minimized the distance of the high magnification edges to that subgraph. Finally, for each edge of the high-resolution graph, we looked for the low resolution edge that was closest after rotation and translation. The average final distance between the low-resolution edges and their high-resolution mapping was saved and used to filter final results. Videos that had an average edge mapping distance superior to 20μm were excluded in further analysis that involved using low resolution network graph attributes.

4.7.5 Hydraulics

Estimation of growth induced water flux

In order to estimate the growth induced flow of water as proposed in [5, 6] and as shown in Fig. 4.2d, we used the estimated volume growth of sink nodes (see 4.7.4). The net flow rate out of those nodes was set to be equal to that rate of volumetric growth. We added an edge to the network with 0 length that connected all the hydraulic grounds as determined in 4.7.4. The net flow rate into that ground node was set to be equal to the sum of the net flow rates out of the growing sink nodes.

We then set all edges to be resistors with resistance $D_{i,j} = \frac{8\mu L_{i,j}}{\pi R_{i,j}^4}$ where $\mu = 1g.m^{-1}.s^{-1}$ is the viscosity of the cytoplasm, $R_{i,j}$ is the hyphal radius of the edge determined as explained in 4.7.4 and $L_{i,j}$ is the length of the edge. We then solved the system as explained in 4.7.5.

This gave us the net flow of water $Q_{i,j}$ in each edge according to this model. We then estimated the average speed in that edge $v_{i,j} = \frac{Q_{i,j}}{\pi R_{i,j}^2}$ that we could compared to the speed observed in the same direction in high resolution.

Carbon flux distribution calculation

The volume creation at the tips is directly proportional to the consumption of carbon. We used the proportionality factors established in 3.6.7 to evaluate the demand of carbon for growth. We hypothesized that the flux of carbon would distribute similarly to the growth induced water flux established above. Such a description is indeed mathematically equivalent to minimization of viscous energy dissipation in the network of resistors.

This is justified by the fact that distribution of currents in a network of resistors follows energy dissipation minimization principle. While the exact distribution of lipid fluxes in the fungal colony is hard to establish precisely (i) The fact that lipid movement is observed in most edges suggests that they are not only following shortest path, the lipid current distributes somehow over all possible paths. (ii) It is likely that the growing colony performs some level of energy dissipation minimization since energy from the plant is a limiting resource. While the relationship between actively driven lipid current in a pipe and energy dissipation is unclear, it is reasonable to hypothesize that part of it is due to viscous drag and resembles the ones of pressure driven fluid flow.

We then set the mass carbon flux in each edge $\phi_{i,j} = \alpha_C Q_{i,j}$ with α_C as defined in 4.7.4

Lipid hydraulic circuit

Estimation of lipid density

Derivation of flow profile in a pipe with moving walls

In cylindrical symmetry We assume:

- Laminar, steady, incompressible, and axisymmetric flow.
- The fluid is Newtonian, and the no-slip condition at the wall is not strictly zero but a different constant velocity v_0.

For an incompressible Newtonian fluid in a cylindrical pipe under these conditions, the radial component of the Navier-Stokes equations simplifies under the assumption of no radial or azimuthal velocities and steady flow. The axial component (along the length of the pipe) becomes:

$$\frac{dP}{dx} = \mu \frac{1}{r} \frac{d}{dr} \left(r \frac{du}{dr} \right)$$

Integrate this equation across the radius of the pipe:

$$\mu r \frac{du}{dr} = - \left(\frac{dP}{dx} \right) \frac{r^2}{2} + C$$

Further integrating:

$$\mu u = - \left(\frac{dP}{dx} \right) \frac{r^2}{4} + C \ln(r) + K$$

- At $r = R_B$ (pipe wall), $u(R_B) = v_0$.
- At $r = 0$ (pipe center), the speed profile cannot diverge so $C = 0$.

Solving for K using $u(R_B) = v_0$:

$$K = \mu v_0 + \left(\frac{dP}{dx} \right) \frac{R_B^2}{4}$$

Then the velocity profile simplifies to:

$$u(r) = - \frac{1}{4\mu} \left(\frac{dP}{dx} \right) (R_B^2 - r^2) + v_0$$

Now, we want the integral of this velocity profile over the internal cross-sectional area to equate B:

$$B = \int_0^{R_B} 2\pi r u(r) \, dr$$

We need to find $\frac{dP}{dx}$ so that the condition is met.

The equation for the pressure gradient $\frac{dP}{dx}$ that achieves a specified non-zero net flow through the inner pipe B is:

$$\frac{dP}{dx} = \frac{8\mu(-B + \pi R_B^2 v_0)}{\pi R_B^4} \tag{4.7.1}$$

Substituting this expression for $\frac{dP}{dx}$ back into the velocity profile:

we obtain :

$$u(r) = v_0 + \frac{2(B - \pi R_B^2 v_0)(R_B^2 - r^2)}{\pi R_B^4} \tag{4.7.2}$$

Electrical circuit equivalent

From equation 4.7.1, we also obtain that the pressure gradient over an edge of length L is given by:

$$\Delta P = L\frac{8\mu(B - \pi R_B^2 v_0)}{\pi R_B^4}$$

which we can rewrite as

$$\Delta P = DB + \Delta P^{(0)}$$

with $D = \frac{8\mu L}{\pi R_B^4}$ the hydraulic resistance and $\Delta P^{(0)} = -\frac{8\mu L v_0}{R_B^2}$

In an edge (i, j) of inner pipe radius $R_B(R_{i,j}, \phi_{i,j})$, we can then define $B_{i,j}$ as the flux through the inner pipe and the pressure drop $\Delta P_{i,j}^{(0)} = \text{sign}(\phi_{i,j}) v_0 \frac{8\mu L_{i,j}}{R_B(R_{i,j},\phi_{i,j})^2}$. In that later formula, the function $\text{sign}(\phi_{i,j})$ is a sign function used to orient the movement of lipids in the correct direction. For physical reasons we set $\text{sign}(\phi_{i,j}) = \tanh(\frac{\phi_{i,j}}{\pi R_{i,j}^2 v_0 \theta_{min}})$ where tanh is the hyperbolic tangent function that vary between -1 and 1 and $\theta_{min} \approx 0.1\%$. This was done to represent the fact that at very low lipid density, our assumptions that lipids are covering the whole surface of the hypha is not justified and we can therefore not represent the pressure drop as we do in equation 4.7.1

We can then write the net cytoplasm flux through the whole pipe $\Xi_{i,j}$ as $\Xi_{i,j} = B_{i,j} + \frac{(1-p_{lipid})}{p_{lipid}}\phi_{i,j}$ where p_{lipid} is the proportion of lipid in the lipid-cytoplasm emulsion and $\phi_{i,j}$ is the lipid flux in the edge.

We can then rewrite

$$\Delta P_{i,j} = D\Xi_{i,j} + \Delta P_{i,j}^{(tot)} \tag{4.7.3}$$

with $\Delta P_{i,j}^{tot} = \Delta P_{i,j}^{(0)} + D\frac{(1-p_{lipid})}{p_{lipid}}\phi_{i,j}$

Which is equivalent to a circuit with a resistor and a voltage drop in series.

Estimation of carbon flux induced backflow

in summary, at a given timestep we:

1. Find the growing nodes and their corresponding weights.
2. Find the sink nodes and connect them to a common ground
3. Establish the carbon flux $\phi_{i,j}$ in each edge as explained in 4.7.5 and solving the circuit equivalent as explained in 4.7.5
4. Compute the inner radius $R_B(\phi_{i,j}, R_{i,j})$ for each edge
5. Establish the circuit element equivalent of all edges as explained in equation 4.7.3
6. Solve the circuit equivalent with zero net flux outside of the circuit to find the net flux of cytoplasm through the whole pipe $\Xi_{i,j}$ in each edge.
7. Find the backflow of cytoplasm in the inner pipe $B_{i,j}$ and the maximum velocity in the pipe using 4.7.2.

Solving of circuit equivalents

We first converted the mathematical graph representing the fungal colony into an oriented graph and assigned to each edge (i, j) a resistance $D_{i,j} = \frac{8\mu L_{i,j}}{\pi R_{i,j}^4}$. For the estimation of carbon flux induced backflow, this resistor was put in series with an oriented tension generator $\Delta P_{i,j}^{tot} = \Delta P_{i,j}^{(0)} + D\frac{(1-p_{lipid})}{p_{lipid}}\phi_{i,j}$.

If we consider E the set of all edges of the oriented graph and N the set of all nodes and their cardinality $|E|$ and $|N|$. Solving the circuit equivalent was done in the following way.

1. **Node and Edge Indexing:**
   - Create a mapping of each node to a unique index in $[\![0, |N|]\!]$. In the following, we assume for simplicity of notations that such mapping has been already done and that all i, j are in $[\![0, |N|]\!]$.
   - Create a mapping M of each edge (i, j) to a unique index in $[\![0, |E|]\!]$.

   We first write the system of equation corresponding to Kirchhoff law at each intersection. $\forall j \in [\![0, |N| - 1]\!]; \sum_i Q_{i,j} = 0$. The last conservation law is not written since it automatically results from all the others.

2. **Node Equations for Mass Conservation:**
   - Initialize matrix $\mathbf{A}$ of size $(|N| - 1) \times |E|$ with zeros.
   - Initialize vector $\mathbf{b}$ of size $|N|$ with zeros.
   - For each oriented edge (i, j), update $\mathbf{A}$ such that $A_{i,M(i,j)} = -1$ if $i \leq |N| - 1$ and $A_{j,\text{edge\_index}(i,j)} = 1$ if $j \leq |N| - 1$.
   - For each node i, set b_i to its source/sink term i. That term can be ΔC_i or ΔV_i depending on which exact hydraulic problem is being solved.

   We then added the constraint corresponding to Kirchhoff's voltage law

3. **Loop Equations for Kirchhoff's voltage law:**
   - Identify a cycle basis using the `cycle_basis` function of `networkx` [14] in the undirected version of G.
   - For each cycle, construct a new row in $\mathbf{A}$ and corresponding value in $\mathbf{b}$ based on the resistances $D_{i,j}$ and pressure generators $\Delta P_{i,j}^{\text{tot}}$ of the edges in the cycle.
   - For an edge (i, j) in the direction of the cycle, add $D_{i,j}$ to the new row in position $M(i, j)$ and $\Delta P_{i,j}^{\text{tot}}$ to $\mathbf{b}$.
   - For an edge (j, i) opposite to the cycle, subtract $D_{i,j}$ from the new row and $\Delta P_{i,j}^{\text{tot}}$ from $\mathbf{b}$.
   - Append the new row to $\mathbf{A}$ and the new value to $\mathbf{b}$.

   Adding such additional constraints resulted in a square matrix $\mathbf{A}$ because of the Euler formula for planar graph $|E| = F + |N| - 2$ where F is the number of faces which is equal to the number of element in the cycle basis plus 1.

Solving the Matrix System Once the matrix system $\mathbf{Ax} = \mathbf{b}$ is constructed, where $\mathbf{x}$ represents the flow rates in the edges $\Xi_{i,j}$, we solve for $\mathbf{x}$ using standard linear algebra techniques:

$$\mathbf{x} = \mathbf{A}^{-1}\mathbf{b}$$

This yields the flow rates for each edge in the hydraulic circuit.

4.7.6 Simple Model of Carbon/Water Flux Proportionality in a network

Simplified graph representation

We built the graph represented in Fig. 4.4a with all edge length equal to $1000\mu m$ which corresponds to the average length of edges in our network. Such network exhibits loops which allow carbon from one plant to feed the growth of a growing tip that is topologically closer to another plant.

Without radial adaptation we set all edge radii to be $3\mu m$ corresponding to the average radius observed in our colonies (see Chapter 3).

In the case where an element of radial adaptation was introduced, we only changed the radii of the two edges connecting to the plants. Those radii were set to keep the volume fraction of lipid constant in those two edges. Considering plant A and B, we can call ϕ_A the flux of carbon in the edge coming from plant A, ϕ_B the flux of carbon in the edge coming from plant B and r_A,r_B the corresponding radii, we can define $p = \frac{\phi_A}{\phi_A+\phi_B}$. By setting $r_A = \sqrt{pS_{tot}}$ and $r_B = \sqrt{(1-p)S_{tot}}$ with $S_{tot} = 18\mu m^2$ the radii verify $\frac{\phi_A}{\pi r_A^2} = \frac{\phi_B}{\pi r_B^2}$.

Setting source and sinks for carbon

In the following, we express all source and sinks for a node k in their volumetric version ΔV_k which is directly proportional to carbon consumption ΔC_k. This is done to allow easier comparison with known order of magnitude of hyphal length growth speeds. For Fig. 4.4c, we varied the total volumetric growth rate ΔV_{tot} from $1\mu m^3/s$ to $30\mu m^3/s$. Which corresponds to a variation from $100\mu m$ to $3000\mu m$ of new hypha built in an hour. $100\mu m/h$ corresponds to the slowest observed growth speeds for hyphal tips (see Fig. 2.3c) while $3000\mu m/h$ is of order of what can be typically observed in growing colonies when integrating the growth of multiple tips in parallel (see Fig. 2.4b).

For Fig. 4.4c, we set the total volumetric growth rate $\Delta V_{tot} = 30\mu m^3/s$. We assumed growth of the tips was not affected by the magnitude of the carbon supply of the closest root and we set the sink term was equal to $\Delta V_{tot}/2$. When varying the ratio p of lipid influx $p = \frac{\phi_A}{\phi_A+\phi_B}$, we set the source term for the node corresponding to $\Delta V_A = -p\Delta V_{tot}$ and $\Delta V_B = -(1-p)\Delta V_{tot}$.

Obtaining carbon flux

We could then solve the corresponding hydraulic problem as explained in 4.7.5 and then convert the volumetric flow rate $Q_{i,j}$ obtained to carbon flux $\phi_{i,j}$ using $\phi_{i,j} = \alpha_C Q_{i,j}$ (see 4.7.5).

Obtaining backflow

From the estimated carbon flux and the edge lengths and radii, we could set the circuit equivalent. To account for volumetric growth, we kept sinks as above at the tips $\Delta V_{tot}/2$. We added a source node connected with 0 length edges to the two plant nodes to represent a water reservoir where we set the source term to be $-\Delta V_{tot}$.

We then solved the circuit equivalent as explained in 4.7.5 to find the net flow through the whole pipe $\Xi_{i,j}$ in all edges from which we could obtain the backflow $B_{i,j}$ using 4.3.2.

Estimation of phosphorous flux

We then estimated the phosphorous flux due to backflow as $P_{i,j} = C_P B_{i,j}$ where we set $C_P = 1.86 mol/L = 58 mg/cm^3$. The ratio of P flux to the plants as shown in Fig. 4.4b were defined using the flux of P in the terminal edges connecting to plants A, P_A and B, P_B. The ratio shown corresponds to $\frac{P_A}{P_A+P_B}$

4.8 Supplementary Figures

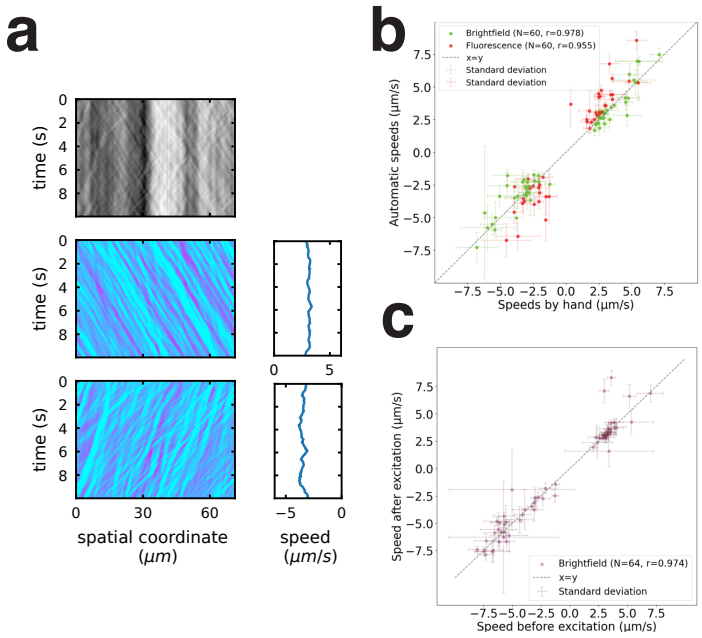

Figure 4.5: **Speed extraction method.** **(a)** Original (top), left filtered (middle) and right filtered (bottom) kymographs from a 10s brightfield video. Extracted speed over time is shown on the right of each filtered kymographs. This example illustrates the constance of speed over these timescales. **(b)** Automatically extracted speed against manually extracted speed. To extract speed by hand, lines following the visually obvious diagonal lines in the raw kymograph were manually drawn. The ressult shows that our method extract speeds reliably. **(c)** Effect of fluorescence imaging on transport. Videos in brightfield were taken before and after 10s of fluorescence excitation with blue light and the speed were compared. We observe no difference between the speed obtained before and after the blue light illumination.

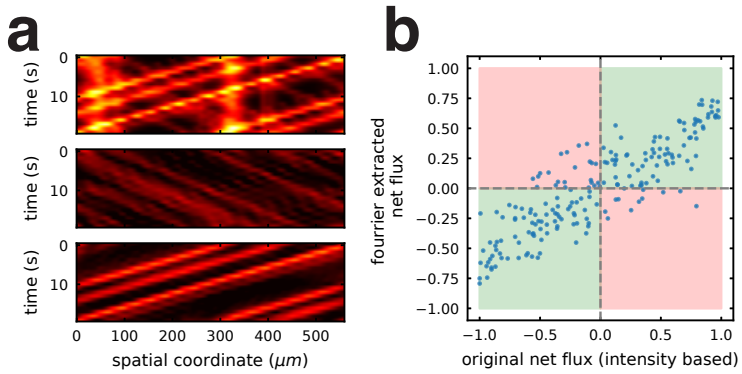

Figure 4.6: **Flux extraction method can resolve net flux direction. (a)** (top) Kymograph generated from SI Video 4 and filtered version for particles moving from left to right (middle) and left to right (bottom). Filtered kymograph are obtained with Fourier transform (see Method). **(b)** Original net flux of artificially generated video against the one computed with the Fourrier method (methods). Well predicted flux direction of carbon (points in green quadrants) as opposed to ill-predicted flux direction (points in red quadrant) is $\sim 85\%$.

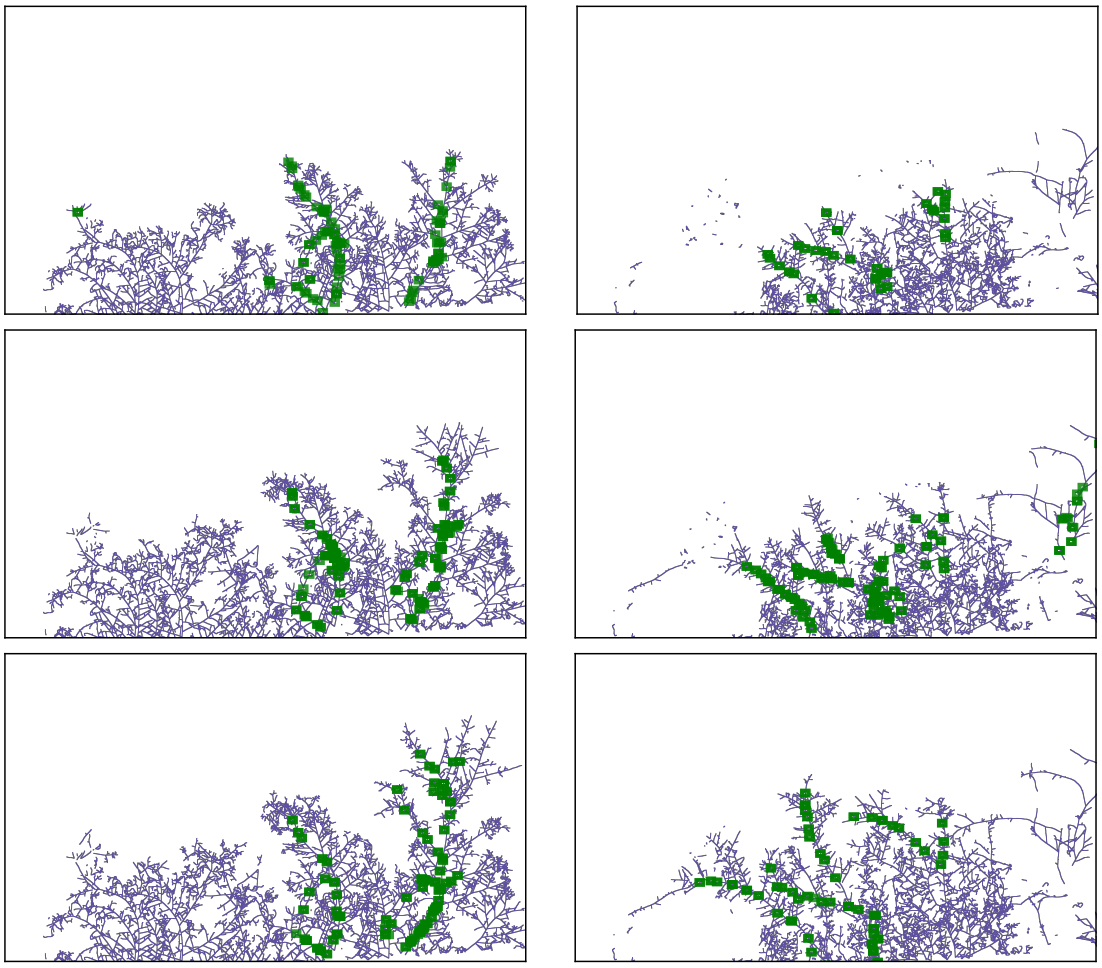

Figure 4.7: **Network and video positions at time of imaging**. Video positions are indicated by green rectangles. Left column corresponds to first colony where the hyphal transect shown in Fig. 4.1 and 4.2 was taken. Right column correspond to another colony.

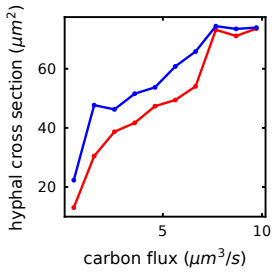

Figure 4.8: **Hyphal cross section increases with instantaneous carbon flux.** We estimated the carbon flux in each edge of the colony using our carbon flux model. We then binned edges in 10 evenly distributed categories corresponding to the estimated flux. Blue curve links the mean cross section in each bin, red curve links the 10th percentile in each bin

Bibliography

1. Kiers, E. T. *et al.* Reciprocal Rewards Stabilize Cooperation in the Mycorrhizal Symbiosis. en. *Science* **333,** 880–882. ISSN: 0036-8075, 1095-9203. https://www.science.org/doi/10.1126/science.1208473 (2023) (Aug. 2011).
2. Bago, B. *et al.* Translocation and Utilization of Fungal Storage Lipid in the Arbuscular Mycorrhizal Symbiosis. *Plant Physiology* **128,** 108–124. ISSN: 0032-0889. https://doi.org/10.1104/pp.010466 (2023) (Jan. 2002).
3. Bago, B., Pfeffer, P. E., Zipfel, W., Lammers, P. & Shachar-Hill, Y. Tracking metabolism and imaging transport in arbuscular mycorrhizal fungi. Metabolism and transport in AM fungi. en. *Plant and Soil* **244,** 189–197. ISSN: 1573-5036. https://doi.org/10.1023/A:1020212328955 (2024) (July 2002).
4. Mangeol, P., Prevo, B. & Peterman, E. J. G. KymographClear and KymographDirect: two tools for the automated quantitative analysis of molecular and cellular dynamics using kymographs. *Molecular Biology of the Cell* **27,** 1948–1957. ISSN: 1059-1524. https://www.ncbi.nlm.nih.gov/pmc/articles/PMC4907728/ (2023) (June 2016).
5. Heaton, L. L. M., López, E., Maini, P. K., Fricker, M. D. & Jones, N. S. Growth-induced mass flows in fungal networks. en. *Proceedings of the Royal Society B: Biological Sciences* **277,** 3265–3274. ISSN: 0962-8452, 1471-2954. https://royalsocietypublishing.org/doi/10.1098/rspb.2010.0735 (2021) (Nov. 2010).
6. Heaton, L. L. M., López, E., Maini, P. K., Fricker, M. D. & Jones, N. S. Advection, diffusion, and delivery over a network. *Physical Review E* **86,** 021905. https://link.aps.org/doi/10.1103/PhysRevE.86.021905 (2021) (Aug. 2012).
7. Howard, J. *Mechanics of motor proteins* en. in *Physics of bio-molecules and cells. Physique des biomolécules et des cellules* (eds Flyvbjerg, F., Jülicher, F., Ormos, P. & David, F.) (Springer, Berlin, Heidelberg, 2002), 69–94. ISBN: 978-3-540-45701-5.
8. Bago, B., Pfeffer, P. E. & Shachar-Hill, Y. Carbon Metabolism and Transport in Arbuscular Mycorrhizas. en. *Plant Physiology* **124,** 949–958. ISSN: 0032-0889, 1532-2548. http://www.plantphysiol.org/content/124/3/949 (2021) (Nov. 2000).
9. Thiam, A. R. & Beller, M. The why, when and how of lipid droplet diversity. en. *Journal of Cell Science,* jcs.192021. ISSN: 1477-9137, 0021-9533. https://journals.biologists.com/jcs/article/doi/10.1242/jcs.192021/265260/The-why-when-and-how-of-lipid-droplet-diversity (2022) (Jan. 2017).

10. Jeffrey, D. J. & Acrivos, A. The rheological properties of suspensions of rigid particles. en. *AIChE Journal* **22,** 417–432. ISSN: 0001-1541, 1547-5905. https://aiche.onlinelibrary.wiley.com/doi/10.1002/aic.690220303 (2024) (May 1976).

11. Nguyen, T. A. *et al.* Fungal Wound Healing through Instantaneous Protoplasmic Gelation. English. *Current Biology* **31,** 271–282.e5. ISSN: 0960-9822. https://www.cell.com/current-biology/abstract/S0960-9822(20)31520-7 (2024) (Jan. 2021).

12. Bieleski, R. L. Phosphate Pools, Phosphate Transport, and Phosphate Availability. en. *Annual Review of Plant Physiology* **24,** 225–252. ISSN: 0066-4294. https://www.annualreviews.org/doi/10.1146/annurev.pp.24.060173.001301 (2024) (June 1973).

13. *Spatio-Temporal Image Processing* (eds Jähne, B., Goos, G. & Hartmanis, J.) ISBN: 978-3-540-57418-7 978-3-540-48145-4. http://link.springer.com/10.1007/3-540-57418-2 (2023) (Springer Berlin Heidelberg, Berlin, Heidelberg, 1993).

14. *NetworkX* en. https://github.com/networkx (2023).

Chapter 5

Density of AM fungal networks across the Earth's underground ecosystems

5.1 Full article

This chapter was entirely formated by Justin Stewart. I included it in here with their formating. Details of my contribution are given in at the end of the text.

Main Manuscript for:

Density of arbuscular mycorrhizal fungal networks across the Earth's underground ecosystems

Authors: Justin D. Stewart[1,2,3#*], Corentin Bisot[4#], Rachael I.M. Cargill[5], Michael E. Van Nuland[2], Heidi-Jayne Hawkins[6,7], Loreto Oyarte Galvez[4,5], Malin Klein[1,8], Marije van Son[4,5], Felix Kahane[4], Kai-Kai Lin[4], Renato Braghiere[8], Vasilis Kokkoris[5], Merlin Sheldrake[1,2], Stuart West[10], Thomas Shimizu[4], E. Toby Kiers[1,2]

[1]Amsterdam Institute for Life and Environment (A-LIFE), Section Ecology & Evolution, Vrije Universiteit Amsterdam, Amsterdam, The Netherlands
[2]Society for the Protection of Underground Networks (SPUN), Wilmington, Delaware, USA
[3]Waag Society Futurelab, Amsterdam, the Netherlands
[4]AMOLF Institute, Amsterdam, the Netherlands
[5]Amsterdam Institute for Life and Environment (A-LIFE), Section Systems Biology, Vrije Universiteit Amsterdam, Amsterdam, The Netherlands
[6]Department of Biological Sciences, University of Cape Town, Cape Town 7701, South Africa
[7]Conservation International, Forrest House, Belmont Park, Cape Town 7700, South Africa
[8]Plant Hormone Biology Group, Green Life Sciences Cluster, Swammerdam Institute for Life Science, University of Amsterdam, Science Park 904, 1098 XH Amsterdam, The Netherlands
[9]Jet Propulsion Laboratory, California Institute of Technology, Pasadena, CA, USA, California Institute of Technology, Pasadena, CA, USA
[10]Department of Biology, Oxford University, Oxford, United Kingdom

*Paste corresponding author name(s) here.
Email : justin@spun.earth
Author Contributions :
Competing Interest Statement: No competing interests are declared.
Classification: Ecology
Keywords: arbuscular mycorrhizal fungi, biomass, carbon, extraradical hyphae, mycelial density

This file includes:

Main Text
Figures 1 to X
Tables 1 to X

Abstract:

Arbuscular mycorrhizal (AM) fungi live in symbiosis with >70% of plant species by forming mycelial networks that extend from plant roots. These fungi exchange mineral nutrients for plant carbon and in doing so help move carbon, water and nutrients across ecosystems, shaping global biogeochemical cycles. It is estimated that plants allocate >1 billion tons of carbon to AM fungi each year, a third of the total carbon accumulated in land per year. However, despite the ecological importance of AM fungi, we lack a quantitative understanding of mycelial network density and biomass across the Earth's terrestrial ecosystems. Here, we collated a database of >4K hyphal density samples from both field and pot studies to estimate mycelial network densities. Using geolocated samples, we trained a suite of Random Forest models to predict mycelial network densities across the planet at 1 km^2 resolution. To convert density to biomass, we used an imaging robot to obtain >280K hyphal measurements to parametrize biomass measurements. We found that globally, soils hold ≈130 quadrillion (10^{17}) km of mycelial networks. Stretched end-to-end, this is approximately equivalent to 1-billion astronomical units (Earth-Sun distance). Converted to biomass, this figure equates to ≈340 megatons of carbon, or ≈6x the biomass of humans on Earth. Our models predict that grasslands hold the densest fungal networks, with the Sudd flooded grasslands in South Sudan a global hotspot. We identified a positive relationship between predicted mycelial network density and net primary productivity across different biomes. To our knowledge, we provide the most robust estimates to date of AM fungal density. These estimates are a first step to better include mycorrhizal fungi in global climate and earth system models and underline the importance of mycelial network infrastructure as crucial points of entry of carbon into belowground ecosystems.

Main Text:

Introduction:

The symbiotic partnership formed between arbuscular mycorrhizal (AM) fungi and land plants is one of the most widespread and important mutualistic associations on Earth. AM fungi have shaped global vegetation structure and biogeochemical cycles by facilitating plant access to soil nutrients and water [1–3]. In some cases, AM fungi provide up to 80% and 20% of a plant's phosphorus and nitrogen, respectively[4–9].In exchange for nutrients, plants supply AM fungi with photosynthetically derived carbohydrates and lipids (hereafter, carbon). Using this carbon, AM fungi build networks of extraradical hyphae that extend far beyond the roots system of their hosts – increasing the foraging area of roots by up to 100-fold [10]. As a key entry point of fixed carbon into underground ecosystems, AM fungi play a pivotal role in the global soil carbon cycle: it is estimated that ~1 billion tons of carbon are allocated from plants to AM fungi every year, approximately a third of the total carbon accumulated in land per

year (land carbon sink)[2,11]. The evolution of this partnership coincided with a 90% drop in atmospheric CO_2 as the fungi facilitated the colonization of terrestrial land by plants over 450 million years ago[12–14]. Today, over 70% of terrestrial plant species rely on AM fungi [1] .

Ultimately, the contributions of AM fungi to plant nutrition, soil structure, and carbon storage depend upon the density and spatial distribution of the fungal network itself – known as extraradical mycelium. Extraradical mycelial networks are made up of filamentous tubular cells, or hyphae. Intraradical hyphae grow within the roots of plant hosts. While new tools are still emerging to track intraradical fungal colonization under lab conditions, we also have a limited understanding of extraradical growth, especially in natural ecosystems [15,16].Specifically, it is unknown how the density of AM networks varies across different underground ecosystems across the Earth, or how much carbon AM fungi store at the global scale. Back-of-the-envelope calculations suggest total hyphal length, (i.e., mycelial network stretched end-to-end in the top 10-cm of soil), to be ~4.5×10^{17} km [17]. However, these calculations do not distinguish between different groups of mycorrhizal fungi (ectomycorrhiza vs AM fungi), nor are they spatially explicit. This means there is no information on how hyphal length varies per ecosystem type, nor how our confidence in these estimates (uncertainty estimates) varies depending on ecosystems and available data[17]. To date, most field quantifications have focused on grassland ecosystems[18–20]. However, even within grasslands, hyphal density of AM fungi can vary widely, anywhere from less than 1 cm cm^{-3} soil to 100 cm cm^{-3} [21,22]. Estimating network densities of AM fungi at high spatial resolution is essential to better understand how AM fungi behave across different ecosystem types. Incorporation of biomass and carbon estimates from AM fungi into global Earth system models would reduce uncertainties in predictions of future terrestrial carbon dynamics [23,24]. In addition, these data could allow for future monitoring of mycelial network carbon under different land management schemes.

Until now, obtaining spatially accurate estimates of AM densities and biomass has been limited by three constraints: (i) lack of standardization across datasets, e.g. pot versus field, different plant hosts, soil depths, (ii) lack of models powerful enough to generate both density predictions and uncertainty measurements at appropriate scale, e.g., 1-km^2, and (iii) lack of high-resolution hyphal trait data at microscale needed to convert length estimates into biomass estimates. In particular, quantifying total network carbon requires precise estimates of hyphal volume based on accurate radius measurements.

We resolved these problems by assembling a database of over 4K unique quantifications of extraradical hyphal densities as a measure of mycelial network density for AM fungi based on a literature search that included 11 languages (Figure 1). These data represent both experimental pot studies (48%) and geolocated field samples (52%) in which the density of AM fungal hyphae (hereafter

mycelial networks) were directly quantified and identified as non-septated (e.g. alive) . Geolocated data are particularly informative because technological advances in remote sensing of climate/vegetation and cloud computing can be used to build spatially explicit machine learning algorithms. We used these datasets to train a Random Forest machine learning model in the Google Earth Engine platform on all geolocated field samples[25]. This allowed us to predict the density of mycelial networks at a 1-km^2 resolution across the Earth's underground ecosystems, including deserts, grasslands, forests, and also in agricultural soils. Next, we combined our predictions with datasets of AM hyphal width obtained via high-resolution image analysis, conducted using an imaging robot, of over 280K individual hyphal measurements for 3 species covering a total of 5 strains of AM fungi: *Glomus aggregatum, Rhizophagus clarum*, and *Rhizophagus irregularis*. This allowed us more accurately to calculate the volume and carbon content of mycelial networks averaged across different fungi. The proportion of carbon in mycelial networks were based on published data on fungal dry matter. We repeated image analyses across multiple strains of AM fungi and used Monte-Carlo sampling to calculate the upper and lower bounds of carbon estimates. We also used SHapley Additive exPlanations (SHAP) analyzes to identify the relationship between net primary productivity (NPP) and mycelial network density[26]. Finally, we harmonized data from pot and field studies to model variation in mycelial network density and carbon across different host plants and fungal genera that allowed us to identify specific, species-level patterns.

Results:

Global length and biomass of extraradical hyphae:

Globally, we estimate that there are ~130 quadrillion km (1.3×10^{17} +/- sd 1.9×10^{16}) of extraradical AM mycelial networks in the top 15 centimeters of terrestrial soil (Figure 2 – link to interactive map in caption). The global average is ~818 million km of mycelial networks km^{-2}. To convert our global mycelial network density predictions to global biomass estimates, we measured > 280K hyphal radii by imaging 28 in-vitro mycelial networks covering 3 species and 5 strains, with at least 4 replicates per strain (Figure S1). We then measured the radius of individual hyphae in the mycelial network. Next, we calculated a mycelial network-wide radius, yielding an average radius of 2.6+/- 0.2 µm across all strains and species (Figures S2-3). We used these values to calculate the global volume and biomass of extraradical hyphae. Our model predicts a global sum of which is ~340 Mt C (+/- 70) of mycelial networks in terrestrial soils, with a global average ~2 tons C km^{-2}. By comparison the biomass of the Earth's AM mycelial networks is ≈6x the carbon stored in all human biomass.

Global variation across ecosystems and land use:

Next, we used zonal statistics to ask which underground ecosystems contain the highest and lowest density of AM mycelium. Our model predicted that grassland soils are home to the densest AM mycelial networks on Earth, with a range ~850-950 million km km^{-2} (Table S1). Based on these estimates, the mycelial networks of AM fungi within just ~40 m^2 of grassland soil are long enough to wrap around the equator, and those in ~400 m^2 of grassland soils would reach the Moon. Our predictions suggest that the total quantity of AM fungal carbon in grasslands alone accounts for ~30% of all carbon stored in mycelial networks globally (in other words, grassland AM fungal networks hold ~10-20% more carbon per km^2 than the global average). We predict that African tropical and subtropical flooded grasslands, thickets, and sparsely forested areas hold the densest networks of all grassland ecosystems (Table S1). These ecosystems include the Sudanese flooded grasslands, Zambezian Baikiaea woodlands, Itigi-Sumbu thicket, and dry Miombo woodlands. Outside the tropics, our model predicts dense networks in the Flint Hills and Nebraska Sand Hill ecoregions in North America, Australia's Arnhem Land tropical savanna, and high elevation mountain grasslands including steppe ecosystems globally.

Biomes that cover a vast extent of the Earth's surface are predicted to hold a greater quantity of AM network carbon and total AM fungal length. As the world's largest biome, boreal forests and taigas, covering ~14% of the Earth's terrestrial surface, are predicted to hold a total of ≈65 Mt C. As expected, these ecosystems, dominated by ectomycorrhizal hosts, contain some of the lowest per km^2 densities mycelial networks, averaging 790 million km km^{-2}. These vast ecosystems which are found at high latitudes including the Interior Alaska-Yukon lowland, Copper Plateau, Okhotsk-Manchurian and Northeast Siberian taigas (Figure 2).

Given the large variation in hyphal densities between ecosystems, we next asked if there were ecosystem-specific environmental factors driving these differences, for example soil chemistry and climate. To do this, we assessed the relationship between a range of environmental variables and hyphal length predictions using the SHAP algorithm. SHAP uses game theory to determine how the individual contribution of each environmental variable creates a mycelial network density prediction. Positive SHAP values indicate that a specific variable value was associated with an increase in predicted mycelial network density. In contrast, a negative SHAP value is associated with a decrease in predicted AM network density. The absolute SHAP value ranks the relative importance of each variable in the model from zero to one. We used SHAP dependency plots to visualize the relationship between individual predictors and our model predictions.

The most important predictors of network length were associated with soil texture, nutrients, and climate (Figure S4). Specifically, our model predicted denser networks in soils with low phosphorus

(imp.= 0.9) and low sand content (imp. = 0.8) (Figure 3). In contrast, we obtained hump-shaped predictions for soil nitrogen content (imp. = 0.6) and mean annual temperature (imp. = 0.5). Predictions of mycelial network density increased as the proportion of AM host vegetation increased (importance = 0.2). Using our SHAP analysis, we asked if there was a relationship between net primary productivity (NPP) and mycelial network density. Because AM fungi are obligate symbionts that receive all their carbon from host plants, we expected to find a positive relationship between higher rates of NPP (NPP, importance = 0.2) and mycelial network density. To test this, we fitted a linear-mixed effects model to account for biome-level variation in NPP between NPP rates and SHAP values. We confirmed our expectation, with our model showing that predicted denser networks were located in areas with vegetation that have high rates of NPP. We consistently found this pattern across all biomes, with the exception of tropical and subtropical broadleaf forests (Figure S5).

A major outstanding question is how different land use strategies affect mycelial networks. Given the potential of AM fungi to increase crop nutrition, protect against pathogens and provide water in drought conditions, farmers are increasingly interested in quantifying the abundance of fungi in their fields. Although our data is not high-resolution enough to draw relationships between individual farming practices and network density, we are able to compare predicted mycelial network density across agricultural versus non-agricultural land, within grassy biomes. Using a linear model, we asked how land use influences the predicted density of AM mycelial networks and their carbon storage. We found, on average, non-agricultural grasslands contain higher predicted densities of AM fungal network, equating to ≈75 million more km km^{-2} (≈0.2 tons C, Figure S5). We then asked how much these losses vary across agricultural intensity, here defined as the proportion of managed and cultivated land per km^2. Using dependency plots from our SHAP analysis we identified that hyphal densities decrease as land use intensity increased.

Effects of host plant and arbuscular mycorrhizal fungal identity on extraradical mycelial network density:

Our global analyses relied on geolocated data from ecosystems across the Earth. However, our literature search resulted in a database of extraradical hyphal densities across experimental pot studies (n=1995 samples), as well as some field samples that could not be geolocated (n=287). Although we did not include these studies in our geospatial model, we used these data to test the relationship between plant host species, fungal genera and mycelial network density. Because we were able to account for different experimental designs between studies, these data allowed us to explore more precisely the relationship between host plant, fungal identity and extraradical mycelial network density.

We first combined our pot and field samples into one database of 4141 samples to estimate plant host and fungal identity level effects on extraradical mycelial network density. Next, we coded the host plants into functional groups including herbaceous crops (n= 1600 samples), grasses (n=715), mixed plant communities (n= 672), trees (n= 132), shrubs (n= 529), forbs (n= 387), and tree crops (n= 106). We then recorded the fungal genera identified in each sample (Figure 1). We found eleven fungal genera that were reported, along with "taxonomically unknown mixed communities" of AM fungi, which accounted for the most frequent group (n=2649 samples). The next most frequent fungal genera were *Funneliformis* (n=452), *Glomus* (n=403), *Rhizophagus* (n=395), *Gigaspora* (n=71), *Scutellospora* (n=56), *Claroideoglomus* (n=53), *Acaulospora* (n=51), *Paraglomus* (n=4), *Septaglomus* (n=4), *Diversispora* (n=2), *Entrophosphora* (n=1).

We found a significant effect of host plant and fungal identity on extraradical mycelial network density using linear mixed effect models ($p < 1x10^{-16}$, Figure S7). There was high variation in hyphal densities between plant functional groups. Grasses had the densest predicted extraradical networks (~15 +/- 28 m cm^{-3}), followed by mixed plant communities (~7 +/- sd 13 m cm^{-3}), trees (~7 +/- 18 m cm^{-3}), shrubs (≈6 +/- 16 m cm^{-3}), herbaceous crops (~6 +/- 9 m cm^{-3}, forbs (~3 +/- 3 m cm^{-3}), and tree crops (~2 +/- 7 m cm^{-3}).

We found significant variation in extraradical mycelial biomass production across the fungal genera represented in our database (Figure S7). Unsurprisingly, the mixed communities of fungi displayed the widest range of hyphal densities. However, even samples within a single genus of fungi (e.g. pot studies with inoculum) showed relatively wide ranges of mycelial network density. We found a wide variation in mycelial network density between genera and species isolates. *Scutellospora sp.* (~9 +/- 10 m cm^{-3}) and mixed communities of fungi (~8 +/- 19 m cm^{-3}), produced the densest extraradical mycelial networks. This was followed by *Glomus sp.* (~6 +/- 11 m cm^{-3}), *Acualospora sp. (*~7 +/- 6 m cm^{-3}*)*, *Claroideoglomus sp.* (~5 +/- 7 m cm^{-3}), *Funneliformis sp.* (~5 +/- 7 m cm^{-3}), *Rhizophagus sp. (*~5 +/- 6 m cm^{-3}), *Gigaspora sp. (*~3 +/- 3 m cm^{-3}), *Septaglomus sp.* (~2 +/- 1 m cm^{-3}), *Paraglomus sp.* (~1 +/- 1 m cm^{-3}), and *Diversispora sp*. (~ 0.2 +/- 0.1 m cm^{-3}). To test whether pot and field values were similar, we compared mycelial network densities per cm^3 in pot versus field using linear mixed-effect models. We found no significant difference in hyphal densities between pot and field studies ($p > 0.05$).

Uncertainty in our length and biomass predictions:

Most of the Earth's soils are unsampled for AM mycelial networks. We searched all available literature across 11 languages, but only found samples in English (332 studies, 4056 samples), Spanish (8 studies, 57 samples), Portuguese (3 studies, 22 samples), and French (1 study, 6 samples). This uneven distribution of data introduces a source of uncertainty in our models when predicting in unsampled soils. To address this uncertainty, we quantified error in our mycelial network density predictions and carbon estimates for every km^2 of Earth. First, we calculated uncertainty estimates of mycelial network density using a repeated-prediction method, calculating a per-pixel coefficient of variation and standard deviations. Globally our predictions have an average 10% coefficient of variation and 14% standard deviation. Uncertainty was highest in tropical forests including the Amazon, Congolian, and Southeast Asian Guinean Rainforests (Figure S8). At Northern latitudes, uncertainty was highest in Canadian Shield Forests, the Pontic Steppe, and the Eastern border of the Tibetan grasslands with China's coniferous and broadleaf forests. Uncertainty was lowest in temperate broadleaf and Mediterranean forests, globally.

Next, we spatially assessed where our model is extrapolating outside of the model's training data by comparing the environmental uniqueness of every prediction pixel to the environment. Areas of high extrapolation have low environmental similarity to where our samples are located. This means our model was predicting outside of the input training data, which can contribute to prediction error. Model extrapolation was lowest in Eastern North America, and Central Asian Steppe grasslands. Boreal forests and taigas represent the least represented ecosystems, (Figure S9). Aside from these high latitudinal ecosystems, we found flooded grasslands were areas of high extrapolation, including the Paraná flooded savannas, Sudd flooded grasslands, and the Everglades. Deserts and xeric shrublands also showed signals of high extrapolation.

Lastly, we asked how our carbon predictions are influenced by hyphal width. To date, no consensus has been reached on how to exactly measure hyphal width across a mycelial network. We used a weighted average that considers the total network architecture (e.g. proportions of different sized hyphae, Figure S2) – a methodology commonly applied to other biological networks such as plant root architecture (23). We also used published measurements of AM fungal hyphal width to compare to our imaged hyphae. Although these measurements largely lack information about the variation around mean hyphal width measurements (e.g. standard deviation) and are subsamples of intact mycelial networks, we used these as upper and lower measured widths to generate a distribution carbon estimates. Of these studies, hyphal radii have been reported to range from 0.6 to 9.0 µm, which leads to a 225-fold difference in hyphal volume. To estimate how this change in hyphal volume impacts our carbon estimate, we simulated 1000 hyphal widths between this range, calculating carbon content for each simulation. As expected, small variations in hyphal width led to large changes in carbon

predictions (Figure S10). For example, if the mean radius of hyphae we imaged were doubled, our biomass prediction would quadruple to ≈1200 Mt carbon.

Discussion:

We provide the first global estimates of extraradical AM mycelial network densities and carbon. Our models predict a total of ~130 quadrillion kilometers of extraradical hyphae in the top 15 cm of soils. For context, this length is ≈1-billion x the distance from the Earth to the Sun. Based on the mean hyphal radius obtained by imaging, the total surface area of these AM fungal hyphae would cover an area ≈4x the surface area of the Earth. Given hyphal turnover is estimated to be 0.1-6.3 x $month^{-1}$ (24–28), we calculate that AM fungal hyphae have the potential to explore up to ~80-5000 million km km^{-2} of soil pore space every month.

Our predictions reinforce the importance of AM mycelial networks as extensive infrastructure for carbon entry into belowground ecosystems. Although the intact and alive mycelial network biomass itself does not represent a significant fraction of the soil carbon pool (~0.2% of 1700 Gt), most plants depend on AM fungi for nutrient acquisition which almost always results in increases in plant biomass – both above and belowground (29, 30). Back-of-envelope calculations estimate that global plant biomass would decrease ~15% (-70 Gt C) if plants were not in symbiosis with AM fungi (29, 31). However, this varies both across plant species and soil conditions. While this estimation has associated uncertainties, see *Methods* Equation B, this calculation reinforces the magnitude of the plant-AM fungal symbiosis on the global nutrient budget. Still, our prediction of mycelial network density and biomass in the Earth's soils is likely an underestimate of the total biomass of all mycelial networks on Earth - our model predictions are limited to topsoils (0-15 cm) and only include AM fungal mycelium. Ectomycorrhizal fungi (EM) are thought to have even more extensive mycelial networks than AM fungi reaching up to 2 km cm^{-3} fresh soil and a relatively slow hyphal turnover of several months[27,28]. Further, our predictions are limited to the living fraction of AM mycelium, as all our samples only included alive, and non-septated mycelium – meaning that dead or partially degraded mycelial networks are not included in our estimates. When considering rates of AM hyphal production, estimated as 33.9-49.7 tons C km^{-2} yr^{-1}, mycelial carbon inputs into soils are comparable to inputs from fine root production[21,29]. These rates, although limited to a single study in grasslands, suggest it not the living stock mycelial networks but instead the turnover (e.g. production and stabilization of necromass) that is the major mycelial carbon sink. This reinforces the idea that mycelial network

infrastructure acts as a delivery system to transport carbon to soil microsites for mineral associated organic matter formation[18,29].

We found that grassy ecosystems hold the densest AM mycelial networks on Earth. This is particularly important because we already know that grassy ecosystems are a “reliable carbon sink”, storing much of their carbon belowground vs, e.g., forests that are susceptible to losses of aboveground biomass carbon via harvesting and fire [30,31]. Our study helps characterize the role of mycelial network infrastructure as part of this reliable carbon sink in grasslands. Despite their importance, grasslands are some of the most threatened but least protected ecosystems on Earth, recent work found that ~95% of grasslands containing global AM fungal biodiversity hotspots are unprotected by current conservation schemes (V1 SPUN, In Review, [32]). Diverse drivers of change (e.g., habitat loss to agriculture; altered regimes of fire and herbivory, climate change) interact to threaten mycelial networks in grasslands, resulting in different outcomes such as desertification but also woody plant encroachment and greening [33,34]. For example, if desertification continues in the Central Asian grasslands at its current pace, the Kazakh Forest Steppe faces potential losses of ~67 million km km^{-2} of AM fungal hyphae through desertification, stretched end-to-end this is ~270 trillion km[35]. In grasslands, such as the Indian Western Ghats, the major threat to network density is the invasion of exotic plant species[36]. In the semi-arid grasslands of inner Mongolia, loss of mycelial networks is aggravated by the introduction of non-arbuscular mycorrhizal fungal hosts as with the planting of *Pinus* trees [36,37]. Similarly, afforestation plans for primary grassy ecosystems in Africa, misidentified as degraded forests, threatens their biodiversity, possibly without any gains for ecosystem carbon [38]. Since very little is known about the AM fungi of African biomes, these networks may be lost before we enumerate them[2,34].

We identified a significant loss of mycelial network density in agricultural fields compared to unmanaged grassy ecosystems with an average loss of ~69 million km km^{-2} . Our SHAP analyses also showed that the intensity of agriculture was correlated with sparser networks holding less carbon. Agricultural land is expected to expand ~700K-1000K km^2 by 2050, putting some ≈48-69 trillion km of mycelial network infrastructure at threat, mostly in Sub-Saharan Africa[39,40]. Agricultural soils are arguably the most degraded soils on Earth with the largest under-saturated pools of mineral associated carbon[41]. Strategies are being developed with the goal of reversing soil degradation in agricultural fields. In fact, initiatives including the European Union’s “Soil Deal for Europe" and “Roads to Removal” in the United States of America aim to increase carbon storage in agricultural fields[42,43]. The infrastructure provided by dense mycelial networks as points of carbon entry into degraded agricultural fields is likely crucial to achieving these goals.

Our SHAP analyses were able to explain global variation in mycelial network density. We identified the most important variables related to the plant-AM symbiosis – soil phosphorus, texture, and nitrogen content. This analysis also allowed us to explore for the first time at the global scale, while controlling for differences in climate and soil chemistry, the relationship between NPP, dominance of AM host vegetation, and mycelial network density. Still, this can be improved with increasing sample coverage, especially in underexplored ecosystems (e.g. the tropics). Further, we also found that pot studies are good experimental proxies for mycelial network density in natural soils. This means treatments commonly applied to pot studies (e.g. tillage, warming), can help inform future spatial models of mycelial network density. SHAP analyses can help researchers design future experiments by identifying which variables should be manipulated or closely monitored when quantifying changes in mycelial network density. Accurately identifying variables that impact AM network density is important as there has been recent demand for increased experimental work to validate and improve theoretical global climate models and keep up with the increasing pace of "Big Data" being generated in ecology and evolution[44].

Our work also highlights the importance of populating carbon models with micro-scale trait data across entire mycelial networks. Here we used the values of hyphal width imaged across > 280K individual hyphae, calculating a network-averaged hyphal width. Past work has estimated, on average, AM fungal hypha radii to range from 0.6 to 9 μm[45]. However, these measurements have not discriminated between the distributions of thicker vs. thinner hyphae, making previous estimates of width across a network uncertain. It is important to consider hyphal radius because even small changes in the radius of hyphal 'cylinder' result in big changes in total mycelial network volume (e.g. volume = $2*pi*r^2$). However, it is unclear how a growing mycelial network proportionally invests carbon in the construction of hyphae of different radii. Exhaustive radii measures over a whole network colony are required to precisely estimate precisely the average radius to convert length to volume. Steps forward for improving this mycelial network carbon estimates rely on linking taxon-specific abundances and hyphal radii to specific plots of land, namely: (i) measuring micron-scale trait data for more fungal species across whole fungal network architectures, (ii) sampling the Earth's soils to identify the most abundant fungal taxa found in different land use types, and (iii) generating global species distribution models to identify species ranges. The infrastructure for completing these steps is already in place and include culture collections (e.g. ≈340 strains in the International Collection of Vesicular Arbuscular Mycorrhizal Fungi), soil sampling campaigns focused on AM fungi (e.g. the Society for the Protection of Underground Networks (global), and Dig Up Dirt (Australia), and computing power of the Google Earth Engine platform[25,46–48].

Our census of the Earth's AM fungal hyphae draws on all available to produce a database of hyphal densities sampled in the Earth's soils and pot studies. The integrated database allowed us to estimate the global length of mycelial networks, densities between ecosystems, and across different vegetation types. These data were also key to identifying and quantifying certain threats to dense fungal networks. Importantly, our research has identified research gaps such as uneven distribution of sampled soils on Earth[49]. Meanwhile, how much carbon constitutes these mycelial networks and soil carbon stocks is limited by our lack of trait data for most species of AM fungi (e.g. radius, turnover, respiration). We also identified the Earth is unevenly sampled for AM fungi. Searching the literature in multiple languages helped increase our geographic spread. Still, filling in these knowledge gaps and reducing uncertainties relies on inclusive action and global collaboration to sample the Earth's AM fungi, and answer recent calls to build mycorrhizal trait databases[50]. Only by completing these steps will we generate an improved understanding of AM fungal hypha in the global carbon budget.

Methods:

Constructing an AM fungal extradical hyphal density database:

We first gathered extraradical hyphal density data using a literature search. We searched Google Scholar and Scopus with the keywords 'hyphal length', 'hyphal density', or 'hyphal biomass'. We then selected studies that identified AM fungi and measured extraradical hyphal length. One method was used to measure extraradical hyphal density across all studies. This method works by extracting hyphae from soil samples using variations of the membrane filter technique[51,52]. Hyphal densities were then determined by the modified gridline intersect method[52]. Staining of associated fungal structures and microscopic observations of morphological features discriminated against AM fungi in samples across studies (e.g non-septate hyphae). As AM hyphae form septae when dead, our data is limited to samples which identified alive AM fungal hyphae, and lacks information on dead/decomposed hyphae. We repeated this query across eleven of the world's most common spoken languages to look for possible samples in areas with known soil microbial data gaps (20). Specifically, we searched in the following languages: Dutch, English, French, German, Greek, Hindi, Indonesian, Korean, Portuguese, Russian, and Spanish. While data we only found in English, Spanish, French, and Portuguese, we highlight that these efforts greatly improved the geographic spread and inclusivity of data. For instance, almost all South American studies were found in Spanish and Portuguese queries.

For each study, we recorded if measurements were made in the field or a greenhouse pot study and categorized dominant plant species by plant functional type (herbaceous crop, tree crop, grass, mixed community, forb, or shrub). We also recorded the genus of each fungal symbiont if reported, for

example in pot studies that used inoculation; however fungal taxonomy was not reported for most field studies (e.g. bulk soil samples with mixed fungal communities). The field studies comprised 2146 individual samples and 1995 pot samples. Only geolocated field studies were used for spatial modeling which come from 1859 unique 1km^2 grid cells, i.e. pixels. The geographic distribution of the samples, host, and fungal genera in our database can be found in Figure 1.

Our field sample database includes samples found on every continent in 9 out of 14 Global vegetated biomes (deserts and xeric shrublands = 61, Mediterranean forests, woodlands and scrubland = 78, montane grasslands and shrublands = 163, temperate broadleaf mixed forests = 813, temperate conifer forests = 42, temperate grasslands, savannas and shrublands = 458, tropical and subtropical dry broadleaf forests = 17, tropical and subtropical grasslands, savannas and shrublands = 109, tropical and subtropical moist broadleaf forests = 118). The pot studies were used in combination with the field studies in modeling the relationship between extraradical hyphal density and host plant/fungal identity (see *Estimating plant host and fungal identity effects* below).

Reported values of hyphal density were unit standardized to m hyphae cm^{-3} soil. For studies in other units (e.g. cm g-^{1}) soil bulk density (BSD) values were used to convert to the standard unit. If BSD was not reported, we estimated it using the SoilGrids BSD layer at 5–15-centimeter depth[53]. If no data was available on BSD at the location of a site or the location was unknown, a BSD value of 1.0 was assumed.

Global predictions and drivers of AM mycelial network density:

We created spatial predictions of AM mycelial network density using a Random Forest regression (RF) algorithm (modified from the pipeline developed by Van den Hoogen 2021)[54]. Briefly, we trained an RF algorithm to learn relationships between hyphal density, environmental and project-specific covariates, and then used these relationships to make predictions of mycelial network density across geospatial environmental data layers. We assembled a global stack of environmental predictor layers and sampled this stack at the locations within the dataset. In total, 34 environmental layers were used including macroclimatic, soil chemistry and texture, land use, vegetation, and topographic variation indices. The details of these layers including units and sources are described in Table S2. All spatial covariate layers were harmonized into a uniform pixel grid projected in EPSG:4326 (WGS84) at 30 arc-second resolutions (~1-km^2 at the equator). Areas where low or no vegetation is expected were excluded from analyses. These included areas covered by permanent snow or ice (e.g. glaciers, Greenland ice cap, Antarctic regions, defined by SoilGrids), barren regions (sparsely vegetated areas defined in EarthEnv), and cities or highly built-up areas[53,55].

A set of project specific variables were generated to correct for study differences that may affect variation in hyphal density measurements. For this, vegetation type was one-hot-encoded based on the main vegetation type of the study. To account for the uneven distribution of samples taken on Earth we created a sample density layer to incorporate as a model covariate[56]. The goal of this was to account for spatial effects not related to the environmental layers. Specifically, we created a kernel density interpolation of distance to sample locations with uniform decay at 0.1 degree from sample locations (created in QGIS 3.24). Distances were then rescaled from zero to one: values of zero indicating an unsampled area, and values of one being a sampled location. This layer was included as a covariate in the stack of environmental predictors used for modeling. Lastly, we included the sample size of each study and soil depth used for each sample in our model to account for differences between studies.

The Random Forest (RF) regression algorithm was used to generate predictions of hyphal density using the Google Earth Engine cloud computing platform[25]. For this, thirty RF regression models were fitted as a function of all previously described predictors. We iteratively tuned the RF hyperparameters (i.e., variables per split [4, 6, 8, 10, 12] and minimum leaf population [2, 4, 6, 8, 10, 12], while growing the forest to 250 trees. All models were fitted on a log+1 transformation of the response variable. The model predictions were then back-transformed to m cm^{-3}, converted to km km^{-2} and then integrated to a soil depth of 15cm.

We then examined which covariate layers were most impactful on mycelial network predictions produced by the RF model. Variable importance scores were calculated using SHAP (Shapley Additive exPlanations) values[57]. SHAP values are a helpful tool to explain the process of how tree-based models reach a specific prediction, like summarizing the magnitude and direction of specific predictors on the target variable. We calculated the SHAP values using the Python (3.9.7) package *shap* on all environmental predictor variables[58]. Briefly, SHAP values show how an increase or decrease in a predictor variable influences a zero-centered prediction of hyphal length. Partial dependency plots were produced using *fastshap* in R (4.2.0)[59].

Model validation, uncertainty, and extrapolation:

There is not a single consensus on the most appropriate spatial model validation and concerns have been raised over the independence of training and testing sets in model validation. Projects that incorporate our predictions should include the uncertainty estimates in their analyses.

We applied multiple cross-validation strategies at both local and global scales to address recent critiques of spatial predictions using machine-learning models. First, we generated global metrics of model fit using three scenarios. (1) A biome-stratified 10-fold cross validation that was repeated for each of the top 10 models fitted which resulted in a performance of R^2: 0.70-0.79 and RMSE: 0.46-0.5 meters hyphae/cm^3. (2) Next, we used a leave-one-out (LOO) approach where the model was trained on all but one pixel and then iterated throughout the dataset producing a similar R^2: 0.72 and higher RMSE: 1.75 meters hyphae/cm^3 (Figure S11). (3) Our most conservative and computationally expensive approach was a spatially buffered leave one out (bLOO) cross validation[60]. bLOO is similar to the LOO method however each fold was generated to leave out points within a range of distance bands [1, 2, 5, 10, 20, 50, 100, 500, 1000, 2000] km. The largest distance band was chosen based on minimizing the distance between sample and prediction locations (Figure S12)[61]. This method showed, as expected, and observed in other studies, that model performance rapidly declined further away from sample locations (R^2: 0.13-0.02 and RMSE: 1.75 m cm^{-3}, Figure S13)[62].

Per-pixel estimates of model fit were used to generate local assessments of model uncertainty. These estimates are helpful given the high variability of global model fit metrics as described above. For this, a repeated prediction method was used. We created 100 bootstrap samples by resampling the dataset, with replacement, stratified across biomes. The best fit model was then fitted on the bootstrapped samples and a prediction layer produced. The mean prediction across the bootstrapped layers was used as our final estimate of per-km^2 hyphal length. These layers were then used to create local uncertainty estimates by calculating the standard deviation and coefficient of variation. Pixels with high local uncertainty indicate areas where the model predicted different hyphae lengths upon each bootstrap iteration compared to areas with low uncertainty estimates.

We further explored the role of spatial structure in our model residuals by testing for spatial autocorrelation using the *SpatialRF* package in R[63]. The *Moran's I* test statistic was produced at a variety of distance bands. Significant, albeit extremely weak (Moran's I: -0.002, $p < 0.05$) spatial autocorrelation was found for distances less than 5000 km. A series of Moran-eigenvector-maps were then generated to include in the model to reduce the present spatial autocorrelation but produced insignificant effects on the Moran's I statistic. We conclude that effects of spatial autocorrelation on our model residuals were weak and not introducing bias in our model given the near-zero coefficient and small spatial scale of autocorrelation.

We identified areas of high model extrapolation by examining the degree of underrepresented environmental/climatic conditions in the training dataset. For this we computed principal components (PCs) for the data to collapse the feature space to fewer dimensions. Next, PC axes were summed to

account for 90% the variation in the environmental feature space. We then evaluated the coverage of the environmental data per-pixel as being internal or external to the convex hull circumscribing the combination of PC axes. We defined the degree of model extrapolation as the proportion of total pairwise combinations for which a pixel lies within the convex hull.

Imaging hyphal network architecure:

Estimating carbon from hyphal length predictions:

Upon calculation of a mycelial network density prediction layer, we converted these data to amount of biomass (measured in megatons carbon, Mt). The amount of carbon per km^2 was estimated using Equation A. To estimate the total carbon in the total length of hyphae we first estimated the corresponding total volume of the hyphae. This was done by assuming all hyphae were cylinders of an effective radius r_{eff}. The effective radius is the square root of length weighted squared radius of all hyphae observed in fully grown colony in axenic conditions (Coco Chapter 2 - Cite). This method of measuring hyphal provides information on hyphal width across an entire network with different classes of hyphae (e.g. runner hyphae and branched absorbing structures), where similar methods are described and suggested for other biological networks such as root system architecture [64].

To measure such effective radius, we established 28 root-organ culture colonies of 3 species and 5 strains of AM fungi in axenic conditions, names *Rhizophagus irregularis* (strains: A5, C2, C3), *Rhizophagus clarum*, and *Glomus aggregatum*, with at least 4 replicates per strain. We established the cultures using a 9 cm split-compartment Petri plate system. The system contained a fungus-only compartment separated from a second compartment that contained Ri T-DNA transformed carrot root (*Daucus carota*) inoculated with a plug of medium containing fungal spores and hyphae. We used Modified Strullu-Romand (MSR) media to establish the cultures and modified the MSR medium in the root compartment to a 1% concentration of phosphate, compared to the fungal compartment, to encourage symbiosis formation. MSR medium was supplemented with 10 grams $liter^{-1}$ of sucrose and 3 grams $liter^{-1}$ of Phytagel as a solidifying agent. The fungal compartment contained a layer of cellophane that encouraged the fungus to grow on a 2D plane and enable imaging of the developing mycelial network. The cultures were imaged every 2 hours with an imaging robot as described in (Figure S1, Traveling Wave Cite). Briefly, to obtain fungal network images, we used our custom-built high-throughput imaging robot to generate high-resolution images of the fungal network every 2 hours for ~30-35 days. The imaging platform was temperature controlled (25 °C) in a dark-enclosed environment with a camera-lens-illumination system that moved together across the samples allowing imaging of multiple plates simultaneously. To achieve this we constructed a customized microscope –

12MP CMOS camera (Basler acA4112-30um) with a 2x objective lens (TL2X-SAP - 2X Super Apochromatic) to take high resolution images (1pixel =1,725mum). This allowed us to generate a full-plate-image composed of a matrix of 10x15 images (5x7mm2 each) with a 20% overlap.

We then selected the timestep corresponding to fully grown colonies (~3-4 days) and used a combination of frequentist and deep learning methods to evaluate the length and radius of all hyphal edges present. This allowed us to find the effective radius r_{eff} for each strain so that their total biovolume V can be linked to their total length L with the following formula $V = \pi r_{eff}^2 L = \sum_{e \in E} \pi r_e^2 L_e$. Considering E to be the set of all edges (individual hyphae) and L_e and r_e to be respectively the length and radius of a given edge e, we can obtain r_{eff} with the following formula $r_{eff} = \sqrt{\frac{\sum_{e \in E} r_e^2 L_e}{L}}$. We then used fixed ratios true for most biological material to convert this total volume to a carbon mass, still this number can be improved with data specific to the AM fungal cell. We use a ratio of dry mass to wet mass, $\boldsymbol{p_{dry}}$, which is generally estimated to be 21% for fungi [65]. Next we assume the ratio of carbon in dry mass, $\boldsymbol{p_{carbon}}$, that we set to 50% [66]. Last we estimate the density of the AM cell, $\boldsymbol{d_{cell}}$, which is estimated to be 1.1 g/cm^3 [65]. This is then multiplied by a soil depth of 15cm.

$$Carbon\ (kg\ km^{-2}\ cm^{-3}) = \text{density prediction} * \pi * {r_{eff}}^2 * \ d_{cell} * p_{dry} * \ p_{carbon} * \text{depth}$$

Equation A. Formula for estimating the total amount of carbon per km2 based on hyphal length and groundtruthed data on hyphal radius. The r_{eff} used in this equation was the mean across all species and strains. We recalculate this formula with the standard deviation this mean r_{eff} and with our density predictions to generate uncertainty estimates in carbon content.

We calculated standard deviations around our carbon estimates by combining the model standard deviation with the standard deviation of radii measurements across strains at the biome and global scale. For this we generated normal distributions of predicted length of hyphae for each biome using the biome sum and standard deviation. We also generated a normal distribution from the mean and standard deviation radii values. A distribution of length and radii values were created using Monte-Carlo sampling (3000 draws per biome). These were then used input into Equation 1 to generate a distribution of uncertainty estimates per biome.

We then ran a sensitivity analysis on our carbon predictions by simulating different hyphal widths. For this we tested how carbon estimates change if hyphae were smaller or larger than those that we imaged. First, we generated 1000 hyphal widths from 0.06-9 µm, recalculating Equation A for each simulation.

Estimating plant host and fungal identity effects on hyphal density:

We combined our field and pot studies to ask how hyphal densities vary across different plant hosts and with different fungal genera. First, we compared our field sites to measurements of hyphal length density in pot studies. Specifically, we test if mean values of hyphal density in field studies are comparable to those reported in pot studies. This is helpful to identify if studies of hyphal density performed in greenhouses are comparable to what is measured in the field. We identified that pot and field studies did not differ in mean reported extraradical hyphal densities (linear mixed effects model, $p > 0.05$).

Next, we used linear mixed effects models fitted with the *lmer* package in R (4.2.0) to estimate plant host and fungal identity (genus) effects[67]. First, we fitted an intercept only null model and then a model with plant functional group as a fixed effect, then with fungal identity alone. Next, we fitted an additive model with both plant functional group and fungal identity. All models were fitted with the source study as a random effect. The best model was identified as the additive model as determined using an ANOVA comparison to the null model ($p < 0.001$) and comparison of Akaike Information Criterion values. This additive model was then assessed to be well fitted using posterior predictive checks, the normality of residuals, homogeneity of variance, and a $R^2 = 0.78$. We then calculated the mean and standard deviation hyphal density per plant and fungal group and plotted these values.

The effect of agriculture on mycelial network density:

We then quantified the effects of agriculture on our mycelial network density predictions, by comparing hyphal densities in cropland and non-agricultural vegetation in grassy biomes. For this we extracted land use information using the ESA WorldCover dataset, sampling 100K random points, and filtering this dataset to cropland, grasses, shrubland, and grassy savannas (which we combined into one category, here termed grasslands)[68]. Next, we calculated the mean difference in mycelial network density per land use. We then fitted an intercept only null model on hyphal length predictions, and a model with land use as a fixed effect. Models were compared using a Chi-Squared test and comparing AIC values. We found that the land use model significantly differed from the null model and had a lower AIC value. Next, we used our SHAP analyses to ask how land use intensity impacts our hyphal length predictions.

Estimating vegetation biomass in a world without plant-AM fungal symbiosis.

The goal of this estimation is to put into context the importance of AM fungi in global carbon stocks and is best interpreted in the context of our assumptions below. Specifically, we estimate how much plant biomass would decrease without AM fungal symbiosis.

Given the following assumptions we calculate global plant biomass in the absence of AM fungal symbiosis. We assume plants are in symbiosis (e.g. colonized) with AM fungi. Most plants (70% species) on Earth form symbioses with AM fungi[1]. Likewise, we assume lack of the plant-AM symbiosis will cause a loss of plant biomass. This is an estimate based on numerous studies, but ultimately, cannot be tested in reality at the global scale. We assume the symbiosis with plants and AM fungi is mutualistic, with benefits being provided to the plant, namely increased biomass. The mycorrhizal symbiosis on average increases plant biomass, as identified using a meta-analysis, but it is worth noting this is not always the case[69]. We assume a global plant biomass of AM hosts as ≈176 Gt carbon. This estimate was made by using the most recent global estimate of global plant biomass, which estimates 450 Gt carbon[66]. We then reduced this estimate by removing biomass estimates for cryptogamic crusts, seagrasses, and marine algae, yielding 442 Gt. We further reduce the estimate by multiplying it by the global mean proportion of AM vegetation on Earth, this proportion was calculated as 40%, from global maps of AM vegetation dominance[70]. We note using this mean value is a source of uncertainty, as the biomass in tropical forests regions with high AM vegetation cover is likely underestimated, and we are overestimating biomass coming from regions with non-AM hosts, e.g. cropland with non-mycorrhizal plants (e.g. brassica crops), as well as coniferous forests.

First we used a log effect ratio that quantified plant biomass benefits in colonized vs uncolonized plants based on a meta-analysis of 420 studies $\ln(biomass_{colonized}/biomass_{uncolonized})$, which was calculated as 0.49[69]. Using our global biomass estimate, corrected for the global mean proportion of AM host vegetation, we create Equation B. $biomass_{global} \times 1 - e^{-\ln(biomass_{colonized}/biomass_{uncolonized})}$. By solving Equation B, we estimate that without AM fungal symbiosis, global plant biomass would decrease ≈70 Gt of carbon, approximately 15% of plant global biomass.

Context calculations:

The numbers presented in this study are so large they are difficult to comprehend without context and comparison to other distances, surface areas, and ecosystems. Thus, we calculated multiple comparisons to provide context on the scale of our predictions.

A) Surface area: We calculated the unfolded surface area of our prediction to put in context both our length prediction and our width data. For this we calculated the area covered using the formula for the surface area of a cylinder. Using the effective radius value from our

imaged fungal networks, this yields 2.2 x 10^9 km^2. We then compared this surface area estimate to the surface area of the Earth, 5.1 x 10^8 km^2. Comparing these surface areas results in the surface area of extraradical fungal hyphae being ≈4x the surface area of the Earth. Strictly speaking, a surface area specific effective radius should have been used but we consider that this does not largely affect this calculation regarding orders of magnitude.

B) Distance: We also put our data in context using distance comparisons. For this we compare our prediction of hyphal length, if stretched end-to-end as 1.3 x 10^{17} km, to the distance of the Earth to the Sun (~150 x 10^6 km). The ratio of these lengths results in our global prediction being ≈1 billion x the Earth-Sun distance.

C) We also produced comparisons for the grasslands where we predicted the Earth's densest mycelial networks. For this we identified how many square meters (m^2) of grassland would hold mycelial networks that if stretched end-to-end would equal the distance from the Earth to the Moon. Across all grasslands we predicted ~1000 km hyphae/m^2. This means that hyphae are long enough to wrap around the Earth's equator (~40000 km) in 40m^2 of grassland. In 400m^2 of grassland, hyphae are predicted long enough to reach the moon (distance of ~380000 km).

D) Kazakh Desertification: Desertification is a threat to many Central Asian grasslands. The Kazakh forest steppe in particular is at threat due to historical land use change and the expanding Kazakh semi-desert at the southern border[35]. Here we forecast what the mycelial network density of the Kazakh forest steppe would be, assuming desertification expanded from the south. To obtain our estimate we multiplied the difference (loss potential) between mean hyphal densities predicted in the forest steppe and the Kazakh semi-desert (~67 million km/km^2) by the area of the Kazakh forest steppe (~4 million km^2), resulting in an estimate of ~270 trillion km of hyphae that could be lost to desertification.

Unquantified uncertainties in our study:

Our study estimates the global length of extraradical hyphae in soil but there are inherent uncertainties we could not explicitly address. We list these uncertainties below:

1. The size of fully intact mycelial networks is unknown. In this study we do not provide evidence for one continuous common mycorrhizal network, at any scale from global to an individual 1km^2 pixel. Our length estimates all are estimates of hyphae stretched end-to-end.
2. The proportion of mycelial network carbon that is intact but dead, or partially decomposed. This study carefully assembled a database where the hyphae belong to arbuscular mycorrhizal fungi by rejecting studies that showed uncertainty as to whether the

mycelium was from AM fungi, or was dead AM fungal hyphae (e.g septated). Thus our prediction is limited to a “standing stock” of alive fungal networks.

3. The hyphal width measured in this study is representative of arbuscular mycorrhizal fungi found in the field. Our study used hyphal width values from 3 species and 5 strains, including ones found globally, to estimate global hyphal volume and biomass. Still, we lack information on hyphal width across the AM fungal phylogeny.

4. Our conversion from hyphal volume to biomass. We assume the dry weight and carbon content of extraradical hyphae using known averages as first-attempt approximations of arbuscular mycorrhizal biomass. While this value likely varies across both individual hyphae and taxa, there is no current estimate for dry weight and carbon ratios for arbuscular mycorrhizal fungi. These unknown values are a major gap for carbon research that incorporates arbuscular mycorrhizal symbiosis.

Acknowledgments:

The authors thank Rob Phillips, the Mycorrhizae lab at VU Amsterdam, and Wessel Padberg for their helpful conversations on this project. We thank James Weedon for reading an early draft of this manuscript. We also thank Johan van den Hoogen for advice on setting up Google Earth Engine. SPUN is supported by grants from the Jeremy and Hannelore Grantham Environmental Trust, Paul Allen Family Foundation, the Schmidt Family Foundation. JDS, ETK, and MK also acknowledge support from NWO Gravity Grant MICROP (024.004.014), NWO-VICI (202.012) HFSP (RGP 0029), and an Ammodo grant. VK and RC are funded by the European Union (ERC, Programme - HORIZON, acronym - NUCLEAR MIX, Project - 101076062). HJH was supported by Conservation International’s Friedman Fellowship (WFF – 1000896). Part of this research was carried out at the Jet Propulsion Laboratory, California Institute of Technology, under a contract with the National Aeronautics and Space Administration. California Institute of Technology. Views and opinions expressed are, however, those of the author(s) only and do not necessarily reflect those of the European Union or the European Research Council. Neither the European Union nor the granting authority can be held responsible for them.

Author Contributions:

JDS, CB, RC, and ETK conceptualized this study. JDS, CB, RC, and VK performed the literature review. JDS conducted the spatial modeling and wrote the first draft. MvN provided feedback about the spatial modeling. MK and MvS helped grow the fungal cultures. LOG, CB, RC, FK, TS, and KL

performed the hyphal imaging and developed the method for measuring hyphal width. All authors provided feedback on this manuscript and contributed to writing the final draft.

Conflict of Interest Statement: ETK is one of the founders of Society for the Protection of Underground Networks (SPUN).

Data Availability Statement: Data and maps will be archived and made available on Dryad prior to publication. Interactive maps will be produced using the Google Earth Engine platform.

Code Availability Statement: Code will be made available on Github prior to publication.

Figures:

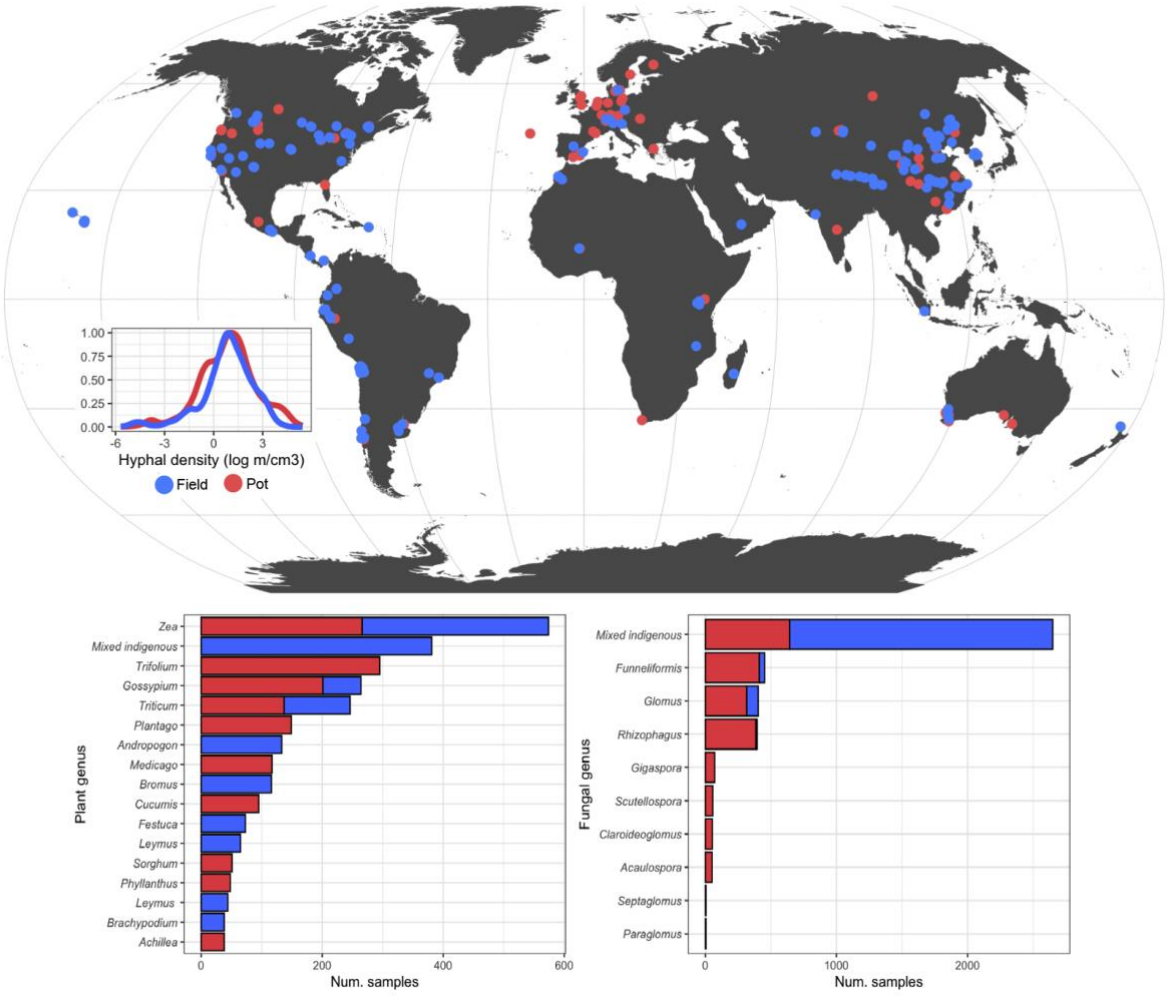

Figure 1: Map of sample locations for field (blue) and pot (red) studies. The field studies were used in our geospatial model to predict the global length of arbuscular mycorrhizal fungal extraradical hyphae. The pot studies were used only for the plant and fungal identity analyses as they do not represent field conditions. The pot studies were geolocated to where the study sourced soil, and if not described, then to the location of the study's institution. The insert panel shows the distribution of the density values, log transformed to aid interpretation for both pot and field studies. The bottom two panels show on the left, the ten most frequent genera for both pot and field studies. On the right are all fungal genera in the database of pot and field studies. Both *Paraglomus* and *Septaglomus* had four samples each in pot studies.

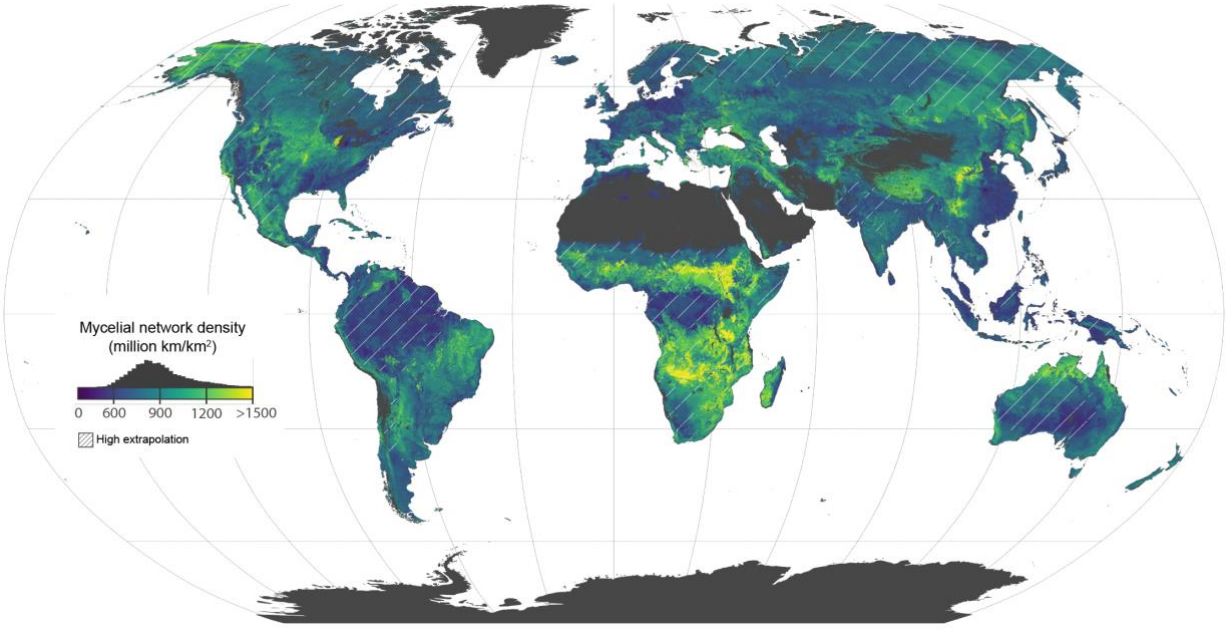

Figure 2. Global map showing the predicted density of mycelial networks produced by arbuscular mycorrhizal fungi. Here, the map is colored by the density of mycelial networks per km^2 of terrestrial land. Brighter colors indicate longer networks and darker colors indicate shorter networks. Areas in grey are not included in the model (e.g. Sahara Desert or Antarctica). We display areas where there is low environmental similarity (less than 95%) compared to the environment where the training data is located as being covered with white hatching (see *Methods* for details on this procedure).Values above 1500 million km were rare and were clipped to 1500 million km for visualization purposes. Biome level summaries can be found in Table 1. An interactive app of the density map shown here can be found at "https://ee-justin618s.projects.earthengine.app/view/hyphaldensity". In this app users can define areas of interest (AOIs) to summarize mycelial network density based on user defined polygons.

Maps of low environmental similarity and per-pixel prediction uncertainty can be found in figures S7-S8, and are also available for download to use for modeling.

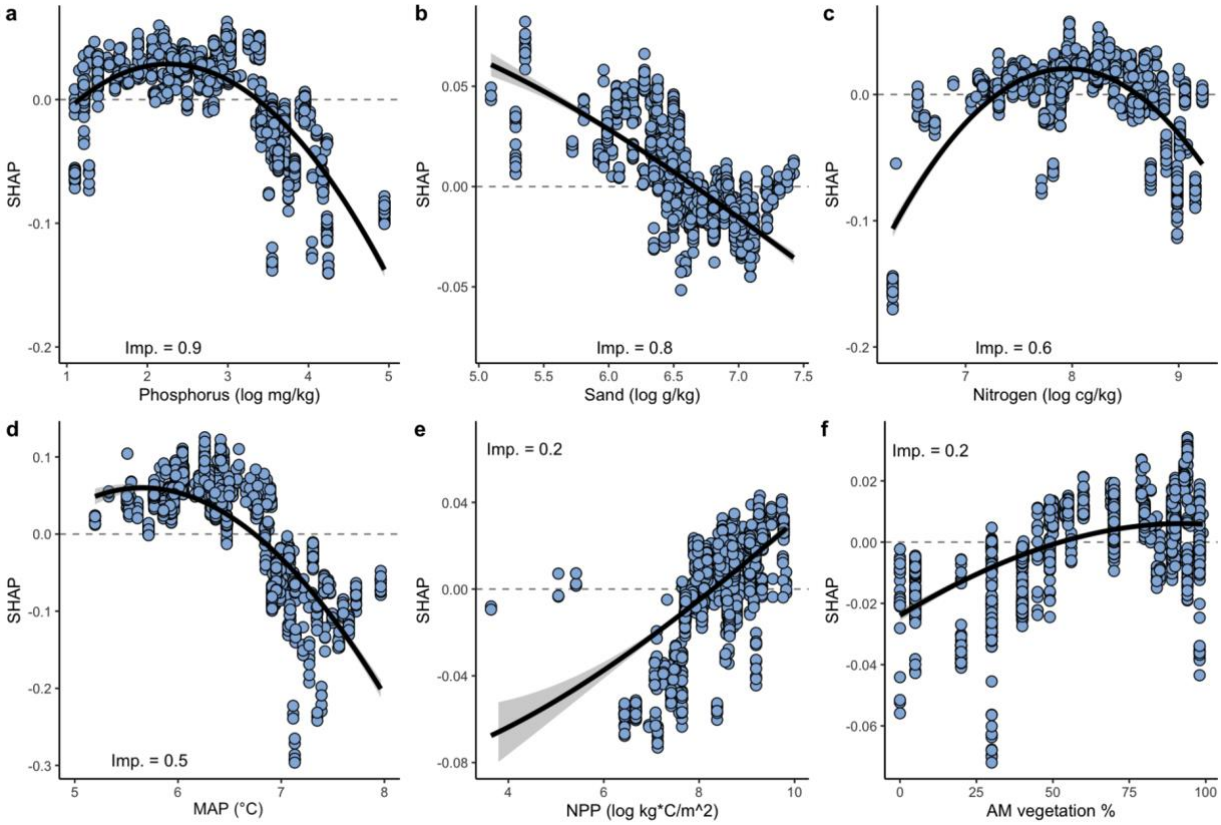

Figure 3: Multi-panel figure showing the top four most important variables identified by our SHAP analysis (a-d) and biologically relevant predictors (e-f) of mycelial network density. Each plot shows the SHAP value on the y-axis, where + and – values indicate increases and decreases in mycelial network density respectively, divided by a dashed line indicating no difference. The x-axis shows the individual variable of interest, all log transformed. The black line is a loess smoothing of the relationship between the variable and SHAP values. Within each plot is the absolute SHAP value, indicating the global importance (Imp.) across all variables, scaled from 0-1.

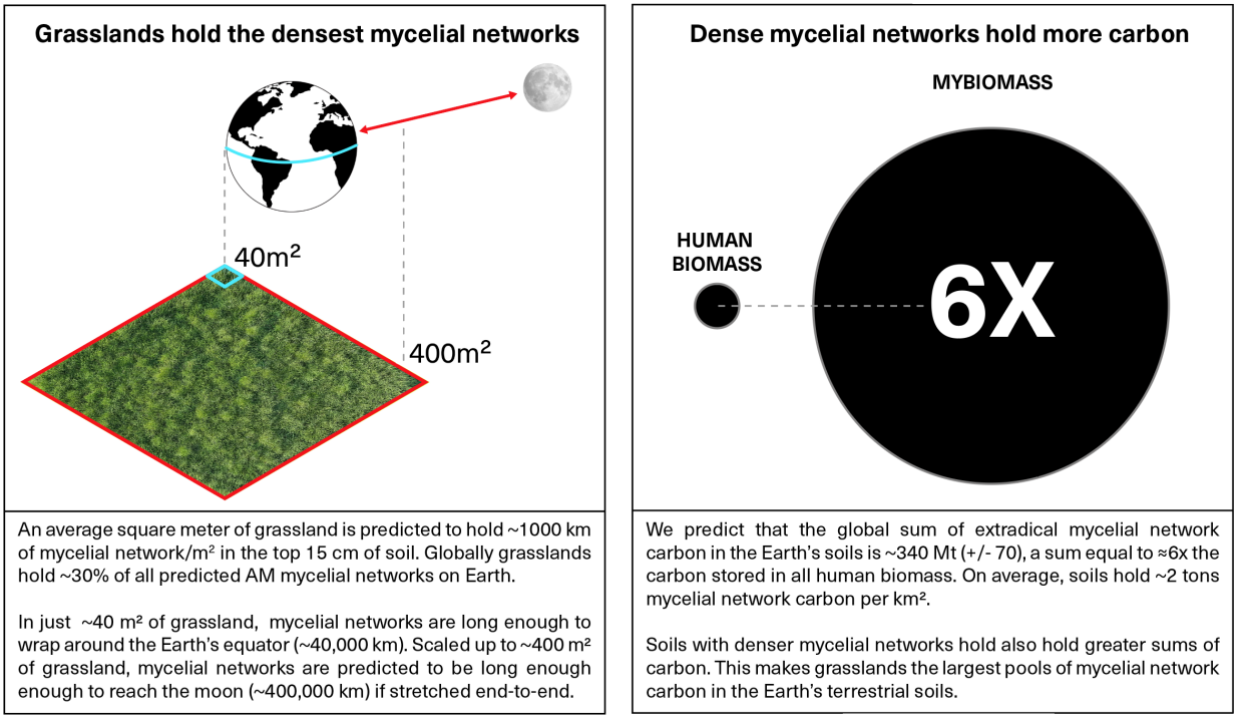

Figure 4. Illustrations of mycelial network density (left) and hyphal biomass (right). These illustrations are to give context to the large numbers in this study. Left: Grasslands are predicted to be a global hotspot for AM mycelial networks, holding on average the densest fungal networks on Earth. For context, in ≈40m^2 of soil grasslands (e.g. a 6 meter by 6 meter square 15 centimeters deep), stretched end-to-end AM fungal hyphae would wrap the equator, and in ≈400 m^2 (e.g. a 20 meter by 20 meter square 15 centimeters deep) hyphae would reach the Moon. Right: The predicted standing stock of AM fungal hyphae are estimated to hold ≈340 Mt of carbon, calculated using the radius of over 1 million hyphae from 3 species/five strains of AM fungal cultures. For context, this is ≈6x the biomass of all humans alive (2018) estimate. Soils holding more fungal networks hold more carbon.

Supplemental Information:

Table S1. Excel file of data sources for environmental covariates used in modeling stored on Dryad.

Table S2. Summary of mycelial network carbon and length estimates, and their respective uncertainties per biome. Biomes were identified using the Resolve database of ecoregions[71]. Here the sum of carbon is shown per biome in Mt with uncertainty estimates. The carbon uncertainty estimate is also in Mt and was generated by combining the standard deviation of length with the standard deviation of measured hyphal radius values. Note that the mean mycelial network carbon per biome is reported in metric tons. Next length summaries are provided again as a sum per biome, the standard deviation of length, and the mean length in one km^2 of each biome.

Biome	Mycelial network length stretched end-to-end km (sum)	Mycelial network length stretched end-to-end km (standard deviation)	Mycelial network density km/km2 (mean)	Mycelial network density coefficient of variation (%)	Carbon Mt (sum)	Carbon MT (standard deviation	Carbon density tons/km2 (mean)
Global	1.3E+17	1.9E+16	8.3E+08	9.4	340.0	5.2	2.1
Boreal Forests/Taiga	2.5E+16	3.8E+15	7.9E+08	8.5	64.8	14.0	2.0
Deserts & Xeric Shrublands	1.2E+16	1.7E+15	7.3E+08	11.1	31.5	6.4	1.9
Flooded Grasslands & Savannas	1.3E+15	1.9E+14	1.1E+09	8.6	3.3	0.7	2.7
Mangroves	1.1E+14	1.6E+13	6.7E+08	10.5	0.3	0.1	1.7
Mediterranean Forests, Woodlands & Scrub	3.1E+15	4.1E+14	8.0E+08	9.0	7.8	1.6	2.0

Montane Grasslands & Shrublands	4.8E+15	6.1E+14	9.4E+08	8.6	12.2	2.5	2.4
Temperate Broadleaf & Mixed Forests	1.4E+16	2.2E+15	7.6E+08	10.1	35.8	8.0	1.9
Temperate Conifer Forests	4.9E+15	6.9E+14	8.4E+08	8.7	12.5	2.7	2.1
Temperate Grasslands, Savannas & Shrublands	1.4E+16	2.1E+15	8.4E+08	9.1	34.7	8.0	2.1
Tropical/Subtropical Coniferous Forests	7.5E+14	1.1E+14	9.0E+08	8.7	1.9	0.4	2.3
Tropical/Subtropical Dry Broadleaf Forests	3.7E+15	4.8E+14	8.4E+08	9.0	9.4	1.9	2.2
Tropical/Subtropical Grasslands, Savannas & Shrublands	2.3E+16	3.0E+15	9.8E+08	9.3	58.3	12.2	2.5
Tropical/Subtropical Moist Broadleaf Forests	1.4E+16	2.1E+15	6.6E+08	11.1	36.6	7.7	1.7
Tundra	1.2E+16	1.6E+15	8.3E+08	8.6	30.7	6.4	2.1

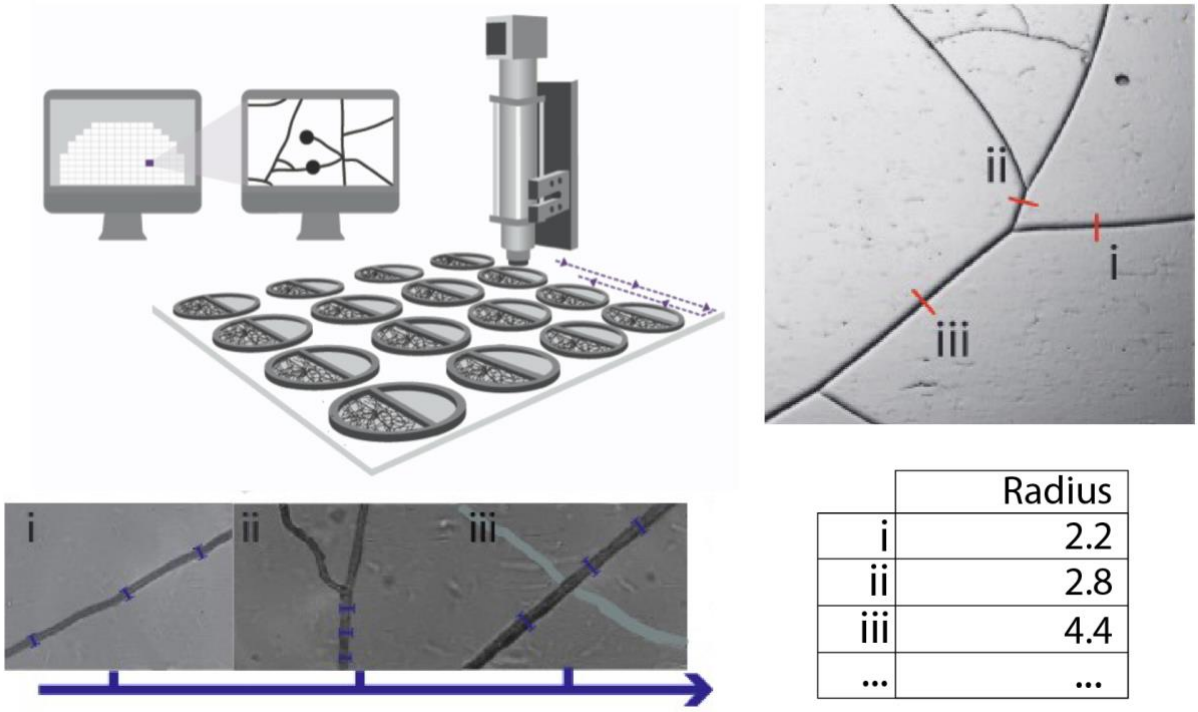

	Radius
i	2.2
ii	2.8
iii	4.4
...	...

Figure S1: High-throughput imaging robot for fungal imaging. Fungal network growth is measured in time and space at high resolution (~1mu per pixel every 2 hours). Hyphal radius values were estimated with transects across the entire network (~10K per plate) and calculating the radius at each transect.

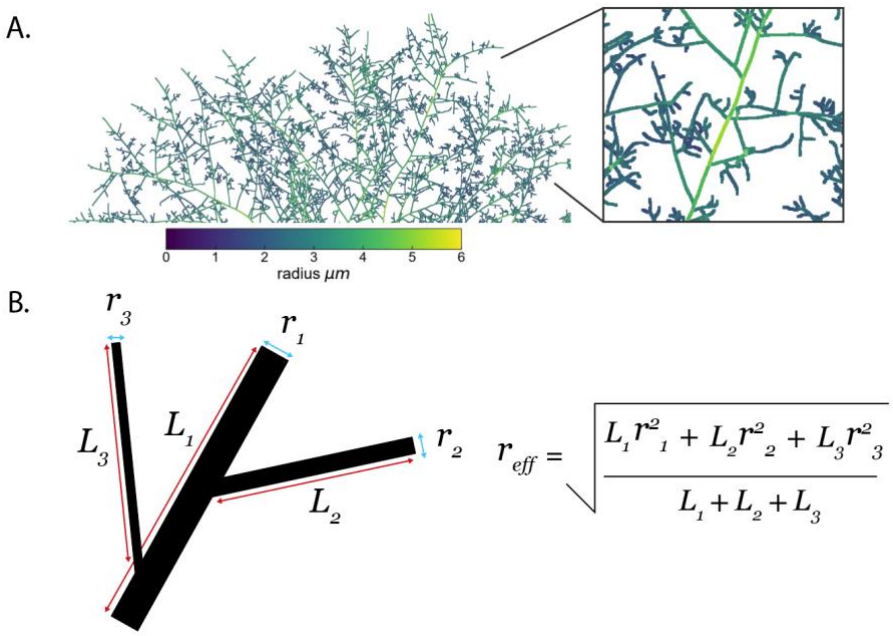

Figure S2: Radius measurements across a whole mycelial network. A.) Example of a network (*Rhizophagus irregularis – C2*) colored by radius. Here ~10K transects were taken along the network image, and used to train a deep-learning model to predict network-wide hyphal width. These width values were then used to calculate a singe average radius per plate. B.) Illustration of method for calculating the radius effective *(r_{eff})*, which is an average radius found across an entire network, weighted by different hyphal sizes. Here on the left is a simplified version of a mycelial network showing three different hyphae with their lengths (*L*) in red and radius (r) in blue. Each hypha is a different length and radius. On the right is the calculation of r_{eff} as a radius weighted by the length size of each individual hypha in the network.

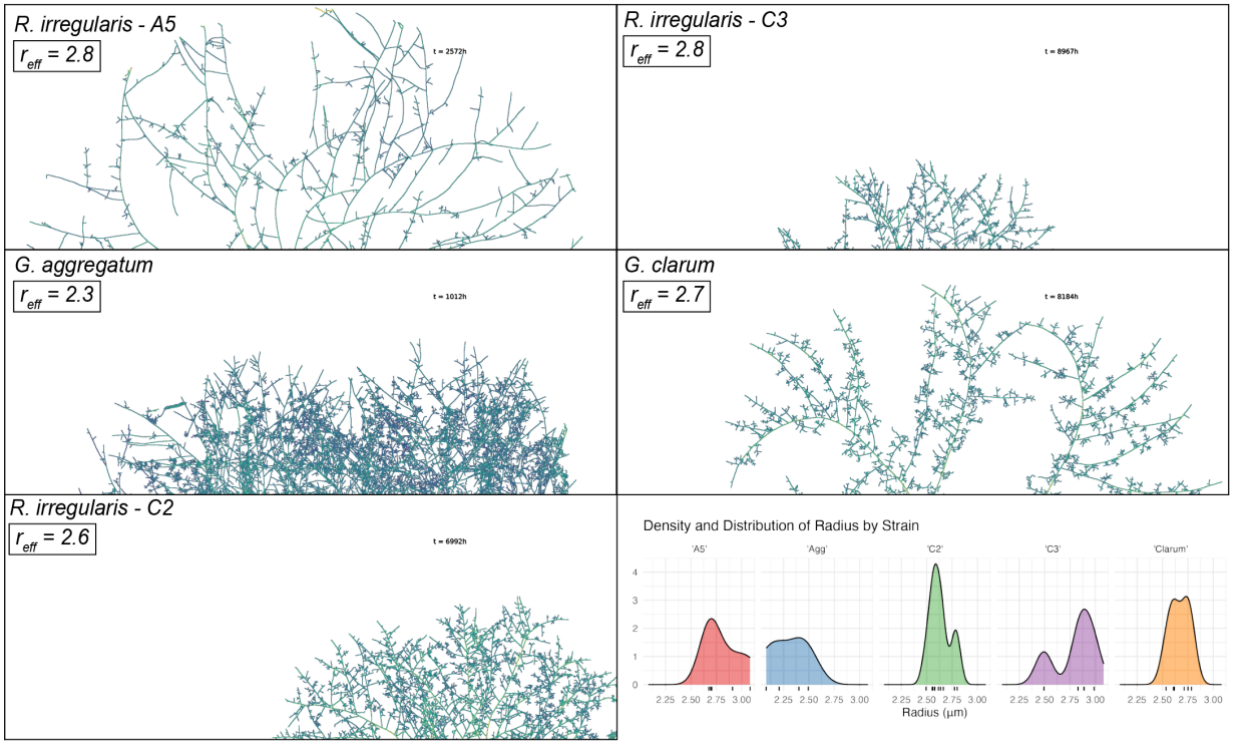

Figure S3: Figure showing the network-wide radius effective (r_{eff}) of the five strains of arbuscular mycorrhizal fungi imaged in this study. A representative network is shown for each strain, with the strain name in the top right of each panel, and the mean r_{eff} across replicates (at least 4 per strain). The age of each plate is shown within each panel, in hours. In the bottom right is a density plot of the r_{eff} across strains and replicates. The tick marks are whole plate r_{eff} values.

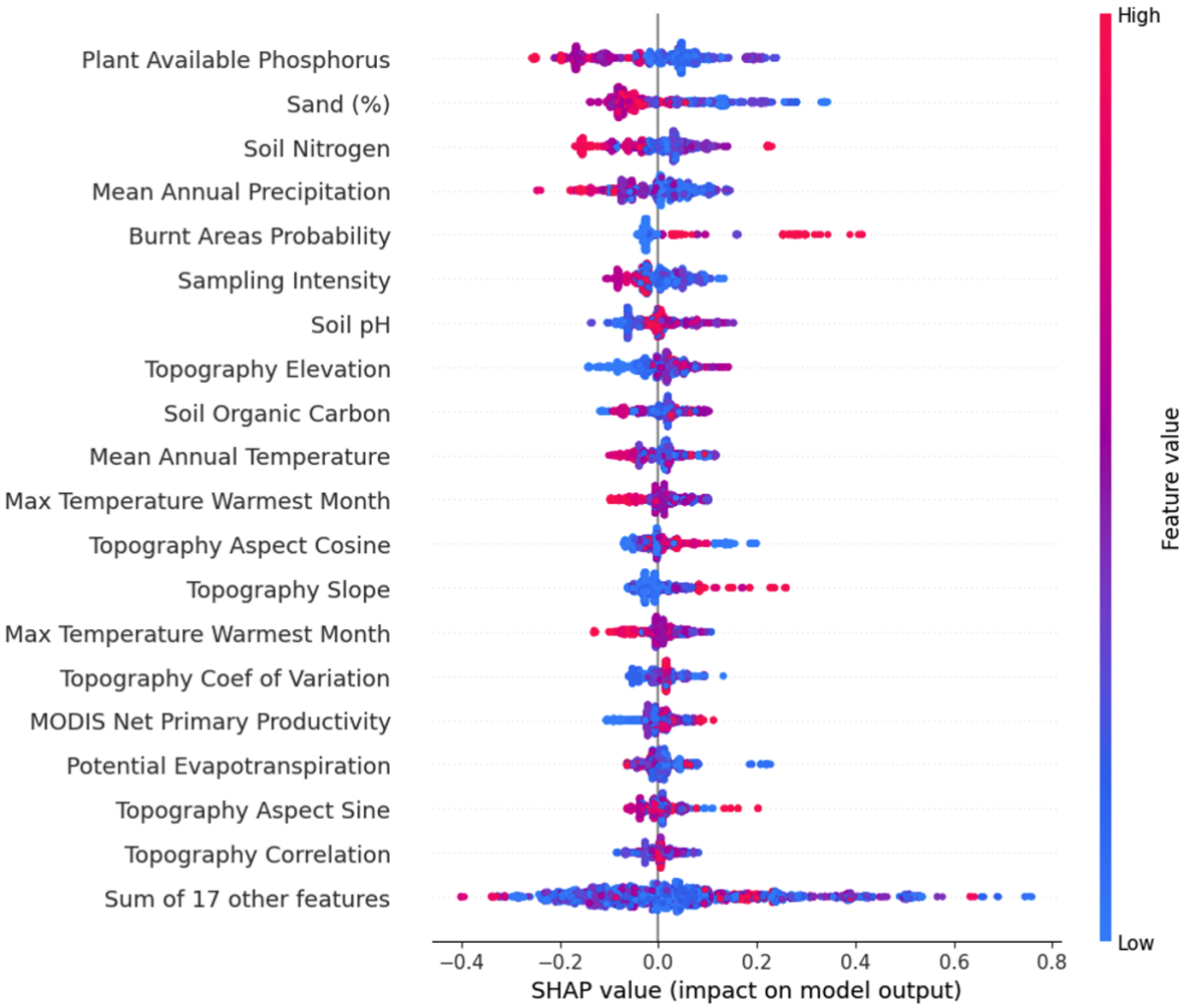

Figure S4: Feature importance values for the Random Forest regression best fit model. This plot ranks the relative importance of each predictor from top to bottom, with the availability of phosphorus being the most important predictor. Point colors represent the values of features from low to high. For example, Phosphorus values on the left of the 0-Line predicted a negative association with mycelium density while values of phosphorus on the right of the 0-Line predicted a positive association. A SHAP value of zero indicates the feature value did not influence model predictions. The color of each point shows the value of an individual predictor, for example red dot on the left of the 0-line for phosphorus indicates a negative association with high phosphorus values.

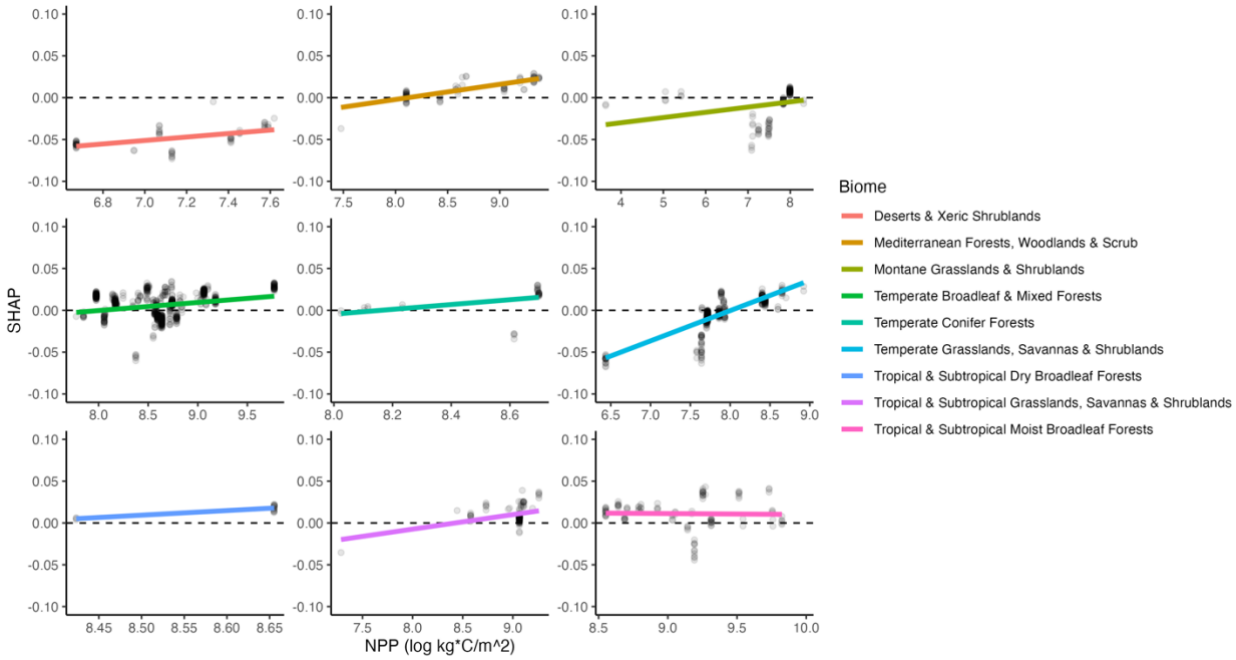

Figure S5: Figure showing the relationship between Net Primary Productivity (NPP) and the SHAP value for every datapoint in our geospatial model. A positive SHAP value indicates that NPP for that datapoint predicted higher network density, and a negative value predicted lower. A linear mixed effects model (biome as random effect) identified that NPP had a significant positive correlation to the SHAP values, on average across all biomes. In other words, as NPP increased, so did the importance of NPP as a predictor of denser mycelial networks in soils. Biome explained a large portion of the variance (72%). The positive relationship varied in magnitude per biome, with all having positive correlations, with the exception of Tropical & Subtropical Moist Broadleaf Forests, which is a biome with high extrapolation and uncertainty.

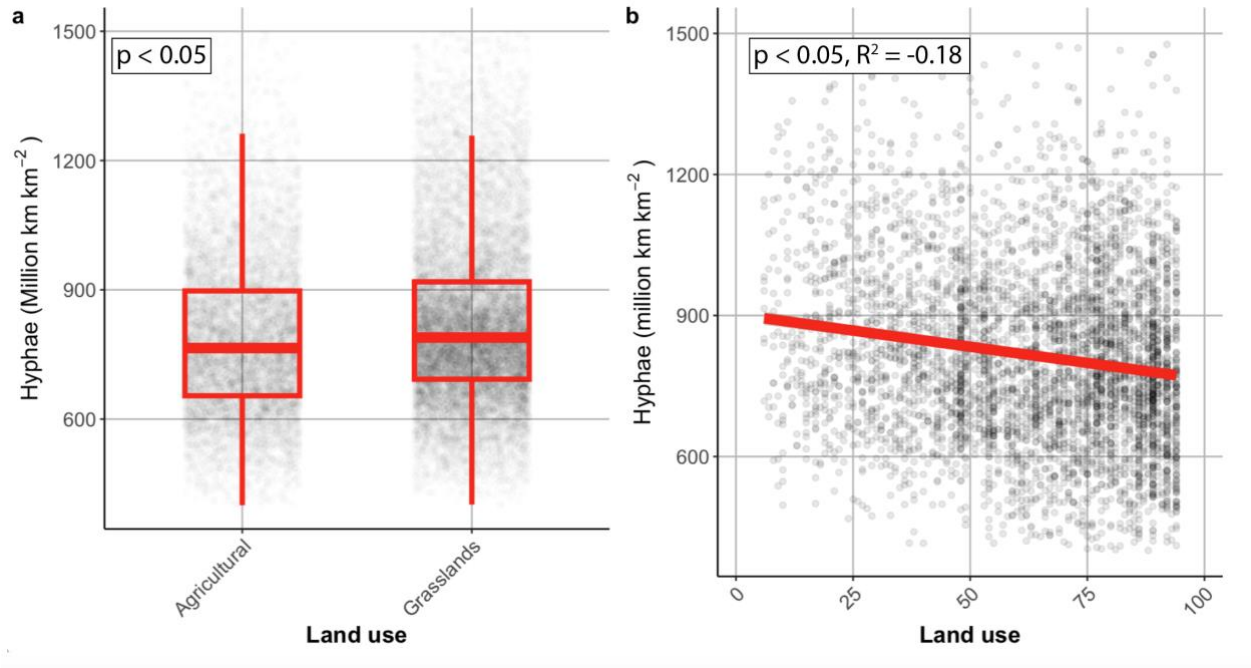

Figure S6: Plots showing the relationship between agriculture and mycelial network density in grassy biomes. a) Agricultural fields have significantly less dense mycelial networks compared to non-agricultural soils (generalized linear model, $p < 0.05$), with a loss of ≈69 million km km^{-2} of mycelial networks. b) Network density decreasing as more land is cultivated/managed, per km^2. The red line shows the model fit ($R^2 = -0.18$, $p < 0.05$).

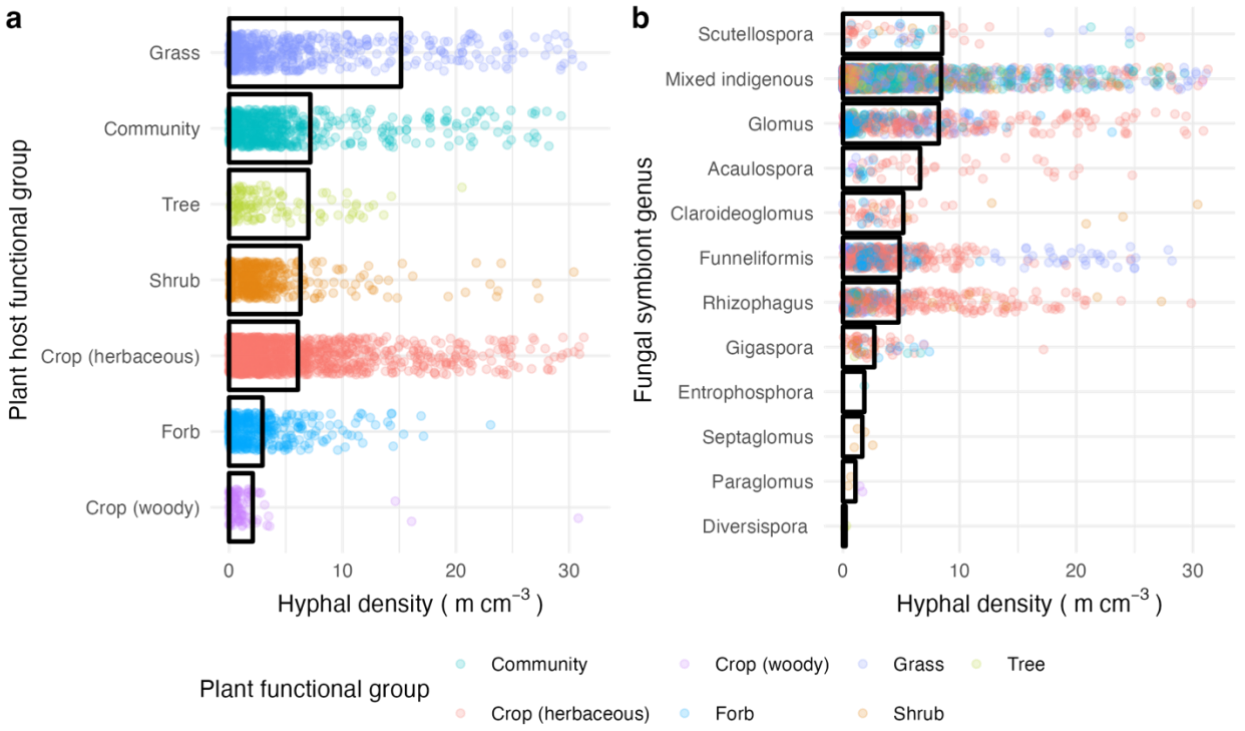

Figure S7: Plots of host and fungal identify effects on mycelial network density production. The X-axes are clipped to the 95th quantile with a max density of 30m/cm^3 for visualization purposes. a.) Plot showing plant host effects on mycelial network density, ordered from top to bottom by the highest mean density per plant functional group. The bar represents the mean density per group. Community refers to mixed plant communities where plant genera were not identified. b.) Plot of mycelial network density separated out by fungal genus and colored by the plant functional group from the study. Again, the bar represents the mean density observed for each fungal genus. Mixed indigenous here refers to unknown mixtures of AM fungi that were indigenous to study site (e.g. no inoculation).

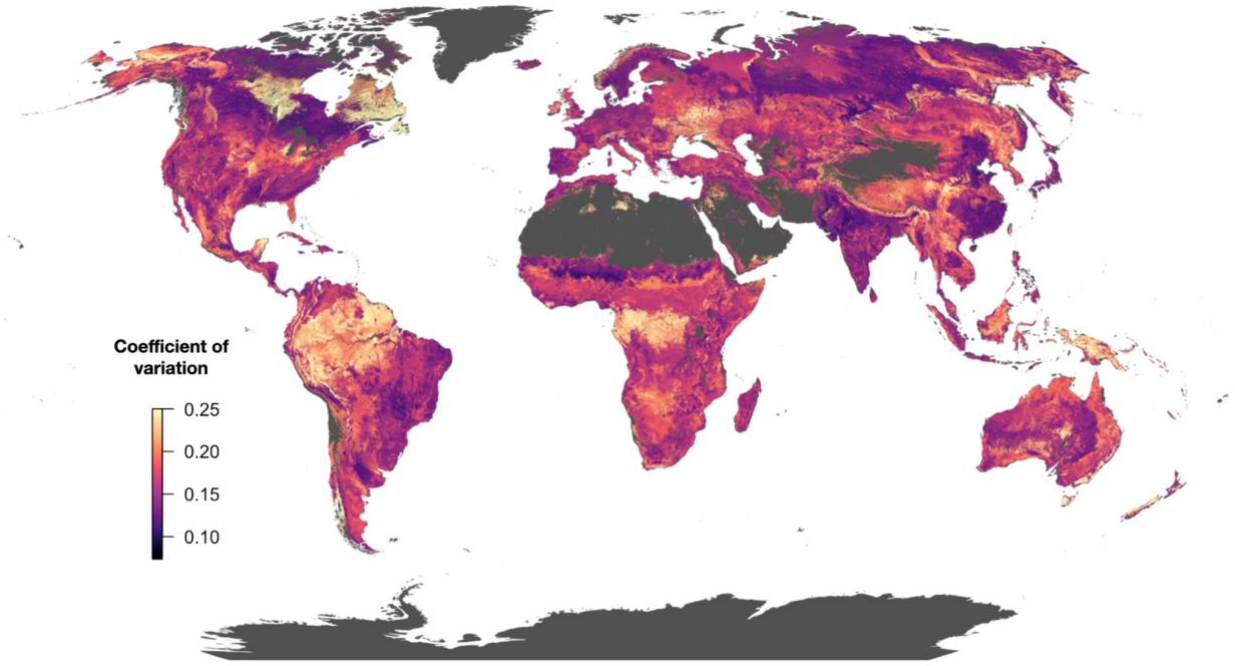

Figure S8: Map of coefficient of variation of the Random Forest model fit. Darker and brighter areas have relatively low or high variation around the mean predicted mycelial network density, respectively. Variance was highest globally in tropical ecosystems including tropical rainforests in South America, Africa, and South East Asia. We also identified high variance in desert regions. This map is available for download as a raster in our supplementary data repository.

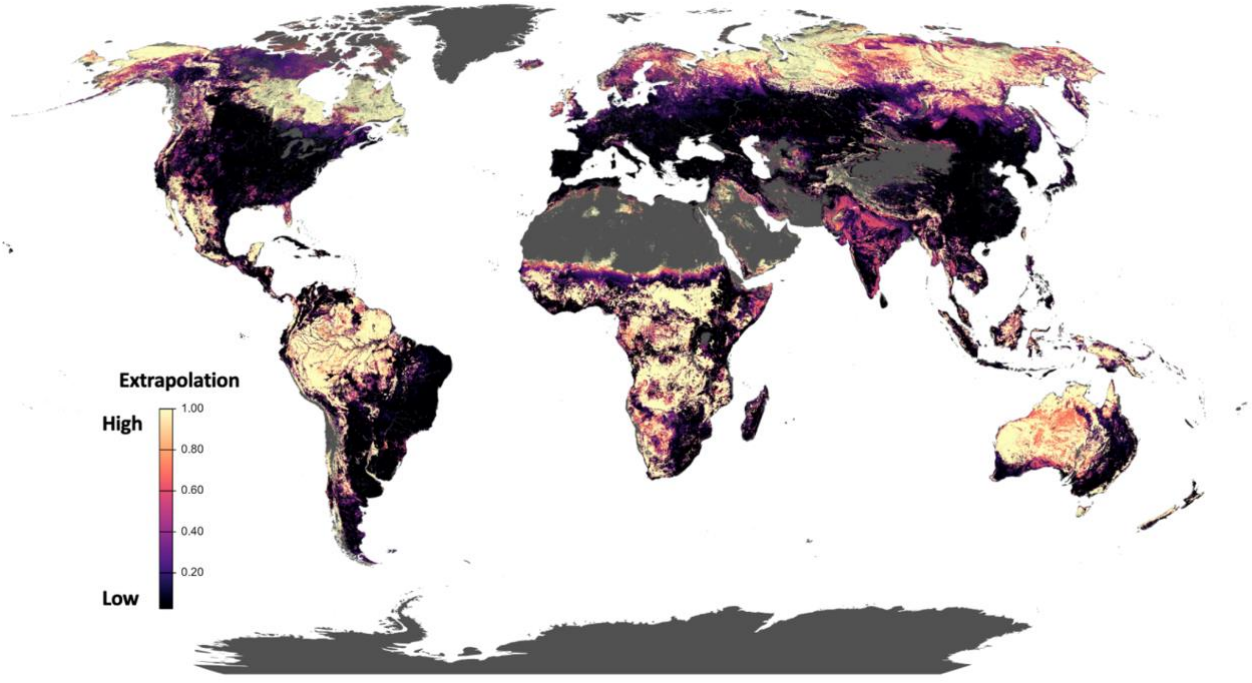

Figure S9: Map of model extrapolation based on comparing environmental predictor space in training data to global prediction space. Extrapolation is higher in areas where climate/vegetation is more dissimilar to that of our model's training data, indicating higher uncertainty. Pixels that have unique environments compared to the training data have higher extrapolation values (brighter) and low extrapolation is marked by low values (darker). This map is available for download as a raster in our supplementary data repository.

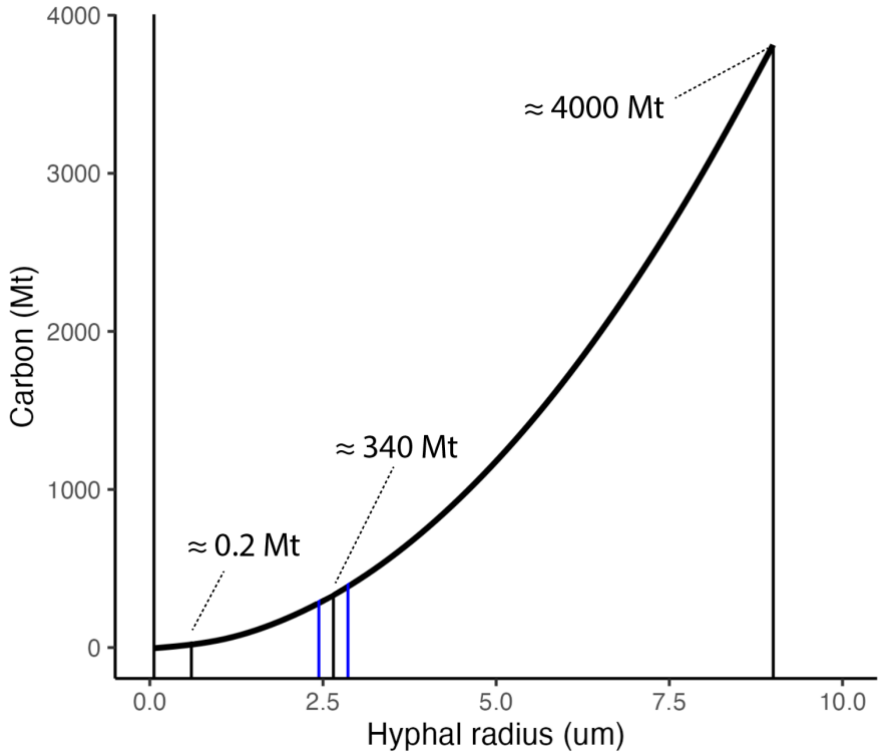

Figure S10: Simulation of carbon stored in mycelial networks shows the importance of measuring hyphal width for carbon models. This figure shows hyphal width on the x-axis with the mean (black) and standard deviation (blue) of the hyphae imaged in our study. The y-axis shows how carbon content quadratically increases at larger hyphal widths. The other noted radius values and carbon measurements are the minimum and maximum radius values found in literature, covering a 225-fold change in hyphal volume.

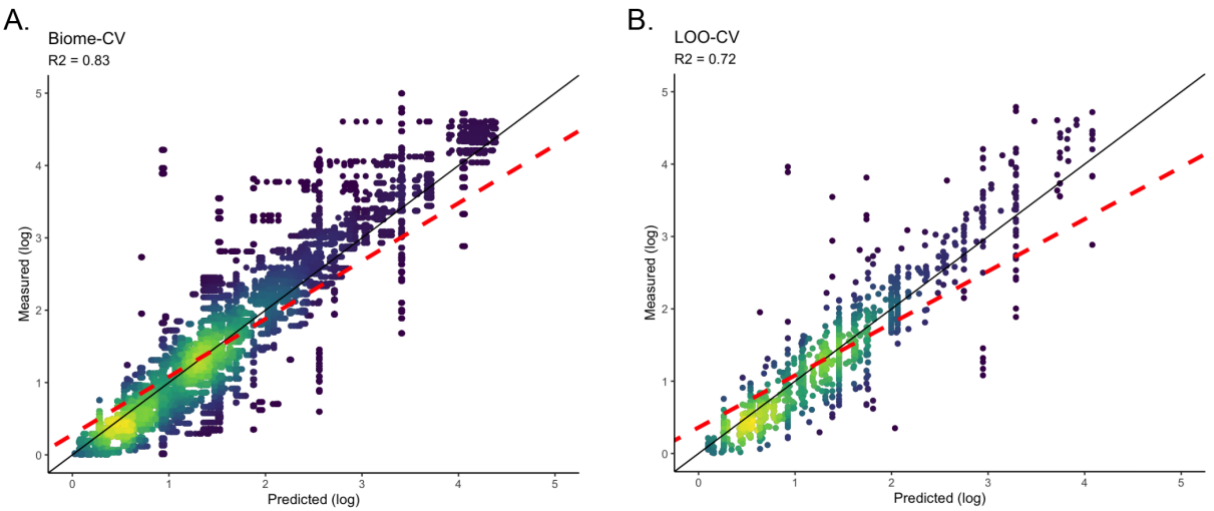

Figure S11: Predicted vs measured plots of cross validation methods. The color of the points indicates the density of points at a given value. The dashed red-line shows how the model predicted, showing relationship between predicted and measured values (with R^2 shown below the plot title). The black line shows the 1-1- relationship of a perfect fit. For both CV methods we found that the model overpredicted hyphal lengths at low values and underestimates high values. A.) Plot showing model fit for the biome-cross validation method. B.) Plot for The LOO-CV method, which is computationally expensive, and was subsampled to 1000 data points.

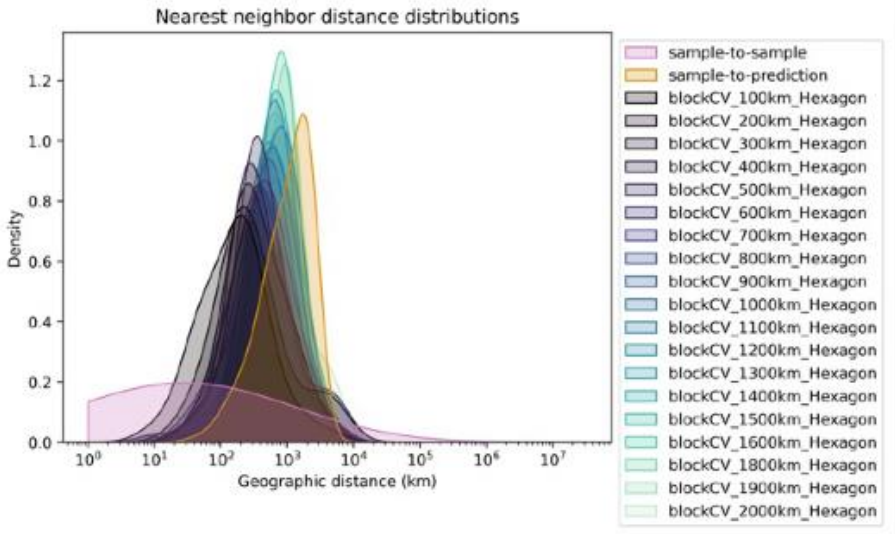

Figure S12: Plot of the nearest neighbor distance function to determine the maximum distance for spatially buffered leave one out cross validation. A series of 19 distance bands were tested to minimize the spatial distance between samples and prediction points. This was found to be at 2000 km.

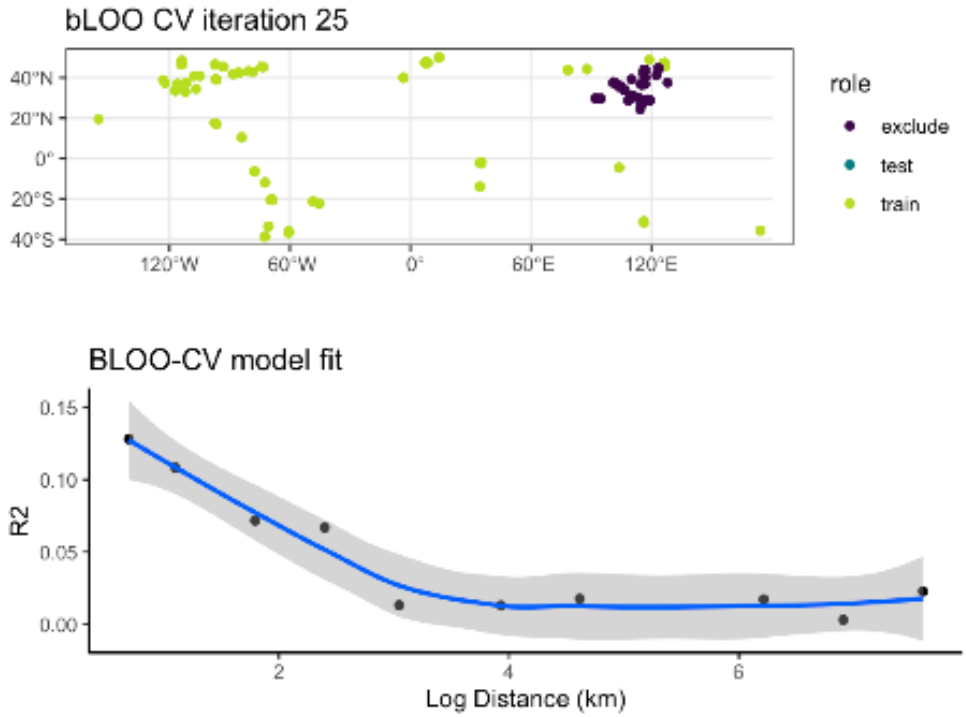

Figure S13: Plots of the spatially buffered leave one out (bLOO) cross validation test. On the top is an example of the 25th fold of this test showing a distance band of 2000 km where training points within this distance are removed. The goal of this is to limit the influence of non-independence between training points and prediction locations. The plot on bottom shows the results of the bLOO test across a series of distance bands on a log scale. Here there was a marked yet expected decrease in model performance as fewer samples were being used to train the model. As the model is trained on an increasing larger distance band the coefficient of determination decreases.

References:

1. S. E. Smith, D. Read, Mycorrhizal Symbiosis, Third Edition. *Mycorrhizal Symbiosis, Third Edition* 1–787 (2008). https://doi.org/10.1016/B978-0-12-370526-6.X5001-6.

2. H. J. Hawkins, *et al.*, Mycorrhizal mycelium as a global carbon pool. *Current Biology* **33**, R560–R573 (2023).

3. A. Kakouridis, *et al.*, Routes to roots: direct evidence of water transport by arbuscular mycorrhizal fungi to host plants. *New Phytologist* **236**, 210–221 (2022).

4. T. J. Thirkell, D. D. Cameron, A. Hodge, Resolving the 'nitrogen paradox' of arbuscular mycorrhizas: fertilization with organic matter brings considerable benefits for plant nutrition and growth. *Plant Cell Environ* **39**, 1683–1690 (2016).

5. J. Leigh, A. Hodge, A. H. Fitter, Arbuscular mycorrhizal fungi can transfer substantial amounts of nitrogen to their host plant from organic material. *New Phytologist* **181**, 199–207 (2009).

6. G. Barrett, C. D. Campbell, A. H. Fitter, A. Hodge, The arbuscular mycorrhizal fungus Glomus hoi can capture and transfer nitrogen from organic patches to its associated host plant at low temperature. *Applied Soil Ecology* **48**, 102–105 (2011).

7. H. Marschner, B. Dell, Nutrient uptake in mycorrhizal symbiosis. *Plant Soil* **159**, 89–102 (1994).

8. H. Etesami, B. R. Jeong, B. R. Glick, Contribution of Arbuscular Mycorrhizal Fungi, Phosphate–Solubilizing Bacteria, and Silicon to P Uptake by Plant. *Front Plant Sci* **12**, 699618 (2021).

9. A. Andrino, G. Guggenberger, L. Sauheitl, S. Burkart, J. Boy, Carbon investment into mobilization of mineral and organic phosphorus by arbuscular mycorrhiza. *Biol Fertil Soils* **57**, 47–64 (2021).

10. E. M. Goltapeh, Y. R. Danesh, R. Prasad, A. Varma, "Mycorrhizal Fungi: What We Know and What Should We Know?" in 3rd Ed., (2008).

11. M. C. Brundrett, Coevolution of roots and mycorrhizas of land plants. *New Phytologist* **154**, 275–304 (2002).

12. N. Dotzler, M. Krings, T. N. Taylor, R. Agerer, Germination shields in Scutellospora (Glomeromycota: Diversisporales, Gigasporaceae) from the 400 million-year-old Rhynie chert. *Mycol Prog* **5**, 178–184 (2006).

13. W. Remy, T. N. Taylor, H. Hass, H. Kerp, Four hundred-million-year-old vesicular arbuscular mycorrhizae. *Proceedings of the National Academy of Sciences* **91**, 11841–11843 (1994).

14. I. Sciascia, A. Crosino, A. Genre, Quantifying root colonization by a symbiotic fungus using automated image segmentation and machine learning approaches. *Scientific Reports 2023 13:1* **13**, 1–8 (2023).

15. E. Evangelisti, *et al.*, Deep learning-based quantification of arbuscular mycorrhizal fungi in plant roots. *New Phytologist* **232**, 2207–2219 (2021).
16. J. R. Leake, D. J. Read, Mycorrhizal Symbioses and Pedogenesis Throughout Earth's History. *Mycorrhizal Mediation of Soil: Fertility, Structure, and Carbon Storage* 9–33 (2017). https://doi.org/10.1016/B978-0-12-804312-7.00002-4.
17. J. Leake, *et al.*, Networks of power and influence: the role of mycorrhizal mycelium in controlling plant communities and agroecosystem functioning. *https://doi.org/10.1139/b04-060* **82**, 1016–1045 (2011).
18. M. G. A. Van Der Heijden, *et al.*, The mycorrhizal contribution to plant productivity, plant nutrition and soil structure in experimental grassland. *New Phytologist* **172**, 739–752 (2006).
19. I. Hiiesalu, *et al.*, Species richness of arbuscular mycorrhizal fungi: associations with grassland plant richness and biomass. *New Phytologist* **203**, 233–244 (2014).
20. C. A. Guerra, *et al.*, Blind spots in global soil biodiversity and ecosystem function research. *Nature Communications 2020 11:1* **11**, 1–13 (2020).
21. R. M. Miller, J. D. Jastrow, D. R. Reinhardt, External hyphal production of vesicular-arbuscular mycorrhizal fungi in pasture and tallgrass prairie communities. *Oecologia* **103**, 17–23 (1995).
22. S. J. McNaughton, M. Oesterheld, Extramatrical Mycorrhizal Abundance and Grass Nutrition in a Tropical Grazing Ecosystem, the Serengeti National Park, Tanzania. *Oikos* **59**, 92 (1990).
23. G. T. Freschet, *et al.*, A starting guide to root ecology: strengthening ecological concepts and standardising root classification, sampling, processing and trait measurements. *New Phytologist* **232**, 973–1122 (2021).
24. P. A. Olsson, N. C. Johnson, Tracking carbon from the atmosphere to the rhizosphere. *Ecol Lett* **8**, 1264–1270 (2005).
25. B. Bago, C. Azcón-Aguilar, A. Goulet, Y. Piché, Branched absorbing structures (BAS): a feature of the extraradical mycelium of symbiotic arbuscular mycorrhizal fungi. *New Phytol* **139**, 375–388 (1998).
26. C. F. Friese, M. F. Allen, The Spread of Va Mycorrhizal Fungal Hyphae in the Soil: Inoculum Types and External Hyphal Architecture. *Mycologia* **83**, 409–418 (1991).
27. P. L. Staddon, C. B. Ramsey, N. Ostle, P. Ineson, A. H. Fitter, Rapid turnover of hyphae of mycorrhizal fungi determined by AMS microanalysis of 14C. *Science (1979)* **300**, 1138–1140 (2003).

28. C. R. See, *et al.*, Hyphae move matter and microbes to mineral microsites: Integrating the hyphosphere into conceptual models of soil organic matter stabilization. *Glob Chang Biol* **28**, 2527–2540 (2022).
29. J. D. Hoeksema, *et al.*, A meta-analysis of context-dependency in plant response to inoculation with mycorrhizal fungi. *Ecol Lett* **13**, 394–407 (2010).
30. M. G. A. Van Der Heijden, *et al.*, Mycorrhizal fungal diversity determines plant biodiversity, ecosystem variability and productivity. *Nature 1998 396:6706* **396**, 69–72 (1998).
31. Y. M. Bar-On, R. Phillips, R. Milo, The biomass distribution on Earth. *Proc Natl Acad Sci U S A* **115**, 6506–6511 (2018).
32. J. C. Dodd, C. L. Boddington, A. Rodriguez, C. Gonzalez-Chavez, I. Mansur, Mycelium of arbuscular mycorrhizal fungi (AMF) from different genera: Form, function and detection. *Plant Soil* **226**, 131–151 (2000).
33. S. L. Stürmer, J. D. Bever, P. A. Schultz, S. P. Bentivenga, Celebrating INVAM: 35 years of the largest living culture collection of arbuscular mycorrhizal fungi. *Mycorrhiza* **31**, 117–126 (2021).
34. University of Kansas, The International Collection of (Vesicular) Arbuscular Mycorrhizal Fungi. *2024*. Available at: https://invam.ku.edu/ [Accessed 19 March 2024].
35. Society for the Protection of Underground Networks, SPUN. *2021*. Available at: https://www.spun.earth/ [Accessed 11 January 2023].
36. Dig Up Dirt | Find your friendly fungi. Available at: https://www.digupdirt.net/ [Accessed 17 March 2024].
37. N. Gorelick, *et al.*, Google Earth Engine: Planetary-scale geospatial analysis for everyone. *Remote Sens Environ* (2017). https://doi.org/10.1016/j.rse.2017.06.031.
38. Y. Hu, Y. Han, Y. Zhang, Land desertification and its influencing factors in Kazakhstan. *J Arid Environ* **180**, 104203 (2020).
39. R. D. Bardgett, *et al.*, Combatting global grassland degradation. *Nature Reviews Earth & Environment 2021 2:10* **2**, 720–735 (2021).
40. G. Sukhbaatar, *et al.*, Assessment of early survival and growth of planted Scots pine (Pinus sylvestris) seedlings under extreme continental climate conditions of northern Mongolia. *J For Res (Harbin)* **31**, 13–26 (2020).
41. N. Alexandratos, J. Bruinsma, World Agriculture towards 2030/2050: the 2012 revision. *WORLD AGRICULTURE* (2012).
42. FAO, Global agriculture towards 2050.
43. K. Georgiou, *et al.*, Global stocks and capacity of mineral-associated soil organic carbon. *Nature Communications 2022 13:1* **13**, 1–12 (2022).

44. EU Mission: A Soil Deal for Europe. Available at: https://research-and-innovation.ec.europa.eu/funding/funding-opportunities/funding-programmes-and-open-calls/horizon-europe/eu-missions-horizon-europe/soil-deal-europe_en [Accessed 19 March 2024].
45. Roads to Removal – Options for carbon dioxide removal in the US. Available at: https://roads2removal.org/ [Accessed 19 March 2024].
46. D. D. Richter, D. Markewitz, How deep is soil? *Bioscience* **45**, 600–609 (1995).
47. J. Canadell, *et al.*, Maximum rooting depth of vegetation types at the global scale. *Oecologia* **108**, 583–595 (1996).
48. R. A. Virginia, M. B. Jenkins, W. M. Jarrell, Depth of root symbiont occurrence in soil. *Biol Fertil Soils* **2**, 127–130 (1986).
49. E. Stokstad, New observatory to bring soil up from the deep. *Science (1979)* **374**, 250 (2021).
50. C. Fang, J. B. Moncrieff, The variation of soil microbial respiration with depth in relation to soil carbon composition. *Plant Soil* **268**, 243–253 (2005).
51. M. Kleber, *et al.*, Mineral–Organic Associations: Formation, Properties, and Relevance in Soil Environments. *Advances in Agronomy* **130**, 1–140 (2015).
52. M. S. Torn, S. E. Trumbore, O. A. Chadwick, P. M. Vitousek, D. M. Hendricks, Mineral control of soil organic carbon storage and turnover. *Nature 1997 389:6647* **389**, 170–173 (1997).
53. F. Oehl, *et al.*, Community structure of arbuscular mycorrhizal fungi at different soil depths in extensively and intensively managed agroecosystems. *New Phytologist* **165**, 273–283 (2005).
54. C. F. Friese, M. F. Allen, The Spread of Va Mycorrhizal Fungal Hyphae in the Soil: Inoculum Types and External Hyphal Architecture. *Mycologia* **83**, 409–418 (1991).
55. R. K. Braghiere, *et al.*, Modeling Global Carbon Costs of Plant Nitrogen and Phosphorus Acquisition. *J Adv Model Earth Syst* **14**, e2022MS003204 (2022).
56. M. C. Urban, *et al.*, Improving the forecast for biodiversity under climate change. *Science (1979)* **353**, aad8466 (2016).
57. J. Cavender-Bares, *et al.*, Integrating remote sensing with ecology and evolution to advance biodiversity conservation. *Nature Ecology & Evolution 2022 6:5* **6**, 506–519 (2022).
58. J. Xia, J. Wang, S. Niu, Research challenges and opportunities for using big data in global change biology. *Glob Chang Biol* **26**, 6040–6061 (2020).
59. M. Chapman, *et al.*, Biodiversity monitoring for a just planetary future. *Science (1979)* **383**, 34–36 (2024).

60. M. I. Mujica, P. Silva-Flores, C. G. Bueno, J. Duchicela, Integrating perspectives in developing mycorrhizal trait databases: a call for inclusive and collaborative continental efforts. *New Phytologist* (2024). https://doi.org/10.1111/NPH.19754.

61. L. K. ABBOTT, A. D. ROBSON, G. DE BOER, THE EFFECT OF PHOSPHORUS ON THE FORMATION OF HYPHAE IN SOIL BY THEVESICULAR-ARBUSCULAR MYCORRHIZAL FUNGUS, GLOMUS FASCICULATUM. *New Phytologist* **97**, 437–446 (1984).

62. J. F. Hanssen, T. F. Thingstad, J. Goksøyr, J. Goksoyr, Evaluation of Hyphal Lengths and Fungal Biomass in Soil by a Membrane Filter Technique. *Oikos* **25**, 102 (1974).

63. D. Tennant, A Test of a Modified Line Intersect Method of Estimating Root Length. *J Ecol* **63**, 995 (1975).

64. J. van den Hoogen, *et al.*, A geospatial mapping pipeline for ecologists. *bioRxiv* 2021.07.07.451145 (2021). https://doi.org/10.1101/2021.07.07.451145.

65. J. M. Kass, *et al.*, The global distribution of known and undiscovered ant biodiversity. *Sci Adv* **8**, 9908 (2022).

66. S. M. Lundberg, *et al.*, From local explanations to global understanding with explainable AI for trees. *Nature Machine Intelligence 2020 2:1* **2**, 56–67 (2020).

67. N. Jethani, M. Sudarshan, I. C. Covert, S.-I. Lee, R. Ranganath, FastSHAP: Real-Time Shapley Value Estimation. Available at: https://git.io/JCqbP [Accessed 18 March 2024].

68. P. Ploton, *et al.*, Spatial validation reveals poor predictive performance of large-scale ecological mapping models. *Nature Communications 2020 11:1* **11**, 1–11 (2020).

69. C. Milà, J. Mateu, E. Pebesma, H. Meyer, Nearest neighbour distance matching Leave-One-Out Cross-Validation for map validation. *Methods Ecol Evol* **13**, 1304–1316 (2022).

70. F. M. Sabatini, *et al.*, Global patterns of vascular plant alpha diversity. *Nature Communications 2022 13:1* **13**, 1–16 (2022).

71. B. M. Benito, spatialRF: Easy Spatial Modeling with Random Forest version 1.1.3 from CRAN. Available at: https://rdrr.io/cran/spatialRF/ [Accessed 20 October 2021].

72. L. R. Bakken, R. A. Olsen, Buoyant densities and dry-matter contents of microorganisms: conversion of a measured biovolume into biomass. *Appl Environ Microbiol* **45**, 1188–1195 (1983).

73. D. Zanaga, *et al.*, ESA WorldCover 10 m 2021 v200. (2022). https://doi.org/10.5281/ZENODO.7254221.

74. N. A. Soudzilovskaia, *et al.*, Global mycorrhizal plant distribution linked to terrestrial carbon stocks. *Nature Communications 2019 10:1* **10**, 1–10 (2019).

Chapter 6

Conclusion

6.1 Synthesis and answer to research question

6.1.1 How do AM fungal colony spread in space over time?

We show in Chapter 2 that AM fungal colony propagation can be well summarized as a travelling wave of hyphal filament. Around a plant root, a front of branching and anatomising hyphal tips advances at a fixed speed v_{wave}. It leaves behind a network of filaments of even density ρ_{sat}. Such phenomenon emerges from the balance between branching and anastomosing that are fungal microscopic morphogenetic traits. Compared to other filamentous fungi, AM colony density is relatively sparse. All of this suggests that the observed travelling wave phenotype constitutes a fungal strategy.

6.1.2 How do these spatial dynamics impact the outcome of the symbiosis and in particular the transfer of nutrients to the plant?

Phosphorous is poorly mobile in soils, which means spatial propagation timing is critical to allow efficient provision of nutrients. Fast and sparse propagation allows to escape the P depletion zone while avoiding overinvestment of hyphal density in regions where it will not be in contact with P. Among AM fungi, some fungal genotypes grow denser (high ρ_{sat}) and slower (low v_{wave}) while other grow sparser and faster. In high P availability conditions, dense and slow genotypes will tend to be able to provide more P to their host over their whole propagation while at low P availability, sparse and fast ones will better be able to access undepleted regions. In cases where plant growth is limited by P supply, spatial dynamics of the AM symbionts plays a key role in determining the outcome of the symbiosis.

6.1.3 Are any control mechanisms in place on the plant and fungal side that enforce proportionality in the bidirectional exchange of resources?

When looking at the position of different AM fungal genotype in $\rho_{sat} \times v_{wave}$ 2d space when grown with a fixed plant host (3.2a), we find that they seem to be positioned along a 1d line. This suggests some external factors constrains AM spatial propagation to this one degree of freedom. We find that a control mechanism that would impose a proportionality between the supply of C from the plant and the supply of P from the AM colony could indeed be constraining travelling wave phenotypes to the experimentally observed 1d line.

6.1.4 How does transport within the AM colony allow to match supply and demand for carbon while maintaining a coherent trade pattern?

Large volume of lipids need to be transported through the colony to fuel the growth of new hyphal biovolume. We show that such lipid movement is most probably generated by molecular motors walking on an oriented graph of microtubule within the hyphal network. The graph is oriented and weighted in a way that seem to result in lipid movement from source to sink following relatively direct paths while distributing over multiple possible alternative routes. Because of fluid incompressibility, the movement of those lipids over the whole network is in theory capable of generating a large backflow. The qualitative and quantitative nature of this backflow is compatible with our observation of flow speed in the network. If the backflow indeed is the consequence of lipid flux, lipid flux and backflow tend to happen in proportional magnitude and opposite direction. This could be a mechanism through which a coherent trade pattern is conserved as the colony grows and when it is confronted to multiple hosts that differ in their carbon supply.

6.2 Discussion and future work

6.2.1 Hyphal density control

In chapter 2 we showed that fungal colony propagation could well be summarized by its wave speed v_{wave} and its saturation density ρ_{sat}. We also showed that ρ_{sat} emerged from the balance between branching and anastomosis. In chapter 3 we have shown that v_{wave} and ρ_{sat} seemed to be strain specific and could also change depending on the root host or nutrient environment. It is however unclear what microscopic growth parameter differ between these conditions. In the case of v_{wave}, the theory put in place in chapter 2 suggests that only the faster runner hyphae at the growing front need to adapt their speed in order for the general wavespeed to vary. We also showed in chapter 2 that ρ_{sat} increases with the rate of branching and decreases with the propensity to anastomose. Fungal colonies can therefore in theory play on those two levers to change their saturation density. It is also possible that additional elements like density dependent stopping propensity or solute concentration dependent behaviour also play a role. Both of these have in common with anastomosis propensity that they hold some level of hyphal density dependence.

I hypothesize that an increase in C supply will often lead to an increase in hyphal growth speed or in branching rate. This is suggested by the idea that growth in the colony is happening "just in

time". There is little to no storage of carbon in the initial phase. Surplus carbon therefore needs to be consumed either by creating new tips or by accelerating the growth of existing ones.

The later option can only be done within the limit of some intrinsic maximal growth speed. It is unclear what underpins such maximal growth speed. While biomolecular effects may ultimately play a role, there is an intimate relationship between resource supply to the growing tip, metabolism and growth material production. In the case of single cell organisms, growth rate is often limited by the volumetric rate of production of the necessary biomolecular material of the cell. The "production volume" in the case of the coenocytic AM colony can extend along the hyphal filament and therefore strongly depends on transport capacities. In theory, nuclei positioned far from the growing tips could still be producing growth material leading to arbitrary high growth rate. Maximal growth speed if therefore intimately linked with transport and therefore with hyphal radius (see 6.2.2). Preliminary data indeed suggests a correlation between hyphal radius at the tip and extension rate (Fig. 6.1a)

Because increase in hyphal growth speed is limited by intrinsic constraints or because it is not a relevant strategy, when experiencing excess C, the fungal colony may also increase its branching rate leading to an increase in saturation density. Figure 3.8 indeed suggests that both adaptations are at play although it is so far unknown if the increase in density is due to an increase in branching rate, to a decrease in anastomosis propensity or to some other unknown microscopic parameter.

At later time, when no more growth of hyphae is possible or strategically desirable, C surplus may also be invested in spores. This could explain the difference in timing we've been observing between colony growth and spore production with spore production happening largely when the colony was already covering the whole plate (see Chapter 2).

We have also shown in Chapter 3 that increasing fungal density is not always an optimal strategy for growing AM colonies. In the extreme scenario where P is depleted in a given region, it is reasonable to assume that hyphal densification should stop. The decrease in density at low P concentration observed in Chapter 3 seem to validate such a hypothesis.

How do microscopic hyphal behaviour parameters like branching rate, anastomosis propensity, stopping propensity or differentiation into BAS vary between strain and conditions? How does the colony integrate different signals and adapts individual hyphal behaviour accordingly? How can adaptation in individual hyphal behaviour lead to coherent strategy at the colony level?

An important element to take into consideration is a local-global information bottleneck. The AM colony strategy is an emergent phenomenon resulting from the behaviour and interaction of multiple growing tips. Those growing tips interact in two ways. First they are connected to the same network which means they can in theory signal over long range through it and share the same supply of carbon. Second they can have some level of local 'self-sensing': already existing hyphal filaments can influence the growth of a hyphal tips either through anastomosis, because it depleted nutrients locally or because of directly emitted signals. In the first case, only direct contact leads to interaction, in the two later examples, the rate or distance of the interaction is limited by diffusion. Can the network maintain a coherent growth strategy with such local short scale interactions? Is some global information processing required ? How would such information processing over the whole network be done? Do internal flows play a role in such long range interactions?

Our model of colony growth presented in 2 and 3 could easily be expended to account for resource allocations, for example using principles and ideas presented in 4. The general idea would be

that carbon supply is "pushing" hyphal growth and branching while phosphorous availability or hyphal density would be "holding" it. Excess carbon arriving in non-growing parts of the network would be recirculated through the bidirectional flux. On longer timescale the microtubule network could adapt following local readout of bidirectionality of lipid fluxes. Lipid flux in both direction being equal meaning that there is not consumption of lipid downstream and the microtubule could depolymerise accordingly. The resulting colony scale resource fluxes could very well represent a coherent strategy that integrates all the resources constraints and opportunities.

Pushing those concepts forwards could benefit the more general field of fungal ecology. The speed-density trade-off is indeed general to the whole filamentous fungi realm and mechanistic understanding is still lacking to fully leverage trait-based framework that are being put in place[1, 2]. Understanding fungal strategies may in turn provide insights into the emergence of multicellularity in fungi. Resource economy arguments have previously been put forward to explain such a transition [3]. We think the information argument put forward above may also play an important role. Fungal colonies exhibit long range coupling between their different parts while single cells colony propagation can generally be understood through local interactions. Could the ability to integrate information over large length-scales compared to single cell diameter be at the heart of the "success" of multicellular organisms?

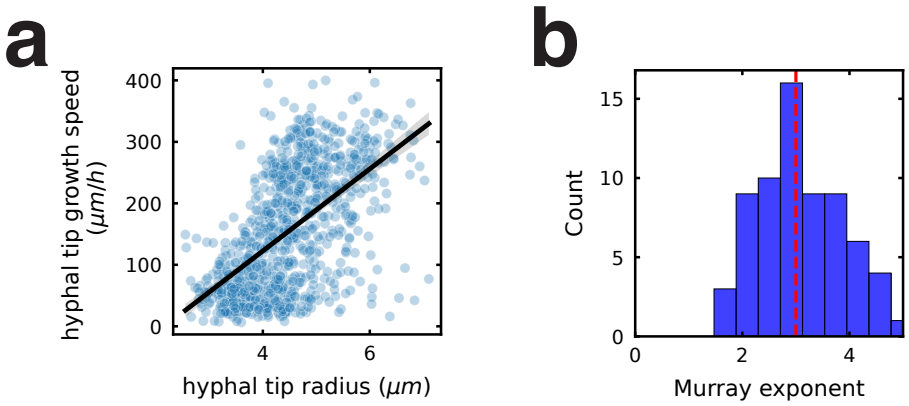

Figure 6.1: **Radius adapatation as the missing link between colony propagation, transport and energetic optimization (a)** Correlation between the radius at the tip of a hypha and its extension speed. Blue points correspond to one recording of a hyphal growth event between two timesteps. Black line represent bootstrap regression on all datapoints. Grey shade correspond to 95% C.I. of the linear fit obtained via bootstrapping. Beyond the correlation, it is important to note that only tips larger than $\sim 4\mu m$ reach growth speed a high as $300\mu m/h$. **(b)** Murray exponents corresponding to the value x for which $r_0^x = r_1^x + r_2^x$ for a set of 261 intersections where radius was manually measured from high resolutions images. r_0 is the maximal measured radius at the intersection. The distribution, although large due to a combination of biological and experimental noise, peaks around a value of 3 indicated by the red dashed line which corresponds to the original Murray exponent.

6.2.2 Hyphal radius adaptation

One of the important conclusion of this work is the fact that hyphal radius is a critical element to take into consideration. It is possibly at the heart of the speed-density tradeoff presented in Chapter 2 and Chapter 3. It plays a role in the distribution of flows at the network level as explained in Chapter 4. Chapter 5 shows that when integrating AM data at the planetary scale, choice of hyphal radius can impact significantly estimates of total hyphal biomass. More fundamentally, the ability of AM fungi to build longer and thinner structures than plant roots may lie at the heart of the 400 million year old symbiosis.

As shown in chapters 2, 3 and 4, radii clearly seem to adapt over time and space following some coherent scheme. The general rule is that hyphae most important for transport of resources (in the terms of betweenness centrality of Chapter 2 or in the terms of carbon flux comuted with the flow model of Chapter 4) tend to have a larger radius, while Branched Absorbing Structures, that are often topological dead-ends,tend to be thinner.

Branching organs of many living organism often display a relationship between different edges of a three-way junction. Such relationship can be the consequence of flux conservation, or power dissipation minimization[4, 5]. In the later case the well known "Murray's Law" has been suggested to explain the radii variation of the blood vessels from aorta ($\sim cm$) to capillaries ($\sim$10 μm) [6]. It states that the sum of all radii cubed is conserved along the flow path. Preliminary data from our system suggest the existence of a "Murray-like" relationship between radii, at least in the case of the larger junctions (Fig. Fig. 6.1b). However the "flow path" is an ill defined concept in our system of bidirectinal flow. Also Murray's law emerges from energetic consideration and minimizes a linear balance between viscous dissipation in Hagen-Poiseuille flow profiles and volumetric maintenance cost. According to Chapter 4, our system exhibits a modified Poiseuille-like flow profile within the "inner pipe" cross section. The radius "seen" by this pressure driven flow is not the full hyphal radius but the radius corresponding to the cross section unoccupied by the lipid emulsion phase. Part of the energetic losses are also probably due to the ATP driven operation of molecular motors.

It is also possible that radial adaptation is driven by other physical constraints like keeping the lipid load below a critical threshold to avoid 100% occupation of the cross section by the lipid phase. A simple analytically solvable model helps understanding what the consequences of such constraints would be. Consider the relationship between carbon flux (ϕ_C), lipid volume fraction (ρ_C), radius (R), and speed (v_0) of lipids in the hyphae we get:

$$\phi_C = \pi \cdot \rho_C \cdot R^2 \cdot v_0$$

If we call $S = \pi \cdot R^2$ the total cross section of a hypha:

$$\phi_C = \rho_C \cdot S \cdot v_0$$

Choosing to assume that the change in area of the hypha's slice happens to reach an objective value of lipid volume fraction ρ_0 we can set the simplest form for the variation of surface area over time.

$$\frac{dS}{dt} = \lambda(\rho - \rho_{ideal})$$

Which we can solve to obtain

$$S(t) = 2\sqrt{\lambda \int \frac{\phi_C(t) - \phi_0(t)}{v_0}\, dt}$$

where $\phi_0(t) = \pi \cdot \rho_{ideal} \cdot S(t) \cdot v_0$

At an intersection between three branches 0,1 and 2 where conservation of carbon flux yields $\phi_{C,0} = \phi_{C,1} + \phi_{C,2}$ there are two extreme cases. In the case where, at early time, $\rho_{ideal} \ll \rho$ in all branches we obtain from the above:

$$r_0^4 \approx r1^4 + r2^4$$

While in the case where at later time $\rho_{ideal} \approx \rho$ we would obtain

$$r_0^2 \approx r1^2 + r2^2$$

The observed relationship between radii at intersection could therefore result from simple local adaptation rules which would result in a variation of observed Murray exponents between values of 2 and 4 which corresponds reasonably well to the data shown in Fig. 6.1b.

The above analytical derivation and discussion about Murray's law is just meant to show an example of how thinking about resource exchange constraint and power dissipation could lead to understanding radius change in time and space. It has so far little to no experimental justification. Further work should focus on carbon flow and radius time series to develop an experimentally and theoretically sound model. Such model could help answering the following questions: does power dissipation minimization shape radius variations in the colony? Or do other physical constraints come into play? How does the colony maintain a coherent hyphal radius distribution in a growing colony?

6.2.3 Beyond the wave?

In chapters 2 and 3 we projected high-dimensional raw images first into the space of temporal graph then into the 2d $v_{wave} \times \rho_{sat}$ space. This dimensionality reduction is justified by fundamental, functional and statistical arguments : (1) fundamentally, those dimensions naturally emerge from microscopic ingredients of fungal morphogenesis as seen in Chapter 2 (2) those dimension have some functional significance as shown in Chapter 3. (3) statistically, projecting in this 2d space seem to resolve treatment differences (change of root host, P availability or fungal strain). Colonies grown in the same conditions tend to show smaller variance within treatment than across treatment in this space.

The colony propagation speed v_{wave} and its saturation density ρ_{sat} are therefore considered to be two important fungal traits. Colony growth is however possibly much richer than this simplistic projection into an ideal 2d space. Further work could highlight what other elements of fungal colony propagation should be considered relevant traits. Such research could start from multiple complementary approaches.

1. Modern statistical tools as well as the large availability of data from out experimental system should allow an unsupervised approach to the problem. The most salient straits from a statistical point of view should naturally emerge from such an approach.

2. Interpreting the functional significance of such traits as well as formulating relevant hypothesis will require a continuous effort of modelling and experiments. Modelling will be necessary to formulate what the impact of the variation in such trait could be in different experimental or real world conditions. Experiments should then come to validate model outputs.

3. Cultivating a theoretical ground will allow to better draw the links between different scales and detail how independent/orthogonal different traits are. This is essential to avoid accumulating redundant observations at various scales and has practical implication for real world applications. The work done during this PhD illustrates well the importance of such theoretical grounding.

One clear remaining frontier is whether transport dynamics as discussed in Chapter 4 really can be considered a "trait" and how such a trait could be expressed in order to integrate all the transport dynamics observed in a growing colony. In Chapter 4 we show that understanding transport dynamics within the colony require an explicit representation of the full temporal graph. We however also suggest that transport dynamics fully determine fungal growth (or the other way around, see Chapter 4) and that transport constraints on colony propagation could well be summarized by an additional cost for fast propagation (see Chapter 3). In that case microscopic transport traits could very well be fundamentally equivalent to coarse grain colony propagation traits.

6.2.4 Towards applications?

The ambition of the research performed during this PhD was mainly fundamental. We see however two ways in which it could serve as a basis to build towards concrete applications.

First, microscopic life is a strong driver of geochemical cycling at the planetary scale. Large scale model parametrization has however often been lacking some fundamental microscopic underpinning[2, 7]. The microscopic life is often represented with phenomenological rather than mechanistic models leading to large uncertainties if not systematic errors[7, 8]. Chapter 5 exemplifies how the kind of microscopic fundamental understanding from the lab can scale to potentially inform larger scale models.

Second, soil life is increasingly being recognized as an important element to take into consideration for the future of soils and agricultural system[9–11]. Leveraging the AM symbiosis has been suggested as a potential option to limit nutrient inputs and mitigate the general adverse effects on the environment of excess fertilization[12]. In the case of direct field inoculation of AM fungal spores the success as so far been variable[12] which may be the consequence of an inappropriate combination of fungal strain $\times$ plant host $\times$ fertilization scheme. Results shown in Chapter 3 may help narrow down the search for conditions under which AM inoculation could be most beneficial both in terms of plant growth but more generally in terms of environmental consequences. Beyond inoculation, agricultural practices can have direct effects on the composition and life cycle of living organisms over multiple year timescales[13, 14]. Current "omic" approach, while instrumental for monitoring are lacking interpretability[7]. Our imaging and work sheds a complementary light on AM fungi life and highlights the importance of the physical fungal density as a functionally significant indicator. Measuring it in field condition is currently tedious and is seldom done in experimental studies. It is even more rarely the case in soil analysis targeted towards end user like farmers. Simplifying the process of measuring AM density in soils could be instrumental to inform soil management practices. Leveraging modern image analysis tools could make the difficult hyphal counting step

automated. Alternatively, future work could try bridging yet an additional gap between "omic" data readily available from soils and physically meaningful AM traits observed in the lab in an analogical way to currently existing work on bacteria[7].

Bibliography

1. Maynard, D. S. *et al.* Consistent trade-offs in fungal trait expression across broad spatial scales. en. *Nature Microbiology* **4,** 846–853. ISSN: 2058-5276. http://www.nature.com/articles/s41564-019-0361-5 (2022) (May 2019).
2. Camenzind, T. *et al.* Towards establishing a fungal economics spectrum in soil saprobic fungi. en. *Nature Communications* **15,** 3321. ISSN: 2041-1723. https://www.nature.com/articles/s41467-024-47705-7 (2024) (Apr. 2024).
3. Heaton, L. L. M., Jones, N. S. & Fricker, M. D. A mechanistic explanation of the transition to simple multicellularity in fungi. en. *Nature Communications* **11,** 2594. ISSN: 2041-1723. https://www.nature.com/articles/s41467-020-16072-4 (2023) (May 2020).
4. Talkington, A. M. *et al.* Dermal Lymphatic Capillaries Do Not Obey Murray's Law. English. *Frontiers in Cardiovascular Medicine* **9.** ISSN: 2297-055X. https://www.frontiersin.org/journals/cardiovascular-medicine/articles/10.3389/fcvm.2022.840305/full (2024) (Apr. 2022).
5. McCulloh, K. A., Sperry, J. S. & Adler, F. R. Water transport in plants obeys Murray's law. en. *Nature* **421,** 939–942. ISSN: 1476-4687. https://www.nature.com/articles/nature01444 (2024) (Feb. 2003).
6. Murray, C. D. The Physiological Principle of Minimum Work. *Proceedings of the National Academy of Sciences* **12,** 207–214. https://www.pnas.org/doi/10.1073/pnas.12.3.207 (2023) (Mar. 1926).
7. Marschmann, G. L. *et al.* Predictions of rhizosphere microbiome dynamics with a genome-informed and trait-based energy budget model. en. *Nature Microbiology* **9,** 421–433. ISSN: 2058-5276. https://www.nature.com/articles/s41564-023-01582-w (2024) (Feb. 2024).
8. Wan, J. & Crowther, T. W. Uniting the scales of microbial biogeochemistry with trait-based modelling. en. *Functional Ecology* **36,** 1457–1472. ISSN: 1365-2435. https://onlinelibrary.wiley.com/doi/abs/10.1111/1365-2435.14035 (2024) (2022).
9. Coban, O., De Deyn, G. B. & van der Ploeg, M. Soil microbiota as game-changers in restoration of degraded lands. *Science* **375,** abe0725. https://www.science.org/doi/full/10.1126/science.abe0725 (2024) (Mar. 2022).
10. Van Groenigen, J. W. *et al.* Earthworms increase plant production: a meta-analysis. en. *Scientific Reports* **4,** 6365. ISSN: 2045-2322. https://www.nature.com/articles/srep06365 (2024) (Sept. 2014).

11. Bender, S. F., Wagg, C. & Heijden, M. G. A. v. d. An Underground Revolution: Biodiversity and Soil Ecological Engineering for Agricultural Sustainability. English. *Trends in Ecology & Evolution* **31,** 440–452. ISSN: 0169-5347. https://www.cell.com/trends/ecology-evolution/abstract/S0169-5347(16)00061-6 (2024) (June 2016).

12. Lutz, S. *et al.* Soil microbiome indicators can predict crop growth response to large-scale inoculation with arbuscular mycorrhizal fungi. en. *Nature Microbiology* **8,** 2277–2289. ISSN: 2058-5276. https://www.nature.com/articles/s41564-023-01520-w (2023) (Nov. 2023).

13. Jansa, J. *et al.* Diversity and structure of AMF communities as affected by tillage in a temperate soil. en. *Mycorrhiza* **12,** 225–234. ISSN: 1432-1890. https://doi.org/10.1007/s00572-002-0163-z (2024) (Oct. 2002).

14. Verbruggen, E. *et al.* Positive effects of organic farming on below-ground mutualists: large-scale comparison of mycorrhizal fungal communities in agricultural soils. en. *New Phytologist* **186,** 968–979. ISSN: 1469-8137. https://onlinelibrary.wiley.com/doi/abs/10.1111/j.1469-8137.2010.03230.x (2024) (2010).